The simulation of transient cross winds on passenger vehicles.

Mark K R. Docton

How to cite:

Docton, Mark K R. (1996) The simulation of transient cross winds on passenger vehicles. Doctoral thesis, Durham University.

The Simulation of Transient Cross Winds on Passenger Vehicles

by

Mark K.R.Docton

A Thesis submitted for the degree of

Doctor of Philosophy

School of Engineering

University of Durham

1996

Declaration

The work contained in this thesis has not been submitted elsewhere for any other degree or qualification and unless otherwise referenced it is the author's own work.

Acknowledgements

I am most grateful to my supervisor Dr. Robert Dominy for the support, guidance and encouragement offered to me throughout this project.

I would also like to thank the staff of the School of Engineering who have provided me with assistance during my period as a research student. In particular I should like to mention the endeavours of Mr. Brian Blackburn and Mr. Ian Glassford.

Thanks must also be extended to the Engineering and Physical Sciences Research Council whose financial support is gratefully acknowledged.

Finally I should like to recognise the contributions of my fellow research students whose expertise, intellect and assistance I have had occasion to appropriate. In particular I should like to thank Stephen Robinson whose enthusiasm has proved invaluable.

The Simulation of Transient Cross Winds on Passenger Vehicles

Mark K.R.Docton

Abstract

This thesis presents an account of the design, development and utilisation of an experimental apparatus, based on a new experimental technique, for the simulation of transient cross winds on passenger vehicles. The new experimental technique utilises the conventional stationary aerodynamic model and wind tunnel configuration. The transient cross wind is created about the stationary model by means of a separate angled air jet whose influence on the model is initially obscured then permitted by means of a rapidly moving shutter. The air velocity, with respect to the vehicle, has been configured to exactly mimic the velocity components experienced by a road vehicle travelling at speed under the action of an instantaneous cross flow region of finite duration.

This new technique improves on an existing moving model technique that requires any aerodynamic instrumentation to move with the model. This can cause the gathered data to suffer from non-aerodynamic borne noise that masks the desired aerodynamic signal. The new technique under investigation allows utilisation of stationary conventional wind tunnel instrumentation and thus avoids data corruption by that means.

This new technique has been found to produce the desired cross wind transient pulse in the wind tunnel working section. A simple 2D aerodynamic model has been subjected to the transient cross wind conditions. The surface pressures induced on the windward side of the model respond quickly to the transient conditions and attain expected magnitudes. The leeward side surface pressures however respond more slowly to the transient conditions but attain highly exaggerated magnitudes compared to those from time averaged conditions. The exaggerated pressure response is especially significant in suction zone at the leeward front corner of the model.

The simulation technique offers significant scope for further study of transient cross wind behaviour. The main challenges in the development of the simulation apparatus, those of the moving aperture system, have been over come and additional aerodynamic experimentation is straight forward.

List of Contents

List of Figures

List of Tables

Nomenclature

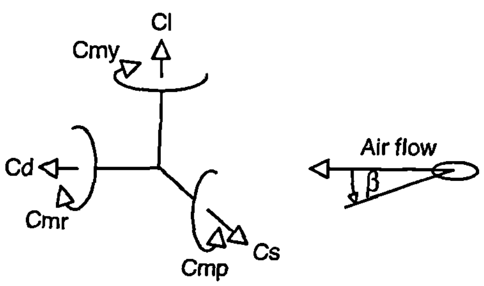
Aerodynamic load sign convention

A	Vehicle frontal area at zero yaw
Cd	Drag force coefficient - Fd / $\frac{1}{2}\rho Au^2$
Cl	Lift force coefficient - Lift force / $\frac{1}{2}\rho Au^2$
Cl f	Front axle lift force coefficient
Cl r	Rear axle lift force coefficient
Cs	Side force coefficient - Fs / $\frac{1}{2}\rho Au^2$
Cs f	Front axle side force coefficient
Cs r	Rear axle side force coefficient
Cmp	Pitching moment coefficient - Pitching moment / $\frac{1}{2}\rho Au^2 l$
Cmr	Rolling moment coefficient - Rolling moment / $\frac{1}{2}\rho Au^2 l$
Cmy	Yawing moment coefficient - My / $\frac{1}{2}\rho Au^2 l$
Cp	Pressure coefficient - $(p - p_\infty) / (p_{O\infty} - p_\infty)$
Fd	Drag force
Fs	Side force
l	Representative vehicle length
My	Yawing moment
p	Local surface pressure
p_∞	Static free stream pressure
$p_{O\infty}$	Stagnation free stream pressure
Re	Reynolds number - $\rho ul / \mu$
Tu	Turbulence intensity - rms air velocity / average air velocity
u	Air velocity
u_{cw}	Resultant cross wind velocity
u_{cws}	Velocity of the moving cross wind source
u_{mj}	Air velocity of the main jet
u_s	Velocity of the moving shutter
u_x	Axial (streamwise) air velocity
u_y	Cross stream (transverse) air velocity
Xcp	Distance of lateral centre of pressure forward of moment centre as % of l
β	Yaw angle
ρ	Air density
μ	Air absolute viscosity

1.0 Introduction

1.1 Overview of Vehicle Aerodynamics

The air flow round a road vehicle is highly complex. A typical vehicle shape may be considered as a bluff body and is thus characterised by numerous regions of separated and therefore turbulent flow. The geometry of a vehicle produces low aspect ratios and as such secondary flow effects are also significant. The proximity of the ground plane to a vehicle under side combined with the presence of rotating wheels provides additional effects on the over all flow regime. These factors render numerical predictions of 3D vehicle air flows beyond current capabilities of correct turbulence modelling (for example [41, 22, 3 & 21]) and therefore experimental investigations are significantly utilised. The flow fields of individual vehicles have been studied but a range of typical time averaged flow regimes present around a vehicle are shown by figures 1.1a and 1.1b [29].

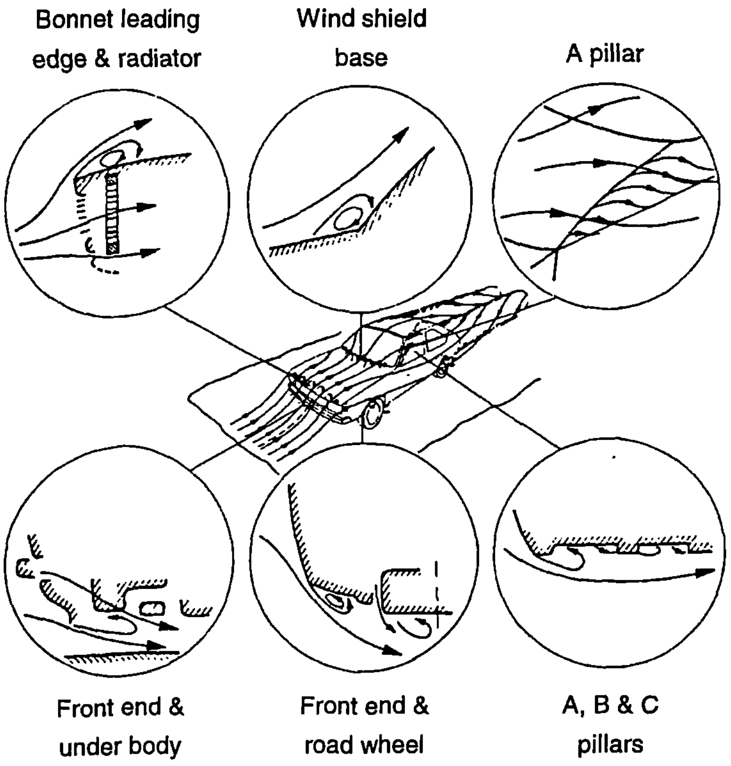

Fig. 1.1a - General schematic of front end vehicle time averaged flow regimes [29].

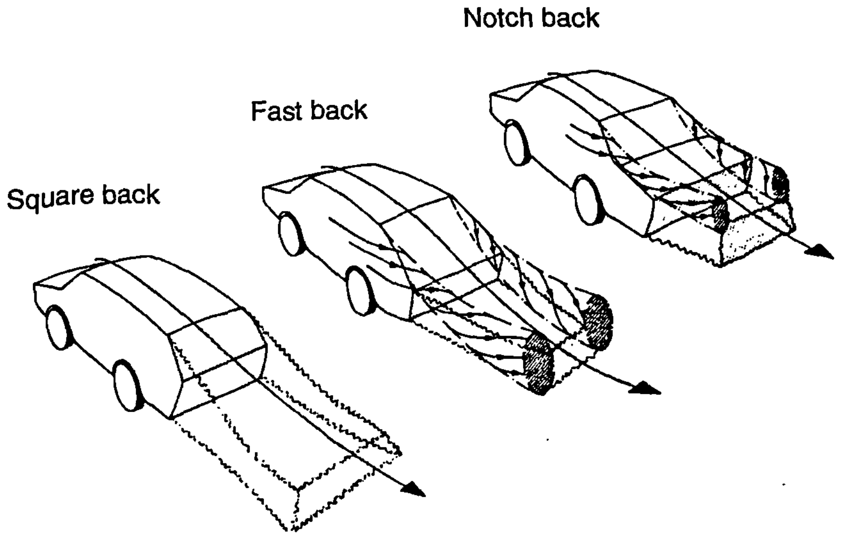

Fig. 1.1b - General schematic of rear end vehicle time averaged flow regimes [29].

Figure 1.1a shows the presence of separations at specific vehicle points, for example at the bonnet leading edge and front wheel. The 3D nature of the flow field may also be seen. Air flow over the bonnet both continues over the top of the vehicle and is also deflected down the vehicle the sides by the presence of the wind shield. The A pillar (the body work pillar at each edge of the wind shield) is also shown to induce a flow separation by figure 1.1a as does the B pillar (the body work pillar between the front and rear side windows). The air flow through the radiator must also be considered as should any flow interaction at the vehicle under side. Figure 1.1b shows the general flow regimes developed at the rear of three typical vehicle shapes (square back, fast back and notch back). The air flow at the rear of vehicles is dominated by a large wake. In the case of the square back the air flow fully separates at the roof trailing edge, C pillar (the rear most body work pillar) and the lower sides of the vehicle. For the fast and notch back shapes the flow remains attached at the roof trailing edge and the resulting low pressure, due to the flow acceleration over back light (the slanted rear portion of the vehicle), entrains flow from the vehicle sides inducing the formation of contra-rotating vortices in the wake. Each of the general effects highlighted by figures 1.1a and 1.1b are significant to a vehicle aerodynamicist in differing ways. It may be summarised [7] that the impact of aerodynamics on the design of road vehicles falls broadly into the categories shown by table 1.1.

Performance	Fuel economy, maximum speed and acceleration.
Stability	Directional and cross wind sensitivity.
Cooling	Engine, transmission and brakes.
Visibility	Spray, dirt deposition and wiper lift.
Comfort	Air conditioning, ventilation and wind noise.

Table 1.1 - Summary of aerodynamic aspects of vehicle design.

Drag reduction has been the significant influence on the direction of vehicle aerodynamic investigations. Lower vehicle drag not only improves the direct performance of a given vehicle but also reduces the fuel consumption and therefore exhaust emissions. The drag force may be minimised by reducing the degree of separation at the vehicle surface for example the leading edge of the bonnet may be rounded and the detail of the A, B and C pillar regions may be smoothed to reduce the separation (see figure 1.1a).

Vehicle stability is determined not by drag but by the other components of aerodynamic force. The aerodynamic lift force and pitching moment of a vehicle determine the distribution of effective down force to each axle and thus affect the under or over steer characteristic whilst the aerodynamic side force, yawing moment and rolling moment of a vehicle affect the behaviour in cross wind conditions. Trends in styling toward more rounded shapes have been blamed for the increased sensitivity of passenger vehicles to cross winds by way of increased yawing moment. However studies show [27] that it is mainly well rounded rear surfaces, especially in hatchbacks, that enhance this susceptibility. Low drag vehicle shapes have also been found to increase the yawing moment induced in a cross wind and so a compromise is necessary between performance and stability. High sided vehicles in cross winds produce large rolling moments which act to over turn the vehicle [9]. The aerodynamic centre of high sided vehicles is typically above the centre of gravity [2] and so are particularly susceptible to induced rolling moments.

The heat generated during the working conditions of a vehicle engine and braking system must be dissipated to ensure efficient operation. The air flow over the vehicle may be utilised to cool vehicle components, for example the engine via the radiator, and to control the passenger compartment environment. Trends toward more compact vehicle designs together with increasing engine powers respectively restrict the space available for cooling systems and require increased heat dissipation and so particular attention must be paid to optimising the cooling air flows. However increased cooling air flows incur a drag force penalty. Typically the total heat control air flow (that of the component cooling and passenger compartment ventilation) comprises up to 20% of the total vehicle drag [17] by virtue of an increased transfer of momentum from the air flow to the cooling component, for example the radiator, and so a compromise must be reached in the aerodynamic design.

The air flow over vehicle surface at the wind shield, side windows and the back light (see figures 1.1a and 1.1b) affects the visibility offered to the driver. In wet conditions spray or drain water from the roof may be deposited on the vehicle at these points. The vehicle wake (see figure 1.1b) offers particular problems. The recirculating wake vortices can entrain, for example, wheel spray or road surface mud with a resulting deposition on the back light region obscuring the rear view for the driver. In addition in wet conditions the wake significantly affects the driver visibility of both trailing and on coming vehicles.

In a similar sense to the cooling air flow required by the engine and brakes the passenger compartment of a vehicle requires a continuous supply of air for ventilation, heating or air conditioning purposes. Ultimately this is derived for the external air flow and so the positioning of the intakes for the passenger compartment air flow (usually from the cowl region at the base of the wind shield) must be considered. The drag force penalty of these air flows is significantly less than that of the cooling air flow but it is important that the ventilation flow is derived from air relatively uncontaminated by emissions and as such the location of the intakes is critical. Noise, additional to that created by the engine and tyres, is induced by the air flow over the vehicle. Regions of flow attachment after separation have been found [30] to produce significant aerodynamic noise, for example the flow immediately behind the A pillar (see figure 1.1a). In addition periodic low frequency noise fluctuations occur at specific speeds at open side windows or sun roofs.

The aerodynamic requirements (see table 1.1) produce numerous areas of concern in vehicle design. The complicated nature of the flow field (see figures 1.1a and 1.1b) has forced aerodynamicists to undertake experimental investigations using simplified vehicle shapes to assist with the understanding of the developed flow regimes. A commonly adopted vehicle shape (the 'Ahmed' model [1]) consists of a cuboid of over all relative dimensions of 3.36 to 1.37 to 1 (length to width to height) and is shown by figure 1.2.

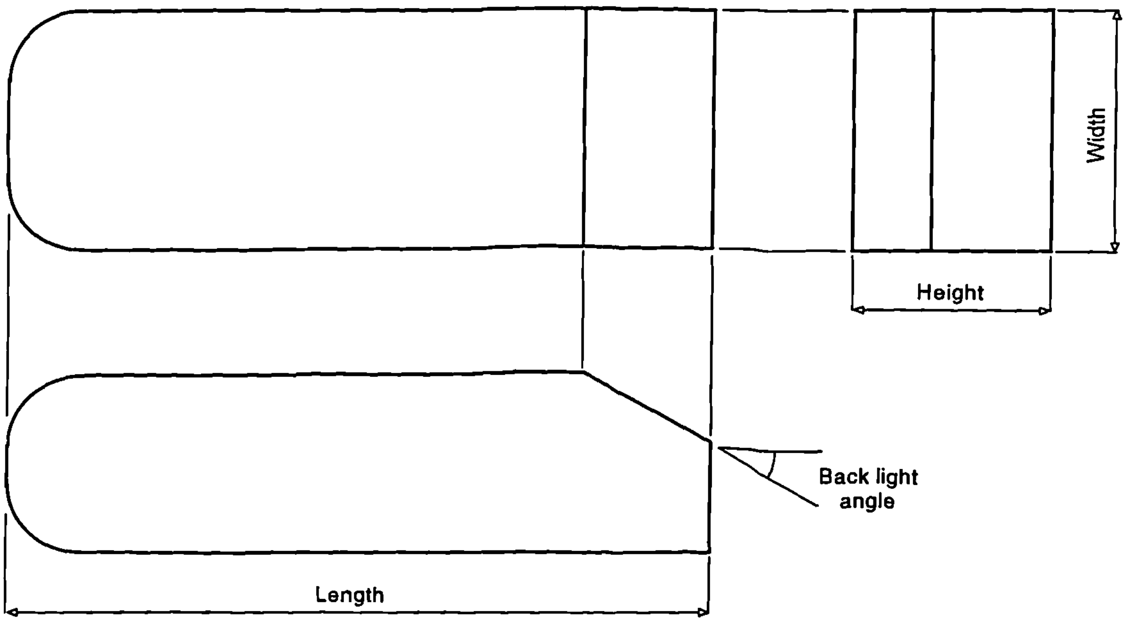

Fig. 1.2 - Simplified 3D vehicle shape.

The corners at the vehicle leading edge are rounded to ensure separation free flow after the front end. The middle section of the vehicle has parallel sides and the rear vehicle section has a slanted upper surface to simulate the back light region (see figure 1.1b). Aerodynamic investigations, both experimental and numerical, have been made on this and similar simplified vehicle shapes (for example [1, 41, 38, 3 & 21]) and particular attention has been devoted to the flow regime developed both at the rear upper surfaces and in the wake with differing back light angles and the resulting effect on drag force. The schematic form of a time averaged wake flow is shown by figure 1.3.

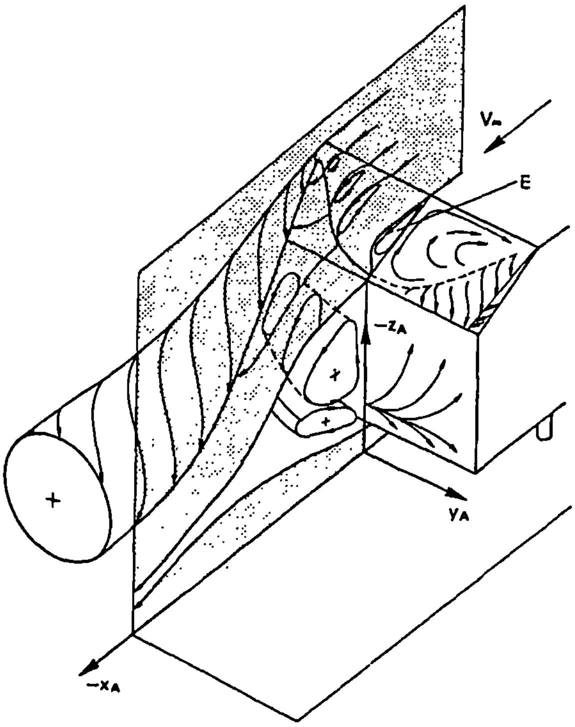

Fig. 1.3 - Schematic form of a time averaged wake flow for a 30° back light angle [1].

Figure 1.3 shows the wake structure for one side of the vehicle only. The time averaged flow regime for the other vehicle side is mirrored about the indicated plane of symmetry. A separation bubble is formed on the back light angle (see figure 1.3, label 'E') whose dominance reduces toward the vehicle side due to the presence of a large entrained wake vortex from the vehicle side. The rear vertical face of the vehicle is also dominated by separated flow which takes the form of lower and upper contra-rotating vortices formed respectively from the under body flow and the reattached flow on the back light. At back light angles of 25° and under the air flow remained attached at the back light region and the strength of contra-rotating side vortices was dependent on this slant angle [1]. At back light angles of 35° and over the air flow fully separated at the back light region [1]. The contribution to drag force at all back light angles was found to be dominated by the rear end pressure drag (~75%), with the remaining drag contributions arising from the front end pressure drag (~5%) and the full body skin friction drag (~20%) [1].

Figures 1.1a, 1.1b and 1.3 illustrate the complex nature of vehicle air flows even for highly simplified shapes but it should be noted that these effects have been studied on a time averaged basis. Any turbulent air flow is time dependent. Only by time averaging the flow effects can the wake be depicted in this way. To gain a true picture of the air flow it is necessary to gain sequenced instantaneous appraisals of the flow. This is readily illustrated by, for example, the alternate wake vortex shedding by cylindrical shapes at specific Reynolds numbers [36]. The shed vortices are known to produce an oscillatory aerodynamic loading on the cylinder with time. If however any measured loading is time averaged no oscillatory nature will be detected. Time averaged aerodynamic parameters are thus quasi-steady as the 'steady' nature of the flow is numerically induced. It has been shown [23] that the instantaneous flow regime at a vehicle back light region is one of multiple small scale shed vortices superimposed on the main attached contra-rotating vortex wake structure. The small scale vortices have also been shown [23] not necessarily to rotate in the sense exhibited by the time averaged results at given vehicle locations. Only by time averaging does a relatively neat and symmetrical wake flow emerge. The vast majority of vehicle aerodynamic investigations have been directed towards time averaged flow regimes developed in steady free stream conditions, in as much as a free stream condition can be steady. The investigations undertaken by the author have been ultimately directed towards time dependent flow regimes developed in transient free stream conditions, where the effects of a fundamental bulk change in the free stream velocity with time are studied.

Studies of vehicle aerodynamics are conventionally undertaken in a wind tunnel. The vehicle is held stationary in the working section of the wind tunnel and an air flow is induced over the vehicle. This relative movement of air to the vehicle creates the effective road speed. To exactly simulate the road conditions it would be required that the ground plane on which the vehicle is mounted in the wind tunnel moves with the same velocity of the free stream working section air flow. This would mimic the correct relative motion of the real road surface to the vehicle. In addition it would be required that the road wheels contact and rotate freely with this moving ground plane. The bulk of wind tunnel vehicle aerodynamic investigations until recently have however been undertaken using a stationary ground plane and fixed wheels which is a simplification to the ideal road going conditions. This simplification has been generally made on the basis of minimising the cost and operational effort of a given wind tunnel facility. The expense of installing a moving ground plane to a wind tunnel combined with the additional experimental complications of suspending a vehicle above the moving ground plane and inducing wheel rotation can prove prohibitive. As vehicle aerodynamics has become more refined the accuracy of the stationary ground plane and fixed wheel configuration has been called into question. Investigations using simplified non-wheeled vehicle shapes (for example [32, 24 & 16]) with and without the influence of a moving ground plane have shown that for low ground clearances, under 10-20% of the vehicle height, the correct moving ground simulation has been shown to produce significant time averaged flow and load discrepancies when compared to a stationary ground simulation. These discrepancies however cannot be readily generalised and are specific to the vehicle geometry tested. Ground clearances of 20% and above (a typical passenger vehicle value) of the vehicle height have been shown to produce negligible time averaged flow and load discrepancies in these cases. If only comparative aerodynamic changes are to be studied, induced by shape modifications to high ground clearance basic vehicle forms using a given wind tunnel facility, a moving ground simulation is not required [32, 24 & 16]. For vehicle shapes with under body detail, low ground clearances or simulated rotating wheels correct moving ground simulation is being increasingly utilised (for example [11, 37, 45, 46 & 6]).

1.2 Transient Cross Wind Aerodynamic Effects

The influence of unsteady cross winds on passenger vehicles is a phenomenon known to all drivers. The transient aerodynamic forces induced on the vehicle can cause rapid driver reaction which is both unsettling and potentially hazardous. Physical features close to the roadside, for example embankments, gaps in hedges or bridge abutments, can enhance the effects of the cross wind by increasing the local cross wind component [15] above that of the ambient wind. The magnitudes of typical natural ambient winds at ground level have been assessed [35] and it may be shown that natural wind speeds close to these physical features of 30 miles per hour or over can occur on 1.5% of occasions. A resultant air flow yaw angle would be induced relative to the vehicle by the vector addition of the cross wind and vehicle velocities. If the direction of this wind is perpendicular to a carriage way and, for example, a 50 mile per hour vehicle velocity is considered the resultant air flow when combined with a 30 mile per hour cross wind velocity would yield a vehicle relative yaw angle of 31° and a vehicle relative flow velocity of 58 miles per hour. A vehicle travelling at speed would be subjected to a sharp change in aerodynamic loading on passing into a region of strong natural air flow across the carriage way as both the relative vehicle yaw angle and velocity change. Initially only the front end of the vehicle would be subjected to yawed flow on entering the cross wind region. The driver of this vehicle would be required to suddenly control the vehicle against the action of this air flow. The remainder of the vehicle would then pass fully into the cross wind and the driver would again be required to control the vehicle against these changing vehicle air flow conditions as the yawed air flow envelopes the entire vehicle. This sudden driver compensation is the potential source of hazard and is distinct from a constant cross wind which requires only a constant steering compensation. Transient effects also occur during the overtaking of other vehicles, particularly high sided vehicles and especially during the presence of a cross wind. Knowledge relating the time dependent aerodynamic load changes induced on a vehicle under the action of transient cross wind conditions is desired so as the allow the vehicle handling implications to be studied with an ultimate aim to reduce the hazard level.

An initial assumption regarding transient cross winds might be that the aerodynamic effects on a vehicle for a given yaw angle correlate directly to the time averaged aerodynamic effects at the same yaw angle. That is to say a vehicle on entering a region of yawed flow from zero yaw conditions switches instantaneously from time averaged zero yaw flow to time averaged yawed flow as the vehicle is enveloped in the cross wind. If this were the case only the relative position of the vehicle, for example at a point when only the front end is subjected to yawed flow, need be considered when calculating the aerodynamic loading and therefore only the time averaged yaw characteristics of a vehicle would require investigation. These time averaged yaw characteristics can be easily assessed in the wind tunnel by setting a vehicle a differing fixed yaw angles with respect to the free stream velocity and recording, for example, the developed time averaged aerodynamic pressures or loads. It is unknown to what level this initial assumption is valid and therefore a method of simulating the aerodynamic effects of transient cross winds is required. This is less easily implemented by virtue of the requirement to simulate a sudden change in vehicle relative yaw angle and velocity. Various simulation methods however are available.

The effects of a transient cross wind on a particular vehicle are usually determined using a full scale vehicle test track and cross wind generation facility. Such a facility comprises a straight section of road with an artificially induced air flow, for example by means of large fans, blowing perpendicularly across the track. A vehicle may be driven at speed through the cross flow region to assess the handling characteristics. However this test technique has several disadvantages at both implementation and results analysis. In addition the benefits of the prediction of unsteady cross wind performance of a vehicle earlier in the design stage, prior to the manufacture of a full scale vehicle prototype, would allow any necessary design modifications to be made at the pre-prototype stage and hence at much reduced cost.

A current vehicle model scale method of unsteady cross wind simulation propels a model along a track through still air to create an axial wind relative to the car (for example [18]). The cross wind effect is then created by passing the moving model through a jet of air which blows perpendicular to the track; usually generated by a wind tunnel with open sides to allow the model to pass across it. This method correctly mirrors the physical conditions present in the real situation, including the relative motion of the vehicle to the ground and potentially the cross wind boundary layer. However the technique requires the instrumentation to move along with the model itself which causes the instrumentation to suffer dynamic transients due to the motion of the model along the track thereby reducing the ability to monitor the aerodynamic model effects that are required. The potential for the study of the vehicle wake is also particularly difficult as the necessary instrumentation is required to travel along behind the model. Experimental results using this technique [18], recording the global transient aerodynamic forces induced on a model, have been gathered and have been shown to suffer from these dynamic non-aerodynamic borne transients. In addition the author is unaware of any experimental results have been presented concerning the local transient aerodynamic model surface effects assessed by means of pressure tappings. The results from these techniques do however suggest that a cross wind duration produced by a simulation technique of approximately three model lengths is required to examine the full nature of any transient aerodynamic effect, although this hypothesis is by no means conclusive.

A simulation method that utilises the established stationary aerodynamic model and wind tunnel configuration would be advantageous as any instrumentation, whether aerodynamic force or pressure monitoring, would be stationary. This both eases the design of the instrumentation and removes any dynamic transients induced by the model movement.

It was the rôle of the author to design, develop, commission and utilise a new transient cross wind simulation test technique based on a stationary model and wind tunnel configuration. Initial conceptual investigations with the resulting design, manufacture and installation of the experimental apparatus to achieve this aim comprised the initial two thirds of the research project duration. The development of the installed experimental apparatus culminating in the aerodynamic assessment of the new test technique comprised equal portions of the latter one third project duration. The nature of the aerodynamic results sought was exploratory so as to determine the validity of experimental technique for any future development. However the results gained were sufficiently thorough not only to validate the technique at this exploratory stage but also to uncover transient aerodynamic phenomena of significant importance.

2.0 Overview of Existing Test Techniques

2.1 Introduction

There currently exist various experimental test techniques to assess the cross wind sensitivity of a particular vehicle shape. The techniques fall into two main categories: time averaged aerodynamic testing and transient aerodynamic testing. These two techniques may be applied to either full or model scale vehicles. Time averaged techniques record, for example, the aerodynamic pressures or loads induced on a vehicle when subjected to a particular constant air flow yaw angle whereas current transient techniques attempt to measure similar parameters whilst subjecting a vehicle shape to a rapid change in yaw angle which is achieved by progressively, along the vehicle length and at the effective vehicle road velocity, exposing the vehicle to yawed conditions.

2.2 Full Scale Test Techniques

Full scale tests are by their very nature the absolute method of aerodynamic appraisal of a vehicle. The parameters measured during the test need not assume Reynolds number independence as the recorded magnitudes of the parameters will be exactly (or very close to) those required for any vehicle loading calculations. In addition the physical size of a full scale vehicle allows the complete detail of the vehicle surface to be incorporated accurately. However full scale tests are expensive both in the cost of the facilities and the man hours required. In addition any alterations to a vehicle shape desired as result of the full scale testing will be costly to implement as, like all production items, alterations late in the development cycle require reappraisal and alteration of production systems, for example a change to the press tooling for vehicle body panel stamping. If an alteration is actually implemented to the vehicle shape it will also have to be relatively minor, for example the addition of mouldings or strakes to the vehicle surface, so as not to detract from the overall styling concept. Full scale vehicle tests however still form part of a vehicle development cycle if only to confirm aerodynamic properties or to use in the development of an ensuing model.

A typical example of a full scale test facility may be found at the Motor Industry Research Association (M.I.R.A.) proving ground [35]. The wind tunnel is a closed section, open return type [28] with working section dimensions of approximately 8m by 4m by 15m (width by height by length). The test section air velocity may be continuously varied up to 36m/s (80 mph). The tunnel is equipped with a sub-ground plane six component force balance connected to a ground plane rotatable turntable on which a vehicle may be positioned. This arrangement facilitates monitoring of time averaged aerodynamic loads at various constant yaw angles. Other aerodynamic instrumentation is available, for example surface pressure tappings and flow visualisation smoke generators, for use in the working section.

2.2.1 Time Averaged Fixed Yaw Testing

Time averaged tests subject a vehicle to a constant yaw angle and measure, for example, the induced aerodynamic pressures or loads. This is usually achieved by the use of a turn table arrangement in a full scale wind tunnel on which a vehicle is mounted. The turn table positions the vehicle at a predetermined range of yaw angles and at each the air flow around the vehicle may be assessed.

This test technique is relatively easy to implement if only the measurement of aerodynamic loads are required but becomes more time consuming if the knowledge of the local pressures developed at the vehicle surface is sought. The measurement of loads gives a global view on the cross wind sensitivity of a particular vehicle where as local surface pressure measurement allows a complete appraisal of the air flow conditions at each point on the vehicle surface in addition to the global effect. The latter is therefore ultimately more useful to an aerodynamicist but as it requires a significant level of vehicle preparation by way of location and fixing of pressure tappings the general practice is to assess only the cross wind sensitivity of a vehicle in terms of induced loads. However full vehicle surface pressure surveys are undertaken and an example of such an investigation may be seen in chapter 9 (additional example given by [25]). The investigation detailed in this chapter was undertaken by the author in conjunction with the Rover Group and examines the cross wind sensitivity of the current Range Rover vehicle.

Constant natural cross winds are not, except in extreme circumstances, particularly hazardous as only a constant steering compensation is required by the driver. Of significant importance however are the vehicle handling implications induced by the aerodynamic effects of transient cross winds.

2.2.2 Transient Yaw Testing

To test transient yaw conditions it is necessary to simulate an idealised standard cross wind transient effect on a vehicle. The generally accepted simulation parameters are to initially subject a vehicle to zero yaw flow conditions then to subject the vehicle to yawed flow conditions for a finite time before finally returning the vehicle to zero yaw air flow. This is best achieved by the use of a test track and cross wind generation facility (for example [26, 40 & 34]) as shown by figure 2.1.

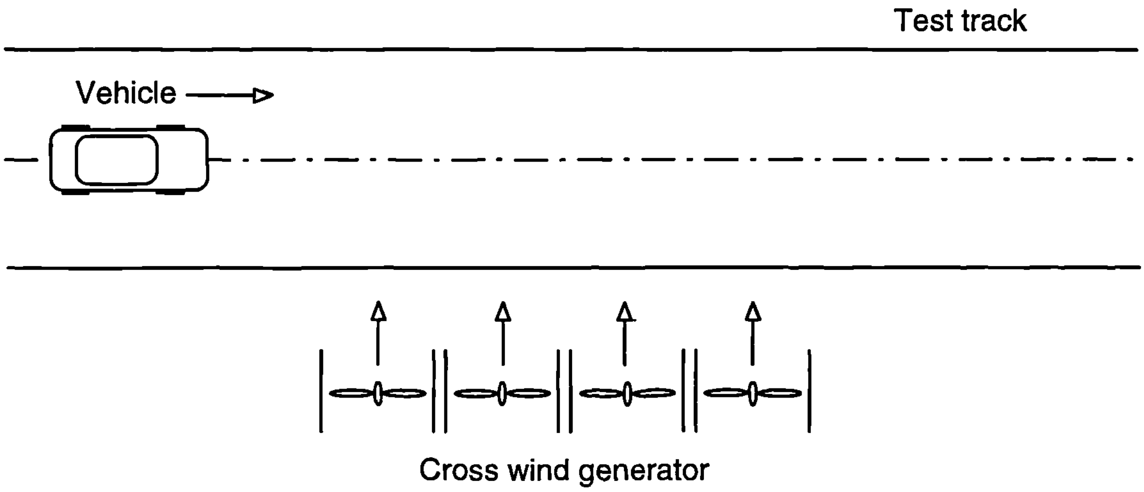

Fig. 2.1 - Schematic plan view of full scale test track and cross wind generation facility.

The test track consists of a straight section of road. Midway along the length of the road is positioned a cross wind generation system acting perpendicularly across the track. The cross wind generation may be achieved by various means (for example a system of fans - see figure 2.1) but must generally induce a large volume of uniform air flow across the test track over a height greater than that of the vehicle and over a width of the order of several vehicle lengths. A driven vehicle may be accelerated to speed along the test track prior to the simulated cross wind region allowing an axial flow regime to develop, passed through this region to finally emerge from the cross flow to return to axial flow conditions. During this test the effects of the transient cross wind on the vehicle may be assessed. The nature of this test requires a drivable vehicle which will probably be needed for additional aerodynamic and non-aerodynamic tests at a later date. This therefore limits the level of instrumentation that may be installed. However accelerometers may be fitted to the vehicle which would ultimately yield information relating the loads developed on the whole vehicle during the simulated transient cross wind. The deviation from the straight line path of the vehicle due to the effects of the simulated cross wind may also be monitored. This can be achieved by trailing a dye fluid from the rear of the vehicle which leaves a visible trace on the test track surface or by integrating the recorded lateral acceleration readings, derived from an accelerometer, to ultimately yield a lateral displacement value.

This transient test technique has several disadvantages. If a constant simulated cross wind region is required ideally the ambient atmospheric air flow conditions at the test track site must be zero. Only if this is the case will the results from testing different vehicles on different occasions be directly comparable. This places a limitation on the testing time available even if very low ambient air flows are tolerated. The test vehicle requires a driver. All drivers have differing abilities and therefore would control the vehicle in differing ways when subjected to the cross flow conditions. This would suggest that the same driver must be used for a given series of tests. Even if this is achieved it is improbable that the same driver will always react in an identical manner between tests. It is possible however to fix the steering wheel during the tests to remove this unknown but still retain the driver to accelerate the vehicle to speed and then to rest. However this latter approach has obvious safety implications. In addition to removing the influence of the driver between different vehicles it is also necessary to remove the non-aerodynamic effects of the actual vehicle. These effects are those induced most notably by the chassis and suspension. When a vehicle is subjected to a cross flow the induced loads on the body will cause it to roll, pitch and yaw. These resulting movements will in turn present a differing vehicle profile to the air flow causing a further change in the loading conditions. It is therefore impossible to examine the pure aerodynamic response of a vehicle shape using this technique without including the dynamic effects of the driver, steering, suspension and chassis.

However this test technique is utilised and a particular example is the cross wind generation facility at the M.I.R.A proving ground. Various vehicles have been tested at this and similar facilities (for example [26, 40 & 34]).

2.3 Model Scale Test Techniques

Model scale techniques offer advantages over those at full scale in that an increased range of potential vehicle shapes may be tested early in the development cycle as the final vehicle shape has yet to be firmly fixed. The resulting tests are also less costly by virtue of the scale of the facilities required. However in order to simulate the full scale conditions correctly the Reynolds number at full and model scale must correlated. For the full and model scale Reynolds numbers to be equal for a given vehicle shape the air flow velocity at the model scale tests must be greater than the full scale test velocity, by a factor equal to that of the scale, for exact dynamic modelling similarity. For example a ¼ scale model must be tested at four times the full scale air velocity. This renders exact modelling impractical for small scale models due to the increasing proximity of the correct simulation velocity to sonic conditions where the compressibility begins to influence the flow.

The separated regions of vehicle flow (see figures 1.1a, 1.1b and 1.3) will control the overall flow regime. These separations are induced at areas of vehicle shape change, for example the roof trailing edge or cowl region. For bluff bodies, including vehicles, where separated flow is predominant the effect differing of Reynolds number on the developed flow regime reduces above certain Reynolds number values allowing scale models to be tested satisfactorily at velocities lower than the ideal [28] by virtue of the flow regime being largely dictated by the shape of the body and not the free stream air flow conditions. For a flat plate held perpendicular to an air flow, thus producing the ultimate bluff body form, Reynolds number independence, based on perpendicular plate length and monitored by induced drag force, occurs at $Re > 1000$ [36]. The air flow regime developed by a flat plate between $Re = 1000$ and a Mach number of ~0.3 is thus entirely independent of free stream conditions as flow separation is always present at exactly the same point (the edges of the plate). For a less bluff body such as a cylinder the air will separate at differing locations depending on both the free stream conditions and the level of surface roughness present on the cylinder. Conditions which allow a laminar boundary layer to form at the cylinder surface will produce a flow regime as displayed by the left hand portion of figure 2.2 whereas conditions which induce a turbulent boundary layer at the cylinder surface will produce a flow regime displayed by the right hand portion of figure 2.2.

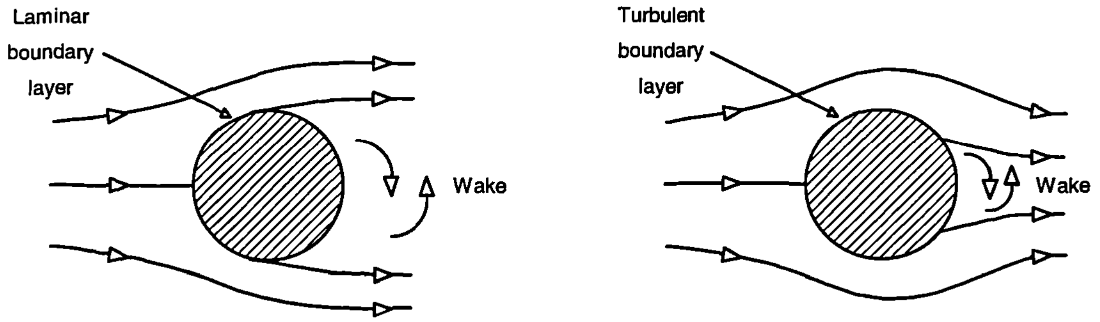

Fig. 2.2 - Cylinder time averaged flow regime for laminar and turbulent conditions.

Increasing the free stream turbulence or surface roughness of the cylinder will encourage the formation of a turbulent boundary layer. Even for laminar free stream conditions and a smooth cylinder surface there exist a critical Reynolds number of $5\mathrm{x}10^5$ [36], based on surface length for a flat plate with zero incidence, at which an initially formed laminar boundary layer will become turbulent. Turbulent conditions are also induced by any region of separated flow due to the formation of an unsteady wake structure immediately down stream of the separation. Thus providing that air flow separation is induced at the same surface point for both full and scaled aerodynamic models at respective free stream air velocities Reynolds number independence may assumed. Bluff body Reynolds number independence is therefore more easily achieved for a flat plate than for a cylinder. Model scale vehicles possess the same level of sharp bulk shape changes as full scale vehicles and will therefore produce the same separated flow regimes. In vehicle aerodynamics the Reynolds number independence may be practically assessed by monitoring, for example, the drag force at a range of free stream air velocities. If the drag force coefficient remains constant across that range a Reynolds number independence is assumed. Modern trends toward smoother vehicle shapes, resulting in reduced front end separation (vehicle rear end separation is practically guaranteed with current designs), will however reduce the accuracy of aerodynamic model tests undertaken at current model scale test velocities. Providing however that only comparative aerodynamic parameter changes are required the scaling criterion transpires to have no severe restriction to valid model aerodynamic testing which is used to a significant level by vehicle aerodynamicists.

The measurement of surface pressures, like full scale testing, still requires more preparation than measuring the aerodynamic loads but is on balance substantially more straight forward than full scale surface pressure measurement. Model scale testing allows other aerodynamic parameters such as wake velocity or surface shear stress measurements to be relatively easily undertaken in comparison to full scale tests.

2.3.1 Time Averaged Fixed Yaw Testing

Time averaged testing at the model scale is similar to the method employed at full scale. A vehicle shape is mounted on a turntable arrangement in the working section of a wind tunnel and the vehicle is yawed to a predetermined range of air flow angles. At each the measurement of time averaged aerodynamic pressures or loads is undertaken. As with full scale testing the measurement of surface pressures is more useful than recording the induced loads. An example of such a test is shown in section 7.2.3.

2.3.2 Transient Yaw Testing

Transient techniques that currently exist at the model scale are, like the time averaged techniques, based on the full scale testing. If one is to simulate a transient cross wind effect at the model scale the first logical approach would be to mimic a full scale test track and cross wind generation facility. Various test facilities have been developed (for example [5, 18, 31 & 47]) which all utilise the same implementation method. A vehicle model is fixed to a straight guide track by a mobile support carriage. The carriage, together with the vehicle is accelerated to speed along the track in bulk still air. This provides the axial air velocity relative to the model. The moving model then passes through a jet of air which is configured to blow perpendicularly to the path of the model; usually generated by a wind tunnel with open sides to allow the model and track to pass across it. This test technique is analogous to the full scale technique, illustrated by figure 2.1, where the test track represents the mobile support carriage and guide track assembly and the cross wind generator represents the perpendicularly acting wind tunnel. Once the model has fully passed through the simulated cross flow caused by the wind tunnel it is brought to rest. This simulation method correctly mirrors the accepted cross wind simulation conditions; those of a step input of uniform cross flow superimposed on the axial flow over the model, including the relative motion of the model to the ground plane. However this technique requires the instrumentation to move along with the model. If, for example, an aerodynamic force balance is attached to the vehicle any non-aerodynamic movements or vibrations of the vehicle induced by the acceleration of the model along even a slightly uneven guide track will be transmitted to the force balance, as ultimately the forces are recorded by changes in the strain at specific locations in the balance. In this way the aerodynamic force data recorded will be corrupted by dynamic model movement signals which mask the desired aerodynamic data.

Examples of the transient side force and yawing moment recorded by a force balance at a moving model facility [18] are shown by figures 2.3a and 2.3b. The loads recorded were induced on a flat plate mounted to the mobile support carriage parallel to the direction of motion. The flat plate ground velocity was 15.0m/s as was the perpendicularly acting cross flow velocity resulting in a relative yaw angle of 45°. Each figure displays both a raw and a resulting smoothed trace. The cross flow velocity was produced by a wind tunnel of dimensions 2.4m by 1.2m (width by height) with open sides to allow the plate to pass through and the flat plate was 0.48m by 0.2m (length by height). The four spikes on the x axis of figure 2.3a represent when the leading and trailing edges of the plate entered and exited the wind tunnel working section and these four points may be transferred directly to figure 2.3b. The wind tunnel width was five times that of the plate length.

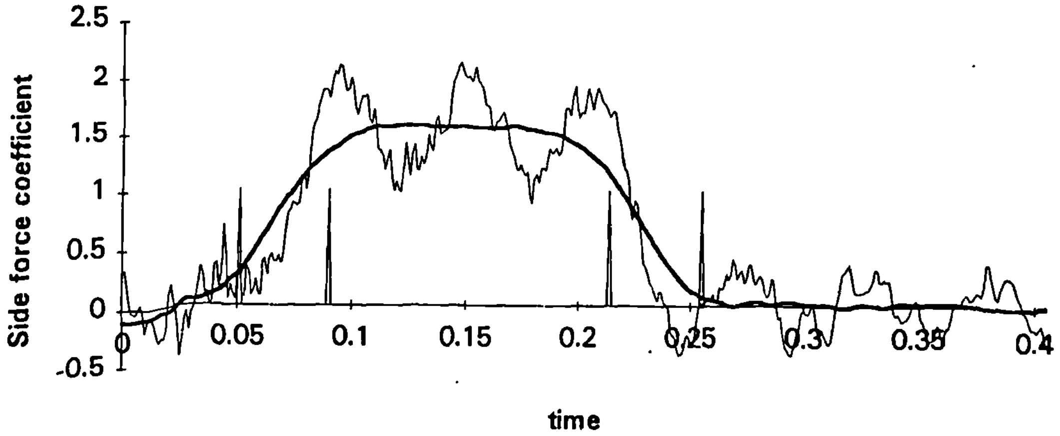

Fig. 2.3a - Moving model force balance recorded transient side force [18].

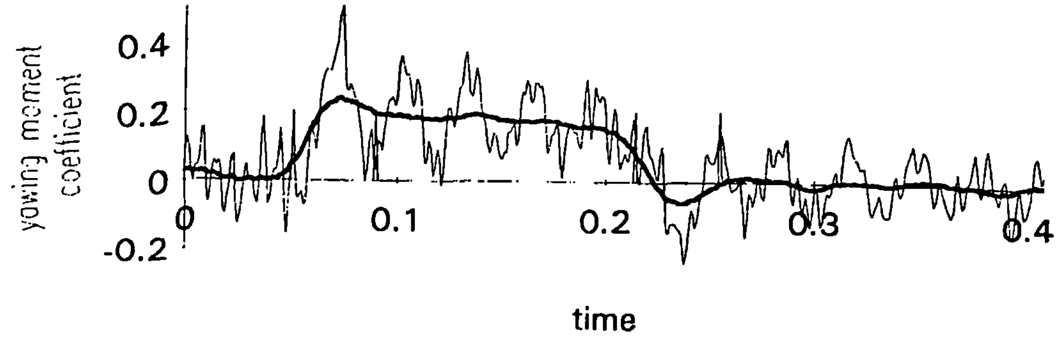

Fig. 2.3b - Moving model force balance recorded *transient yawing moment [18].*

The raw traces displayed by figures 2.3a and 2.3b are clearly oscillatory. The oscillating frequency was found [18] to match with the natural frequency of the plate and balance system. It may be observed that the correlation between the smoothed and raw traces is poor. Critical to assessing vehicle handling in cross wind conditions is rate of change of induced yawing moment. Any data smoothing applied reduces the observed rate of change resulting in poor handling predictions. The vibration in the force balance system can be seen to be relatively low prior to the entry of the plate leading edge to the wind tunnel. After this point the change in aerodynamic loading, which crucially is the desired data, causes non-aerodynamic vibrations to be initiated rendering highly corrupt data. Averaging the data over a number of experimental runs will have little effect as the aerodynamic load change will occur at the same point producing phase matched vibrations of similar magnitude. In addition smoothing any data from this type of test is potentially hazardous if the induced aerodynamic load frequency is unknown as this may be at a similar frequency to the force balance natural oscillations. The design of a force balance relies on a compromise between stiffness and sensitivity. A stiff force balance will have a high natural frequency, ideally greater than the aerodynamic load frequency to be monitored, but the deflections induced at the strain gauges will be small for a given load rendering low sensitivity. The transient loads recorded by this and other similar facilities suggest [5 & 18] that a cross wind transient duration of approximately three model lengths is required to observe a level portion to the smoothed transient aerodynamic loads induced on the model. The simple model geometry utilised for this particular test required a cross wind duration of ~1 plate length to capture the full yawing moment transient (1 plate length correlates to 0.04s and the plate leading edge entered the wind tunnel at 0.05s - see figure 2.2b).

A force balance used in a moving model test technique is also unable, with the limited track acceleration distances currently utilised, to record the drag component of force as rapid acceleration of the model induces large inertial loads in the drag direction rendering the use of a sufficiently sensitive load cell impractical. In addition the potential for an aerodynamic survey of the vehicle wake is made particularly difficult by virtue of the requirement of any instrumentation having to travel along behind the model as it is accelerated along the guide track. Stationary instrumentation may be used to survey the wake but would be required to be positioned at differing points along the path of the model over a number of experimental runs so as to build up a time dependent survey of a single wake point relative to the vehicle. There are also practical disadvantages relating to the design of such a facility. Actually gathering the data from a moving model necessitates, unless data telemetry is utilised, cabling to trail behind the moving model. The laboratory space required for the acceleration guide track is also significant (17m [18] - even this track length prevents drag force measurement). Complimentary studies of the time averaged behaviour of the model to yawed air flow is made difficult as a different experimental configuration is required. Also the overall scale of the tests is fixed by the width of the wind tunnel which must be of the order of several model lengths.

The data corruption induced by the model acceleration is the key disadvantage of the moving model technique and as a result most of the current research effort is being directed to mitigating this effect (vibration mode analysis of the force balance and aerodynamic model together with structural modifications to both the model and guide track [19]) as opposed to investigating the relevant aerodynamic phenomena.

Transient cross wind simulation techniques that utilise the conventional stationary model and wind tunnel configuration have the advantage of no data corruption induced from the acceleration of the model along a guide track. Investigations have been undertaken [4] using this conventional configuration but with the addition of up stream turning vanes to the wind tunnel working section as shown to scale by figure 2.4. The turning vanes were configured to oscillate in the tunnel working section so as to induce a sinusoidal yaw angle variation to the free stream velocity. The turning vanes had a chord of 0.2m and were positioned 0.4m from one another. The aerodynamic model used was a simplified vehicle shape, similar to that shown by figure 1.2, and had over all dimensions of 0.317m by 0.114m by 0.083m (length by width by height). The leading edge of the model was 0.7m down stream of the trailing edge of the turning vanes and the working section of the wind tunnel was 0.914m by 0.914m by 4.5m (width by height by length). The turning vanes were configured to oscillate over a ±15° range. The oscillating frequency of the turning vanes could be adjusted between the range of 2 to 20 model lengths, calculated in conjunction with the nominal free stream velocity.

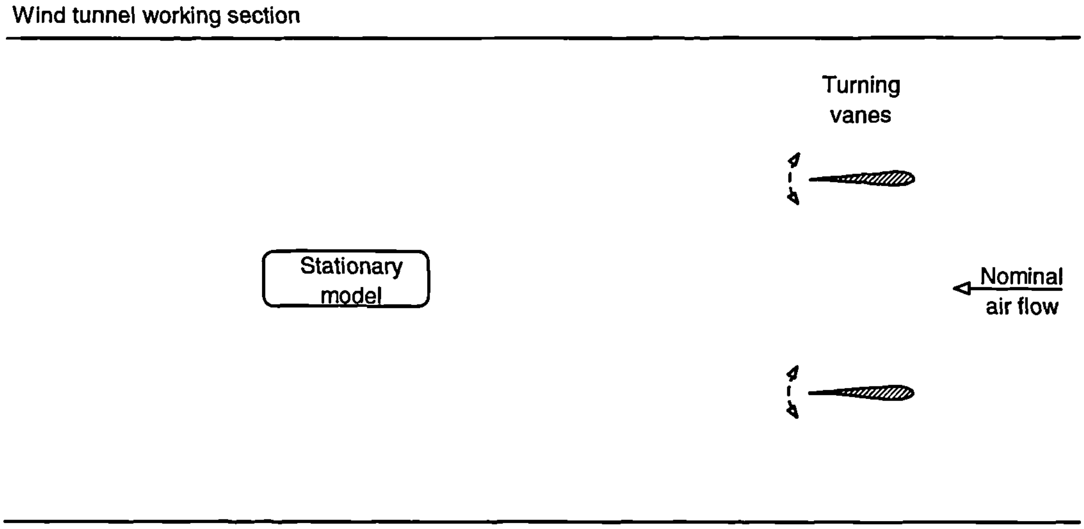

Fig. 2.4 - Plan view of turning vane cross wind simulation working section.

Measurements taken behind the turning vanes under oscillation [4] indicated that the actual induced air flow angle was approximately two thirds of the physical turning vane angle. That is to say a ±15° turning vane oscillation induced only a ~±10° oscillation in the air flow. With the turning vanes stationary and axial to the stream wise direction the model was set at a range of fixed yaw angles and the time averaged induced drag force, side force and yawing moment were monitored using a force balance. The model was then repositioned axial to the stream wise direction and the transient aerodynamic loads were monitored with the action of the oscillating turning vanes. The time averaged induced loads for a given model yaw angle were compared to the transient induced loads for the same oscillating rms flow angle. The maximum rms flow angle investigated was 5° and the Reynolds number, based on model length, was $4.5x10^5$. It was concluded [4] that over this range of yaw angles there was no significant difference between the time averaged and transient induced aerodynamic loads induced on the model. That is to say the transient loads may be predicted safely from the time averaged loads.

This technique has the advantage of utilising the stationary model configuration but is still restricted. The wakes induced behind the turning vanes will inevitably present an uneven velocity profile to the flow in the working section at the model leading edge. The maximum air flow yaw angle simulated using the turning vanes is also limited by the maximum unseparated incidence of the turning vanes to the flow. The wake produced by a separated aerofoil would substantially affect, more so than an unseparated wake, the air flow conditions up stream of the model. The maximum peak to peak air flow angle of ±10° is also too low compared to a realistic maximum yaw angle induced relative to a vehicle in road going conditions (see section 1.2). In addition the simulated cross wind velocity profile, that of a sinusoid, does not match the desired step input yaw angle requirements for cross wind testing.

2.4 Overview

All of the test techniques detailed above attempt to simulate the yawed air flow conditions that would be present in the environment for a real vehicle to encounter. Inevitably all the techniques are compromised to a certain degree by their assumptions. The time averaged technique assumes that only constant air flow conditions exist in reality which is clearly untrue. In addition any natural cross wind possesses a boundary layer velocity profile which is rarely accounted for by the technique where a uniform cross wind velocity over the full vehicle height is simulated (see figure 2.5). The boundary layer size associated with a natural air flow varies with the terrain but it may be calculated, using an accepted boundary layer profile for open ground [15], that the natural air velocity increases, from zero velocity at ground level, by a factor of 1.3 over the full height range of a typical vehicle body (0.25m to 1.5m). This boundary layer profile is shown to scale by figure 2.5. The height of a wind tunnel boundary layer is typically of the order of under 10mm, depending on the ground simulation technique.

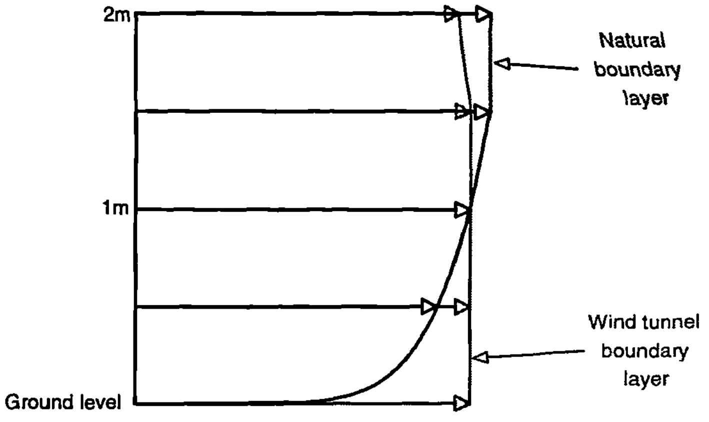

Fig. 2.5 - Natural boundary layer and wind tunnel velocity profile.

The turbulence intensity of the air flow in wind tunnel testing is also too low when compared to that encountered in natural air flows. Turbulence levels in natural air flows are such that the natural wind velocity could suddenly either double or drop to zero [15]. Typical refined wind tunnel turbulence intensities are of the order of 1% [35]. When modelling the characteristics of a natural air flow in the wind tunnel the turbulence length scale, measured by relative eddy to vehicle size, must also be considered. Natural air flows possess eddies up to many times the size of the vehicle [4] and so their effect can only be studied in a wind tunnel, where eddies are relatively small (a typical low speed wind tunnel possess turbulent wave lengths of 1×10^{-4}m to 0.4m and develops aerodynamic frequencies of 1Hz to 10kHz [44]), by using a small model. A small model however reduces a given test Reynolds number and also produces low aerodynamic loads which may be difficult to monitor.

The transient cross wind simulation techniques recognise the unsteady nature of natural air flows and do have capability to simulate the correct boundary layer and turbulence level, not necessarily the turbulence length scale though. Assumptions are made however regarding the velocity profile, relative to a vehicle, of a natural transient cross wind. The oscillating turning vane technique assumes a sinusoidally oscillating velocity profile. The moving model technique assumes that pockets of uniform cross flow with respect to the vehicle occur at discrete positions along a carriage way which a vehicle has to pass through, either side of which axial air flow conditions prevail. This later assumption however is not unrealistic as most drivers will be able to testify and is ultimately necessary if a scientific assessment of the effects of transient cross winds on passenger vehicles is required.

What is called for therefore is a transient cross wind simulation technique at the model scale which avoids the disadvantages associated with the moving model technique but produces the desired magnitude and step input nature of a natural cross wind velocity profile.

3.0 Conceptual Overview of the New Technique

3.1 Introduction

The key disadvantages of existing transient cross wind simulation techniques (see section 2.3.2) may be avoided if the conventional stationary wind tunnel and model configuration is utilised. This approach would remove the non-aerodynamic data corruption borne from the model motion and would also ease the design of any instrumentation used as it is not required to move with the model. If however the vehicle model is kept stationary the cross flow region has to be moved with respect to the model. This has been achieved [4] but with a sinusoidally varying yaw angle of restricted magnitude as opposed to the desired step change (see section 2.3.2).

New methods to achieve the relative movement of a cross flow region about a stationary model have been investigated by the author and are outlined below (sections 3.2 and 3.3).

3.2 Moving Cross Wind Source Technique

3.2.1 Concept

This test technique is the first logical approach to simulating a transient cross wind about a stationary model and as such was initially investigated by the author.

This test technique involves an axial air flow over the model being generated by a conventional wind tunnel configuration of a main jet and a stationary model and therefore allows all of the available wind tunnel aerodynamic refinements, such as a moving ground plane, to be used in conjunction with the technique. The cross wind is generated by a separate flow of air acting in a direction perpendicular to the axial air flow. By moving the source of this separate air flow, at the same velocity as the axial air flow, alongside the stationary model a resultant cross wind is created as shown by figure 3.1.

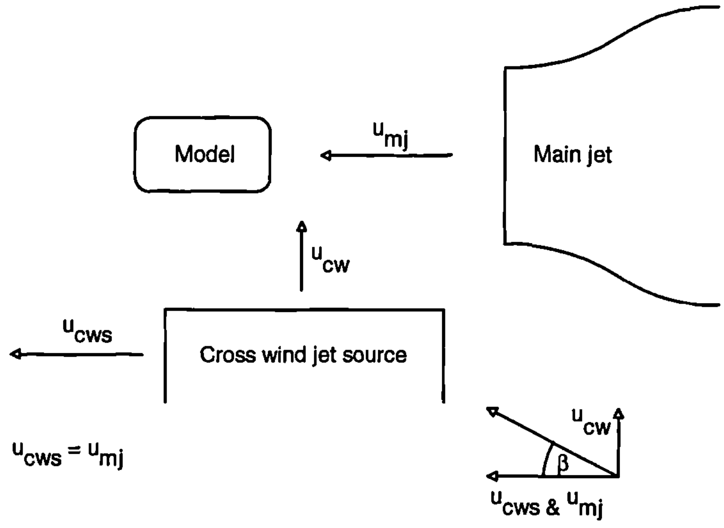

Fig. 3.1 - Plan view of moving cross source technique.

This technique is reversal of the moving model technique (see section 2.3.2). Instead of passing a model at speed through a perpendicularly acting air flow a moving source of perpendicularly acting air flow is passed alongside a stationary model. The streamwise component of the air flow relative to the model is created by the main jet and the transverse component of air flow relative to the model is created by the cross wind jet (see figure 3.1). Control the gust duration can be achieved by altering the width of the cross wind source.

The implementation difficulties of this technique are centred around the acceleration to speed of the cross wind source duct (see figure 3.1) and the generation of a uniform and consistent cross wind jet from within the moving duct. The shear layer interaction between the two jets as they combine is an additional area of concern.

3.2.2 Development

Cross Wind Source Acceleration

The acceleration of the cross wind duct source to the speed of the main jet would be necessary for the validity of the test technique. Any such duct would have to be light and rigid to allow the correct velocity to be attained in the laboratory space available. Various acceleration methods (elastic bungee cord, compression springs and pneumatic cylinders) were examined by the author [13] and it was decided that elastic bungee cord could be utilised to accelerate the cross wind duct providing the air flow emerging from it was of the desired quality.

Cross Wind Generation

If a stationary fan was used to create the cross wind air flow a flexible conduit would have to connect the fan with the moving duct opening that produces the cross wind. However this arrangement would produce transient effect within the cross wind duct itself as the conduit changes in length and shape so as to remain connected to the moving duct opening. If an air flow could be created from within the moving duct this problem would be solved. A light and rigid fan system could be mounted within the duct to provide the air flow. Such a system utilising a bank of 12" diameter twin blade propellers powered by electric motors was investigated by the author [12]. The propellers were found however to only produce a satisfactory air velocity when operating in bulk still air and not with any significant moving air flow angular incidence to the propeller rotational axis. The apparatus requires the bank of propellers to move with the cross wind duct therefore inducing a relative velocity perpendicular to the propeller rotational axis at the duct inlet. Such a fan system would therefore require the addition of turning vanes at the inlet to the cross wind duct so as to optimise to oncoming air flow to the fan system within the duct. The action of the turning vanes would be to collect and channel bulk still air toward the propellers in a direction parallel to the rotational axis as the whole duct and turning vane assembly moves at speed in bulk still air. Addition of the turning vanes would however increase the size and mass of the duct system and thus reduce the speed to which it may be accelerated to in the available laboratory space. In addition the air flow velocity profile produced by a propeller is both uneven (higher velocity toward the jet core) and cylindrical in section. Any duct would therefore be required to both induce jet uniformity, by inclusion of diffusion and contraction elements to the duct, and alter the jet exit shape to a rectangular form. Light weight composite materials were investigated for the construction of the duct and turning vane assembly and the mass of the duct system combined with the effective moving mass of the elastic bungee cord was calculated to be at minimum approximately 30kg.

3.3 Stationary Cross Wind Source Technique

3.3.1 Concept

As with the moving cross wind method the axial air flow is generated by a conventional wind tunnel configuration of a main jet and a stationary model. The correct resultant cross wind velocity can be achieved by angling a independent air flow across that of the main flow so as to give the correct cross component of velocity whilst matching the axial velocity as shown by figure 3.2.

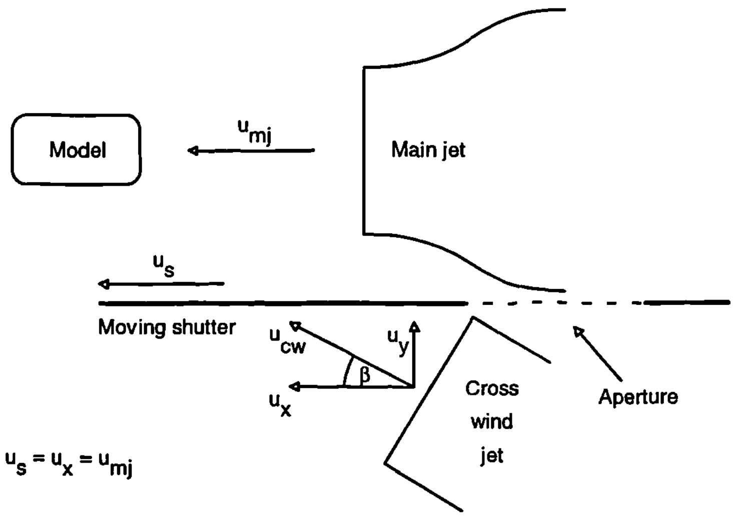

Fig. 3.2 - Plan view of stationary cross wind source technique.

Initially a movable shutter, containing an aperture, is placed between the model and the cross wind jet, obscuring the effects of it on the main flow, the model would be subjected to only the axial flow produced by the main jet. If the shutter was then moved rapidly in a down stream direction, with a speed equal to that of the main jet, a cross flow would act on the model as the shutter aperture moves across the line of sight of the cross wind jet with respect to the main jet working section. As the apertures moves fully across the cross wind jet line of sight the jet would be once more obscured from acting on the working section. Providing the velocities of main jet (u_{mj}), the cross wind jet axial component (u_x) and the shutter (u_s) were matched the two jets would progressively combine, during the movement of the shutter and aperture, at the same axial velocity but with a transverse air velocity (u_y) component superimposed on the air flow in the working section of the main jet wind tunnel (see figure 3.2). This arrangement would therefore simulate a transient square wave cross flow pulse from axial flow conditions in the working section and the pulse would sweep through the working section with the speed of the main jet. A stationary point in the working section would therefore be initially subjected to axial flow, then be subjected to yawed flow at the same axial velocity and finally returning to axial flow as the shutter and aperture passes completely across the line of sight of the cross wind jet. This method allows the control of the cross wind yaw angle (β) by matching the axial and transverse velocity components. In addition the duration of the cross wind transient may be controlled by altering the length of the shutter aperture.

By retaining the conventional well established wind tunnel test techniques wherever possible the implementation difficulty of this technique rested with the method of providing the transient nature to the simulation by means of a movable shutter.

3.3.2 Development

Cross Wind Shutter System

The movable shutter is required to be accelerated to the velocity of the main jet (see figure 3.2). The practical restrictions placed on the moving shutter are therefore similar to those placed on the moving cross wind duct highlighted in section 3.2.2; primarily those of low mass and restricted space. Initially a rigid shutter system was evaluated [12] on an exploratory test rig. The shutter was 2m long and had no aperture in it. However by configuring the shutter initially to obscure the effects of the cross wind jet on the working section and then pass fully across the line of sight of this jet the trailing edge of the shutter would correspond to the leading edge of any aperture placed in a longer shutter (see figure 3.2). The effect of this apparatus therefore was only to simulate the input and not the removal of a cross wind pulse in the working section. The investigations with this apparatus proved to be promising [12] but concern was addressed to the physical size of a shutter and aperture system which would simulate both the input and removal of a cross wind pulse in the working section. Such a shutter would have to obscure the effects of the cross wind source on the model during the shutter acceleration to the required velocity (u_s). Any aperture would then have to allow the cross wind to develop over the model for the required distance (the order of three model lengths - see section 2.3.2) and then once again obscure the cross wind source for the remaining distance over which the shutter was brought to rest. During this entire length the shutter would have to be travelling at the main jet speed (u_{mj}) so as to produce the correct velocity component triangle. Figure 3.3 shows the required shutter dimensions.

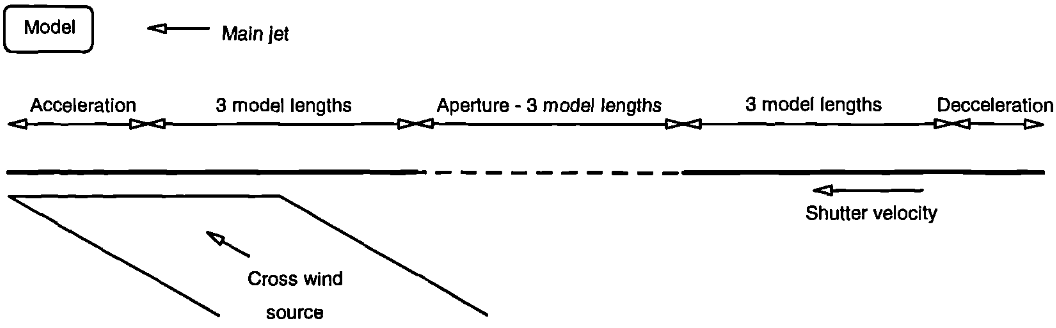

Fig. 3.3 - Rigid shutter dimensions.

The size of any aerodynamic model must be as large as possible so as to approach the correct dynamic modelling similarity and allow the modelling of a sufficient level of surface detail (see section 2.3). However the effects of wind tunnel blockage of the model frontal area with respect to the main jet wind tunnel exit area must be kept low. The main jet wind tunnel available for these test (see section 4.1.1) was of open section, open return type [28] of jet dimensions 0.85m by 0.55m (width by height). Ideally the presence of an aerodynamic model in a open section wind tunnel should not deviate the path of the outer flow stream line from that which is exhibited by the same stream line with an empty working section. If this stream line is deviated the resultant model surface pressures would be of greater magnitude than normal as the air flow would have been accelerated round the blockage increasing the effective air speed of the tunnel. Investigations have been undertaken concerning these blockage effects [39]. A road going vehicle was aerodynamically assessed in two separate open section wind tunnels. The two tunnels were of differing jet areas ($20m^2$ and $10m^2$) and therefore produced differing blockage ratios (11% and 21% respectively). Each test consisted of initially measuring the dynamic pressure developed in the working section without the presence of a vehicle. The vehicle was then placed in the working section and the stagnation surface pressure coefficient was calculated based on the initial empty tunnel dynamic pressure. A stagnation pressure coefficient of unity would imply that no blockage effect had occurred. The stagnation pressure coefficients for the two separate wind tunnels were calculated to be 1.025 and 1.069 for the 11% and 21% blockage ratios respectively [39]. It may be calculated that this corresponds to a 1.2% and 3.4% increase respectively in tunnel air velocity. A blockage ratio of approximately 10% was considered reasonable by the author so as to allow a aerodynamic model of sufficient size to be utilised. This restriction placed the model length at ~0.5m, when considering the frontal area to length ratio of a typical vehicle (see figure 1.2), which corresponds a 1/8 scale medium sized vehicle.

Despite the calculated short acceleration distances required for the shutter, using elastic bungee cord for the accelerations, the main length contribution comes from the central shutter section making the length of this portion of the order of 6 m, based on a 0.5m model length (see figure 3.3). The total length of the shutter was calculated to be approximately 9m. This distance is only just compatible with the available laboratory space.

A more compact shutter system would be possible if instead of using a rigid shutter system a flexible belt could be used. The flexible belt arrangement would be in a similar sense to that of a camera film between two spools (see figure 3.4).

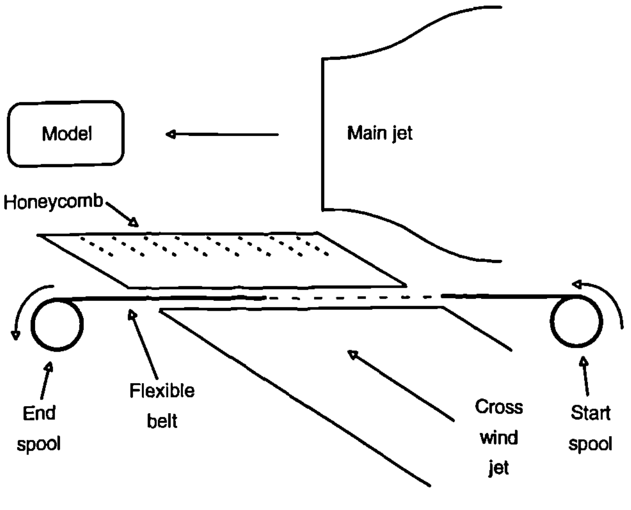

Fig. 3.4 - Flexible belt arrangement.

Prior the start of an experimental run a substantial length of the flexible belt would be wound to the 'start spool' (see figure 3.4) with the remaining much smaller length of the belt wound to the 'end spool'. This initial flexible belt positioning relative to the two spools is analogous that of a camera at the beginning of a film. The end spool may then be rotated to speed by a suitable drive mechanism in such a way as to unwind the belt from the start spool to be collected by the end spool. The initial length of belt wound to the start spool would be proportional to the acceleration distance and therefore time available to the drive system to attain a particular speed. Thus a short belt length would require a high power drive mechanism and a longer belt length would require a lower power drive mechanism. In the same way as the rigid shutter system the flexible belt would have an aperture placed in it to allow the cross wind jet to act in the working section of the wind tunnel. The flexible belt would be collected and brought to rest at the end spool at the completion of the experimental run.

Cross Wind Generation

Using this stationary cross wind source test technique the generation of the actual cross wind jet is straight forward. Any fan system used would be stationary and as such may be of conventional form. Investigations undertaken suggested that the use of centrifugal fans should be employed. Centrifugal fans are relatively inexpensive and can provide high volumetric air flow rates for a given size (impeller diameter). Axial fans typically induce large flow rates but only over a small pressure rise. Centrifugal fans can induce comparable flow rates over greater pressure rises. The use of a centrifugal fan system would therefore allow for a greater level of pressure loss, caused by the addition of multiple gauze screens for increased air flow uniformity, in the cross wind duct prior to exit. In addition centrifugal fans are readily available in a range of sizes.

3.4 Discussion of the New Test Techniques

3.4.1 Selection of Implementation Technique

Practical implementation of either the moving or stationary source cross wind transient test technique favours the method which requires the acceleration of the lightest and smallest component of the apparatus. Simulation accuracy favours the acceleration of the component whose movement would induce least detriment to the velocity profile uniformity of the generated cross wind. Such constraints suggest the adoption of the stationary cross wind method with moving shutter arrangement. The moving shutter (see figure 3.2) is a lighter and smaller component in comparison with the cross wind jet source (see figure 3.1). In addition the moving shutter does not actually generate the cross wind jet but merely obscures the effect of it on the main jet. The shutter motion therefore has a lower significance to the uniformity of cross wind jet than the motion of the source of the jet. It is intuitive that the acceleration to speed and then to rest of the cross wind jet source and turning vane assembly would induce transient fluctuations in the air flow emerging from the duct as the relative inlet air flow velocity to the duct would change as it accelerates. The stationary cross wind source test technique was therefore selected.

In considering the design of the cross wind shutter system the main restriction proved to be one of available laboratory space. The rigid shutter system (see figure 3.3) although technically possible proved to be too large and so the more compact flexible belt system was adopted. Such a belt would have placed in it a similar aperture to that of the rigid shutter to allow the cross wind to act on the model over a specific duration. The belt could run up to speed gradually over the initial wound length of belt on the start spool, using an electric motor to drive the end spool, thereby eliminating the need for an explosive style acceleration mechanism as for the rigid shutter. The use of an additional duct section, containing honeycomb (see figure 3.4), beyond the belt would allow a degree of flow straightening to help eliminate the flow end effects of the belt aperture as it traverses the cross wind duct. This system is more compact and would fit easily in the available laboratory space and would even allow for a longer apertures to increase the model length of cross wind transient to be placed in the belt. It also has the advantage that multiple apertures may be placed in the belt to allow several cross wind transients to be simulated over a single belt run. However the manufacture of such a belt system is slightly more complex than the equivalent rigid shutter system when considering the construction accuracy of the spools, their alignment and the belt tensioning requirements. But it was felt that the advantages of the flexible belt system out weighed the implementation difficulties and therefore this was the selected design solution for the transient cross wind test apparatus.

There are several disadvantages common to both the moving and stationary cross wind source test techniques. As the wind tunnel concerned is of the open section variety the air quality decays with distance down stream of the jet exit due to the action of the shear layer between the jet and the bulk air. The shear layers are highly turbulent and can therefore have an unsteady influence on the open jet. This places a limit on the distance which the model may be placed down stream so as to receive an air flow of a sufficiently low turbulence level. This in turn dictates the minimum cross wind angle that can be tested satisfactorily with this apparatus to 20° and more realistically 25° to 30°. This is not too disadvantageous however as the maximum effect (certainly in terms of yawing moment and less so for side force) of a cross wind is experienced by most vehicles at approximately 30° [15] and this is also a realistic maximum cross wind angle that could be experienced by a vehicle moving at speed on the road (see section 1.2). This would therefore allow the models to be tested in their worst case condition. With this test technique it is essential that the cross wind is fully developed by the time it is incident on the model if the experimental configuration is to simulate the required conditions accurately. The resultant yaw angle of the combined cross wind and main jets would produce a region of yawed flow that may be estimated by projecting the line of action of the cross wind jet into the working section (see figure 3.2). Only with a model placed sufficiently down stream will the projected flow have passed across the full width of the test section so as to produced the desired yawed air flow immediately up stream of the model over the full working section width.

3.4.2 Implementation Overview

Aside from the selected implementation method for the apparatus there of course potentially exist other possible design solutions to the simulation of transient cross winds about a stationary model. Several were conceptually and practically considered but on balance due to the exploratory nature of the aerodynamic investigation, the available laboratory space, the time scale of the project and expense of any proposed solution the method based on the conceptual outline above was selected.

4.0 Design of the Test Apparatus

4.1 Existing Apparatus

4.1.1 Main Jet Wind Tunnel

The existing main jet wind tunnel is of the open jet, open return variety. The jet emerging from the tunnel is rectangular in section and has dimensions of 0.85m (width) by 0.55m (height). The wind tunnel is powered by a 55kW three-phase induction motor which drives a large centrifugal fan and the open jet wind tunnel is mounted to the outlet of this fan. A motor speed controller provides a continuously variable drive speed to the fan up to the maximum speed. The maximum air velocity attainable over the wind tunnel exit area is ~24m/s. The unit was originally designed to operate as a suction based fan to draw air through a separate annular test rig, which is still in research use, and when mounted to the fan inlet restricts the wind tunnel exit velocity to ~14m/s. The original design requirements of the unit were to produce a large pressure ratio (~5kPa) across the annular test rig and as such the fan is not ideally suited for use with a low speed wind tunnel. The open jet tunnel has two gauze settling screens either side of a plenum followed by a contraction ratio of 2.8, which falls within the recommended [28] contraction ratio for open return tunnels, although greater contraction ratios are desirable. The air flow quality in the tunnel is not ideal (the recorded turbulence levels are ~2.5% at the jet core compared to similarly sized refined wind tunnel facility [35] turbulence level of 0.6%, albeit with a closed test section) and the spatial velocity variation over the whole jet area was found to be within ±5% of the mean velocity at maximum speed [13] (the same refined wind tunnel facility possess a velocity variation of ±1% of the mean [35]). The wind tunnel therefore does not match the requirements for those of refined aerodynamic testing. However due to the relatively exploratory nature of the investigations undertaken by the author towards developing a wind tunnel technique the velocity variation and turbulence levels present in the air flow were deemed satisfactory.

For a given wind tunnel there exists a maximum aerodynamic model size that can be tested satisfactorily in the facility. The parameter in question is termed blockage and is the percentage ratio of the aerodynamic model frontal area to the nominal jet area of the tunnel. Ideally the blockage ratio should be as small as possible. For a real vehicle on an open carriage way the blockage ratio approaches zero. The effect of model blockage in an open section wind tunnel is to deviate the path of the outer stream line from that exhibited by the same stream line with an empty test section. This causes an increase in the effective air speed of the working section by virtue of the flow acceleration around the blockage (see section 3.3.2). Empirical blockage correction methods are available to account for this velocity increase but all essentially conspire to produce a Cp of unity at the leading edge of the aerodynamic model. Open section tunnels have been validated with blockage ratios of up to 89% [28] with empirical correction. A more typical blockage value however would be ~10% (see section 3.3.2 and [39]). No blockage correction was applied to any of the data gathered and the blockage ratio for the aerodynamic model used was 6.0%. It may be estimated, extrapolating from values given in section 3.3.2, that this blockage ratio in an open section tunnel induces a 0.15% increase in velocity which correlates to a stagnation pressure coefficient of 1.003, calculated using the empty working section dynamic pressure.

4.2 Design Requirements

4.2.1 Cross Wind Transient

Previous work (see section 2.3.2) in the area of transient cross wind effects has suggested that a duration of three model lengths for the simulated cross wind region might be required to assess the full nature of any transient aerodynamic phenomena. With the absence of any rigorous experimental data to confirm this it was decided that a cross wind region of at least this value should be initially simulated. As detailed in section 3.4.1 a cross wind (or yaw) angle of 30° would simultaneously represent not only the realistic worst possible natural cross wind angle but also the yaw angle at which a maximum value of yawing moment is induced on a typical vehicle shape. It was therefore decided to initially simulate a three model length cross wind transient during which period a 30° yaw angle is incident in the working section of the wind tunnel. The potential to increase the duration of the cross wind region would also be required.

4.2.2 Shutter System

The shutter system, based on a flexible belt, would have to be light weight to allow for the necessary acceleration, strong to resist the tension in it caused by the acceleration and controllable to match the belt velocity to that of the main jet (see figure 3.2).

4.2.3 Operation and Implementation

The operation of the experimental apparatus would have to be repeatable to allow rigorous comparative experimentation, implementable in terms of cost, time scale and available space and safe in use. The potential data retrieval rate from the apparatus must also be considered in that the amount of set up time between experimental runs should be minimised.

4.3 Design Solution

The intended simulation apparatus would take a form illustrated to scale by figure 4.1, based on a flexible belt and spool assembly, which will be discussed fully.

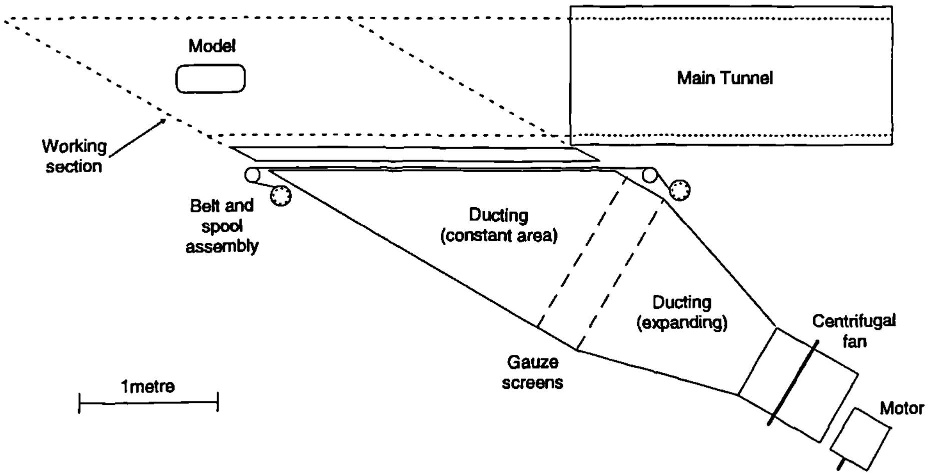

Fig. 4.1 - Schematic plan view of simulation apparatus.

4.4 Detail Design

4.4.1 Flexible Belt

Material

The selection of the optimum flexible belt material was crucial to the success of the experimental apparatus (section 4.2.2). In addition to a high strength to weight ratio the wear on the belt material must be considered. Existing belt materials, used for wind tunnel moving ground simulations, were examined. Such belts are usually a composite of a wear resistant fabric backing with a smooth flexible plastic surface and as a result are relatively bulky (~3mm thick) and dense (0.75kg/m^2) in addition to being expensive. An alternative belt material was selected that was strong, light, flexible and of low cost. The selected material was the heavy duty polythene used for damp proof membranes in the construction industry. The material is widely available in 50m x 4m wide sheets at low cost. The material was suitably thin (0.32mm) and light (0.29kg/m^2).

Tracking and Tensioning

The tracking and tensioning of the belt system potentially was the most difficult area of the design solution. During an experimental run the full length of the belt must be transferred neatly at speed from the start to the end spool (see figure 3.4). However the action of the air flow emerging from the cross wind duct would act to force the belt away from the duct exit. A low blockage wire mesh was therefore used to restrain the belt to the desired straight path between the two spools. The porous nature of the mesh allowed the cross wind jet to flow through the aperture and into the working section in the desired manner. In addition the cross wind jet air flow would act evenly over the restrained section of the belt thus ensuring that the belt would not flap unduly and would also ensure that the belt remained substantially flat as it was held against the mesh. The fact that the belt system was vertically mounted also posed potential problems due to the possible sagging of the belt under the self weight. Because of the low density of the belt, the relatively high tension in it and the air flow pressure on the belt it transpired that the self weight effect was minimal.

Belt systems that are continuous (i.e. a loop of belt) possess significant tracking problems. Any misalignment in the belt at any point ultimately will have an effect on the rest of the belt as the ensuing belt has to follow that misaligned path with the errors being continually back feed into the system. Design features such as specially shaped rollers or active belt tension monitoring have to be incorporated to continuous systems that operate at speed. Uncontinuous belt systems (i.e. a discrete length of belt) are less problematic. The nature of the belt dynamics for the selected design provide that the tension present in the belt as the end spool is driven (see figure 3.4) is largely devoted to the acceleration of the belt system as the remaining forces are frictional. This is the opposite situation with a continuous belt where the drive force of the belt is low compared to the total tension present.

The main design problem therefore shifted to ensuring that the spools were axially parallel so as to produce an even drive tension across the full height of the vertical belt. The belt assembly (see figure 4.1) required two spools at each end of the system one of which would store the flexible belt and the other would guide the path of the belt to/from the storage spool. The manufacture of the spool support system allowed a degree of movement to the spool mounting brackets, positioned at each end of the spools, with respect to the support frame and thus provided a necessary level of spool alignment adjustment with belt in situ.

Acceleration System

The flexible belt system was required to accelerate from rest to a desired speed over a given length of belt. The longer the initial length of belt wound to the start spool the longer the acceleration time available to attain a specific speed. This longer acceleration time would reduce the torque requirements for any drive system at the end spool (see figure 3.4). It was decided that the most convenient means to drive the end spool was by the use of a three phase induction motor. Such motors deliver high torque during their acceleration. It was therefore necessary to calculate the power requirements of a motor to accelerate the whole system to the required speed. Providing the maximum load of the system was not greater than the maximum rated load of the motor the belt speed would ultimately correlate to the rated speed of the motor. The design issue concerned the duration and therefore length of belt required for this acceleration. The load of the accelerating system may be calculated from the parameters of the proposed apparatus and are shown by table 4.1.

Item	Parameters	Loads
Spool	Diameter, length, wall thickness, stub axle dimensions and material density.	Rotational inertia of spools (Σmr^2).
Flexible belt	Height, total length, thickness and material density.	Rotational inertia of belt on spools (Σmr^2).
Cross wind duct	Area, leakage flow not acting on belt, frictional coefficient of belt on porous mesh.	Frictional torque of belt on mesh (T_F).
Motor	Power, rated rpm, inertia, efficiency, rated torque and effective torque.	Effective torque & motor inertia (T & Σmr^2).

Table 4.1 - Parameters in belt acceleration calculations.

A given length of belt would allow a given speed to be attained for a given delivered torque. Increasing the belt length would increase the rotational inertia of the spools, due to additional belt mass wound to the spool, which would compromise any desired higher belt speed intended by the addition to the belt accelerating distance. The calculation process is therefore iterative. A spread sheet software package was formulated to assist with the calculations based on the methodology shown by table 4.2.

Premise	*Total load x (Final rotational speed / Acceleration time)= Effective torque* $T_F + \Sigma mr^2 \times (\omega_{final} / t_{accn}) = T$
Step 1	Guess final rotational speed based on desired belt velocity
Step 2	Adjust the acceleration time to balance and the premise equation
Step 3	Calculate the required belt length and resultant inertial load
Step 4	Repeat steps 2 to 4

Table 4.2 - Belt acceleration calculation method.

Any iterative calculation method is potentially unstable. However by adjusting the weighting of the correction step per iteration stability was achieved easily. The parameters given by table 4.1, which were independently adjustable, were checked to confirm that varying each produced an expected qualitative increase or decrease in belt acceleration length.

Some assumptions were made to simplify the analysis by using only the parameters detailed by table 4.1. For example an induction motor generally follows the standard torque characteristic, shown by figure 4.2, as it accelerates to the rated speed.

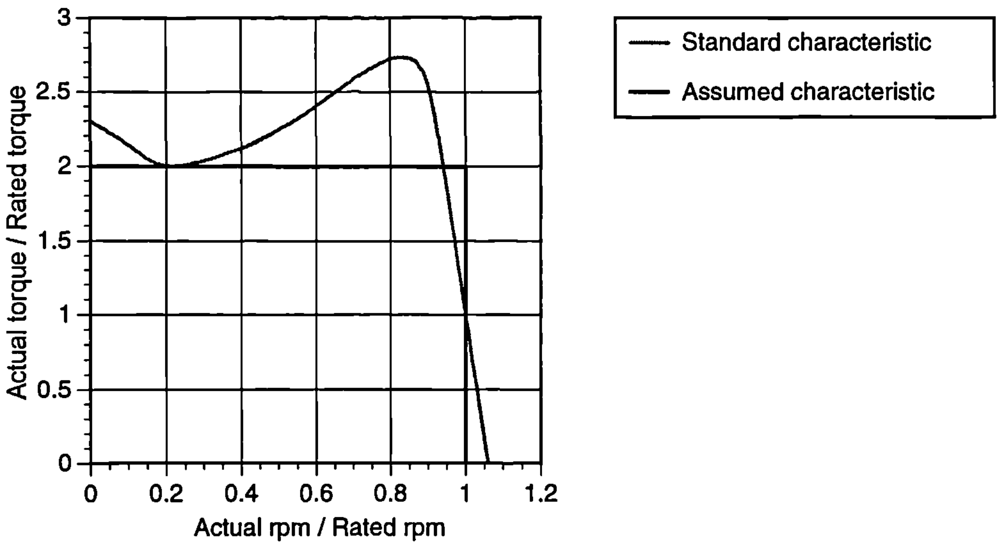

Fig. 4.2 - Standard and assumed induction motor characteristic.

For simplification it was assumed that during the acceleration the effective torque delivered by the motor was a constant factor of two above the rated torque. This is not an unreasonable assumption and errs to the side of caution.

The design calculation method proved to be accurate within 10% (see section 5.3.2) of the actual speed attained for the length of belt selected and in addition provided the author with information regarding the relative magnitudes of the inertial loads in the total system.

The motor selected for the apparatus was a 1.1kW unit with a rated speed of 1410rpm which was calculated to provide a belt velocity of ~9m/s with a 25m total belt length, including the aperture section. A more powerful 3.75kw unit rated at 2865rpm was available which was calculated to provide a ~17m/s belt speed using a 50m total belt length. During the design process the author was unable to find any previous work relating to any similar accelerating belt systems, although the simple calculations undertaken were expected to give a reasonable belt speed prediction. Not known therefore was the exact nature of the dynamic response of such a system. It was therefore decided to select the lower powered motor to validate both the dynamic behaviour of the belt system and the aerodynamic response of the working section with the potential to replace the motor to provide higher speeds (and therefore Reynolds numbers) for future investigations.

The slowing of the belt system to rest at the end of an experimental run was also required. Electromagnetically actuated clutch/brake systems were examined but proved not only have high inertial loads but to also to be relatively expensive for what was at the design stage an unproven wind tunnel test technique. Simple design solutions are often optimum and it was discovered that the application of a small frictional load to the two storage spools (see figure 4.1) brought the system to rest relatively smoothly and quickly. The frictional braking was achieved by a flexible bristle brush system which held the belt to the spool over almost the full height of the belt during the entire experimental run. The flexible nature of the bristles allowed the fixed brush system to maintain contact with the belt at all times despite the fact the outer diameter of the storage spools changed continuously over an experimental run as the belt was wound from one spool to the other. The operator simply had to cut the motor power at any point after the full length of the belt was collected on the end spool. The brush system had an additional function at the end spool. With the entire belt length of the belt stored on the end spool and with it still rotating there was a tendency for the loose outer belt end spin out from the spool under the action of centripetal force. The brush system not only supplied physical restriction to this effect but also provided a friction derived winding tension to the whole belt on the spool to keep it in position as it was brought to rest.

The operation of the apparatus after each experimental run consisted of rewinding the belt back onto the start spool whilst leaving a suitable belt length stored at the end spool to provide drive to the belt. The belt end was secured to the start spool by means of tabs which were inserted in to slits in the start storage spool. By holding the tabs in position and winding the on spool the belt would take to the spool. During an experimental run the belt would be fully unwound and the tabs would be pulled free of the spool. Safety guards, designed to contain any potential loose component and to provide restricted access to moving parts, were then be placed in position and power could be delivered and then cut to the motor at the relevant point. The actual run time of the motor was under 5 seconds whilst the turn around time between experimental runs for the apparatus was approximately 20 minutes.

4.4.2 Cross Wind Ducting

The geometry of the cross wind ducting (see figure 4.1) had to match that of the existing main jet wind tunnel whilst being inclined at 30° to it and must produce a uniform across the width of the aperture as it passes across the face of the duct. This could not be achieved with the use of a single aperture. As a single aperture initially encroaches across the duct face only a small exit area is presented to the flow resulting in a high emerging velocity, exacerbated by the steep pressure characteristic present with a centrifugal fan. As the aperture continues to move to present the full exit area to the duct the velocity would fall and would remain at this lower value before rising once more as the aperture size reduces having fully passed across the face of the duct. To help ensure the cross wind jet keeps a uniform velocity profile as the belt aperture moves across the duct exit it is necessary to maintain a constant duct exit area. This can be achieved by having a second set of apertures contained in the belt (see figure 4.3).

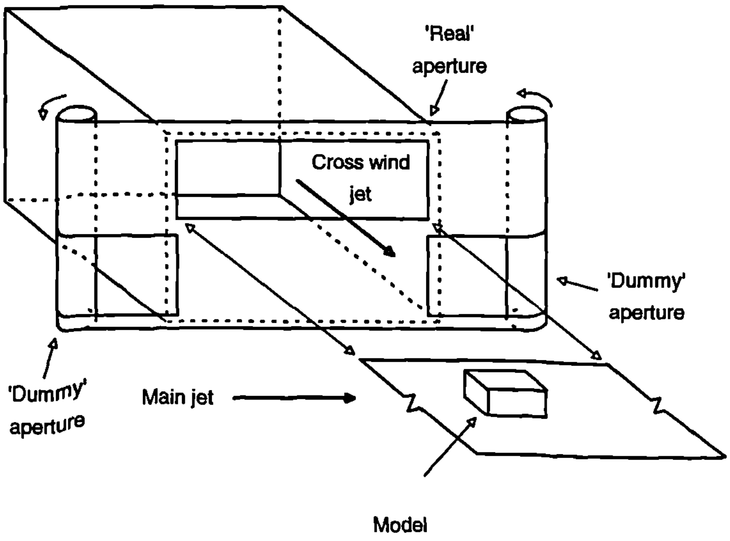

Fig. 4.3 - Schematic 3D view of belt geometry.

If the second set of 'dummy' apertures were arranged to exhaust beneath the working section and were positioned in exact opposition to the first set of 'real' apertures a constant area would be presented to the duct as the belt moved across the exit. With this configuration only the real apertures exhaust into and have an effect on the working section of the wind tunnel apparatus. This design feature required that the duct height and therefore the belt height had to be at least double that of the main jet (0.55m) to provide for the dummy apertures. The duct height was set at 1.2m with the belt height at 1.4m.

The remaining duct dimensions were configured to deliver a reasonably settled flow to the duct exit. The centrifugal fan system (see figure 4.1) exhausted in to a diffusing duct section. There then followed two gauze screens either side of a short plenum. The final section of the duct was tapered to align to the edge of the main jet. There was no contraction in this final duct region as it was of constant duct stream wise cross section. The aperture area during an experimental run would provide a minimum step contraction ratio of 2 (as the aperture area would be half the duct area at maximum - see figure 4.3). It was difficult to justify the manufacture of a smooth contraction to the duct exit as it was felt that required manufacturing complexity was not compatible with the exploratory nature of the tests.

A honeycomb flow straightening section was added to the extreme exit of the cross wind duct (see figure 3.4). This section to the duct comprised of discrete blocks of honeycomb as shown by figure 4.4.

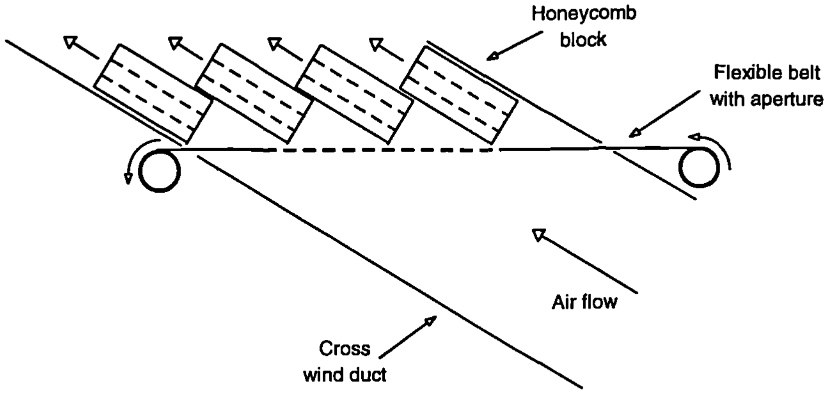

Fig. 4.4 - Schematic illustration of honeycomb geometry.

The honeycomb blocks were to help eliminate any air flow end effects at the aperture leading and trailing edge as it passed across the exit of the cross wind duct. The staggered geometry of the honeycomb blocks however presented an uneven geometry to emerging flow from the honeycomb producing a equivalent potentially uneven flow velocity profile. A more satisfactory honeycomb geometry could have been achieved by using a single piece of honeycomb cut diagonally from a large honeycomb block. This was however deemed unnecessary for the exploratory nature of the test apparatus. The actual apparatus comprised 14 honeycomb blocks in the configuration shown positioned across and inclined duct length (the length of the straight section of belt) of 2.25m. Each block had plan view (by figure 4.4) dimensions of 0.15m by 0.09m.

4.4.3 Centrifugal Fan System

Fan Selection

Having established the desired flow magnitude and geometry of the cross wind unit it was possible to select a particular centrifugal fan size to achieve the desired flow rate. Knowledge of the local sectional geometry of the duct system allowed the local velocity to be calculated from the total flow rate. Estimations of the pressure loss expected over the entire duct were then made. The pressure loss for a particular component may be calculated by $\frac{1}{2}k\rho u^2$ where k is the loss coefficient for that component and is defined as the total pressure loss across the component divided by the initial dynamic pressure (for example through each gauze screen in figure 4.1 $k = 2$ [42]). Approximately one half of the total duct pressure loss was calculated to be at the duct exit with the remainder induced equally at the two gauze screens. The pressure loss induced by the diffuser section and the remaining duct length was calculated to be minimal. Manufacturers details of fan characteristics (charts relating flow rate, pressure loss, power required and fan rpm) were then used to select a suitable centrifugal fan. It transpired that an optimum cost solution was to utilise two identical medium sized fans with two separate motors as opposed to one single large fan and motor unit. The selected fans ('Nicotra AT 18-18') were two 0.46m impeller diameter units each having an exit area of 0.46m by 0.56m. Each fan was driven by a 5.5kW three-phase induction motor.

Fan Control

As the precise test velocity of the flexible belt was not known it was felt that continuous speed control of the cross wind duct fan system was required to allow empirical matching of the relevant velocity components (see figure 3.1). Increasing the fan speed would increase the cross wind velocity emerging from the aperture but would decrease the belt velocity due to the increased frictional force of the belt against the porous mesh of belt (see section 4.4.1 - Acceleration System). A continuously variable speed controller was therefore combined with the fan system to allow small adjustments to be made to the air flow rate so as to allow full control this frictional force and therefore the ultimate speed of the accelerated belt. The two 5.5kW motors were powered in parallel via the speed controller to each of the centrifugal fans.

4.4.4 Support Framework

The belt acceleration system, cross wind ducting and centrifugal fan system were supported by separate sections of designed steel frame work. Safety guards formed part of the frame work to prevent ingress and egress of objects to the moving parts of the apparatus.

4.4.5 Realised Design

Figure 4.5 shows a view of the whole test apparatus. The main jet wind tunnel and working section may be seen down the left hand side of the figure. The cross wind ducting and belt acceleration system may be seen on the right. Top right is the centrifugal fan system followed by the remaining cross wind ducting. The motor and end spools may be seen at the bottom right hand side with the start spools central towards top of figure 4.5. The frame at the cross wind duct exit holds the honeycomb blocks (not shown).

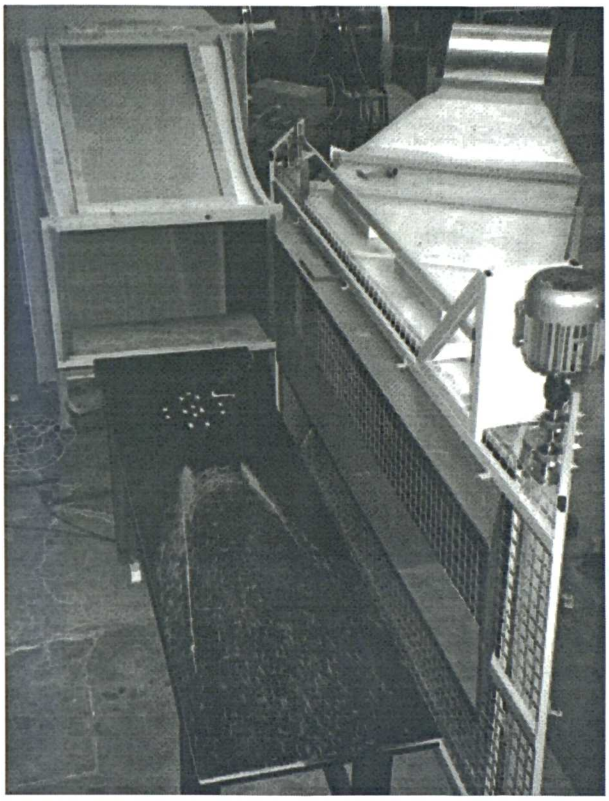

Fig. 4.5 - View of whole test apparatus.

Figure 4.6 shows the flexible belt acceleration system. Visible are the two end spools, the left hand of which is the guide spool and the other is the storage spool. The motor which drives the storage spool is at the top of the figure. The belt is shown stored on the right hand spool. The power control to the motor can be seen at the lower right hand side of the figure. Also visible is the spool and motor support frame work.

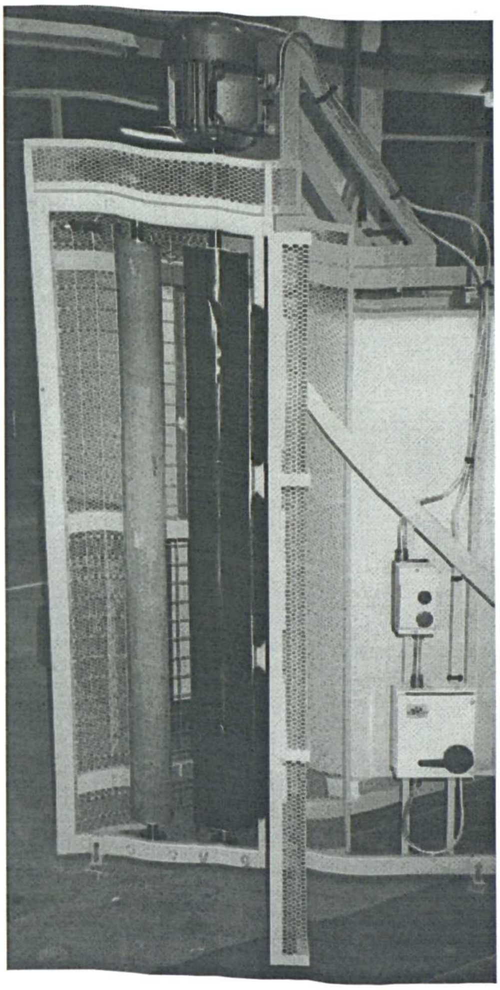

Fig. 4.6 - View of flexible belt acceleration system.

Figure 4.7 shows the centrifugal fan system. Visible in the background are the two centrifugal fans (left hand side) vertically above one another and the two corresponding motors on the right hand side. The left hand foreground shows the motor power control unit comprising of main switches (bottom) and speed controller (top). Also visible is the fan and motor support frame work.

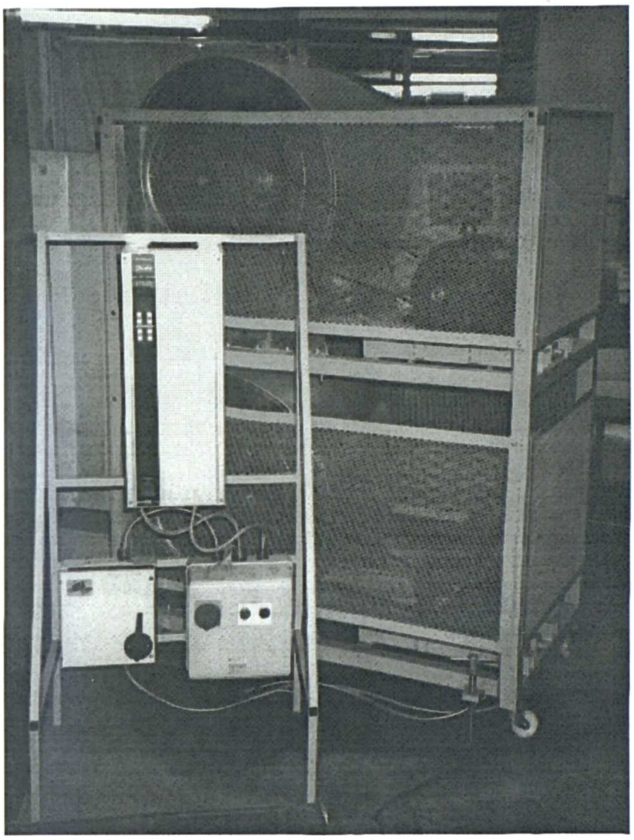

Fig. 4.7 - View of centrifugal fan system.

Figure 4.8 shows a side view of the test apparatus. Visible is the main jet exit (left hand side) and the working section extending to the right of the figure. The motor and end spool arrangement (reverse view from figure 4.6) may be seen, together with support frame work, to the top right of the figure. Also visible is the porous mesh to support the belt viewed through the honeycomb support frame, without the honeycomb present, in the central region of the figure.

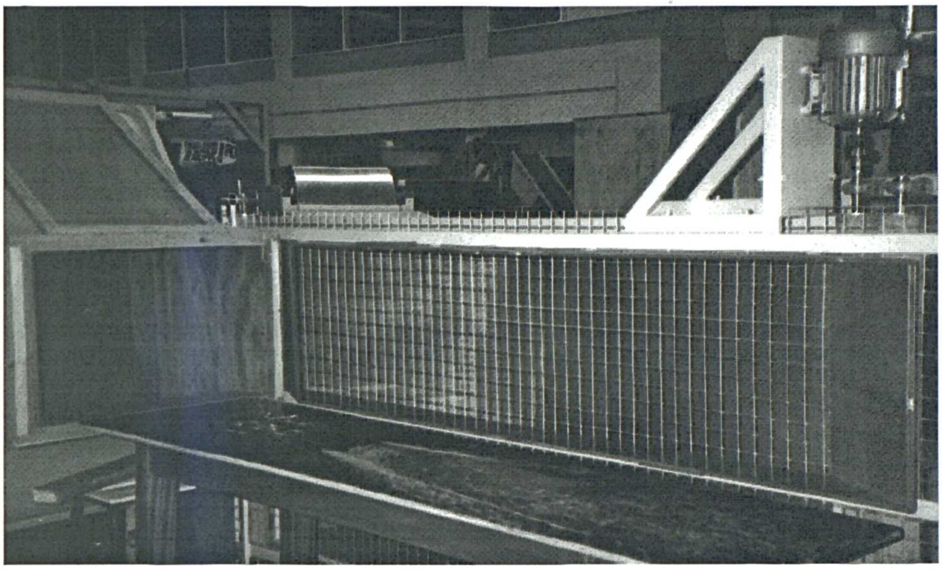

Fig. 4.8 - Side view of test apparatus.

5.0 Development of the Test Apparatus

5.1 Introduction

The test apparatus, having been installed, required commissioning. Most commissioning and development effort was directed toward the flexible belt system. The test technique required that the flexible belt travelled at a specific velocity across the face of the cross wind duct which in turn had to provide a specific resultant velocity of transient air flow into the working section of the main wind tunnel. It was necessary to undertake this matching on an empirical level. In addition the exact dynamic behaviour of the belt system during an experimental run was not known. The quality of the belt tracking and the effect of removing sections of the belt for the apertures required by the simulation also needed to be investigated.

5.2 Flexible Belt

5.2.1 Tracking and Tensioning

To assess the tracking and tensioning behaviour of the belt under dynamic conditions during an experimental run the belt was initially traversed slowly by hand to and from the start and end spools. The cross wind centrifugal fans were run at low power during these hand driven tests to examine the effect of the cross wind air flow on the straight section of belt. During each traverse the behaviour of the belt was monitored visually at key points and adjustments were made to the relative spool alignment if necessary so as to achieve a uniform tension over the full height of the belt. This process was undertaken each time the belt geometry was altered. The tracking of the belt system proved to be unproblematic. From the hand driven tests it was discovered that, providing an even belt tension was ensured, the cross wind duct air flow assisted greatly in holding the straight portion of belt between the two sets of spools both flat to the porous mesh and aligned to the spools (see section 4.4.1 - Tracking and Tensioning).

5.2.2 Initial Development

Dynamic Behaviour of Continuous Belt

Initial investigations were undertaken using a 25m length of solid (no apertures) belt. If the dynamic behaviour of the belt system proved problematic with a solid belt the addition of apertures would intuitively exacerbate the situation. Several dynamic tests were undertaken and after each the belt was examined wear or damage. The belt material proved to be highly wear resistant and no damage to the belt was observed. Slight degradation in belt quality was however observed at the loose outer belt end which was able to partially spin out from the end storage spool under the action of centripetal force at the end of the experimental run and contact some of the support framework. However this effect was mitigated by the addition of an extra flexible brush system diametrically opposed (with respect to the end storage spool) to the first set (see section 4.4.1 - Acceleration System).

Belt Geometry Modifications (I)

With the dynamic behaviour of the solid belt established and deemed satisfactory apertures were placed in the belt. Initially only a limited number and size of apertures were placed in the belt to examine any alteration in dynamic behaviour. The aperture geometry is shown to scale by figure 5.1.

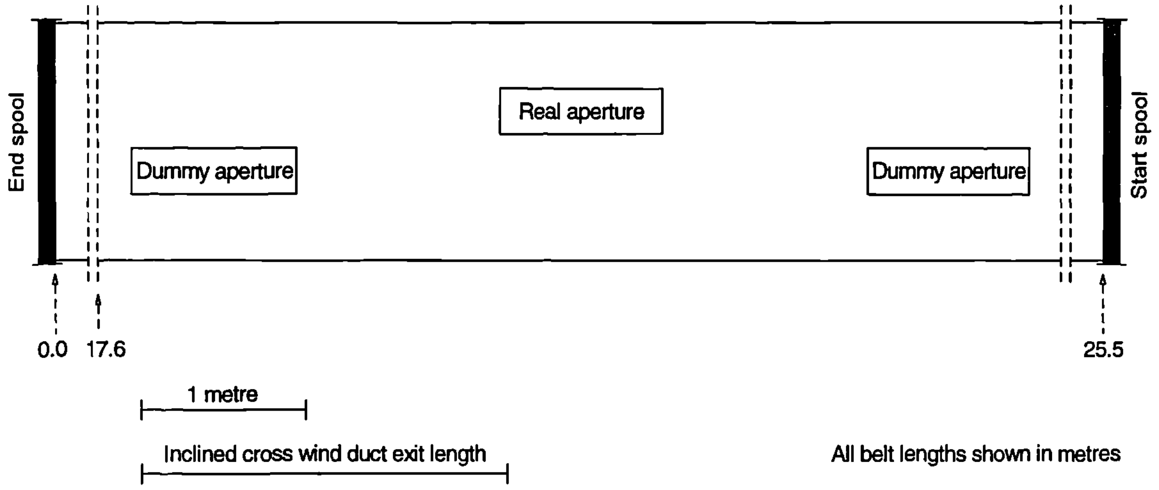

Fig. 5.1 - Stage I belt geometry.

Such a geometry was designed to simulate a single (one real aperture) cross wind pulse in the working section of the wind tunnel. Each aperture was 1m by 0.25m (length by height). The length of the straight section of belt, which matches the inclined cross wind duct exit length (see figure 4.1), in addition to the scale is shown by figure 5.1. By using an optical sensor (see section 6.6.2) it was possible to measure the velocity of the belt system using the aperture leading and trailing edges as triggers to the sensor.

The purpose of these initial belt geometry modifications was to examine how much the apertures detracted from the dynamic behaviour of the belt system. In the hand driven tests (section 5.2.1) it was discovered that there was a tendency for the middle region of the vertical aperture edges to buckle and kink radially outwards when following a curved path round the spools as shown by figure 5.2.

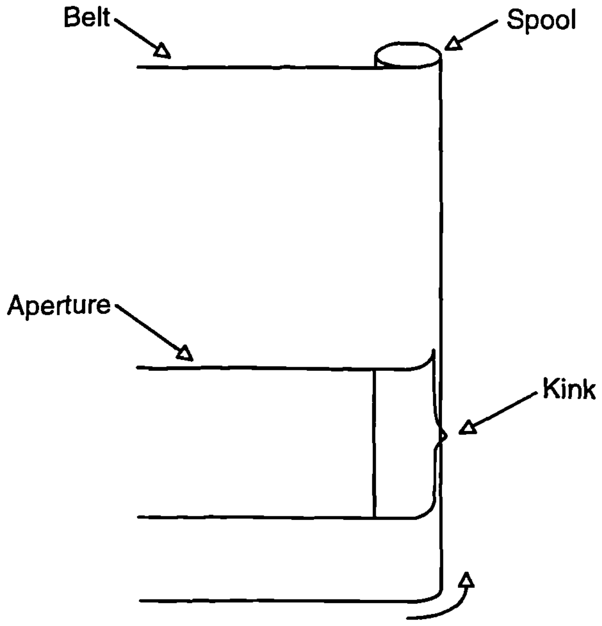

Fig. 5.2 - Deformation of flexible belt at spools.

This would cause the belt system to snag on the porous mesh and some support frame work during an experimental run. Thin yet rigid plastic strengthening strips were added to the aperture vertical edges which remedied the problem. It should be noted that the radial kinking at the spools was not a centripetal effect as it occurred under static conditions.

Initial measurements of the belt velocity at the apertures indicated that the belt did not attain a maximum velocity. During the operation of the apparatus the speed of the end spool drive motor could be qualitatively assessed aurally. The motor failed to gain any substantial speed over the initial solid portion of the belt but accelerated significantly as the apertures passed across the face of the cross wind duct suggesting that the high pressure created by the centrifugal fans under restricted flow caused a high level of friction between the belt and the restraining porous mesh. No aerodynamic measurements were made in the working section at this stage as the dynamic behaviour of the belt system was being optimised.

5.2.3 Further Development

Belt Geometry Modifications (II)

From knowledge gained from the initial belt investigations it was decided to place additional apertures in the existing belt. To assist with the acceleration of the belt over the initial portion perforations could be placed in the belt to allow air from the cross wind duct to flow through the belt and therefore not contribute to the frictional load on it. It was decided also to both enlarge and increase the number of the existing real and dummy apertures in the belt. This new belt geometry is shown to scale by figure 5.3.

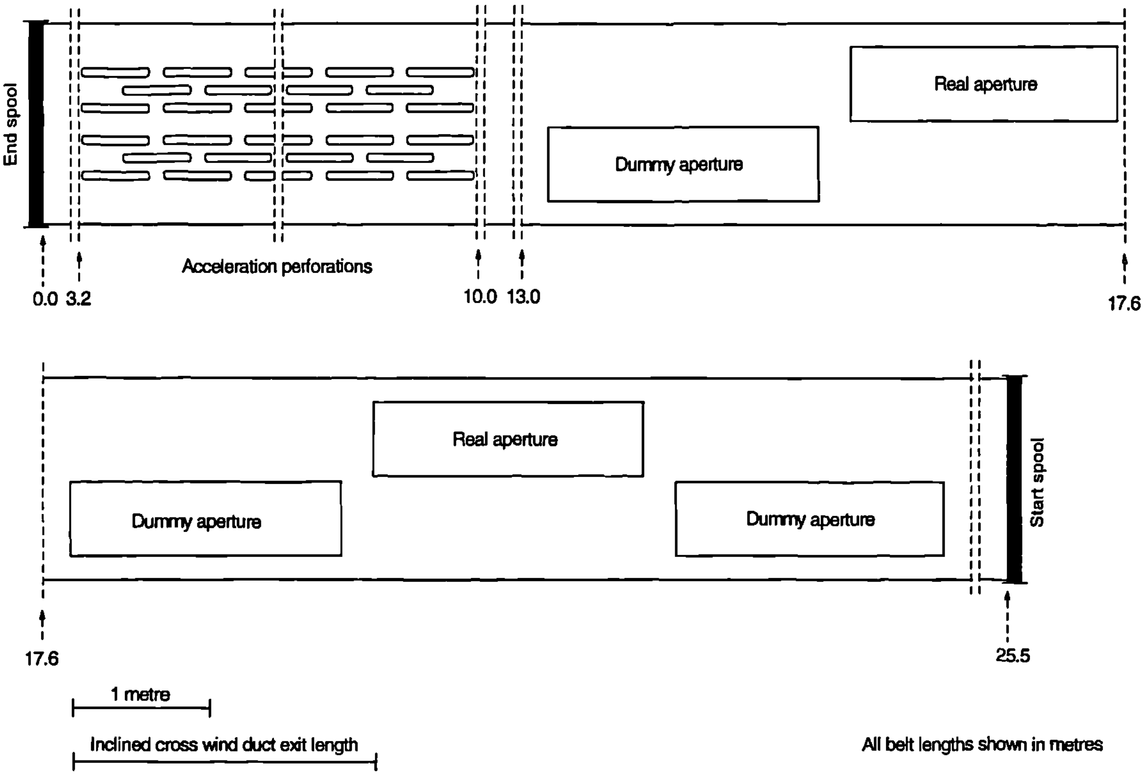

Fig. 5.3 - Stage II belt geometry.

Such a geometry was designed to simulate two cross wind pulses in the working section of the wind tunnel. The main apertures were 2m by 0.5m (length by height) which were configured to match closely with the height of the main jet. The length of the apertures corresponded to four model lengths. The acceleration perforations consisted of 0.5m by 0.05m rounded cornered slits cut transversely in the belt in a staggered fashion. This layout would produce a satisfactorily uniform a distribution of belt tension. The addition of these perforations assisted in the acceleration of the belt system as higher and more uniform belt velocities were attained across the main aperture region. Problematic again however were the vertical edges of the apertures. The same level of plastic strip strengthening was applied to these edges but by virtue of the increased aperture height the kinking effect was more substantial and the stiffening proved to be inadequate. Various alternative methods of belt strengthening were applied to the aperture edges but the problem could not be mitigated satisfactorily. The belt material, whilst retaining structural integrity, was being weakened at the points where the belt kinking snagged with sections of apparatus. Continued testing with different strengthening strips and experimental belt guide systems at the spools ultimately proved destructive to the integrity of the belt. From the failure mode of the belt it was apparent that an aperture edge snagged causing a belt tension increase, ultimately causing a failure in the narrow belt region between the aperture and the belt edge (see figure 5.3). The belt deformation problem was deemed to be ultimately solvable with this aperture height but did not justify further effort at this stage of the evaluation process.

5.2.4 Final Development

Belt Geometry Modifications (III)

An entirely new belt was manufactured for what proved to be the final belt geometry which is shown to scale by figure 5.4.

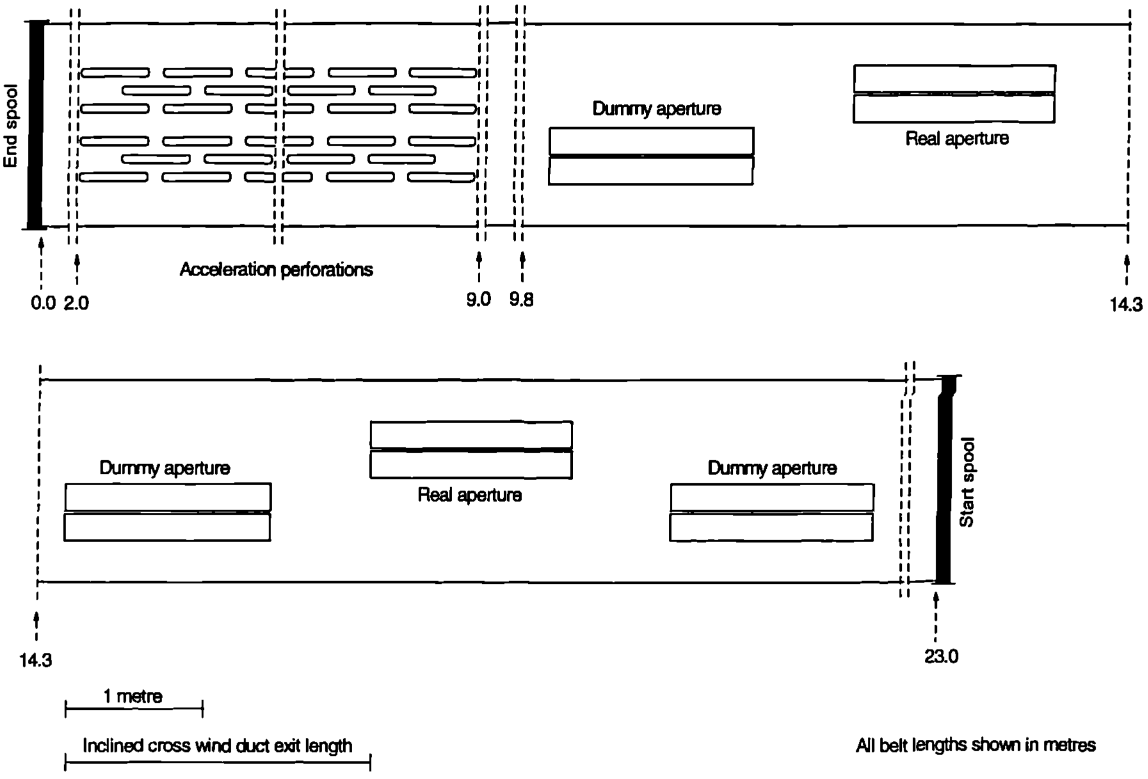

Fig. 5.4 - Stage III belt geometry.

Such a geometry was designed to simulate two cross wind pulses in the working section of the wind tunnel. The main apertures were 1.5m by 0.35m (length by height). The length of the apertures corresponded to three model lengths. Acceleration perforations were again included to assist with the initial acceleration of the belt system. The vertical height of the apertures which had proved problematic with the stage II belt geometry was reduced and the original stage I plastic strengthening strips were applied to these aperture edges. In addition a thin (0.01m) horizontal strip of belt material was allowed to continue across the full length of the aperture at mid-height. This measure proved to be highly effective in reducing the kinking of the belt at the spools as the horizontal strip allowed the a component of belt tension to act at the potentially problematic belt region. The blockage effect of the strip on the aperture was under 3% and it was deemed that flow disturbances induced in the strip wake would decay substantially before reaching the model as this distance corresponds to ~80 strip heights. The operation of the apparatus proved to both straight forward and repeatable with this final belt geometry. One possible area of concern was the fact that the vertical height of the aperture and therefore the height of the emerging air flow was 0.35m where as the main jet height was 0.55m. As the lower edges of the main jet exit and the aperture were at the same level the cross flow emerging from the aperture would not fully envelop that of the main jet. A shear layer would therefore be present in the working section level with the top edge of the aperture.

5.3 Matching of Belt and Fan System

5.3.1 Method

With the dynamic behaviour of the apparatus established and the final geometry of the belt fixed it was necessary to establish the correctly matched velocity components for the aerodynamic experimentation. By positioning a stationary real aperture centrally to the inclined length of the cross wind duct and adjusting the cross wind fan speed is was possible to measure the cross wind velocity, u_{cw}, and therefore calculate the axial component, u_x, and the cross component, u_y (see figure 3.2). Once u_x was known a experimental run could be undertaken and the belt velocity, u_s, could be measured during that run. It was required that u_x and u_s were equal. If initially u_s was too low for the measured u_x decreasing the cross wind fan speed would not only allow the belt to attain a higher velocity by virtue of reduced belt friction but would also reduce the stream wise cross wind component due to the lower air flow induced by the fan through the aperture. By adjusting the cross wind fan speed in the desired sense and with an estimated magnitude between experimental runs a matched velocity for the apparatus was attained (see section 5.3.2).

5.3.2 Conclusions

Despite the presence of the acceleration perforations the belt velocity continued to increase slightly over the main aperture region. The average belt velocity over the first real aperture (see figure 5.3) was 8.48m/s. The average velocity over the second real aperture was 9.01m/s. The median of these two values is 8.75m/s. The main jet velocity, u_{mj}, was set to match this median value. This variation represents an average ± 3% belt velocity variation on the main jet velocity and this can be calculated to induce an error from the desired 30° yaw angle of +0.8° at the first real aperture and -0.7° at the second aperture assuming the same air flow velocity emerging from each aperture over the experimental run. No efforts were directed to producing a more uniform belt velocity. The settings of the main jet speed controller and cross wind jet speed controller required to match the apparatus were both coincidentally at 33Hz out of a maximum electrical drive frequency of 50Hz available for each of the speed controller units.

With the mechanical development of the apparatus complete to a satisfactory standard an aerodynamic investigation of the wind tunnel working section, using instrumentation detailed by chapter 6, could be undertaken. The methods and results are presented in chapter 7 and the discussion of the results is presented in chapter 10.

6.0 Instrumentation

6.1 Introduction

To monitor both the mechanical performance of the designed apparatus and the aerodynamic effects in the wind tunnel working section various items of instrumentation were required. The instrumentation was either expressly designed or configured from existing equipment or available components. The simulation technique, based on a stationary aerodynamic model, allowed standard instrumentation to be utilised albeit with required fast response.

6.2 Pressure Transducers

6.2.1 Selection

The ultimate aim of the this transient cross wind simulation technique is to measure transient surface pressures induced on a particular vehicle shape. As a result fast acting pressure transducers were required to capture high frequency pressure variations. Five piezoelectric differential pressure transducers were purchased with individual salient characteristics shown by table 6.1.

Manufacturer	Sensor Technics
Type	103LP10D-PCB
Pressure range	±1000Pa
Rise time (10-90%)	0.2ms
Natural frequency	~20kHz
D.C. supply	12V
Output range	1-6V
Zero pressure offset	3.5V

Table 6.1 - Pressure transducer characteristics.

Each transducer was approximately 0.03m by 0.03m by 0.05m and all five were mounted together as a unit of approximately 0.15m by 0.1m by 0.04m to facilitate electrical connection to a single power supply to be used for all the transducers. Each transducer in addition to electrical connections had two pressure ports between which the pressure differential was measured.

6.2.2 Calibration

To calibrate the transducers a pitot-static tube was positioned to record stagnation and static pressure in the main jet working section. The two recorded pressures were connected in the same sense to each of the five pressure transducers using two five way tubing joints. The same two pressures were also connected to a oil based fluid micromanometer. This arrangement allowed the same dynamic pressure to be concurrently applied to the five pressure transducers and the micromanometer. Readings were taken visually for the micromanometer and the individual transducer voltages were recorded at 200Hz over a period of one second using a P.C. based data logger (see section 6.6.2) then averaged. A zero reading was taken with no main jet velocity followed by several readings over a range of discrete jet velocities followed by a additional final zero reading. The results of a typical calibration are shown by figure 6.1.

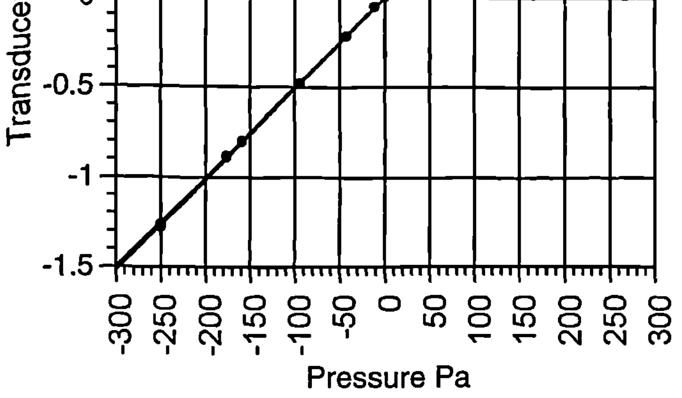

Fig. 6.1 - Typical pressure transducer calibration.

Figure 6.1 shows the transducer voltages induced by both positive and negative pressure differentials applied to the transducer ports. A particular calibration of all five transducers, each with a linear best fit, is displayed by figure 6.1. In total four separate calibrations were undertaken over the full period of the experimentation and each constant of proportionality was found to differ by a maximum of 1.53% from the mean for an individual transducer. The rms constant of proportionality variance was bounded by a maximum of 0.55%. It can be concluded that the pressure transducers were both repeatable and linear over the pressure range tested.

6.3 Aerodynamic Probe

6.3.1 Selection of an Aerodynamic Probe

In order to assess fully the viability of the experimental test technique it was necessary to record the dynamic air flow behaviour in the working section in terms of both velocity and flow angle. It was decided this may be best achieved using either a five hole probe or a hot film probe. These two probe types have differing characteristics. Ultimately it was deemed that a five hole probe should be used for the experimentation providing the dynamic response of the probe was sufficient. Five hole probes are more robust, less expensive and can operate in an unfiltered air supply. In addition the use of a five hole probe was compatible with the existing five fast response pressure transducers (see section 6.2).

6.3.2 Design Requirements

To optimise the dynamic response of the probe it was necessary to ensure that the tube length between the probe tip and the transducers was kept to a minimum. The pressure transducers in isolation are fast acting but if significant tube lengths are used to record transient pressures the signal is both damped and shifted in phase with increasing tube length. The minimum tube length requirement is in opposition to the practicality of positioning the probe at a variety of points in the working section. If the transducers were fixed in position a considerable tube length would be required to allow the probe to traverse the entire working section. It was therefore necessary to investigate the maximum tube length that could be used so as to not detract from the dynamic performance of the probe.

6.3.3 Initial Dynamic Response Tests

Exploratory investigations were undertaken using a primitive pressure pulse generation rig. The rig consisted of 0.02m diameter air jet configured to exhaust to a 1mm bore total pressure probe. The action of the air flow on the total pressure probe was periodically obscured then permitted by means of a rotating circular disc with apertures in line with the air jet placed in the disc periphery. The disc was rotated by means of a small adjustable speed d.c. motor. Thus as the disc rotated a periodic pressure pulse was delivered to the total pressure probe as each aperture passed the line of sight of the air jet. Four pressure transducers (see section 6.2) were connected to the pressure probe by means of a four way tubing joint and four lengths of flexible plastic tubing. However the tubing used to make these four separate connections was of differing lengths. The tube lengths were 0.2m, 0.4m, 0.8m and 1.6m and the tubing used had a bore of 1mm. The secondary pressure port on each of the transducers (see section 6.2.1) was open to atmosphere via a long section of tubing terminating away from any flow interference. Each of the transducer voltages were recorded at 4kHz and the calculated pressures were phase corrected using the speed of sound and the tube length differentials. Figure 6.2 shows the results of the dynamic pressure response of the four separate tubing lengths which are each represented by a single trace. When considering the cross wind simulation apparatus it is possible to calculate the frequency represented by a single model length half wave step pulse of cross flow at the axial test velocity. A model length of 0.5m at a velocity of ~10m/s corresponds to 10Hz. Increased frequency resolution corresponds to increased transient pressure temporal resolution. The air flow velocity also allows calculation of the expected magnitude of total pressure. These initial dynamic pressure transducer response tests recorded a maximum pressure magnitude which corresponds to a dynamic pressure based flow velocity of ~18m/s. The half wave pulse width developed corresponds to a periodic frequency of ~30Hz, although as the pulse is of square wave form the rapid rise time corresponds to a much higher frequency of ~400Hz (see figure 6.2).

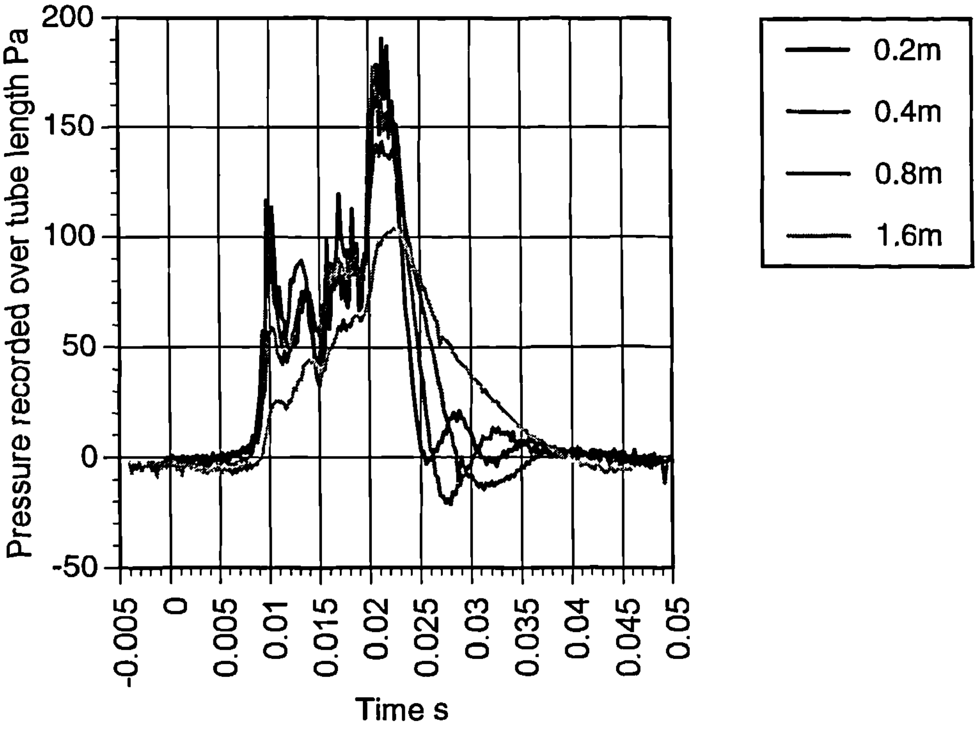

Fig. 6.2 - Dynamic pressure response with differing tube lengths.

The exact definitive pressure variation local to the probe tip in addition to the effect of the interaction at the four way tubing joint of the harmonics developed by each tube were not known. However what was known was that each of the pressure transducers received the same pressure signal from the total pressure probe and any degradation of the received pressure signal at the transducer was solely due to the length of connecting tubing concerned. It can be observed that while the induced phase shift by virtue of the tube length differential may be corrected for (the rise point of the traces is coincident) the damping effects caused by differing tube lengths are significant. Clearly increasing the tube length increased the damping effect on the signal. The 0.2m, 0.4m and to a lesser extent the 0.8m tube length can be seen to capture a similar transient signal over the width of the pulse. However the settling characteristics of each tube length after the pulse are different. It may be interpreted that during the pulse signal there is a forced response and after the pulse the signal is a natural response of the transducer and tube system. Ideally the tube length should be zero for optimum dynamic response however as this is impractical it was decided to limit the tube length utilised to as short as possible under 0.8m.

Using the same exploratory pressure pulse rig the influence of tube bore was also studied. Probes which had a smaller bore opening at the actual probe tip compared to the bore of the tubing immediately behind the probe tip were found to suffer from increased signal damping. Probe systems which had a continuous bore from probe tip to transducer were significantly less damped. Whether the damping was increased by the small bore size at the opening or the change in bore immediately behind the opening was not investigated. As a result it was decided to design the five hole probe system using a single and relatively large tubing bore throughout.

6.3.4 Probe Design

The tip of the designed five hole probe was a forward facing pyramid type as shown by figure 6.3.

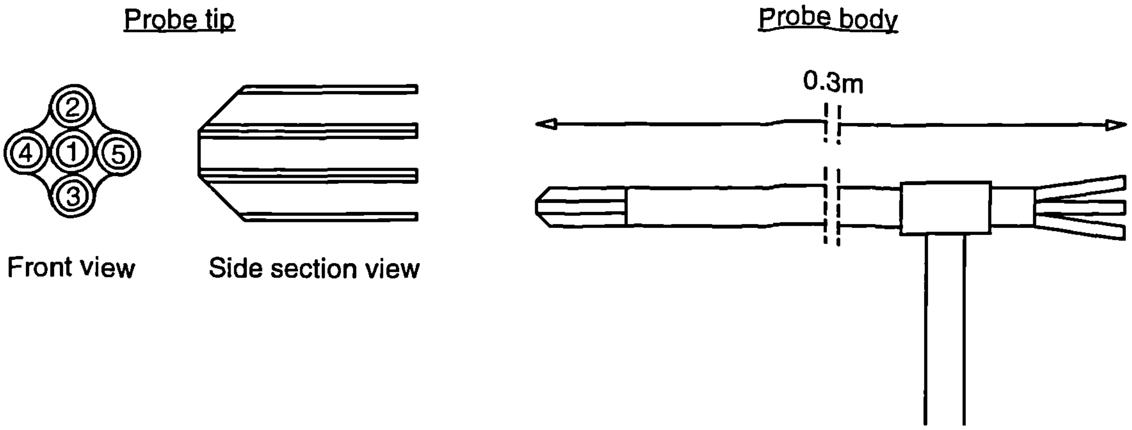

Fig. 6.3 - Probe geometry and tapping numbering system.

The probe was constructed from five 1mm internal bore steel tubes which were sheathed in a straight section of 6mm internal bore tubing. The separate tubes at the probe tip were held together by an epoxy resin and then ground to a 45° angle as shown by figure 6.3. Particular care was taken to ensure the grinding process did not induce geometric aberrations to the tube openings at the tip. The probe length was 0.3m and the five steel tubes were splayed slightly at the rear to facilitate the attachment of flexible plastic 1mm bore tubes to connect the probe tappings to the five separate transducers. It was found that the length of plastic tubing necessary to attach the probe to the transducers whilst allowing positioning of the probe in the wind tunnel working section could be restricted to 0.2m giving a total probe tube length of 0.5m per tapping. It was expected this tube length would produce a satisfactory dynamic probe response (see figure 6.2). The probe sheath was attached to a separate steel tube section which allowed the probe body to be held at various points in the wind tunnel working section.

6.3.5 Probe Calibration

The probe was calibrated using an existing calibration rig. The probe calibration rig was fully automatic and consisted of probe mounting device which could be rotated in two mutually orthogonal planes by two independently controlled stepper motors. An air flow, produced by a small centrifugal fan, enveloped the region occupied by the mounted probe. The geometry of the calibration rig was such that the relative position of the probe tip was fixed in relation to the air flow as the probe was rotated. The probe tappings could be connected to a pressure transducer which was in turn connected to an analogue input card of a P.C.. The P.C. controlled the stepper motor positioning, recorded and averaged the five probe tip pressures for each probe position. The stepper motor resolution was 66 steps per degree. The air flow emerging from the fan was passed through a honeycomb flow straightening section followed by two separate gauze screens to ensure a reasonably uniform velocity profile at outlet.

The five hole probe shown by figure 6.3 was positioned by the calibration rig sequentially from -30° to +30° inclination to the nominal air flow direction in a given orthogonal plane at 2° intervals. At each interval the probe was further positioned at -30° to +30° inclination in the alternate orthogonal plane again at 2° intervals. This procedure calibrated the probe to a ±30° on coming air flow cone angle. This cone angle is a typical maximum operation range for a five hole probe. The two orthogonal axes are nominally termed yaw and pitch. At each probe position the five recorded pressures produced values of yaw and pitch coefficient, shown by figure 6.4a, together with total and static pressure coefficients, shown by figures 6.4b and 6.4c. The nominal air flow velocity for the calibration was 38.5m/s and for clarity only a 10° interval calibration is shown. The precise definitions for the calculated probe coefficients are shown by table 6.2.

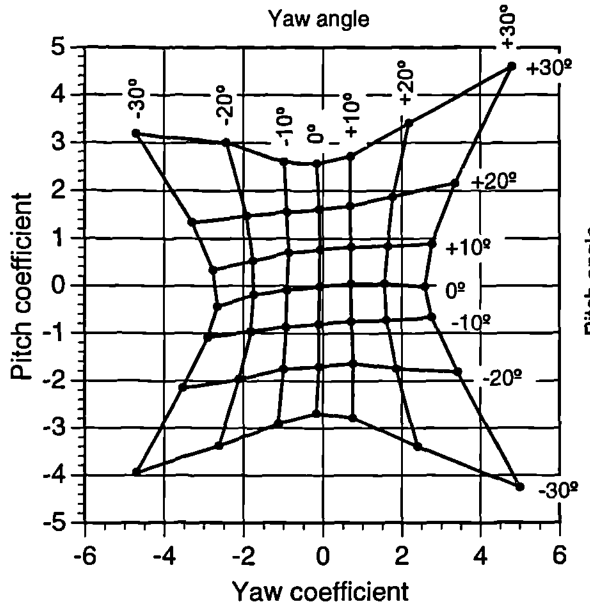

Fig. 6.4a - Five hole yaw and pitch coefficients with probe angle.

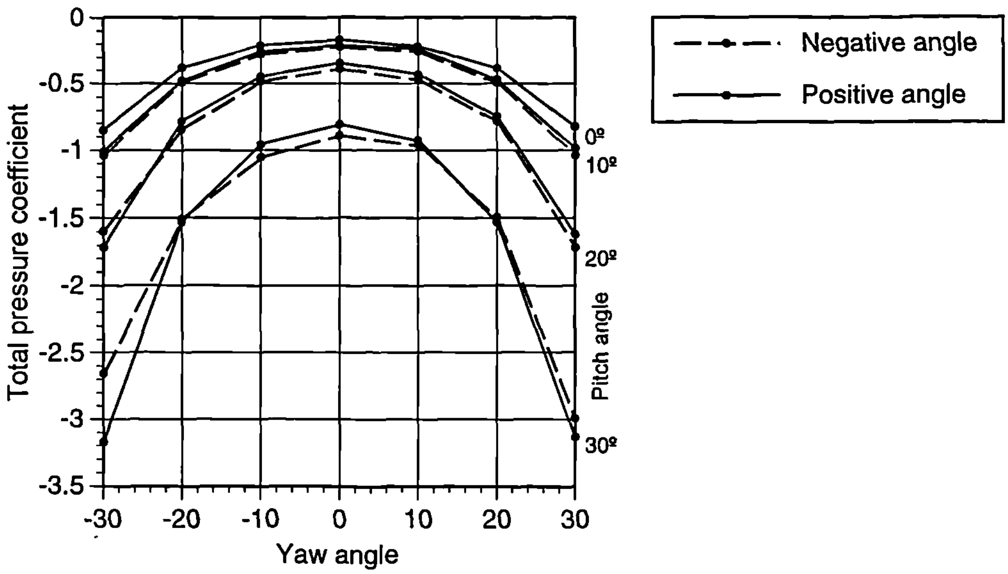

Fig. 6.4b - Five hole total pressure coefficient with probe angle.

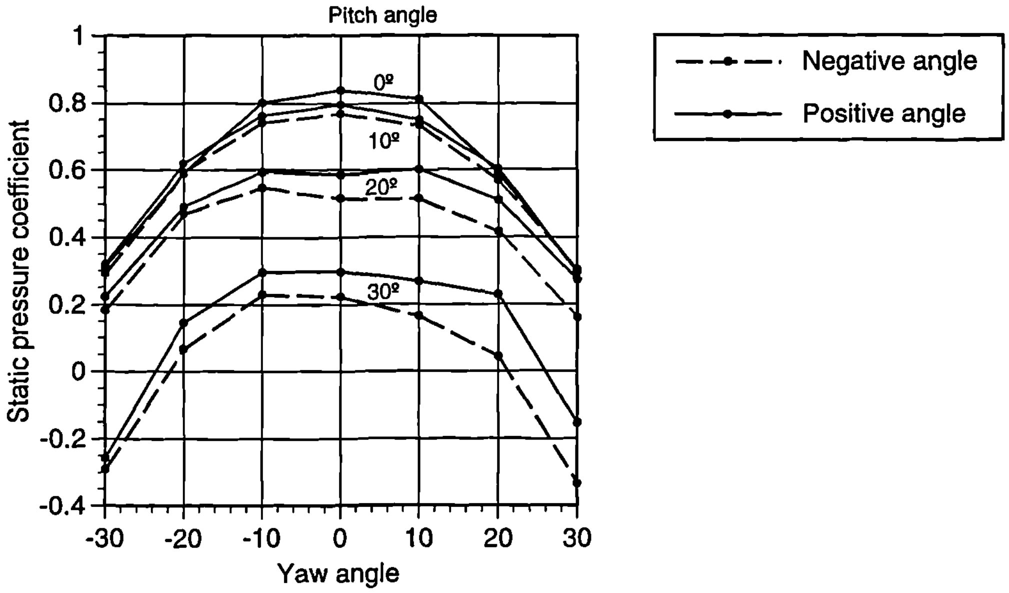

Fig. 6.4c - Five hole static pressure coefficient with probe angle.

Parameter	Definition
Probe yaw coefficient	$(p_4 - p_5) / (p_1 - p_{av})$
Probe pitch coefficient	$(p_2 - p_3) / (p_1 - p_{av})$
Probe total pressure coefficient	$(p_1 - p_{total}) / (p_1 - p_{av})$
Probe static pressure coefficient	$(p_{av} - p_{static}) / (p_1 - p_{av})$
p_1, p_2, p_3, p_4 & p_5	Probe tip pressures 1,2,3,4 & 5 (see figure 6.3)
p_{av}	$(p_1 + p_2 + p_3 + p_4) / 4$
p_{total}	Pitot total pressure recorded local to probe tip
p_{static}	Pitot-static pressure recorded local to probe tip

Table 6.2 - Five hole probe calibration definitions.

The probe was calibrated on three separate occasions and on each the alignment of the probe in the calibration rig at a zero degree precalibration datum was achieved visually. This alignment method proved to be accurate to within ±0.5° between calibrations. The level of accuracy was facilitated by virtue of the fact that the probe axis was of significant length (see figure 6.3) and could be easily aligned with any datum straight edge. The probe calibration coefficients were also shown to be repeatable and in addition the coefficient values measured followed expected trends as displayed by existing probes. Slight asymmetry of the probe coefficients may be observed and will have been caused by corresponding asymmetry at the probe tip induced during manufacture.

The air velocity used for the probe calibration was 38.5m/s where as the expected experimental velocities to be monitored would be ~9m/s. It would have been more satisfactory to calibrate the probe at this latter velocity but the actual calibration velocity used was a lower limit of the centrifugal fan unit used with the calibration rig. There would therefore be potential for Reynolds number based flow discrepancies between the experimental and calibration probe tip flow regimes resulting in possible induced error in the conversion of experimental pressures to interpreted velocities using the calibration data. Discrepancies have been assessed to be up to 5% of the true dynamic pressure between Reynolds number ranges, based on probe tip diameter, of 2×10^3 to 20×10^3 [14]. Additional discrepancies of ~1.5° for every 10° degree recorded flow angle have been found over Reynolds number ranges of 3×10^3 to 40×10^3 [14]. The Reynolds number range for the probe shown by figure 6.3 between operation and calibration velocities was 2×10^3 to 12×10^3 and so comparable discrepancies were expected. Turbulence based discrepancies have also been qualitatively investigated for this type of probe and have been found to be low for ±15° on coming flow cone angle but up to 1° in terms of actual to recorded flow angle outside this range [8]. The actual five hole probe and pressure transducer system was compared to a pitot-static probe for time averaged steady air flow parallel to both probe axes. The probe pressures were each recorded over a period of one second at 200Hz then averaged and the interpreted probe axis velocity and dynamic pressure were calculated. The pitot-static tube, connected to a fluid micromanometer, was concurrently positioned in the same air flow and the dynamic pressure developed was calculated. The five hole probe interpreted a 4.7% higher dynamic head and a corresponding 2.3% higher probe axis velocity than the pitot-static probe for a 7.94m/s air velocity recorded with the latter probe. This difference correlated to the expected level of discrepancy and was therefore deemed satisfactory.

6.3.6 Dynamic Response Tests

With the five hole probe having been calibrated (see section 6.3.5) for steady flow conditions it was necessary to establish the dynamic response of the complete probe and transducer system to be used for the experimental investigations. It was decided to achieve this by concurrently monitoring a transient air flow by both the five hole probe and a hot film cylindrical element probe. The hot film element comprised a high purity platinum film deposited on to cylindrical quartz substrate. The anemometer operation was that of constant probe element current.

The optimum transient air flow to be monitored would be that which would be ultimately measured and is therefore that produced by the transient cross wind simulation apparatus. It was felt that a simple yet valuable dynamic response assessment could be achieved by using a single velocity component hot film probe mounted in the working section so as to measure predominantly the cross component, u_y, of working section velocity (see figure 3.2). Thus for this assessment the hot film probe single wire element was parallel to the nominal axial direction of the air flow produced by the main jet.

A relationship exists between the air velocity normal to the probe element and the voltage necessary to maintain a constant probe current. An linearised form of this relationship ($\sqrt{}$air velocity versus hot film voltage^2 [20]) was assumed. The hot film probe was calibrated over a range of flow velocities up to approximately 11m/s, nominally perpendicular to the probe element, produced by the main jet wind tunnel. A pitot-static probe concurrently recorded the dynamic pressure via a fluid micromanometer. The hot film probe voltage was recorded at 200Hz over a period of one second then averaged for each velocity setting of the main tunnel. Table 6.3 shows the salient hot film probe characteristics and figure 6.5 shows the resulting calibration of air velocity to hot film voltage.

Manufacturer	T.S.I.
Type	1211-20
Element diameter	50μm
Element active : total length	1.0 : 1.67mm
Anemometer upper frequency	120kHz

Table 6.3 - Hot film probe characteristics.

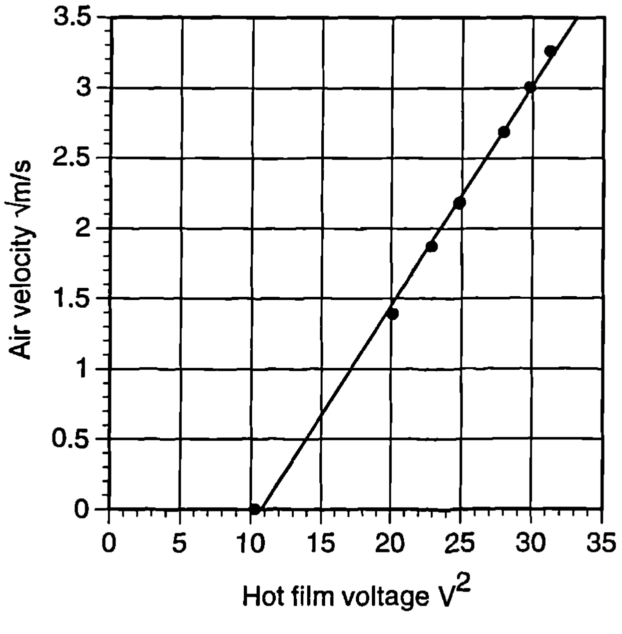

Fig. 6.5 - Hot film calibration of voltage to air velocity normal to probe element.

Figure 6.5 shows that the probe calibration follows the expected correlation of the square of the hot film voltage to the root of the air velocity [20].

With the hot film calibration undertaken it was now possible to undertake a dynamic response test. The five hole probe and transducer system was placed to monitor air flow in a representative position in the wind tunnel working section. The expected transient flow regime induced by the cross wind simulation apparatus would be an initial axial flow condition followed by a sudden transition to a yawed flow of 30° then returning to axial flow conditions. This would occur twice in a given simulation as apparatus was configured to deliver two such air flow transitions to the working section (see section

5.2.4). So as not to induce excessive flow angles to the probe axis an optimum probe alignment would therefore be to set the five hole probe axis at -15° to the axial wind tunnel flow which would then allow the expected 30° air flow angle change to result in a +15° air flow angle to the probe axis. This would keep the expected working section transient air flow within a ±15° on coming flow cone angle to the probe axis (see figure 6.6). The hot film probe was placed to monitor flow as close as possible (within 0.02m) to the five hole probe tip with the probe element perpendicular to the nominal axial direction main jet air flow (u_x) with the probe body down stream relative to the element as shown schematically by figure 6.6. The probe tips were positioned vertically to one another and therefore figure 6.6 shows only the relative alignment of the probe axes. Both probes were clamped rigidly.

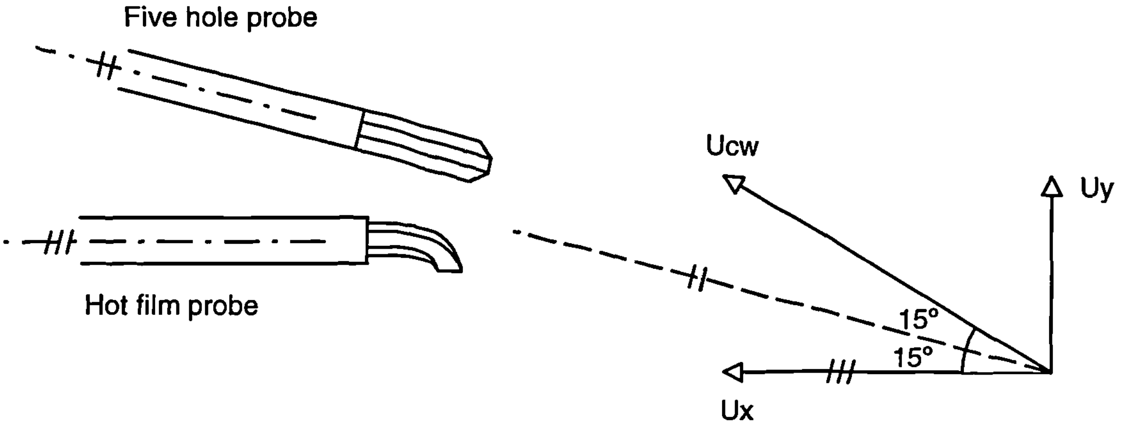

Fig. 6.6 - Schematic alignment of probes during dynamic response tests.

An experimental run of the test apparatus was undertaken and the five hole probe voltages and the hot film voltage were each concurrently logged at 2.4kHz over a period of ~1.6s. The voltages were then smoothed (see section 6.6.4) by a factor of three to produce and effective logging frequency of 790Hz. The smoothing level produced no visible effect on the recorded voltages and was undertaken for data compression purposes only. Figure 6.7 shows the interpreted transient values of cross stream velocity, u_y, against time for both the hot film probe and the five hole probe.

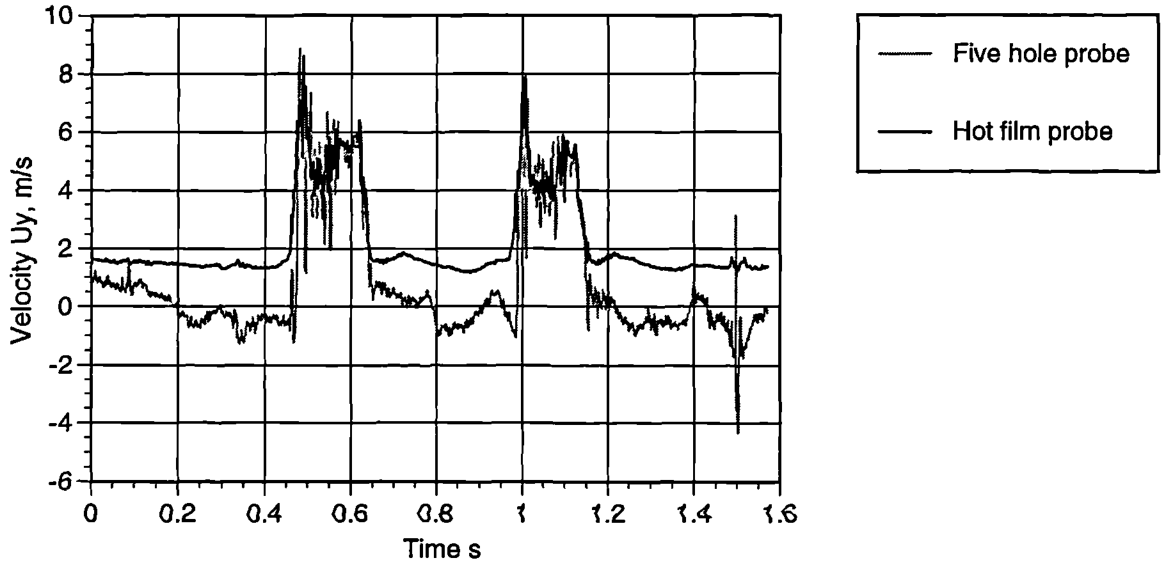

Fig. 6.7 - Comparison of five hole and hot film probe cross stream velocity.

The form of this and similar results will be discussed fully in chapter 10 but addressed here is solely the correlation between the two probe types. Below 2m/s the correlation of the two probe interpreted velocities is poor. However at these values the hot film probe was subjected to a predominant air velocity (u_x) parallel the axis of the element (see figure 6.6) and not in the perpendicular flow direction relative to the element used in the calibration. The effect of two component flow on a single component hot film probe has been investigated and has been found to correlate to relationship [20] given by table 6.4.

Parameter	Definition
Interpreted air velocity perpendicular to element ($U\perp$)	$U\perp = U\sqrt{(\cos^2\alpha + k^2\sin^2\alpha)}$
U	Actual air velocity relative to probe
α	Actual air flow angle relative to $U\perp$
k	Empirically derived parameter

Table 6.4 - Two component flow effects on a single component hot film probe.

A typical constant value for k (table 6.4) may be taken to be 0.2 [20] although in reality k varies slightly with flow angle and velocity for a given probe. The equation given by table 6.4 is such that at high angles of α (up to 90°) the correlation of interpreted to actual perpendicular element velocity is poor with the correlation improving with decreasing angle towards a perfect correlation at $\alpha = 0°$. Thus for the flow conditions of u_x and u_y at approximately 9.0m/s and 0.0m/s respectively, producing an α of 90°, the interpreted hot film u_y velocity would be 1.8m/s by the equation in table 6.4. This correlates well to the hot film probe trace (figure 6.7) which exhibits a interpreted velocity of ~1.5m/s. During the action of each of the two cross wind pulses when u_x and u_y were ~9.0m/s and ~5.2m/s respectively, producing an α of 60°, the interpreted u_y velocity would be 5.5m/s by the equation in table 6.4. This increased correlation is exhibited by the traces in figure 6.7 as the two probes match closely at the higher u_y velocities. No analysis of the behaviour of the actual probe in two component flow was undertaken and so no specific value of k (table 6.4) for the probe was established. As the dynamic response of the five hole probe system was being investigated it was deemed more important to analyse the frequency response of the two probe systems than exactly correlate the interpreted velocities. Thus the velocity magnitudes interpreted by the hot film probe using a typical constant k value were considered acceptable.

The hot film probe anemometer used had an upper cut off frequency of 120kHz. However the recorded data was sampled at effectively 790Hz. For a given sampling frequency the range of frequencies captured is half that frequency. Thus it may be concluded that for air flow disturbances below 395Hz the five hole probe and transducer system operates satisfactorily as the general dynamic response of the two probe systems may be observed to be similar by virtue of the close correlation of the two traces above 2m/s shown by figure 6.7. The dynamic response can be quantitatively assessed by undertaking a Fourier analysis of the two recorded traces. Such an analysis was performed on the data displayed by figure 6.7 for data points over a velocity of 2m/s only, as the hot film probe was deemed unsatisfactory below this value. Velocity values below 2m/s were set at a zero value for both traces. This analysis yielded data relating frequency against velocity magnitude for the two traces. Figures 6.8a and 6.8b for clarity show this data set from 0Hz to 100Hz and then from 0Hz to 25Hz respectively. The response of the two probes from 100Hz to the upper 395Hz limit was that exhibited by the flat trace portion of figure 6.8a.

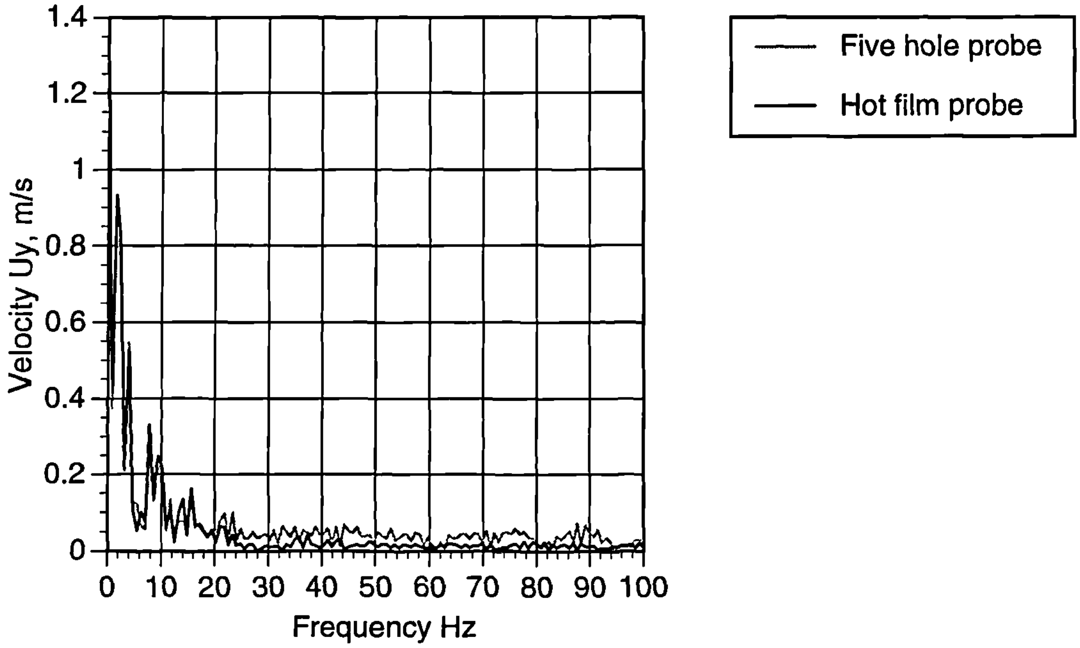

Fig. 6.8a - Comparison of five hole and hot film probe response up to 100Hz.

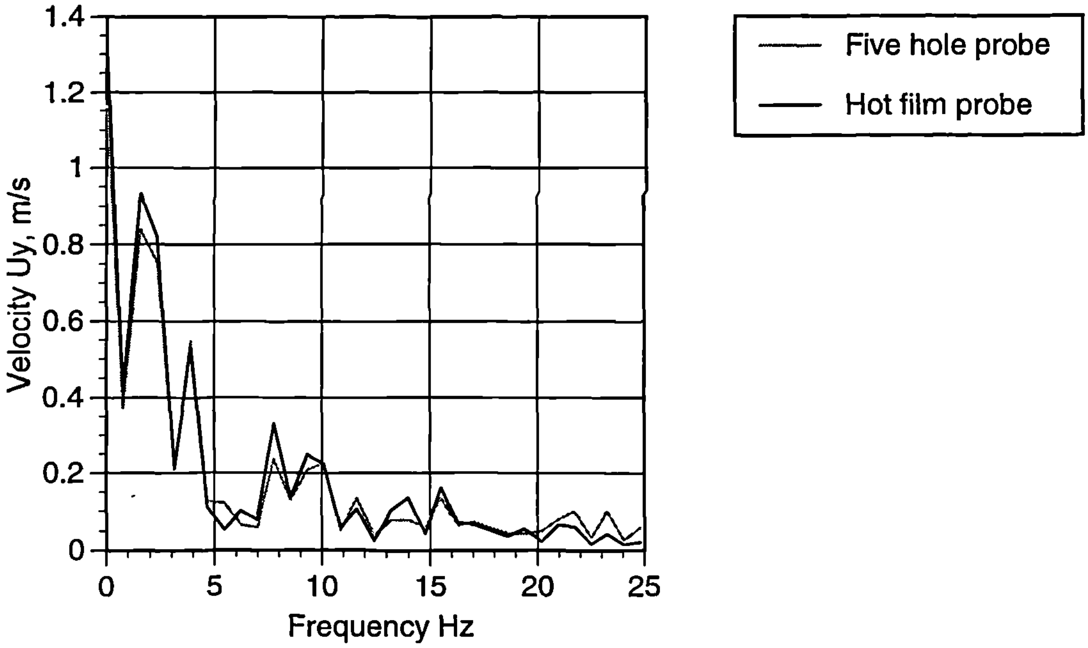

Fig. 6.8b - Comparison of five hole and hot film probe response up to 25Hz.

length due to a combination of differing belt speed and trigger point. Having quantified the level of temporal repeatability of the apparatus the same parameter may be assessed for the actual air flow conditions induced in the working section. The common pressure tappings to the experimental runs (figures 7.35b and 7.35c) exhibit a close level of correlation between runs. In figure 7.35b the height of the trace band at horizontal sections is ~10Pa (15% of maximum recorded transient pressure at tapping '0'). A similar range is exhibited by the secondary common pressure tapping values shown in figure 7.35c. Time dependent readings taken under turbulent air flow conditions will never be repeatable. It is therefore possible that the spread of data exhibited by figures 7.35b and 7.35c is entirely correct. Only by undertaking an increased number of experimental runs will this be established.

The data from table 10.2 suggests that the repeatability of the actual belt velocity is high while the repeatability of the trigger point is less so suggesting that a simple correction may be applied to the data by shifting the separate data sets temporally to force the x/l = 0 marker to coincide. The results of this are shown in figure 7.36a an summarised in table 10.3 below.

	Velocity of belt	Marker x/l = 0	Marker x/l = 1	Marker x/l = 3	Marker x/l = 4
Mean value	8.4789 m/s	0.4823 s	0.5442 s	0.6590 s	0.7208 s
Range of values	0.3600 m/s	0.0000 s	0.0075 s	0.0117 s	0.0102 s
Rms	0.1140 m/s	0.0000 s	0.0017 s	0.0028 s	0.0032 s
Range based *x/l* value	*0.0424*	*0.0000*	*0.1218*	0.1901	0.1657
Rms based x/l value	0.0134	0.0000	0.0280	0.0460	0.0513

Table 10.3 - Modified repeatability of experimental apparatus between runs.

Table 10.3 shows an improved grouping of data over table 10.2 in all relevant categories. Specifically the extreme worst case is that some of the model surface pressures are out of synchronisation by ~19% (cf. ~48%) of the model length. The rms values exhibit a similar factor of improvement over table 10.2. Figures 7.36b and 7.36c show the newly correlated transient readings from the common pressure tappings. In

6.4.2 Model Design

To cross correlate experimental data standard representative vehicle model shapes are used in the field of vehicle aerodynamics. One widely investigated 3D shape, the 'Ahmed' model shown by figure 1.2, is based on an rounded front cornered cuboid of relative dimensions of 3.36 to 1.37 to 1.00 (length to width to height) and as such has typical vehicle aspect ratios. It was decided to manufacture a 2D model with the same length to width aspect ratio but with end plates fitted to the top and bottom of the model to restrict the flow to 2D. The resulting model is shown by figure 6.9.

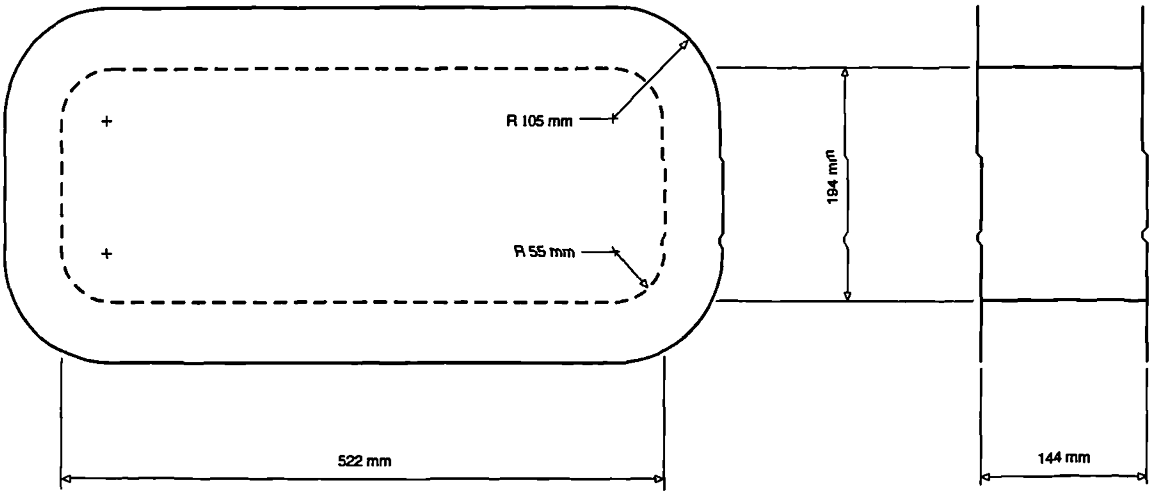

Fig. 6.9 - Model geometry.

The model corners were rounded so as to allow the effects of any shift of aerodynamic separation point at the model surface induced by the simulated transient cross wind conditions to be studied. The model end plates, sides and front were manufactured from 3mm deep plastic panels and the rounded corners were formed from curved plastic sections of the same thickness. The resulting model was supported from below at three points by separate stings fixed to the lower end plate when positioned in the working section. The stings were positioned at the geometric centre of the shape and at two symmetrical positions either side of the model longitudinal centre line approximately coaxial with the radii centres' at the rear of the model. Pressure tappings (see figure 7.2) were set into the full model perimeter, mid way between the two end plates, using short lengths of 1mm internal bore stainless steel tubing extending in to the central hollow model region in which the five pressure transducers (see section 6.2) could be positioned and connected by means of flexible plastic 1mm internal bore tubing. The total length and bore of tubing between the tapping face and pressure transducer was exactly the same (0.5m) as that used with the five hole probe (see section 6.3.4) and as such has the same dynamic response characteristics (see section 6.3.6). The mass of this pressure tapping model was approximately 3.6kg and it was decided that this would be excessive when examining dynamic force behaviour using a force balance. A conventional force balance, using deflection strain gauges, and model arrangement is essentially a spring, mass and damper system and as a result possesses second order dynamic characteristics such as over shoot and settling time to step inputs. Reducing the mass of the system improves the response to a step input. Thus a second model for use with a force balance was constructed with identical dimensions (see figure 6.9) but manufactured from a light yet rigid high cell density foam material. The model was 0.6kg and therefore comprised one sixth the mass of the pressure tapping model. This model was supported in the working section by an identical sting system.

The height of the model position in the working section was selected to allow the cross wind jet air flow to exhaust from the real apertures (see section 5.2.4 and figure 5.3) evenly above and below the model end plates. The aperture height was 0.35m and the model height was 0.144m leaving potentially a 0.103m height of cross wind flow extending vertically beyond both model end plates. Concern was addressed to verifying whether this flow was even over the intended model height and therefore whether the height occupied by the model would be enveloped fully in the cross wind conditions produced by the simulation apparatus during an experimental run. Without the model present in the working section the five hole probe was placed at a representative position in the wind tunnel working section so as to monitor air flow in at three vertical points, over three separate experimental runs, at a fixed position relative to the length and width of the intended model orientation. The model, placed in the working section, would occupy a 0.144m height centrally to the real aperture. Two of the monitoring points were 0.03m above and below of this full height and a third was central to this height. Non-dimensionalising the probe position to the model height, h, and relative to the vertical intended model centre these three monitoring points were at -0.7, 0 and +0.7. The five hole probe data was logged at 2.4kHz and smoothed by a factor of three (see section 6.6.4). The results of this procedure are shown by figure 6.10.

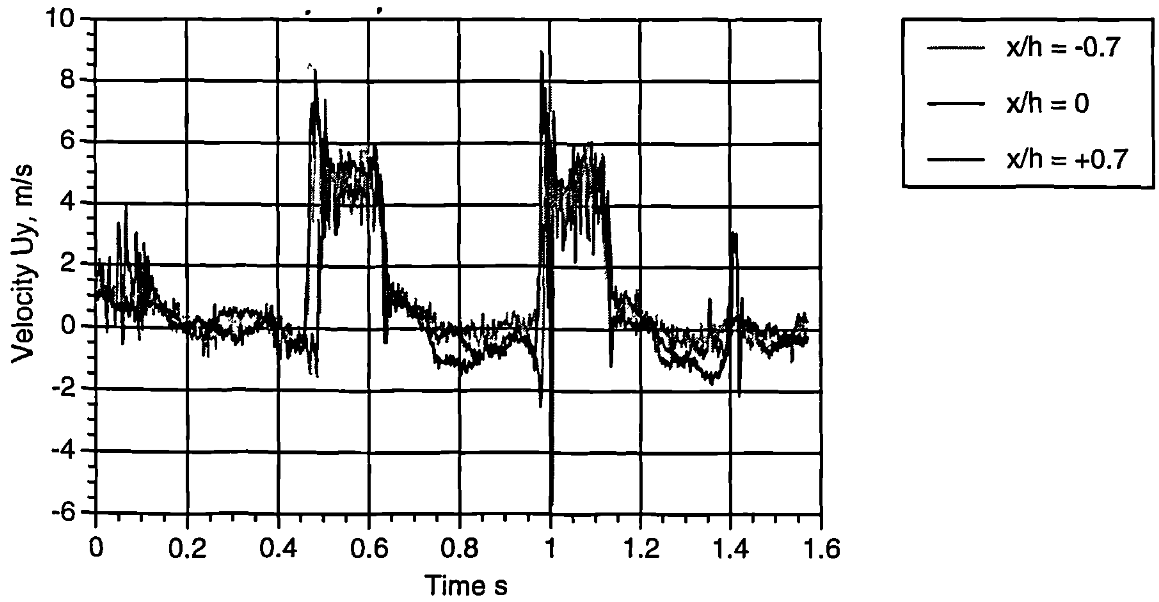

Fig. 6.10 - Cross stream velocity at differing heights in the working section.

The differing rise point of the x/h = +0.7 trace shown by figure 6.10 was not investigated but was probably induced by slightly differing belt speed and data logging trigger signal produced by the apparatus on that particular experimental run (see section 6.6.2). More important however is that the cross wind simulation apparatus produces a satisfactorily similar magnitude of transient cross flow region over an adequate height with respect to model position in the wind tunnel working section.

6.5 Six Component Force Balance

6.5.2 Design Brief

A six component force balance was expressly designed to examine the aerodynamic loads induced on a model shape under the transient cross wind conditions produced by the simulation apparatus. The balance would have to be of fast response to monitor the transient aerodynamic loads and sufficiently small to include the possibility of mounting within an aerodynamic model. A wide range of expected loads would have to be catered for allowing differing model sizes and increased test velocities to be utilised for future studies using this experimental technique.

6.5.2 Design Concept

In order to allow the measurement of all the three mutually perpendicular components of force and moment induced on an aerodynamic model it is necessary to construct six component force balance. An ideal six component force balance must be capable of individually measuring a single component of force from a single point of action without influencing or being influenced by any other of the five force or point of action combinations. This is difficult to implement in practice because strain gauge load cells, which rely on deflection, are used to measure the forces. Any deflection in a given direction, no matter how minute, will cause compensatory movements within the structure of any force balance so as to produce smaller deflections on the other load cells which give rise to induced apparent forces. The design of a balance must therefore be one of minimisation of these induced forces and at the same time paying attention to the overall stiffness of the structure for anti-vibration purposes.

A method of transmitting any aerodynamic forces acting on the model to an individual load cell must be chosen. To minimise the induced forces any such transmission link must be stiff in the direction of the desired force transmission and pliant in all others so as to limit the effect of the link on the other forces. A conventional [42] link utilises a thin rod which is stiff axially but pliant in bending and torsion.

6.5.3 Detail Design

A force balance was designed and is shown schematically shown by figure 6.11.

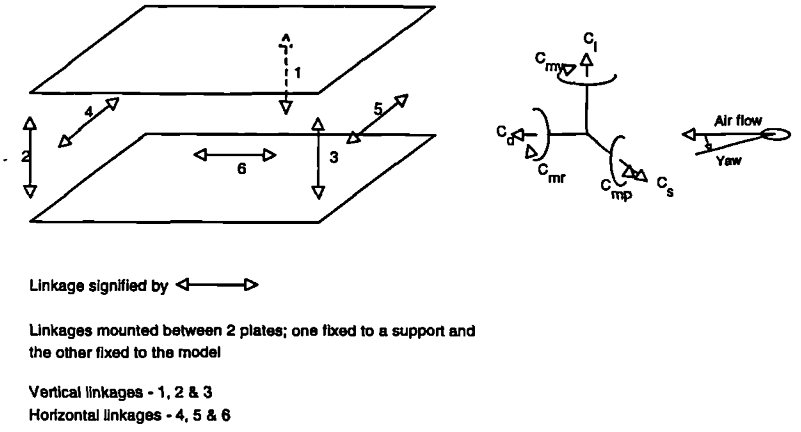

Fig. 6.11 - Schematic force balance design with force components.

The design consisted of two metal plates held apart from one another by six thin links. The links were positioned axially in three mutually orthogonal planes to as to render the plates fixed in position relative to each other. The links were attached at one end directly to one of the plates and at the other end indirectly, via a strain gauge load cell positioned to monitor the linkage axial force, to the opposite plate. A force applied for example in the vertical plane would directly load links 1, 2 and 3 significantly (see figure 6.11) as in this sense those links were rigid (a thin rod is axially stiff) but would indirectly load links 4, 5 and 6 insignificantly (a thin rod is relatively plaint in bending and torsion). The resulting loads, either direct or indirect would be monitored by the six strain gauge load cells. Six load cells were purchased for the force balance each with salient characteristics shown by table 6.5.

Manufacturer	Graham & White Instruments (GWI)
Type	535Q
Full scale load (F.S.L.)	±60N
Full scale deflection	0.6mm
Safe overload	150% of F.S.L.
D.C. input	10-20V
Output to input sensitivity	2mV/V (at F.S.L.)

Table 6.5 - Load cell characteristics.

The full scale load for the cells was selected to not only support both the self weight of the balance and the model but to also allow a wide range of aerodynamic loads to be monitored (see section 6.5.2). The load cell capacity also rendered the balance sufficiently stiff and safe for accidental over load when in use. Estimations of expected aerodynamic loading and desired magnitudes of load cell monitored forces allowed the design and positioning of the structural components within the balance. These components were designed to be of high stiffness (>100 times) compared to the load cells so as to ensure that any aerodynamic induced loads caused predominant deflections in only the load cells where the forces could be monitored. The links were manufactured from 1.6mm diameter steel rods. The remainder of the balance was aluminium throughout. Each plate (see figure 6.11) had dimensions of 0.298 by 0.173 by 0.01m. Each load cell was 0.072m by 0.056m by 0.029m and one load bearing face of each cell was fixed to one plate by means of a bracket. The other load bearing face was fixed to a linkage which in turn was fixed to the opposite plate. The internal distance between the two plates was 0.076m. The resulting balance was compact and the realised design is shown by figure 6.12.

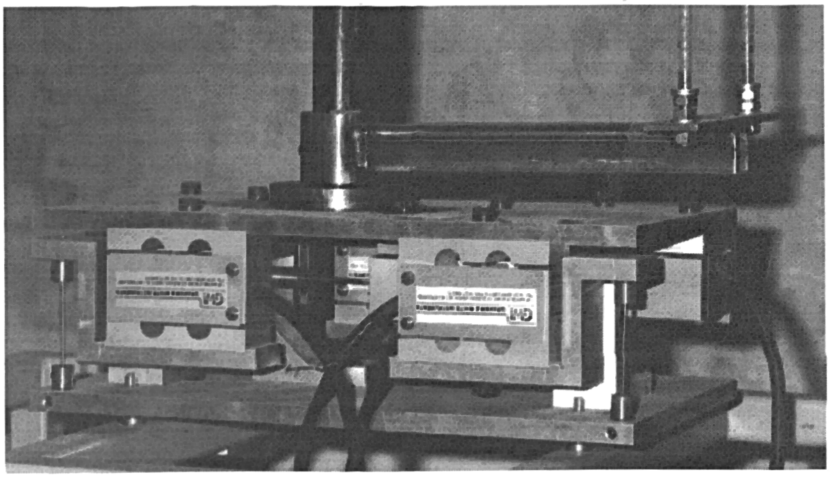

Fig. 6.12 - Realised force balance.

Figure 6.12 shows a side view of the balance. Although this balance may be fitted within an aerodynamic model an external sting support system was used for simplicity. The three vertical stings (see section 6.4.2) may be seen extending off the top of the figure to support an aerodynamic model. The lower end of the stings were fixed to the top plate of the balance beneath which six load cell, bracket and linkage units are housed, two of which may be seen clearly. The top face of each load cell is fixed directly to the top plate and a shaped bracket connects the lower face of each load cell to a vertical thin steel rod linkage, two which can be seen beneath the extreme corners of the top plate. The lower end of the links are fixed to the bottom plate which is in turn fixed to a support frame.

The electrical outputs from each load cells were connected, via an amplifier unit, to a data logger (see section 6.6.1). The amplifier unit consisted of a six, one for each load cell, separate amplifiers whose individual salient characteristics are shown by table 6.6.

Manufacturer	Analog Devices
Type	AD524
D.C. Supply	±6-18V
Max input signal differential	±10V
Input signal gain settings	1, 10, 100 or 1000

Table 6.6 - Amplifier characteristics.

6.5.4 Calibration

The force balance, having been manufactured, required calibration. A conventional [42] calibration consists of primarily loading the balance in steps up to then reducing from a maximum expected load in each of the six pure load components in turn. Those components are nominally labelled lift force, drag force, side force, rolling moment, pitching moment and yawing moment. Extreme care must be taken to ensure that known loads are applied to a single component only. For example when calibrating the lift component only known vertical forces should be applied. In addition no turning moment should be applied to the balance about an arbitrary balance load centre. This load centre should be consistent during entire the calibration procedure. At each loading the induced voltages in all six load cells are recorded thus monitoring the induced voltage in the main loading component and the induced voltages in the five remaining components. This procedure allows the calculation of the six separate direct component load to voltage constants of proportionality and thirty indirect component load to voltage constants of proportionality. If at this stage these constants of proportionality are sufficiently linear the balance calibration is complete. Further secondary calibration may be undertaken by loading all the combinations of paired pure loads and recording the induced voltages. A summary of a calibration process is shown by table 6.7.

	Primary calibration (applied loads)	Secondary calibration (applied loads)				
Loading sequence	Part I	Part I	Part II	Part III	Part IV	Part V
1	Lift force(L)	L & S	S & D	D & R	R & P	P & Y
2	Side force (S)	L & D	S & R	D & P	R & Y	
3	Drag force (D)	L& R	S & P	D & Y		
4	Rolling moment (R)	L & P	S & Y			
5	Pitching moment (P)	L & Y				
6	Yawing moment (Y)					

Table 6.7 - Primary and secondary force balance calibration.

Increasing orders (primary, secondary or tertiary - all combinations of three pure loads) of loading yield increasingly accurate calibrations. Only a primary calibration was undertaken and figures 6.13 to 6.18 show the applied pure loads (N or Nm) against the induced voltage components. The amplifiers (see table 6.6) were set to a gain of 100. Each load was incremented from zero to and then from a maximum value returning to zero. This full cyclic loading is shown by each figure and allows any hysteresis effects to be examined.

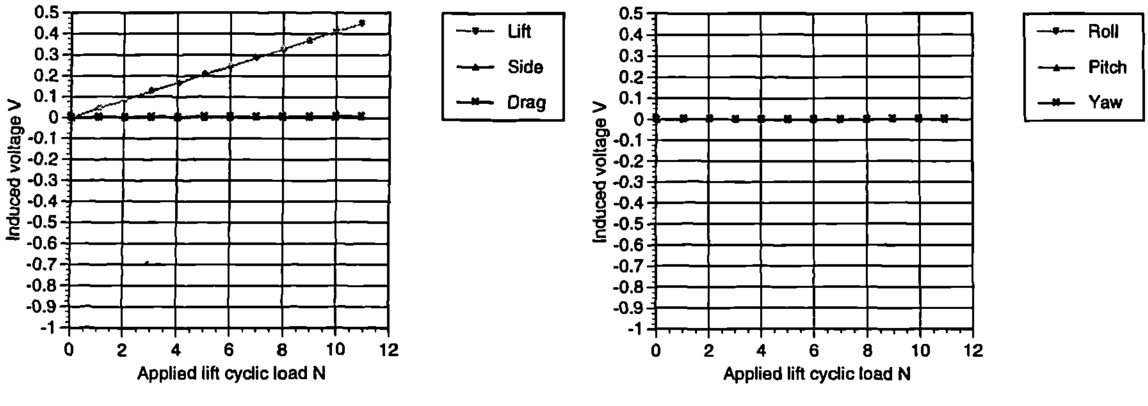

Fig. 6.13 - Pure lift force induced direct and indirect voltages.

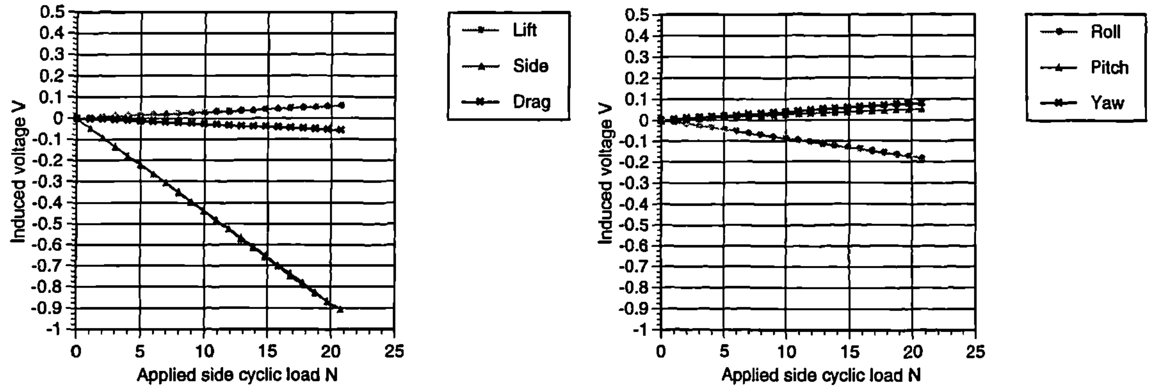

Fig. 6.14 - Pure side force induced direct and indirect voltages.

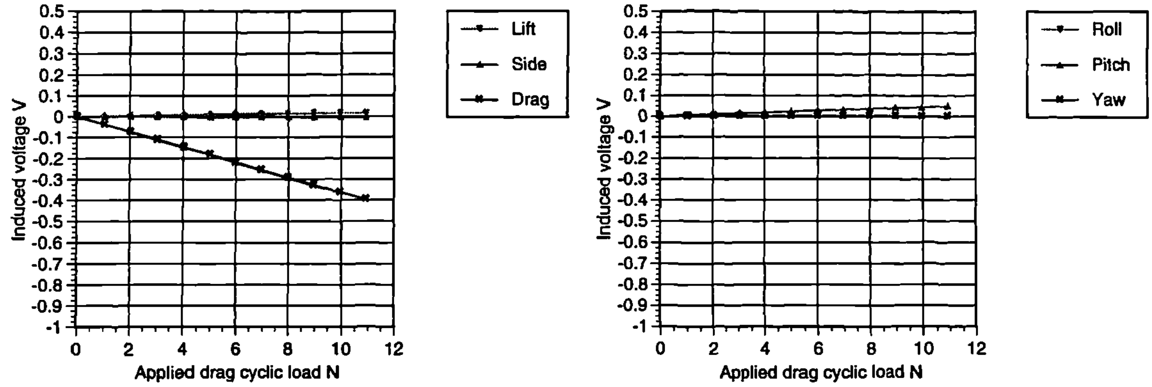

Fig. 6.15 - Pure drag force induced direct and indirect voltages.

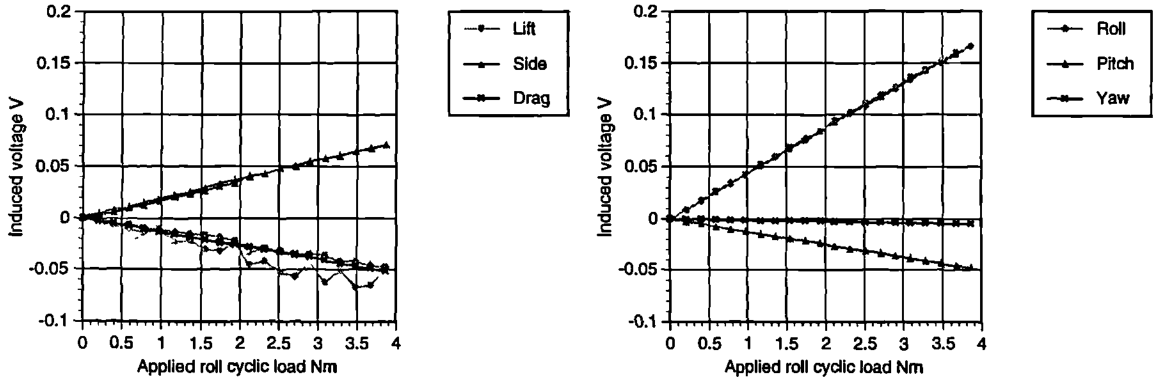

Fig. 6.16 - Pure rolling moment induced direct and indirect voltages.

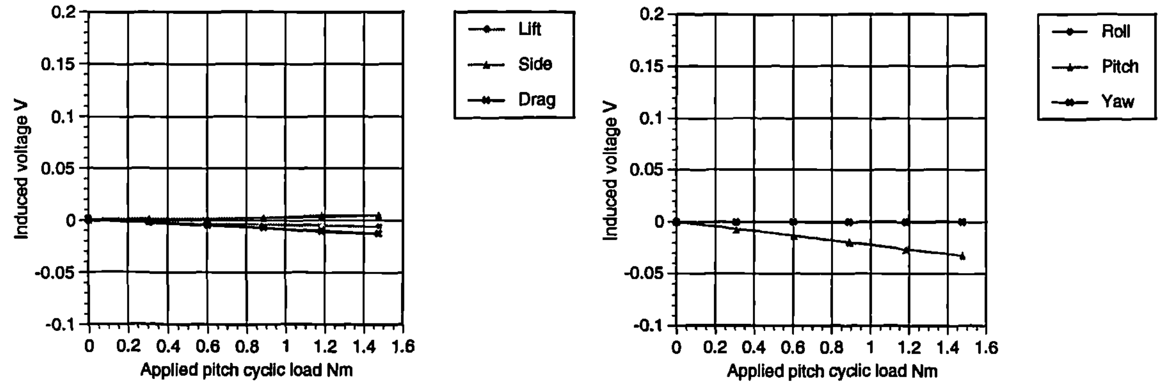

Fig. 6.17 - Pure pitching moment induced direct and indirect voltages.

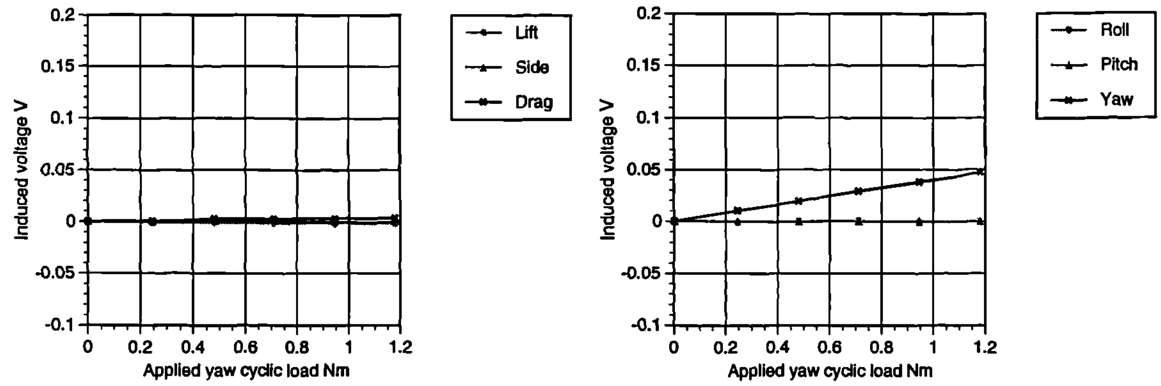

Fig. 6.18 - Pure yawing moment induced direct and indirect voltages.

Figures 6.13 to 6.18 show that all the induced direct or indirect voltages are satisfactorily linear. Negligible hysteresis is displayed except for a small level exhibited in the lift component when loading rolling moment (see figure 6.16). The reason for this is unclear and was not investigated as the lift component shows negligible hysteresis in all other loading components. It may be possible that an additional level of friction was present during the rolling moment calibration, such as the pulley system used to apply the loads to the balance not being correctly lubricated. The gradients of the best fit to each of the 36 traces displayed by figures 6.13 to 6.18 were calculated and are shown by table 6.8.

Applied loading	Lift force	Side force	Drag force	Rolling moment	Pitching moment	Yawing moment
Induced loading	V/N	V/N	V/N	V/Nm	V/Nm	V/Nm
Lift force	0.0410	-0.0028	-0.0017	-0.0152	0.0038	-0.0020
Side force	0.0005	0.0440	0.0004	0.0185	-0.0028	0.0026
Drag force	0.0006	0.0028	0.0363	0.0134	-0.0092	-0.0035
Rolling moment	-0.0014	0.1219	0.0001	0.5970	0.0048	-0.0013
Pitching moment	0.0057	0.0401	-0.0620	0.1951	0.3043	-0.0072
Yawing moment	-0.0004	0.0080	-0.0013	-0.0071	-0.0023	0.3530

Table 6.8 - Force balance loading proportionality.

The data shown by table 6.8 represents a matrix relating a known applied load to a unknown induced load cell voltages. To be able to relate known voltages to unknown loads this matrix requires inversion. The inversion process then allows each load component to be calculated from an equation containing the six inverted proportionalities each multiplied by the six measured voltage components (see [42] for full method). An example of the balance equation for the lift component only is shown by table 6.9. It must be stressed that the entire 6 by 6 matrix requires inversion to extract the balance equation for a single component.

	Calibration matrix values	Inverted matrix values
Component	Recorded voltages in a given component from an applied lift force V/N	Interpreted lift force from recorded voltages in a given component N/V
Lift	0.0410	24.4361
Side	0.0005	-0.2297
Drag	0.0006	0.6529
Rolling	-0.0014	0.7158
Pitching	0.0057	-0.3006
Yawing	-0.0004	0.1411

Table 6.9 - Balance equation constants for the lift component.

Thus the interpreted lift load may be calculated by multiplying the recorded voltages in each of the components by the respective inverted constants of proportionality given by the right hand column of table 6.9 and then summating the six separate load values.

With primary calibration complete the formulated balance equations were then validated. The validation procedure comprised three stages. Firstly each maximum pure load component was individually applied to the balance and the balance interpreted load was calculated using the balance equations. Secondly the first process was repeated but using ¼ of the maximum load. Finally each secondary paired pure loading (see table 6.7) was applied to the balance for a single condition of both loads in each pair at ¼ of the maximum load and again the balance interpreted load was calculated. The results of the calibration validation are shown by tables 6.10 to 6.12. In each table the actual applied load in each component (either the maximum or ¼ load) corresponds to 100%. The balance interpreted loads are expressed as a percentage of the particular component load. For example the second column of table 6.10 shows the balance interpreted loads when applying the maximum lift load of 10.9N (see figure 6.13). The maximum loads for each of the remaining components are 20.7N, 10.9N, 3.86Nm, 1.48Nm and 1.17Nm (see figures 6.13 to 6.18) respectively continuing down the column. These second column values relate the interpreted loads as a percentage of each respective maximum load. Table 6.11 shows the same results but when applying ¼ maximum loading as does table 6.12. The nominal ¼ loads in each component were 3.02N, 5.00N, 3.02N, 0.965Nm, 0.306Nm and 0.245Nm respectively.

Applied loading 100% of max load	Lift force	Side force	Drag force	Rolling moment	Pitching moment	Yawing moment
Induced loading	% of max load	% of max load	% of max load	% of max load	% of max load	% of max load
Lift force	**100.21**	0.16	-0.61	2.36	-0.08	0.05
Side force	0.19	**99.41**	-0.01	0.04	-0.10	0.00
Drag force	-0.08	-0.08	**99.76**	-0.09	0.16	-0.05
Rolling moment	0.21	0.13	0.10	**99.69**	-0.06	-0.11
Pitching moment	-0.30	-0.17	-0.36	-0.58	**100.12**	-0.33
Yawing moment	0.20	-0.11	-0.02	0.13	-0.13	**99.77**

Table 6.10 - Calibration validation for single component maximum loads.

Applied loading 100% of ¼ load	Lift force	Side force	Drag force	Rolling moment	Pitching moment	Yawing moment
Induced loading	% of ¼ load	% of ¼ load	% of ¼ load	% of ¼ load	% of ¼ load	% of ¼ load
Lift force	**100.08**	1.70	0.65	2.99	-0.70	-0.44
Side force	0.83	**99.40**	-0.07	0.47	-0.57	0.30
Drag force	-0.04	-0.13	**99.18**	-0.04	0.80	0.09
Rolling moment	1.61	0.04	-0.04	**100.63**	-0.69	0.19
Pitching moment	0.69	-3.46	-1.93	-2.09	**102.12**	-0.95
Yawing moment	-0.29	-1.43	-1.02	0.16	-1.18	**99.59**

Table 6.11 - Calibration validation for single component ¼ loads.

Induced loading	Lift force (L)	Side force (S)	Drag force (D)	Rolling moment (R)	Pitching moment (P)	Yawing moment (Y)
Applied loading 100% of ¼ load	% of ¼ load	% of ¼ load	% of ¼ load	% of ¼ load	% of ¼ load	% of ¼ load
L & S	**97.85**	**101.44**	-0.55	-0.22	-1.49	-2.49
L & D	**99.69**	-0.24	**100.85**	0.82	-4.21	0.37
L & R	**99.82**	-0.61	-0.93	**101.47**	-0.68	1.20
L & P	**97.77**	-0.31	0.55	-0.07	**103.87**	-0.65
L & Y	**99.54**	-0.31	0.10	0.78	1.47	**100.25**
S & D	4.60	**99.81**	**99.87**	-1.81	-4.52	-1.72
S & R	1.76	**99.15**	0.29	**101.18**	-3.38	-3.84
S & P	0.14	**100.40**	0.53	-0.37	**99.42**	-3.51
S & Y	6.05	**99.32**	-0.93	-2.36	-0.82	**101.36**
D & R	5.49	-1.03	**100.06**	**100.15**	-1.32	3.19
D & P	-1.87	0.47	**-98.87**	0.61	**96.68**	1.46
D & Y	-0.33	0.36	**98.16**	1.50	-2.62	**99.43**
R & P	5.78	-1.00	-0.76	**100.78**	**100.38**	-0.57
R & Y	-2.90	0.37	0.24	**102.02**	0.52	**102.99**
P & Y	1.17	0.65	0.71	-0.04	**99.49**	**98.56**

Table 6.12 - Calibration validation for paired component ¼ loads.

Tables 6.10 to 6.12 may be examined in detail but it may be summarised that a maximum discrepancy magnitude of 2.36% was exhibited at single component maximum loading, 3.46% at single component ¼ loading and 6.05% at paired component ¼ loading. The bulk of the discrepancies in each case being significantly below these maximum values. It should be noted that these percentage discrepancies are largely borne from the formulation of the balance equations by only undertaking a primary calibration and are not error tolerances. Primary calibration assumes all effects are linear and any non-linear effects are not compensated for in the calibration. The primary balance calibration was deemed to be satisfactory.

6.6 Data Capture and Processing

6.6.1 Introduction

A data capture system was required to record principally the voltages developed by the five pressure transducers (see section 6.2), used for both the five hole probe and aerodynamic model pressure tappings, and those developed by the six load cells in the force balance (see section 6.5). The data capture system would have to be capable of concurrently logging at least six separate voltage signals at sufficient frequency to monitor the full nature of any transient effects developed.

6.6.2 Data Capture System

The data capture system was based from a desktop P.C.. The data logging capability was achieved by fitting an expansion card, with salient characteristics shown by table 6.13, to the P.C..

Manufacturer	Amplicion
Type	PC-30PGH
Input channels	Up to 8 differential voltages
Individual channel gains	1, 2, 4 or 8
Max input range	0-10V (differential)
Maximum logging rate	200kHz over 1, 2, 4 or 8 channels

Table 6.13 - Logger card characteristics.

As the minimum number of signals to be logged was five (the five hole probe) the card was configured to log all eight channels as the next closest logging option was four (see table 6.13). The experimental simulation time for the apparatus was approximately 1.6s over which the maximum number of samples achievable by the P.C. software running the card had to be divided. The maximum limit for the software ('Waveview') was 30000 and this resulted in a maximum 2381Hz per channel logging rate over a period of 1.573s.

The P.C. software package incorporated a optional trigger system to start the data capture period when channel '0' (the eight channels were labelled '0' to '7') recorded a specified voltage level. As data had to be recorded over a short and specific time period the trigger feature was utilised. Channel '0' was connected to a optical sensor (RS No. 302-508) which comprised a transmission and reception sensor built in to the same sensor head. Any material surface brought within ~0.05m of the sensor would be detected as the transmitted signal would reflect off the material surface to be received by the sensor. This sensor was placed close to the flexible belt (see section 5.2) surface in line with the dummy apertures (see figure 5.4). As the flexible belt moved relative to the stationary sensor the data logger recorded either the presence of the belt (a high signal) or the presence of an aperture (a low signal - no belt) immediately in line with the optical sensor. The data logger was set to trigger on the leading edge of the first dummy aperture. As the length of the belt region between each dummy aperture was known the belt velocity could be calculated by examining the duration of the high channel '0' signal of the recorded data for a particular experimental run. The remaining channels ('1' to '7') could be utilised to record any further voltages. The optical sensor required a power supply (10-30V d.c.) as did the pressure transducers (see table 6.1). Both power requirements were achieved using a single standard adjustable mains driven 0-30V d.c. power supply unit set to a constant value of 12V throughout the experimentation. The force balance load cells (see table 6.5) and amplifiers (see table 6.6) had a separate manufactured mains driven regulated d.c. supply complete with adjustable channel gains and load cell voltage off set values.

6.6.3 Data Capture Methods

The five hole probe and aerodynamic model surface pressure were recorded in the same fashion. Prior to each experimental run the datum voltages for each individual transducer were recorded by the data logger at 200Hz per channel over a period of one second. The laboratory ambient pressure, using a Vernier mercury barometer, and temperature, using a mercury thermometer, were then recorded. An experimental run was then undertaken recording the five transducer voltages and the optical sensor voltage each at 2381Hz over the experimental run time of 1.573s (see section 6.6.2). Channel '0' at the logger card was set to a gain of unity and each of the transducer channels ('1' to '5') had a gain of 2. The two pressure ports on each transducer were connected at one port to either a five hole probe tapping or a model surface tapping with the other port being open to atmosphere via a long section of tubing terminating away from any flow interference.

Data from the force balance was gathered using a similar method. Prior to each experimental run the six load cell datum voltages were recorded again using the logger and again at 200Hz per channel for one second. An experimental run was undertaken and the six load cell voltages in addition to the optical sensor voltage were recorded at 2381Hz over 1.573s. All six load cell amplifiers were set to a gain of 100 (see table 6.6). At the logger card channel '0' at the logger card was set to a gain of unity. The three vertical load cells (numbers 1, 2 and 3 and also channels '1', '2' and '3' - see figure 6.11) were set to a card gain of 4 and the three horizontal cells (4, 5 and 6 and also channels '4', '5' and '6'- see figure 6.11) were set to a card gain of 8.

6.6.4 Data Processing

Computer programs were formulated to assist with the processing of the gathered data. For the five hole probe the transducer datum voltages were averaged. Using these average datums and the calibration constants of proportionality (see 6.2.2) the actual transducer voltages recorded during the experimental run were converted to an absolute pressure. The ambient pressure and temperature readings then allowed the gauge pressure to be calculated. An existing program was available which for a given set of five hole probe pressure readings would interpolate, using the calibration data (see figures 6.4a to 6.4c), to produce probe interpreted values of resultant velocity and flow angle. The five hole probe was calibrated up to a ±30° on coming flow cone angle. The probe was set to receive axial air flow (u_x) at -15° to the probe axis and transverse air flow (u_y) at +15° to the probe axis (see figure 6.6). This positioning placed the expected flow angle range of 30° centrally to the 60° (±30°) full calibration range of the probe thus allowing a 15° air flow 'safety' band either side of the expected range. As no calibration data was available outside this larger cone angle any of the five recorded probe tip pressures which did not fall within the calibration for a particular time point yielded blank values of angle and velocity for that time point. The blank value is manifested as a discontinuity in the interpreted transient trace.

The processing of the model surface data was exactly the same as that of the five hole probe up to the production of gauge pressure values which was the final required form.

The force balance data was processed by initially calculating average datum values per load cell and then, using the actual experimentally recorded balance voltages in conjunction with the balance equations (see section 6.5.4), the balance interpreted loading during the experimental run was calculated.

The processed data for the five hole probe, model surface pressures and force balance were in time dependent form. The formulated programs incorporated an option to reduce the number of time points processed thereby smoothing the data. This was achieved by averaging discrete juxtaposed recorded voltages over specific number of time sample points. The number of time sample points in each block could be set from within the formulated programs. This number was proportional to the data compression factor and correlates to the data smoothing level. Data smoothing may also be achieved using a similar method which utilises a rolling time point block width to voltage averaging procedure. This however produces no data compression. The juxtaposed block and rolling block smoothing levels were compared on typical data sets using typical and equal smoothing levels (block widths) and no visible difference was exhibited by the resulting traces. A smoothing level of 3 was selected for the transient five hole probe, surface pressure tappings and force balance processed data resulting in reduction of the 2381Hz sampling frequency to an effective 794Hz. Unless otherwise stated all the transient data has been processed in this way (from 2381Hz to 794Hz) and all the time averaged data has been sampled at 200Hz per channel over one second and then averaged.

The unprocessed data (at 2381Hz) from the optical sensor (see section 6.6.2) was used to calculate the belt velocity. The duration of the two belt regions between the dummy aperture (see figure 5.4) was known and the time dependent signal from the optical sensor allowed two separate belt velocities to be calculated. As the position of the optical sensor was fixed and known it was possible from these calculated values of velocity determine the precise time points of relative positions of the real apertures and therefore the position of the cross wind region with respect to the model.

7.0 Experimental Investigation and Results

7.1 Scope of Investigation

The results presented here are those of the first stage of experimental investigation possible with a new wind tunnel technique. The investigation was based on a 2D analysis of the wind tunnel working section under both steady and simulated transient cross wind conditions firstly without then with the presence of a simple 2D representative vehicle model. The data was obtained from a horizontal plane through the working section of the tunnel away from the effects of the ground plane. The interpretation of these results is presented in chapter 10.

7.2 Method and Results of Investigation

The investigation method focused two main areas. Firstly a point by point investigation of the whole working section without the presence of the model and secondly and investigation of the flow effects on the model placed in the working section. These two aspects were further divided into a time averaged and a transient investigation. The point by point investigation was undertaken to ensure that the system created the required flow field correctly and to determine the optimum position for the vehicle model. Once this was established the model was placed at this position in the working section and the flow effects on it were studied. The investigations of the transient response of the working section and both the time averaged behaviour and the transient response of the aerodynamic model were performed with the main wind tunnel (see figure 3.2) configured to deliver the same axial velocity to the working section. Where applicable the cross wind jet was also configured to deliver the same components of velocity to the working section over the entire course of the investigation. Thus the data presented in sections 7.2.2 to 7.2.4 which was gathered during separate experimental runs over a period of time may be directly compared and contrasted.

The layout of the working section for the investigation is shown by figure 7.1. The survey grid shows the position of all the nodes in the point by point survey of the working section. The author was not aware of any previous work of this type on the transient combination of two open jet tunnels and it was hoped that this portion of the research work would yield important information regarding the validity of this simulation technique in general.

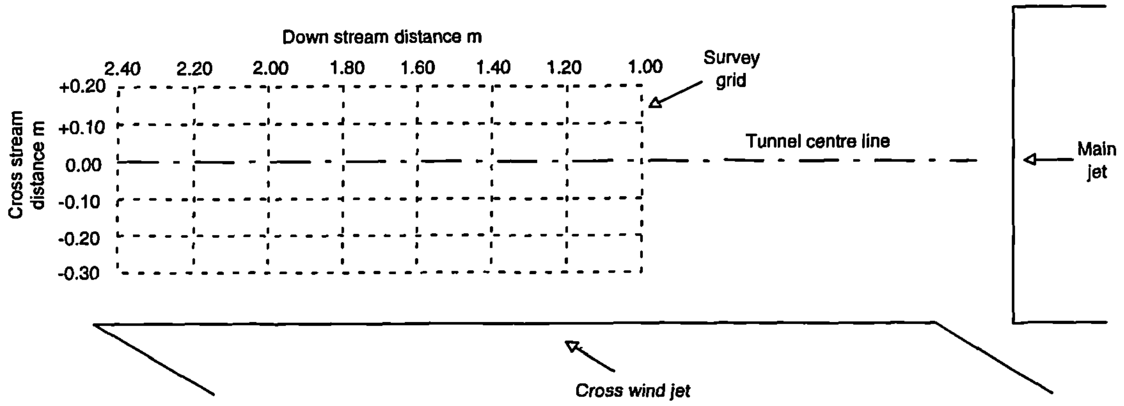

Fig. 7.1 - Layout of the tunnel working section.

Once the point by point survey was complete an optimum model position was located. The model, shown by figure 7.2, was placed in the working section for investigation. The model was fitted with end plates top and bottom (see figure 6.9) to ensure a reasonable approximation to 2D air flow round the model surface was exhibited.

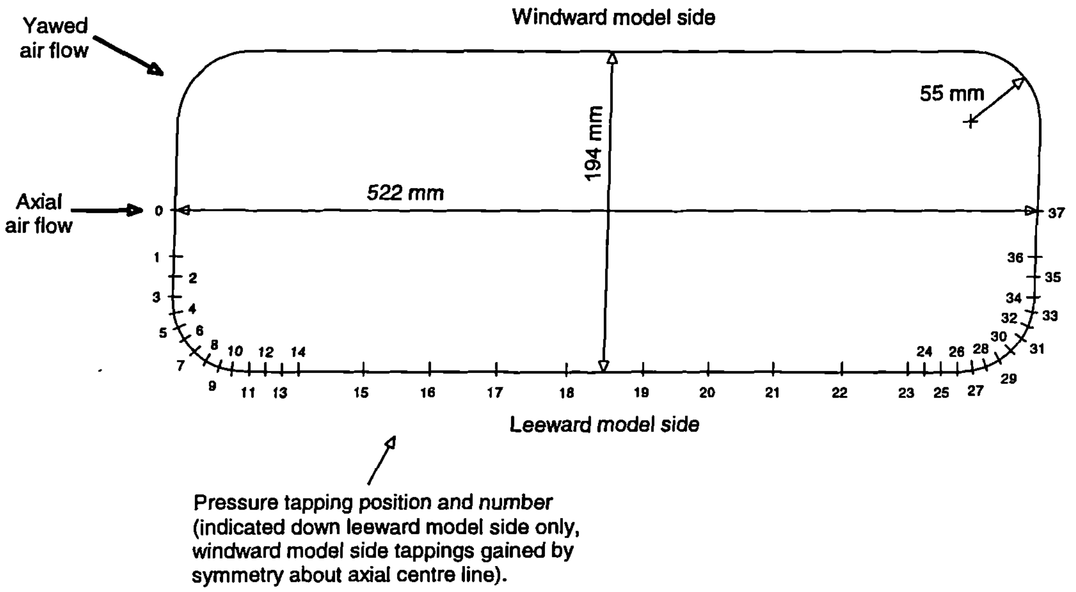

Pressure tapping position and number (indicated down leeward model side only, windward model side tappings gained by symmetry about axial centre line).

Fig. 7.2 - Schematic plan view of 2D model geometry.

The optimum position of the model was determined to be with the geometric centre located at a position of 2.02m downstream and -0.10m cross stream (see figure 7.1). The model was located to occupy a working section position in which the magnitude of the cross wind transient was fully developed in terms of yaw angle with down stream working section distance (these results are presented and interpreted in sections 7.2.2 and 10.1.2 respectively). The model had 74 pressure tappings positioned on its surface which were concentrated about regions of suspected high pressure gradient as can be seen by figure 7.2.

7.2.1 Time Averaged Behaviour of Working Section

The following results were gained from data recorded from the centre line of the tunnel working section (see figure 7.1) using the five hole probe. The plots map the exit flow from the cross wind duct and flexible belt system under time averaged conditions without the addition of the main jet.

For the first investigation the probe was placed 1.80m down stream and the belt was incremented along it's normal path in such a way as to allow an aperture to pass fully (from leading edge to trailing edge of the aperture) across the 'line of sight' of the probe. After each increment the conditions were allowed to settle and a probe reading was taken. This procedure thus recorded the time averaged behaviour, as observed by a single point, of the belt and duct system exhausting into the working section. This procedure mimicked the exact movement of the components of the apparatus during an experimental run. This investigation was undertaken to examine any flow asymmetry developed at the aperture exit by moving the aperture across the face of the duct. The results are shown in figure 7.3a. A zero x axis indicates that the probe monitoring point was located along the nominal centre line of the flow emerging from the aperture. A negative x axis indicates that the nominal centre line of this air flow was in direct line with a point to the left, or up stream relative to the working section survey grid (see figure 7.1), of the probe monitoring point. The two traces shown are the axial (u_x) and cross stream (u_y) components of the flow. The corresponding flow angle variation is shown in figure 7.3b.

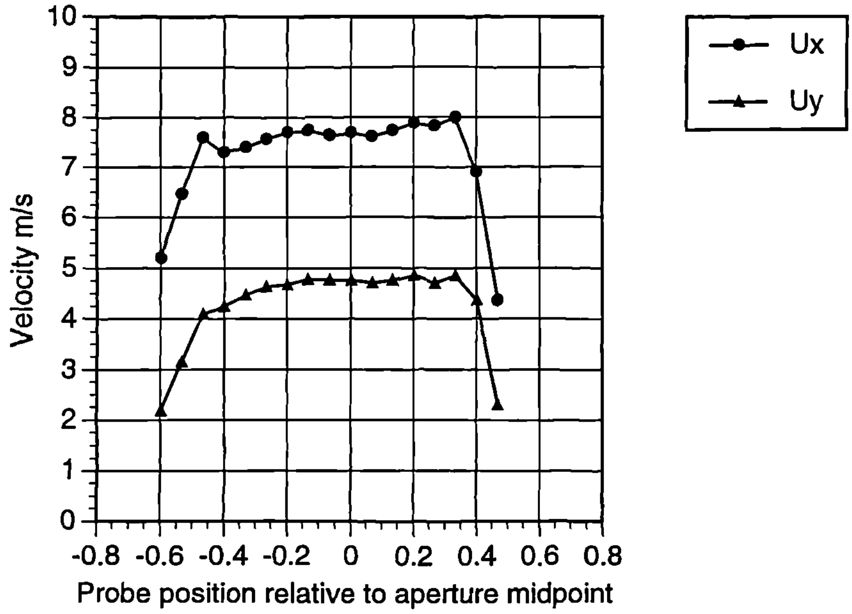

Fig. 7.3a - Time averaged working section velocity produced by aperture movement.

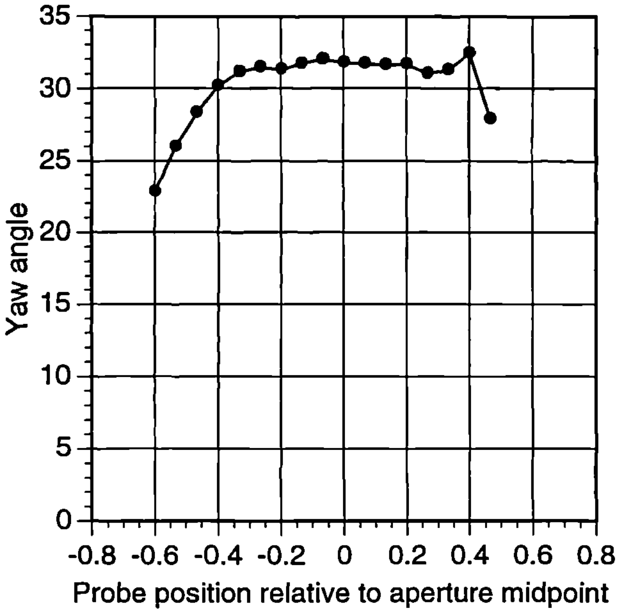

Fig. 7.3b - Time averaged working section yaw angle produced by aperture movement.

In the second investigation the belt remained stationary with the aperture centrally positioned at the cross wind duct exit. This time the probe was traversed along the tunnel centre line in such a way as to pass through the full width of the air flow emerging from the aperture. This differs from the first investigation in that the aperture was stationary with respect to the duct exit so as to examine any flow asymmetry developed within the duct that would be manifested at the aperture exit. Figure 7.3c shows the recorded axial and cross stream velocity components an the resultant yaw angle is displayed in figure 7.3d. Again a negative x axis indicates that the nominal centre line of this air flow was in direct line with a point to the left, or up stream relative to the working section survey grid (see figure 7.1), of the probe monitoring point.

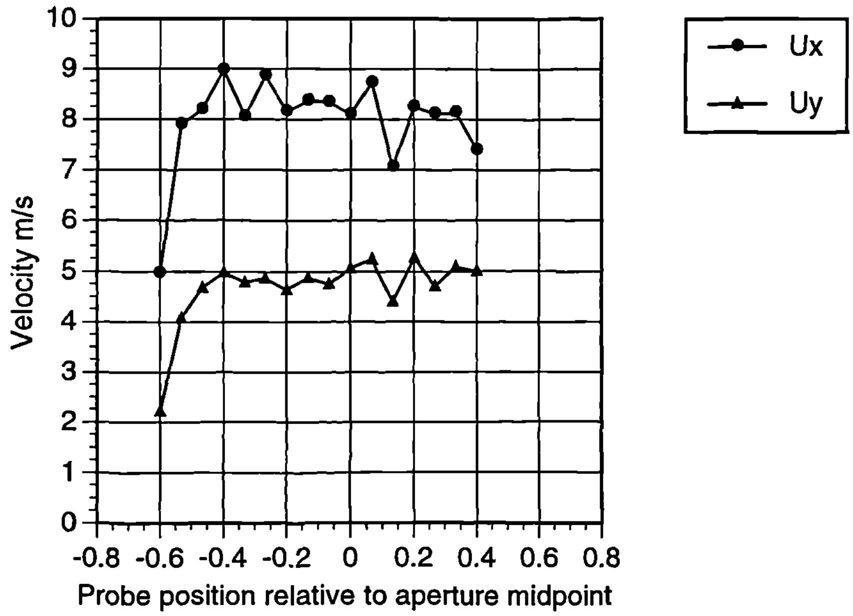

Fig. 7.3c - Time averaged working section velocity produced by probe movement.

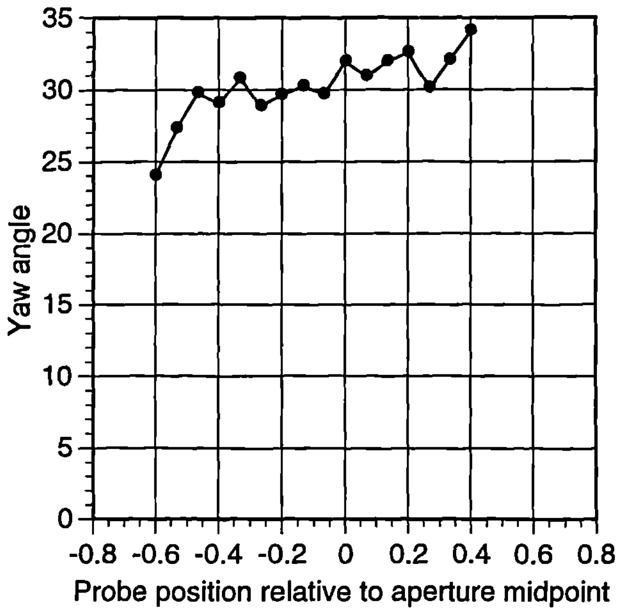

Fig. 7.3d - Time averaged working section yaw angle produced by probe movement.

7.2.2 Transient Response of Working Section

The following results were gained from data recorded from all of the points on the survey grid in the tunnel working section (see figure 7.1) using the five hole probe. Each point was surveyed in turn during separate experimental runs with the five hole probe. The data logger was triggered to start logging at the same time point for each run allowing the separate traces to be plotted together on the same time axis. Each plot contains the data from four separate points from the same survey line. There were in total six survey lines in the tunnel working section, each parallel to the tunnel centre line, at cross stream distances of +0.20m, +0.10m, 0.00m, -0.10m, -0.20m and -0.30m (see figure 7.1). Each survey line contained eight survey points at evenly spaced down stream distances from 1.00m to 2.40m. For clarity each plot displays the traces for alternate points along each survey line. The down stream distances are labelled for each of the four traces per plot.

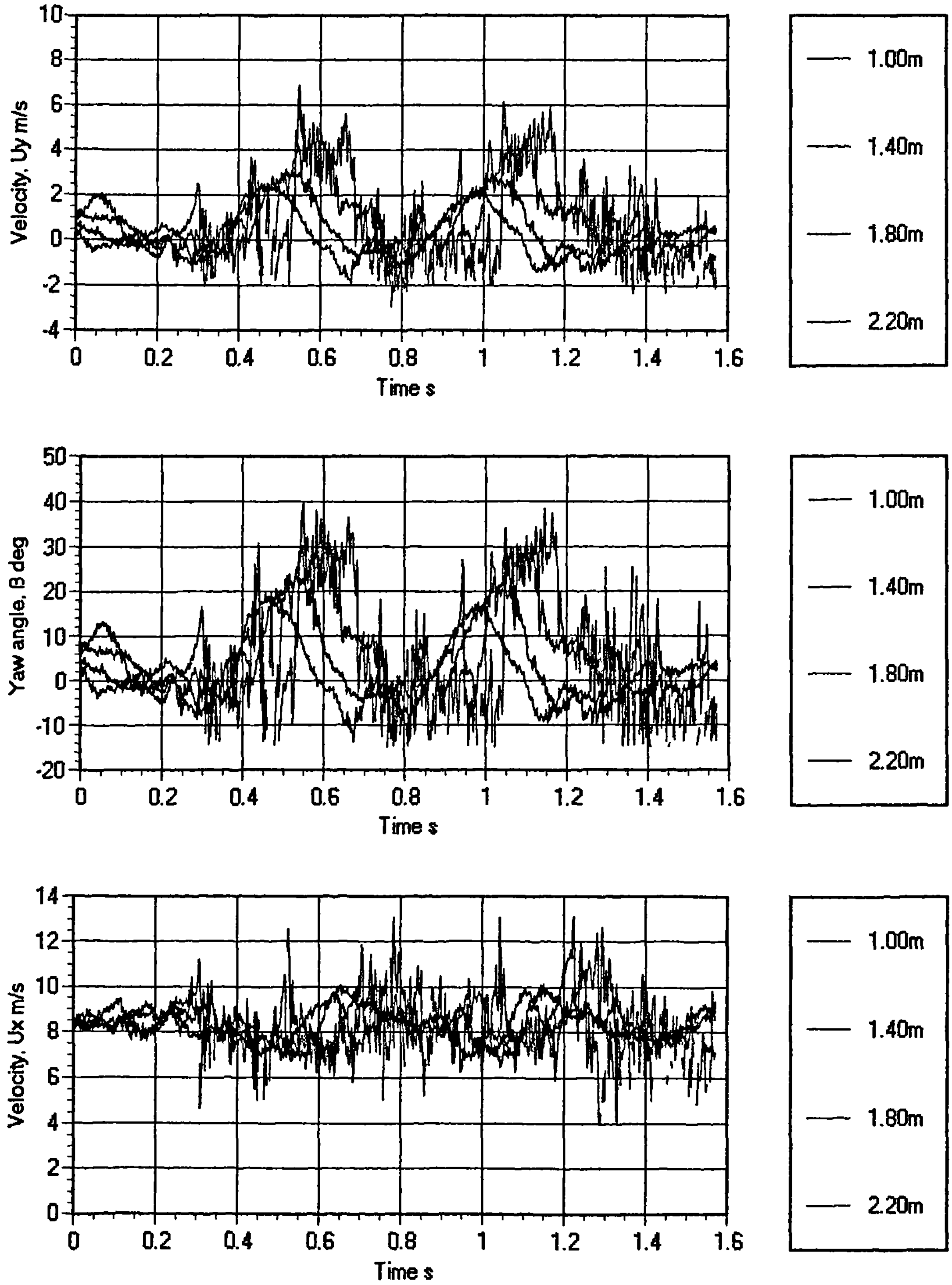

Figs. 7.4a, b & c - Cross stream velocity, yaw angle and axial velocity respectively against time for +0.20m survey line.

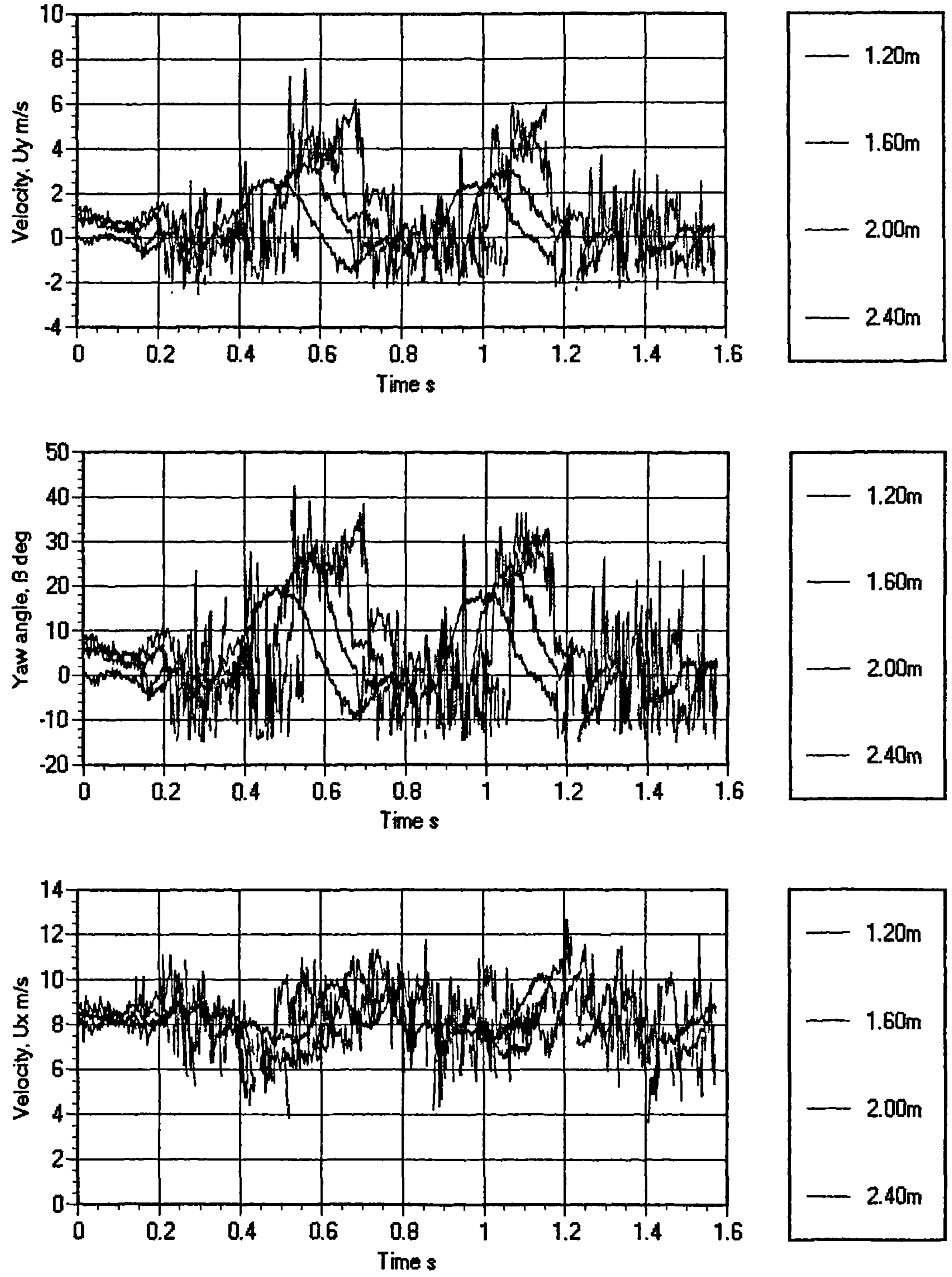

Figs. 7.5a, b & c - Cross stream velocity, yaw angle and axial velocity respectively against time for +0.20m survey line.

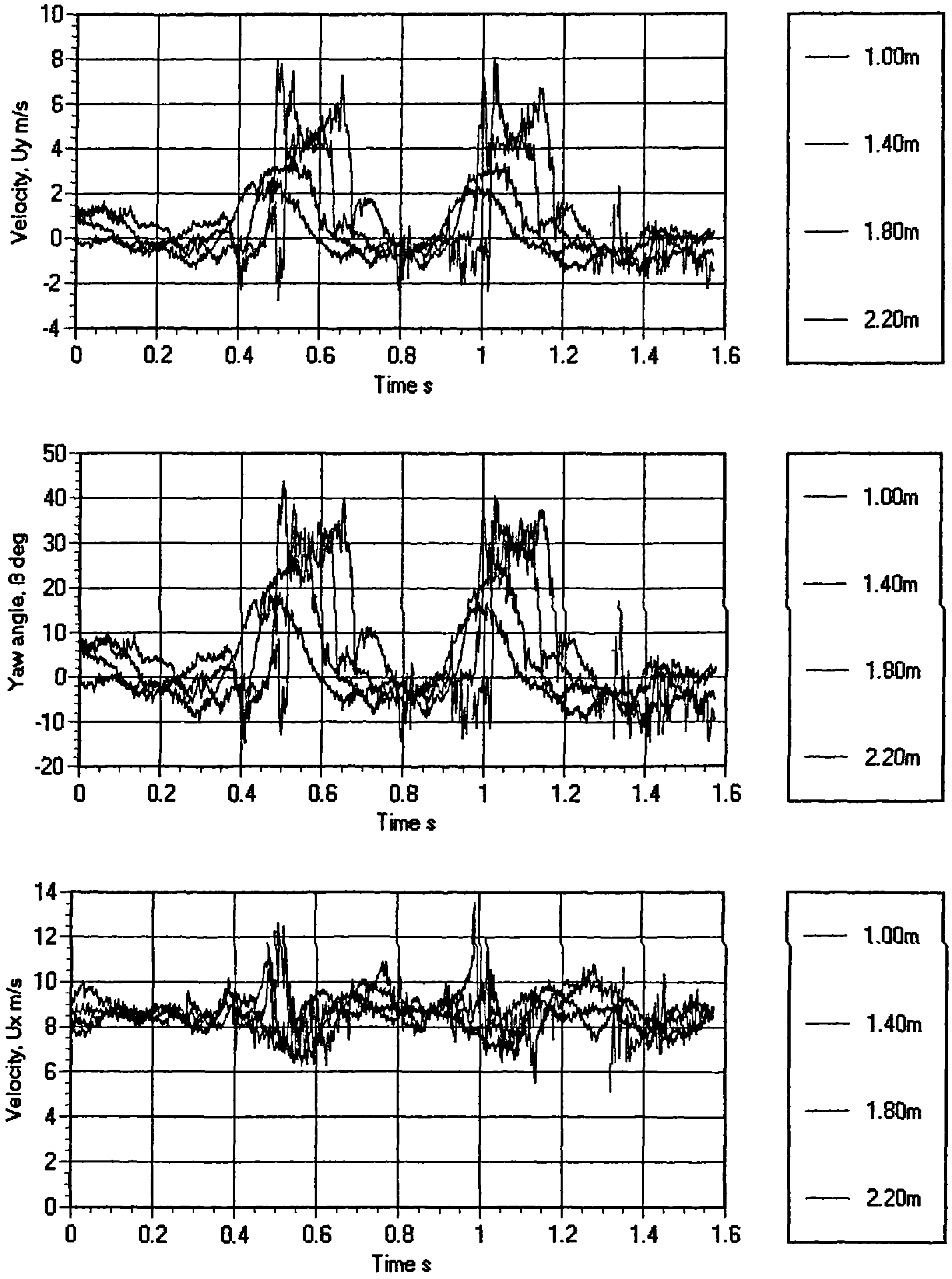

Figs. 7.6a, b & c - Cross stream velocity, yaw angle and axial velocity respectively against time for +0.10m survey line.

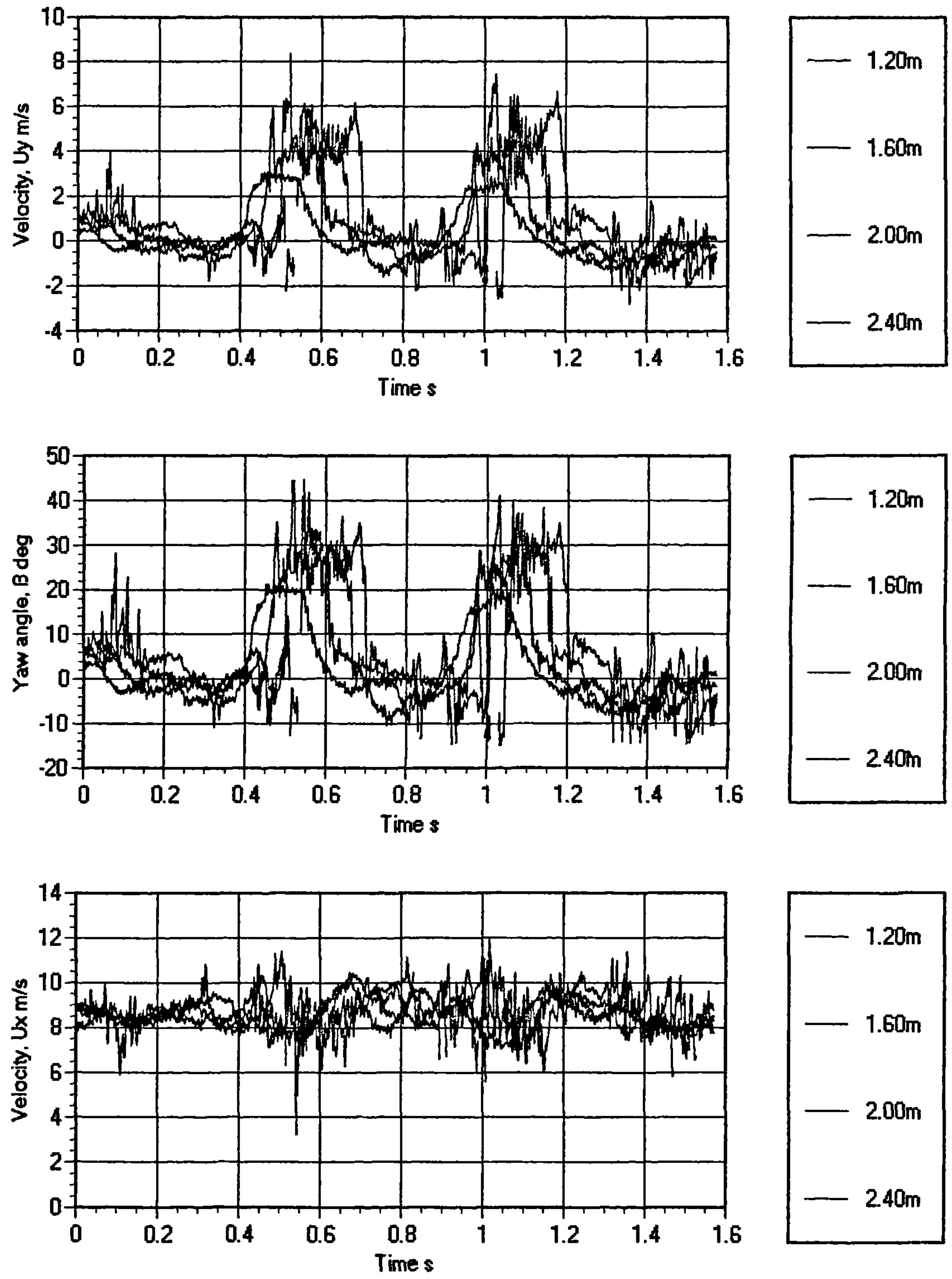

Figs. 7.7a, b & c - Cross stream velocity, yaw angle and axial velocity respectively against time for +0.10m survey line.

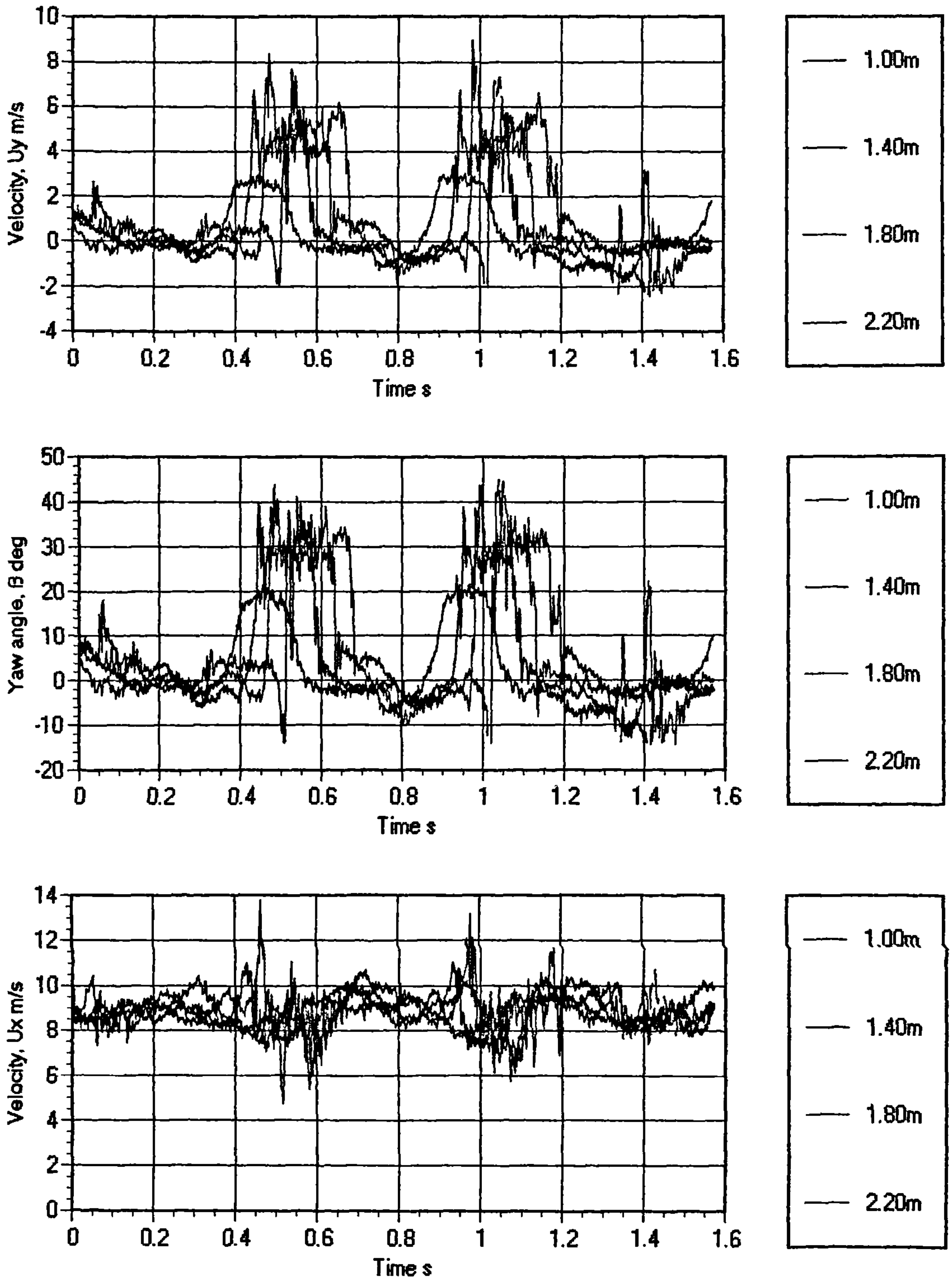

Figs. 7.8a, b & c - Cross stream velocity, yaw angle and axial velocity respectively against time for 0.00m survey line.

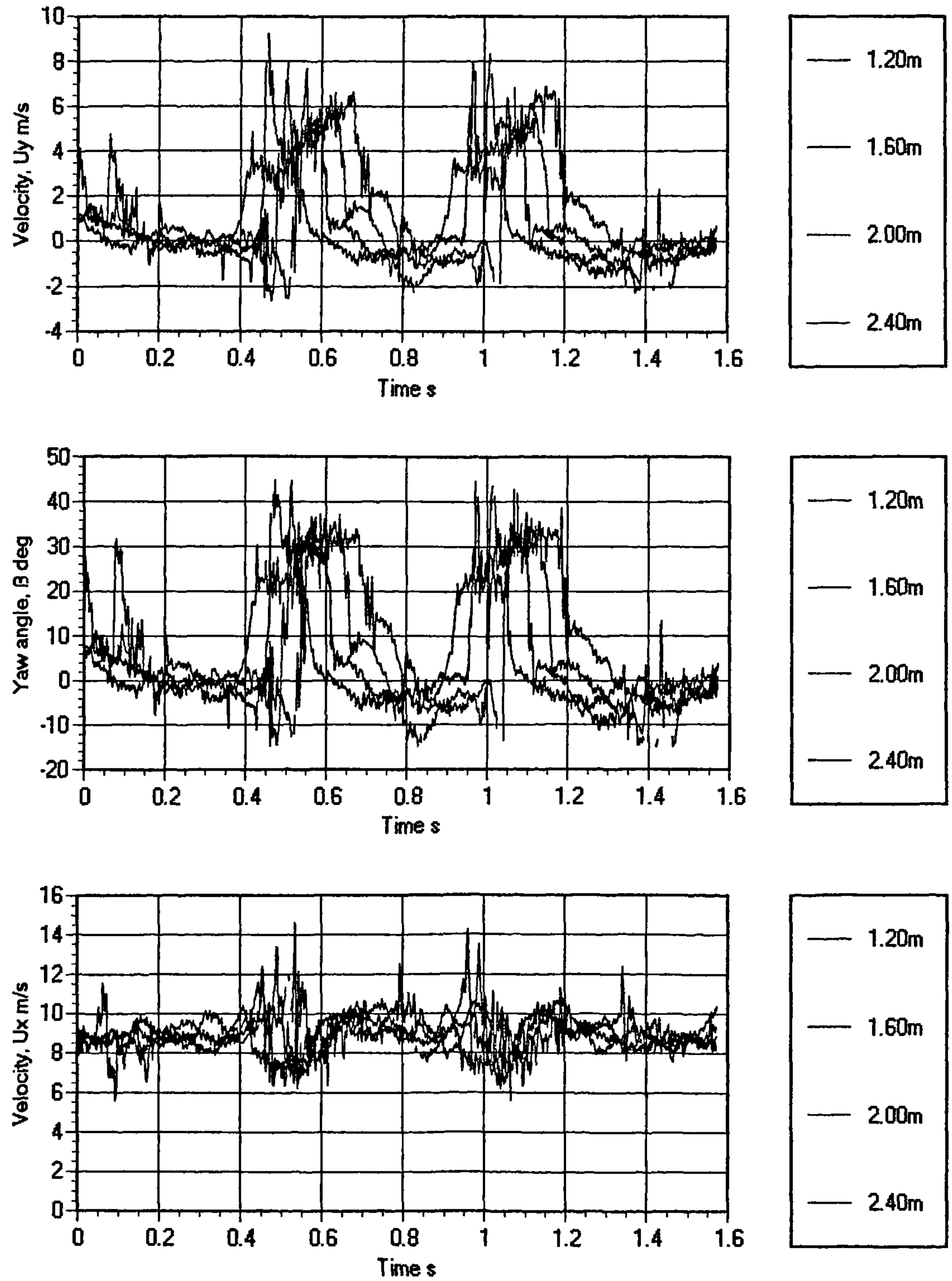

Figs. 7.9a, b & c - Cross stream velocity, yaw angle and axial velocity respectively against time for 0.00m survey line.

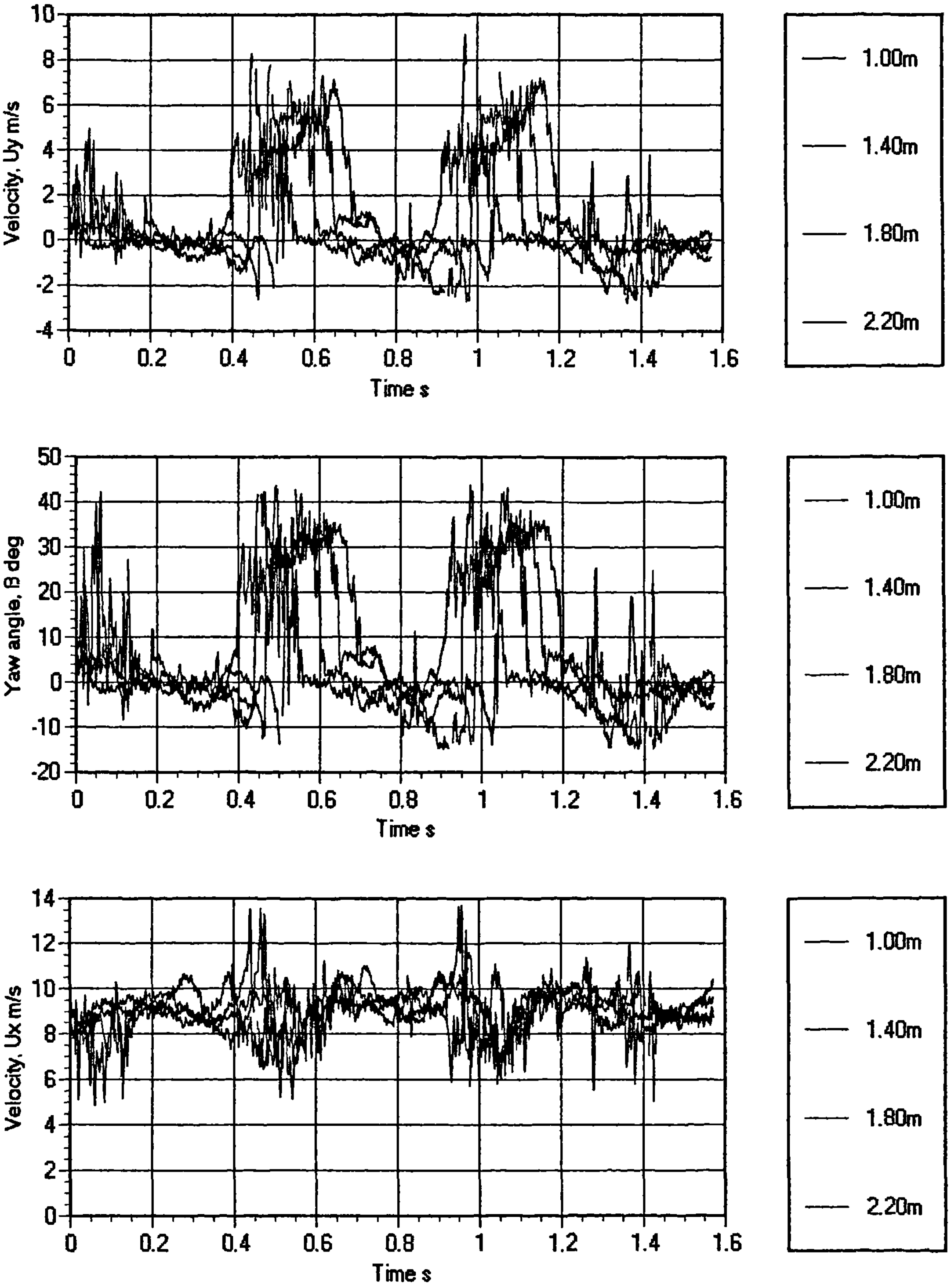

Figs. 7.10a, b & c - Cross stream velocity, yaw angle and axial velocity respectively against time for -0.10m survey line.

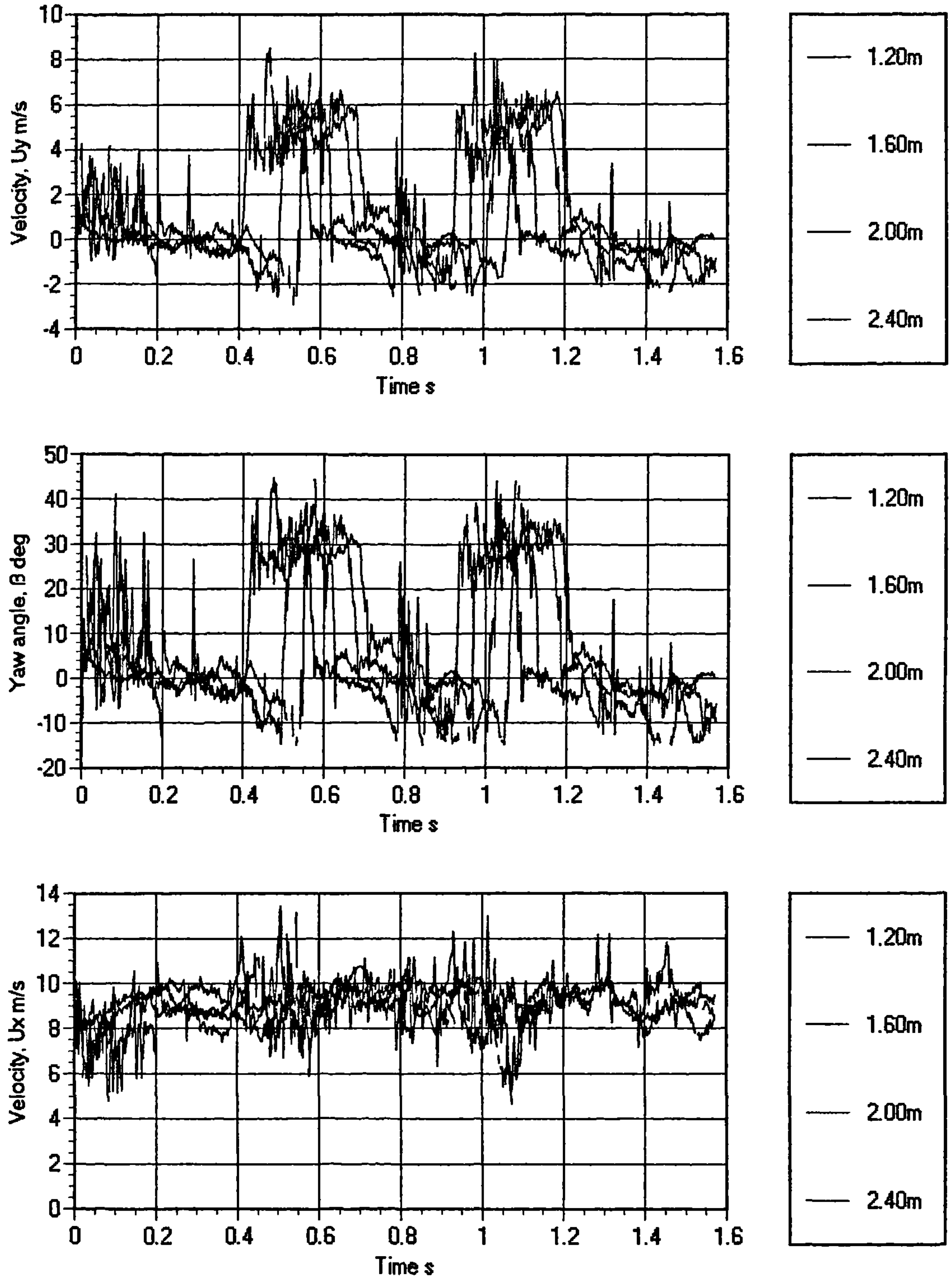

Figs. 7.11a, b & c - Cross stream velocity, yaw angle and axial velocity respectively against time for -0.10m survey line.

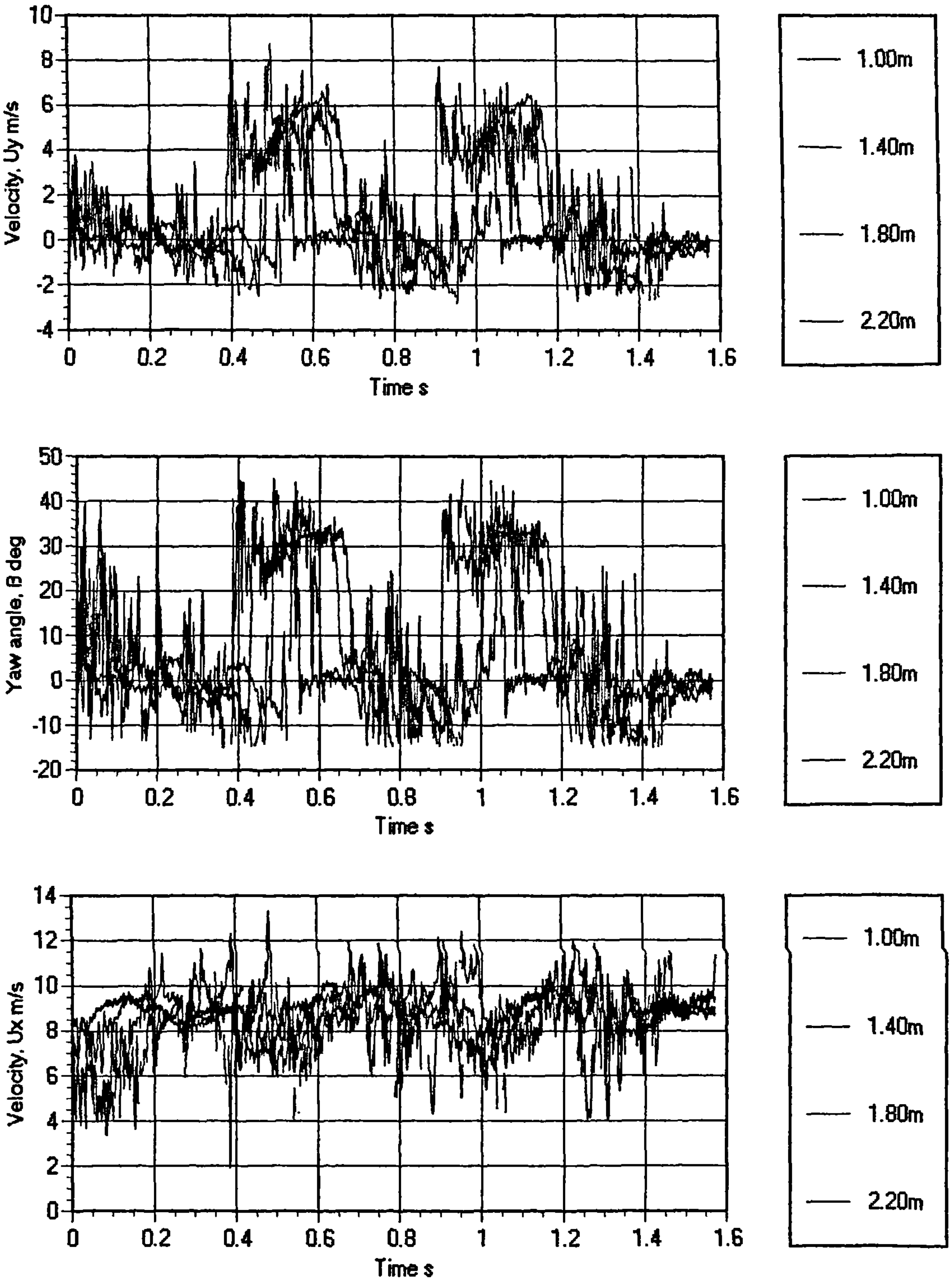

Figs. 7.12a, b & c - Cross stream velocity, yaw angle and axial velocity respectively against time for -0.20m survey line.

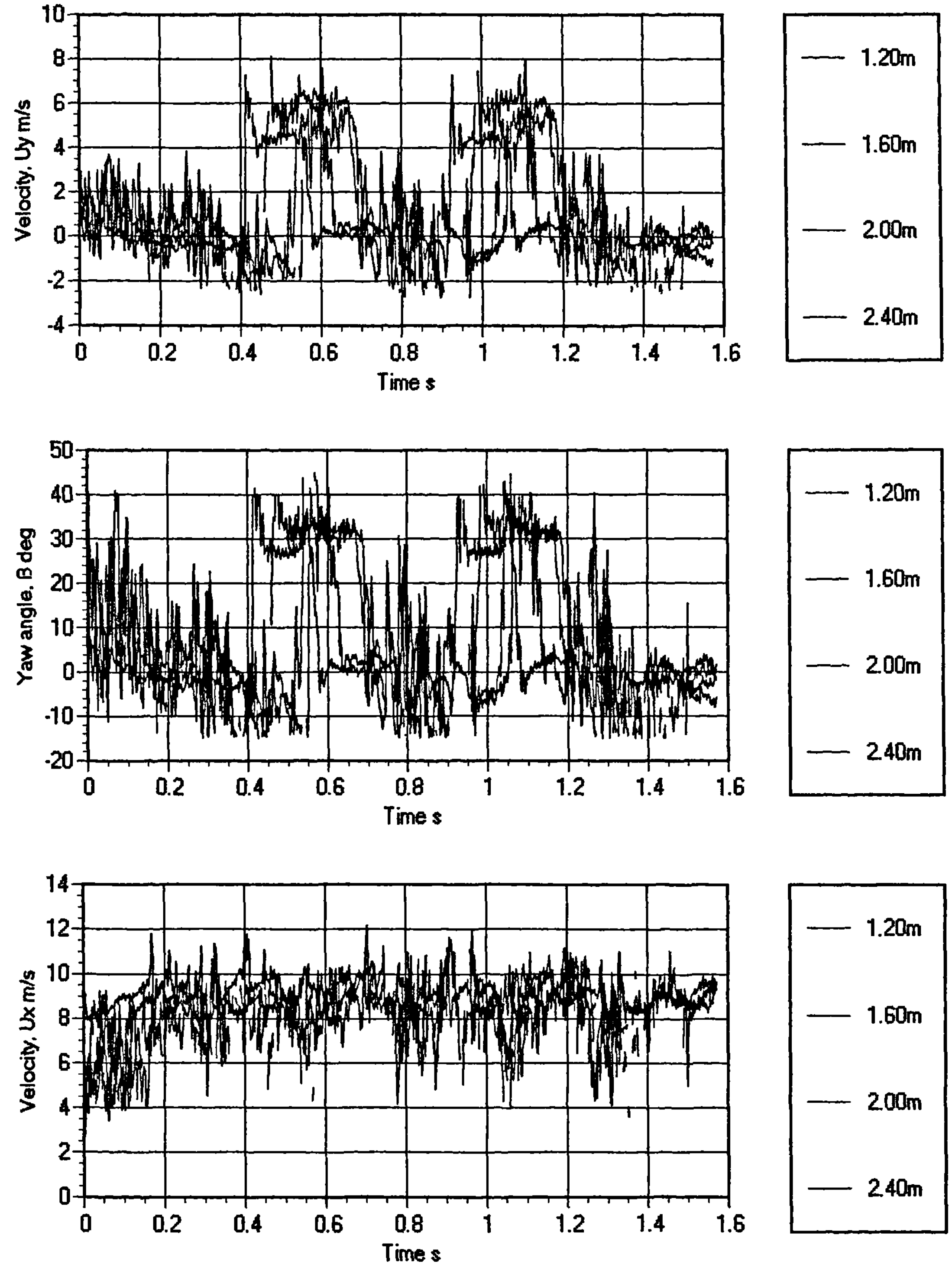

Figs. 7.13a, b & c - Cross stream velocity, yaw angle and axial velocity respectively against time for -0.20m survey line.

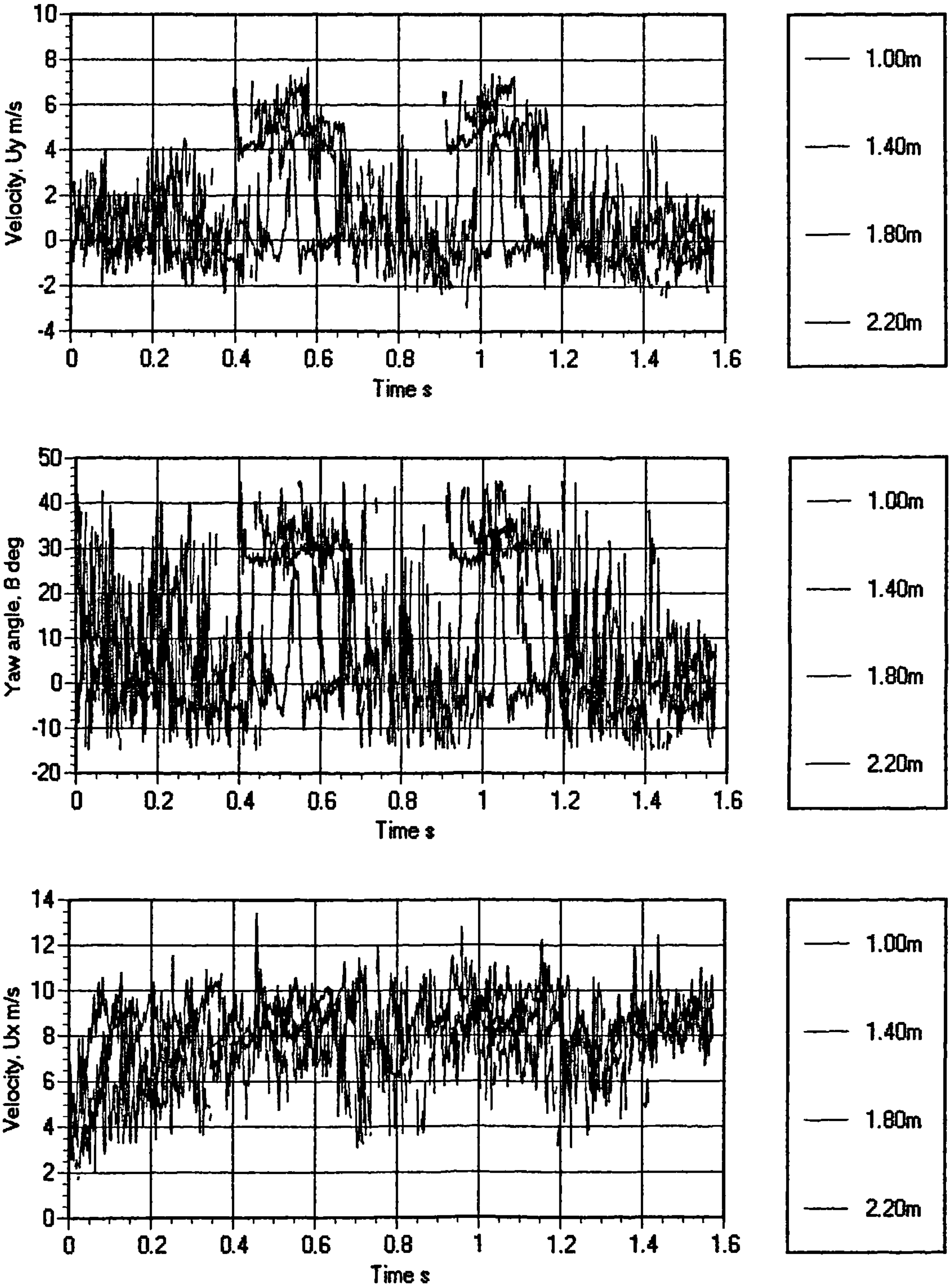

Figs. 7.14a, b & c - Cross stream velocity, yaw angle and axial velocity respectively against time for -0.30m survey line.

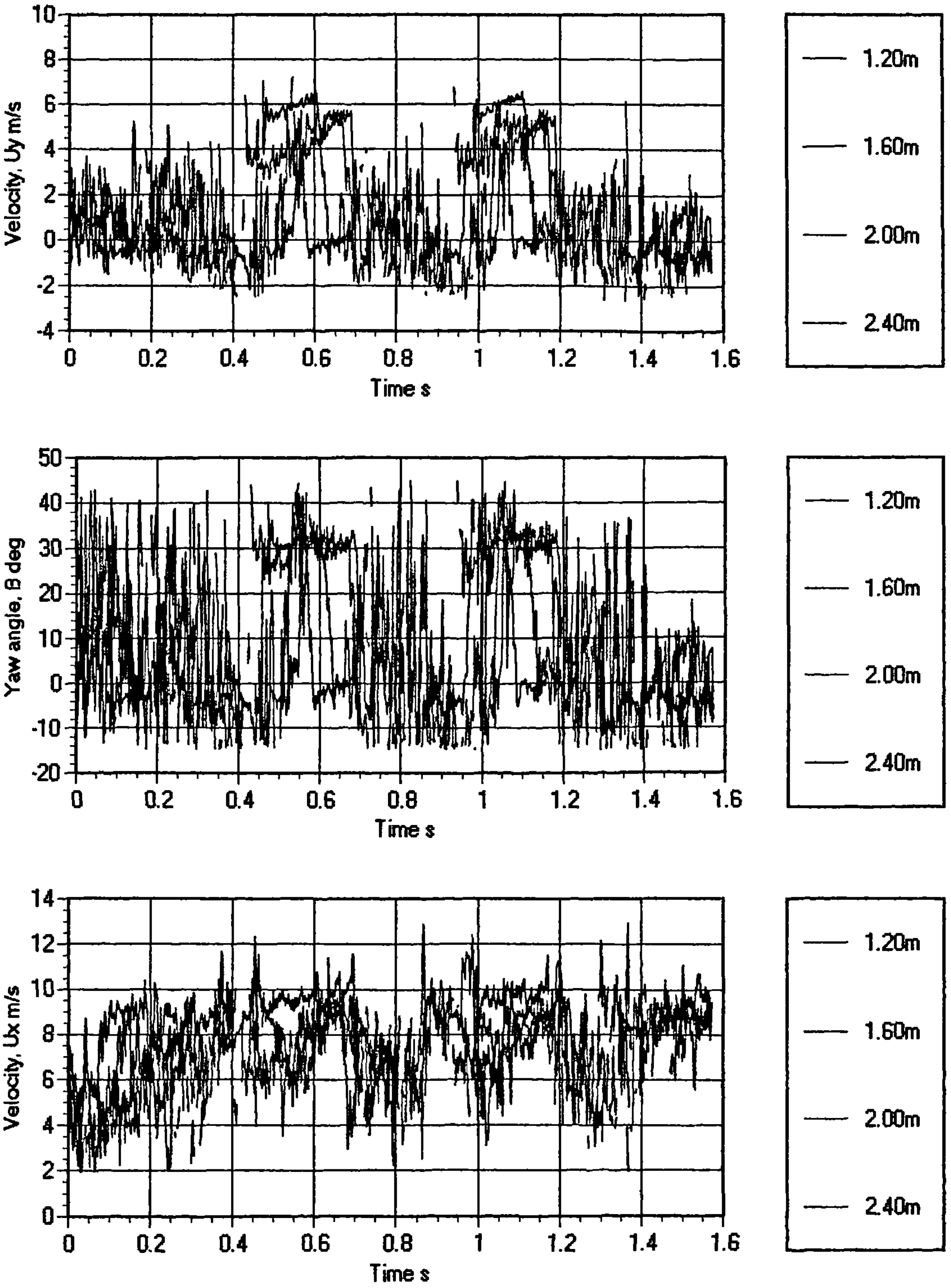

Figs. 7.15a, b & c - Cross stream velocity, yaw angle and axial velocity respectively against time for -0.30m survey line.

7.2.3 Time Averaged Behaviour of Aerodynamic Model

The following results, shown by figures 7.16a and 7.16b, are those of time averaged surface pressure induced on the model at the pressure tappings shown in figure 7.2. The model was placed in the working section and yawed by 10° steps from -40° through 0° to +40°. This procedure is the conventional method used to determine the fixed yaw behaviour of an aerodynamic vehicle model. For clarity the data gathered from the negative (leeward model side) angles is shown separately from the positive (windward model side) angles. The data for the 0° yaw angle is common to both plots. The Reynolds number for tests was $3x10^5$ based on model length. The wind tunnel used for the tests was of open jet variety thus the free stream static pressure, p_∞, is atmospheric pressure and the model surface pressure, p, is a gauge pressure value. During a transient experimental run it was expected that initially the relative air velocity to the model would be u_x (see figure 3.2). As the cross wind transient pulse is delivered to the working section the relative air velocity changes to u_{cw} at an angle of 30° whilst the axial velocity, u_x, remains constant. This produces a potential ambiguity in the non-dimensionalising of the surface pressures to a Cp value. The dynamic pressure relating to either u_x or u_{cw} may be used. Using u_x is entirely correct in the initial stage of the run as this is the relative air velocity to the model. However during the transient pulse the relative air velocity increases to u_{cw} (u_x / $\cos\beta°$ - see figure 3.2) and so the stagnation Cp value recorded would be greater than unity by a factor of the ratio of the two respective resultant dynamic pressures. For a 30° yaw angle this factor is 1.333 ($\frac{1}{2}\rho u_{cw}^2 / \frac{1}{2}\rho u_x^2$). Conversely using u_{cw} to calculate the Cp value is entirely correct during the transient cross wind pulse but would yield a Cp stagnation value below unity by the same factor during the axial flow conditions during an experimental run. It was therefore deemed less ambiguous to plot the surface pressures developed at the model as gauge pressure values. The test velocities (see section 7.2) for the entire course of the investigations detailed in sections 7.2.2 to 7.2.4 were matched thus direct comparison of the actual model surface pressures recorded is legitimate, negating the need for a Cp results format. So as to remain consistent it is necessary to also plot the time averaged model surface pressures as a gauge pressure value. However by examining these time averaged stagnation pressures developed at the model front in figures 7.16a and especially 7.16b it is straight forward to visually translate the pressure values to a Cp value by merely dividing the surface pressure at a particular point by the stagnation pressure. Thus a pressure value of ~50Pa represents a Cp value of unity.

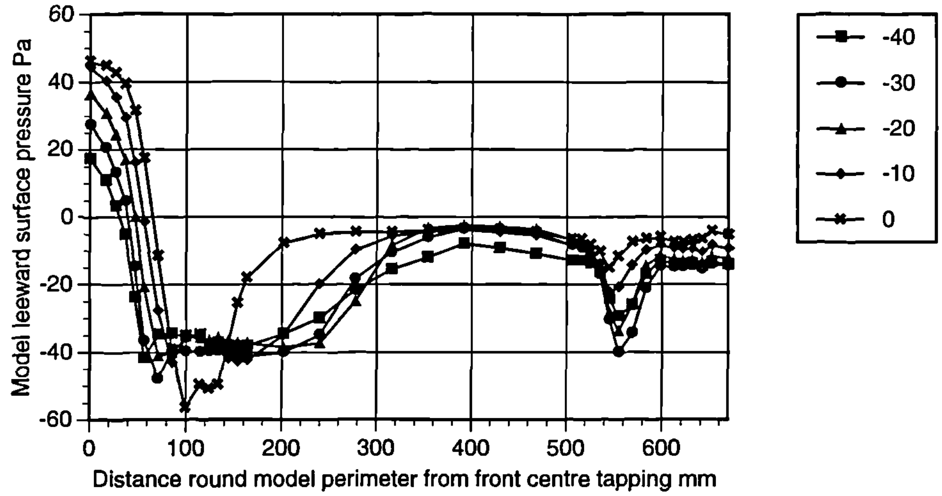

Fig 7.16a - Leeward surface pressure with yaw against surface distance round model.

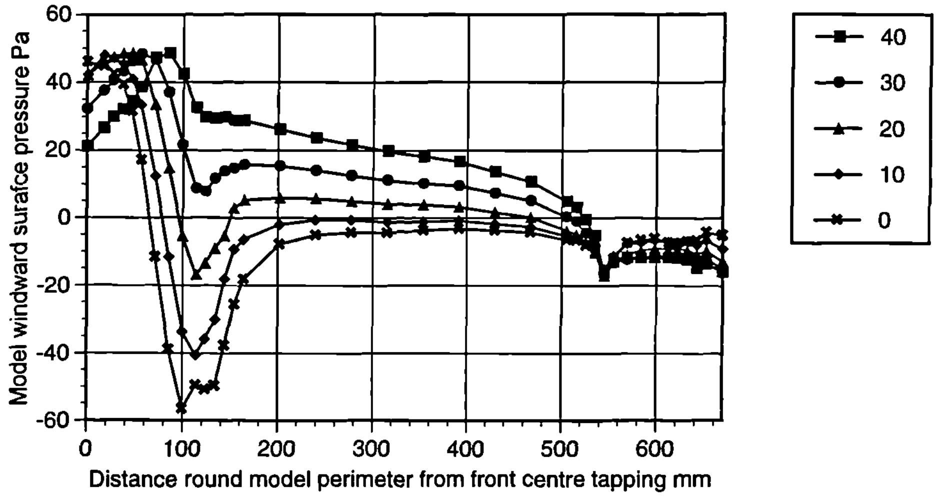

Fig 7.16b - Windward surface pressure with yaw against surface distance round model.

Figures 7.16c and 7.16d are those of the rms values recorded for the time averaged pressures shown by figures 7.16a and 7.16b. The time averaged and rms values were gained from a 200Hz sample over a period of one second.

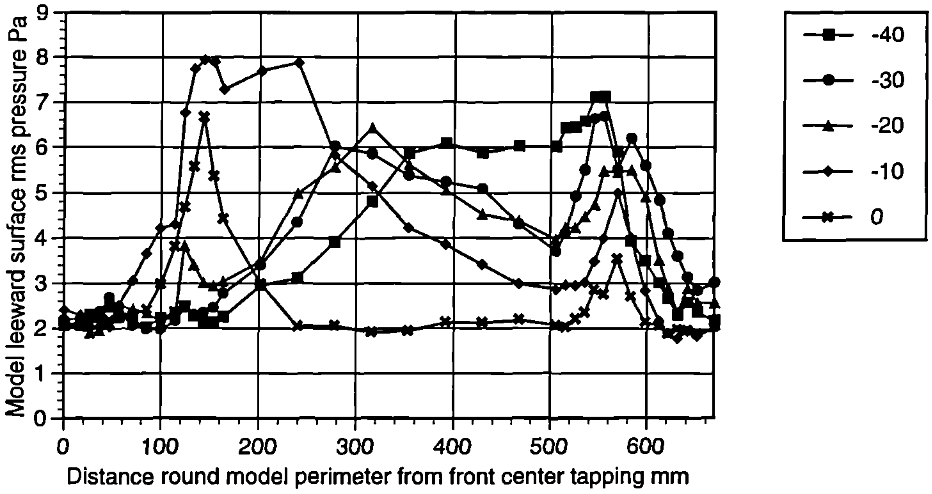

Fig. 7.16c - Leeward surface rms pressure with yaw against distance round model.

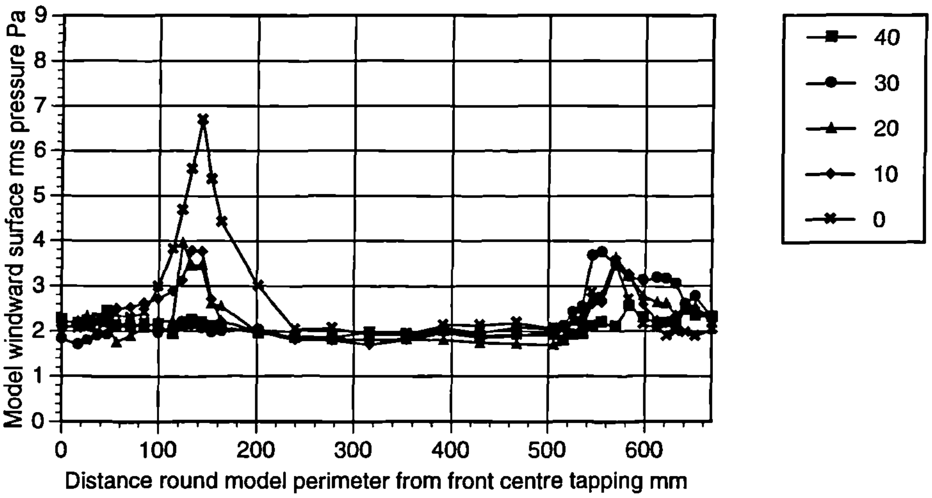

Fig. 7.16d - Windward surface rms pressure with yaw against distance round model.

7.2.4 Transient Response of Aerodynamic Model

Surface Pressure Investigation

The following results were gathered from a number of separate transient runs with the model placed in the optimum position in the working section as detailed previously. Each trace represents the pressure variation with time of a single tapping on the model surface against time under the transient conditions. Each plot displays five traces gathered from a single experimental run and each trace is labelled with a corresponding tapping position (see figure 7.2). Tapping '0' is at the front face centre position on the model and tapping '37' is at the rear face centre position. All the other tapping positions carry an additional 'W' or 'L' label corresponding to the windward or leeward side of the model (see figure 7.2). Thus, for example, tapping '18 W' is located on the windward model side at position '18' and tapping '18 L' is positioned exactly opposite on the leeward model side. In order to monitor the repeatability of the air flow conditions simulated in the working section from run to run the surface pressure at tapping '0' was always recorded (except for two final runs) to verify that the data gathered from the different runs could be directly compared.

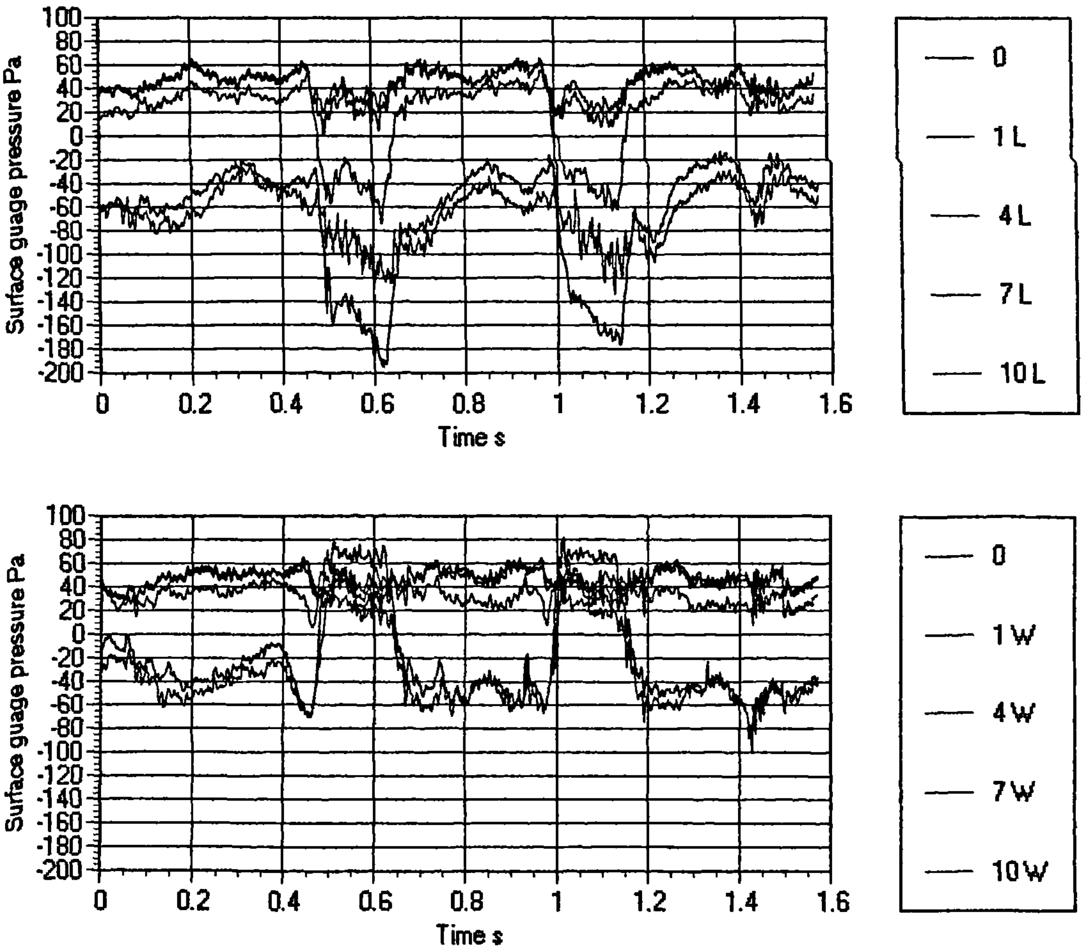

Figs. 7.17 & 7.18 - Transient model surface pressure.

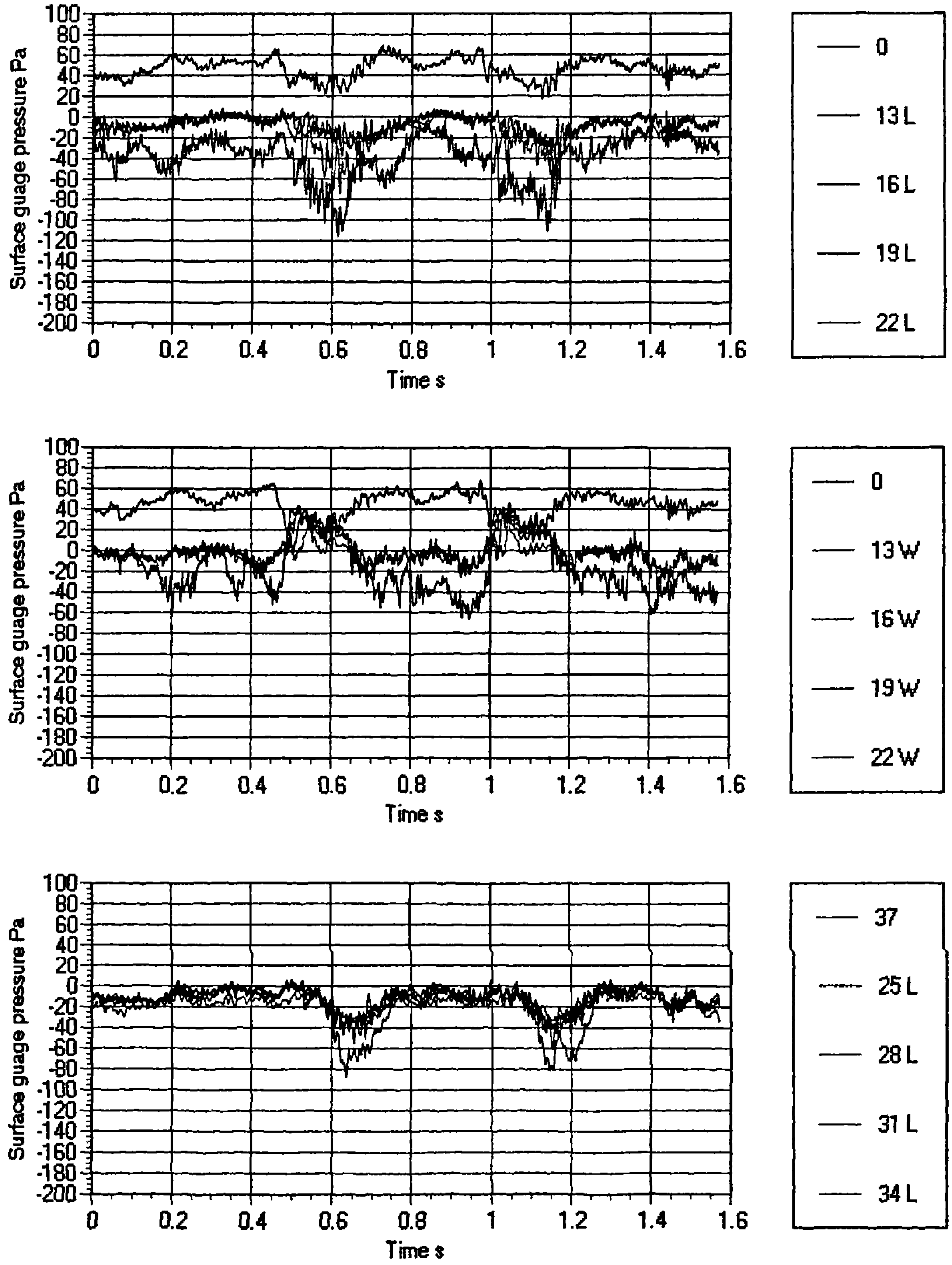

Figs. 7.19, 7.20 & 7.21 - Transient model surface pressure.

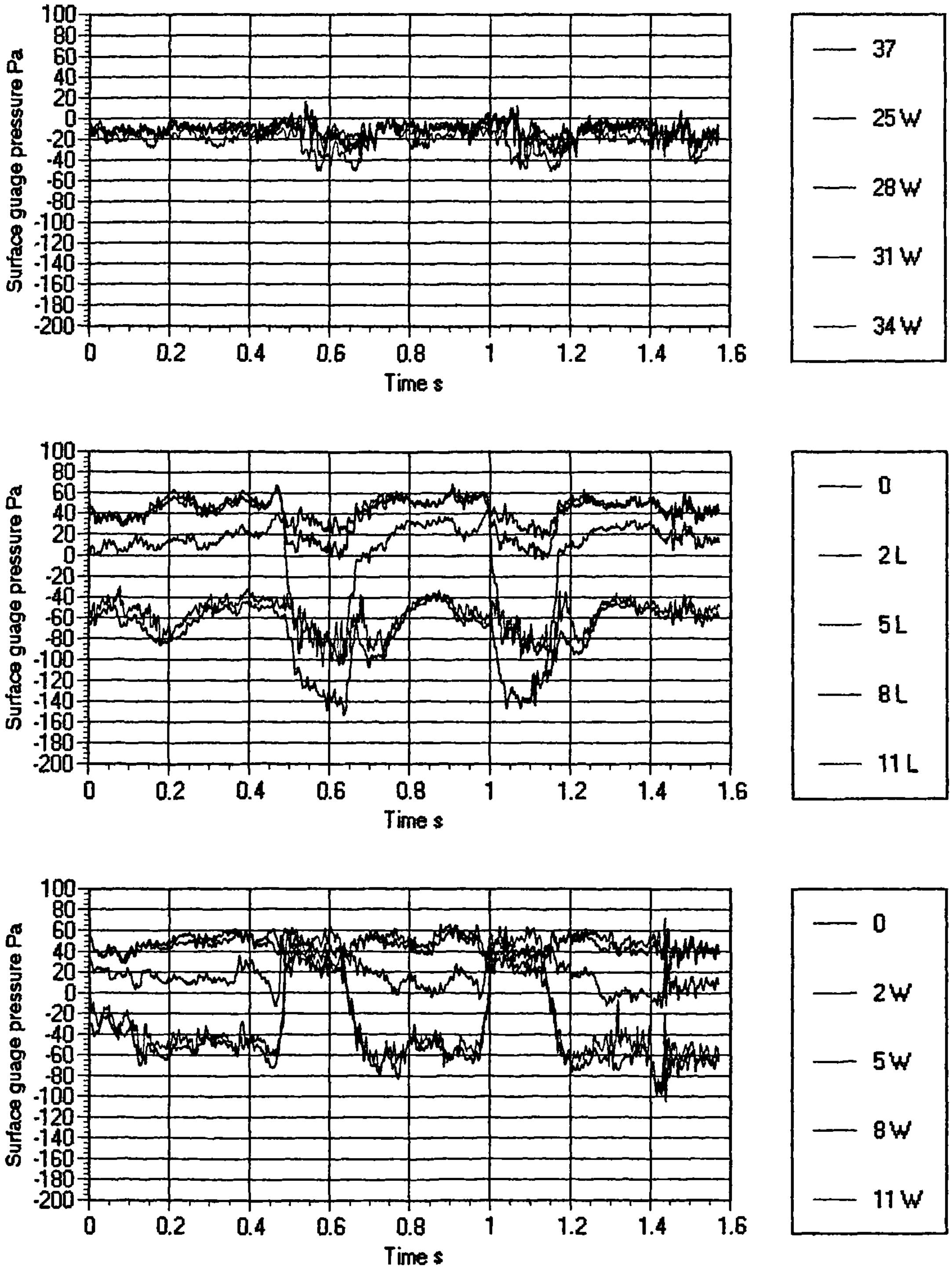

Figs. 7.22, 7.23 & 7.24 - Transient model surface pressure.

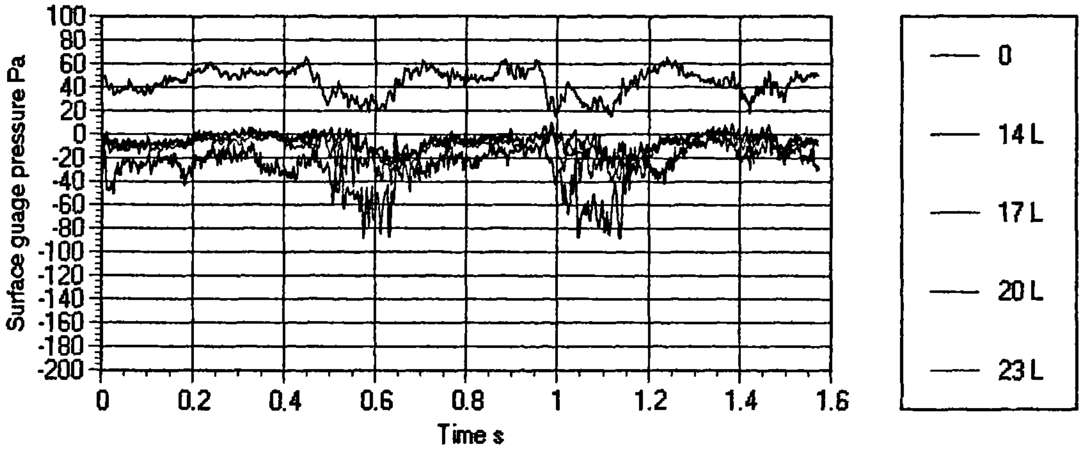

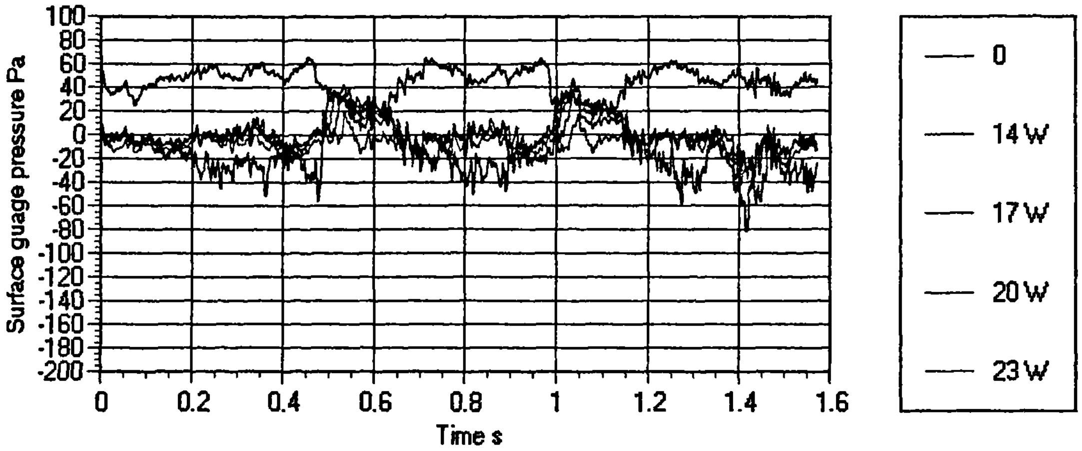

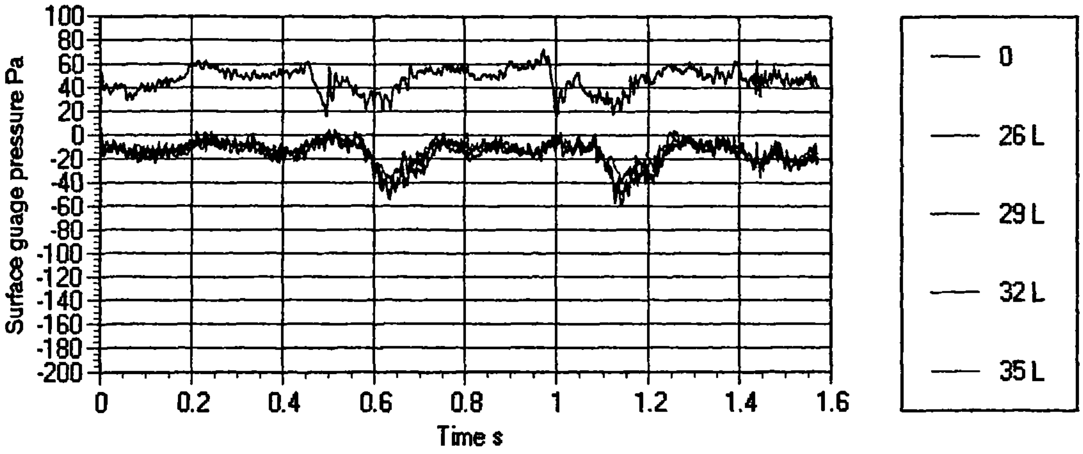

Figs. 7.25, 7.26 & 7.27 - Transient model surface pressure.

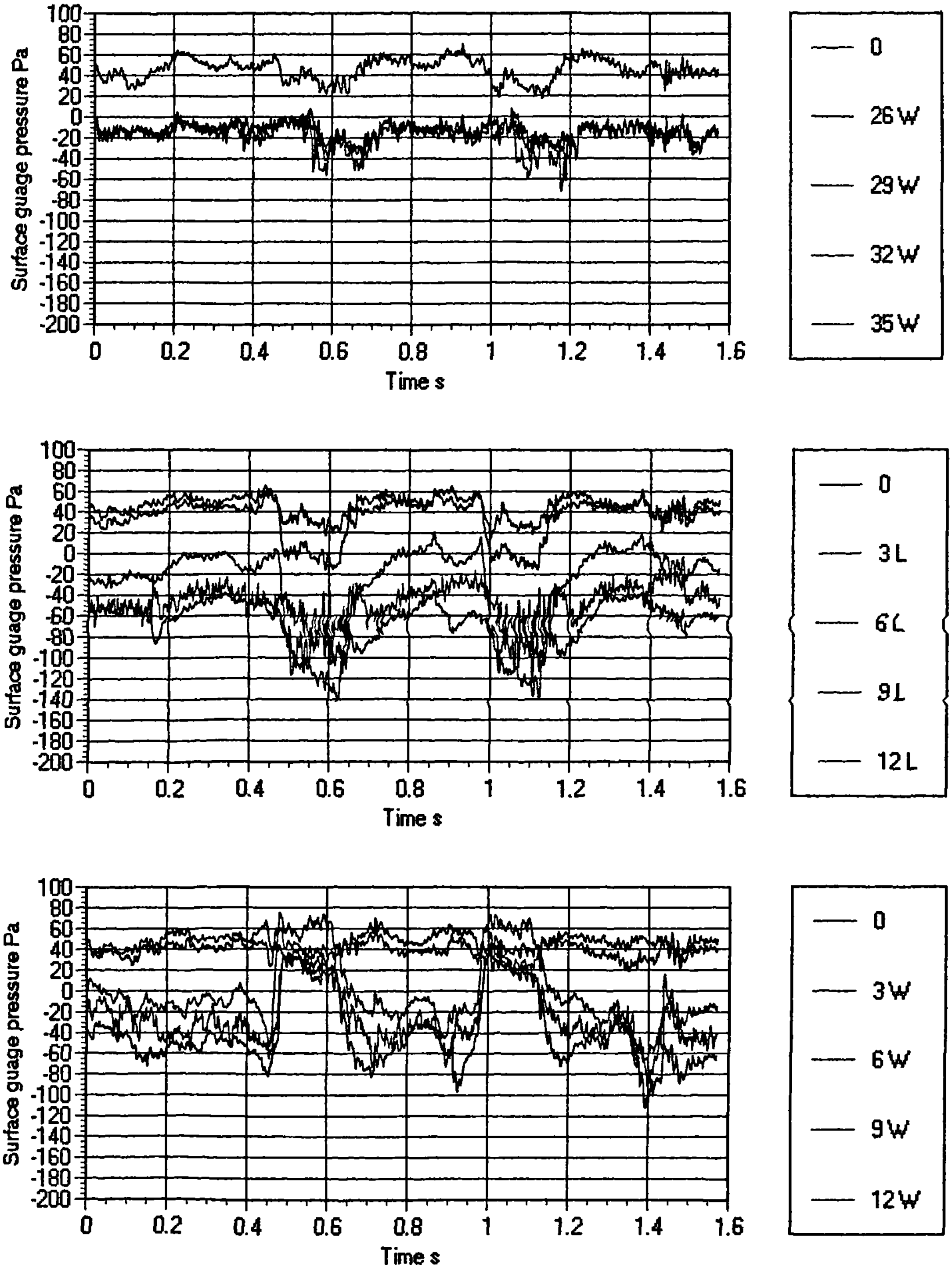

Figs. 7.28, 7.29 &7.30 - Transient model surface pressure.

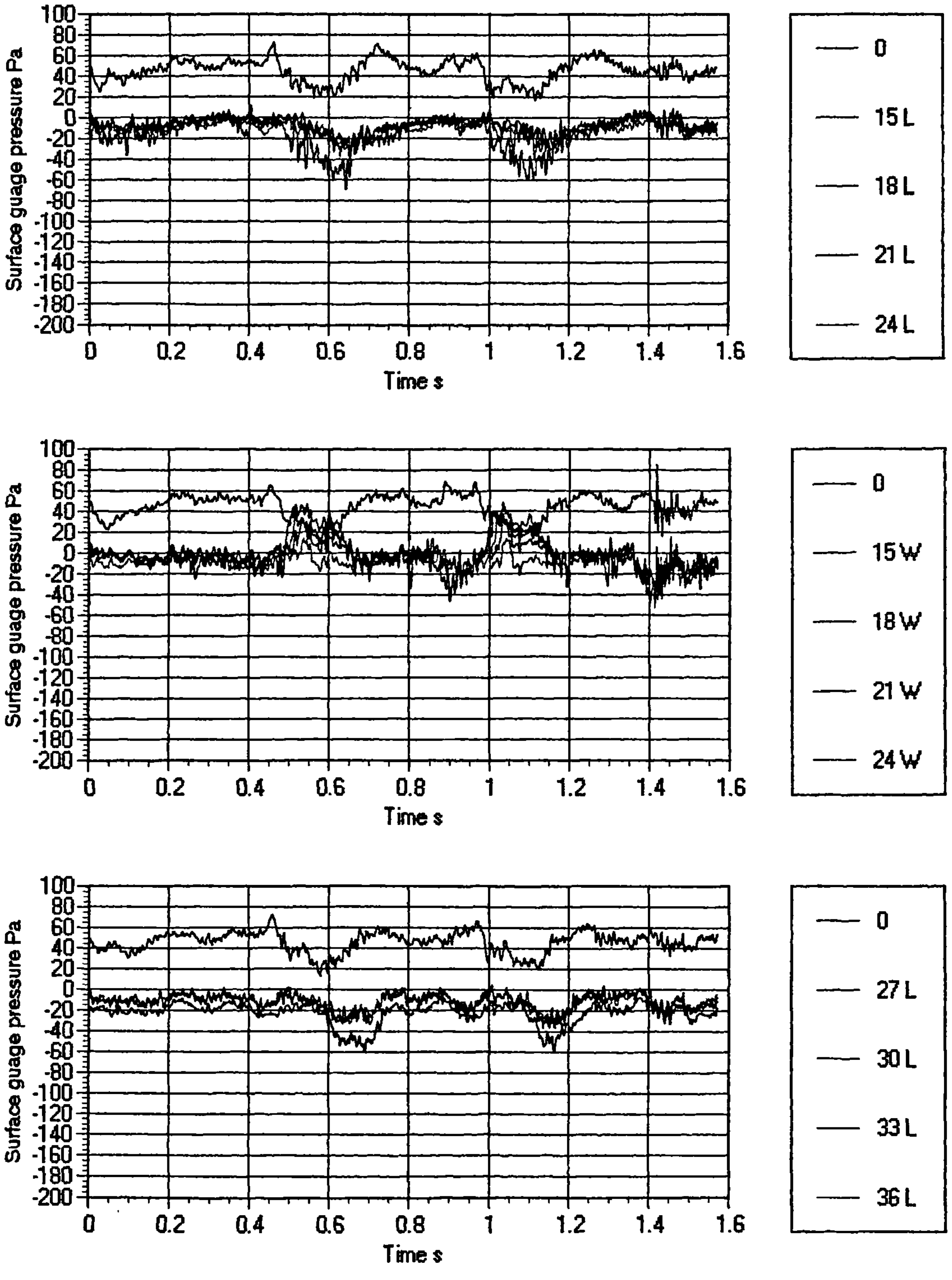

Figs. 7.31, 7.32 & 7.33 - Transient model surface pressure.

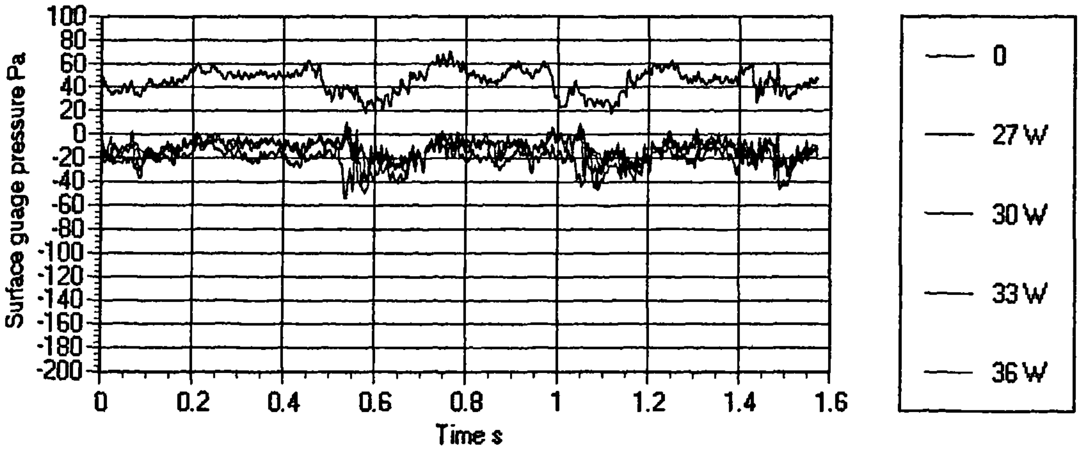

Fig. 7.34 - Transient model surface pressure.

Using transient pressure data gathered from all the model tappings it is possible to build up a picture of the flow field round the model. The pressure data can also be combined, using the model geometry, to calculate the pressure derived forces and moments induced on the model when subjected to transient cross wind conditions. However it first must be verified that the pressure data, gathered over a separate experimental runs, may be combined.

The repeatability of the apparatus over the 18 experimental runs required to build up the full model pressure response can be quantified. During each run the flexible belt velocity could be calculated using an optically triggered sensor (see section 6.6.2). The left hand plot in figure 7.35a displays the separate belt velocity readings for each run indicated by a small horizontal dash. The median of the all the values is indicated by a large horizontal marker. Figure 7.35a represents the data recorded over the first transient pulse only for increased temporal resolution.

The distance, x, of the model leading edge into the cross wind region relative to the model length, l, may be non-dimensionalised based on the test velocity to produce a x/l time axis. Thus for each cross wind transient pulse there exist four chronological marker points: leading edge of the cross wind transient in line with the leading edge of the model (x/l = 0), leading edge of the cross wind transient in line with the trailing edge of the model - i.e. model fully enveloped in cross flow conditions (x/l = 1), trailing of the cross wind transient in line with the leading edge of the model (x/l = 3) and trailing edge cross wind transient in line with the trailing edge of the model - i.e. model fully enveloped in axial flow (x/l = 4). The right hand plot in figure 7.35a displays the time values at these four points over the same 18 experimental runs each represented by a small horizontal dash in the relevant column. The median of the all the values is again indicated by a large horizontal marker.

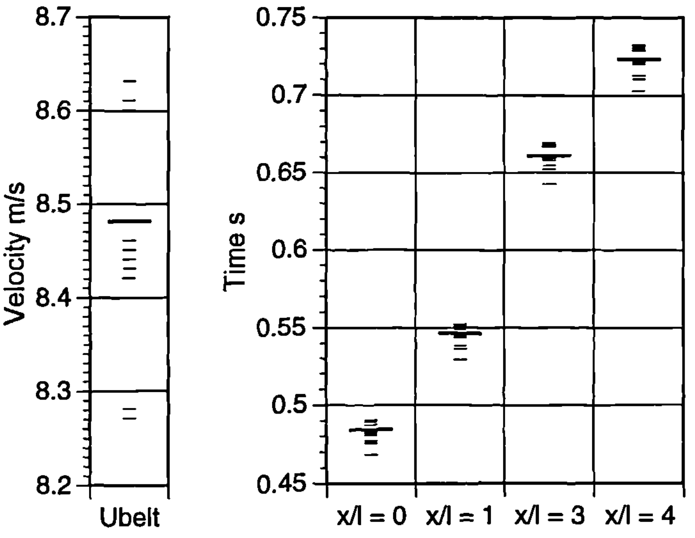

Fig. 7.35a - Raw correlation of velocity & temporal markers for experimental runs.

The statistical spread of data displayed by figure 7.35a may be examined in table 10.2 (section 10.2.2). It transpires that the velocity variance is low whilst the variance displayed by the marker points is high.

It is possible to also assess the repeatability of the air flow in the working section between runs by comparing the pressure data from a common pressure tapping used for each of the runs. Tapping '0' was common for all but two of the runs, where tapping '37' was common (see figure 7.2). Figure 7.35b displays the surface pressure recorded at tapping '0' for 16 of the 18 experimental runs required to build up the full model surface pressure survey and figure 7.35c displays the surface pressure recorded at tapping '37' for the remaining two runs. Again for increased temporal resolution figures 7.35b and 7.35c show the pressure data recorded over the only first of the two transients present in a single experimental run. The data has been directly superimposed on the same time axis and has been additionally smoothed by a factor of thirteen from the data displayed in figures 7.17 to 7.34. This smoothing factor was selected as it allowed a further reasonable level of data compression combined with a negligible effect on the general shape of the traces - i.e. only relatively high frequencies were filtered.

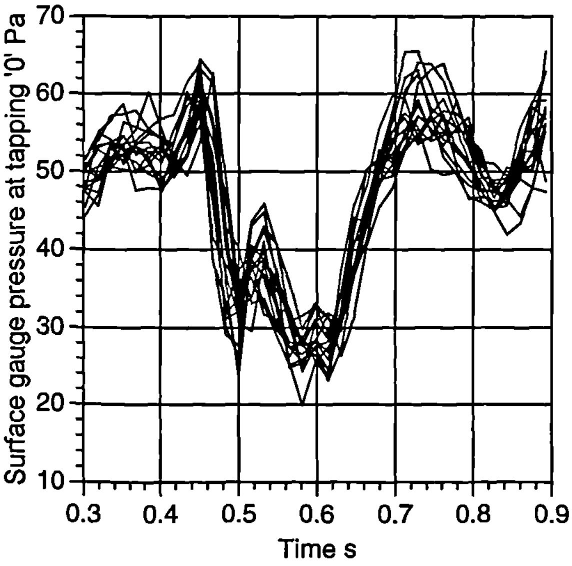

Fig. 7.35b - Raw correlation of transient model surface pressure at tapping '0'.

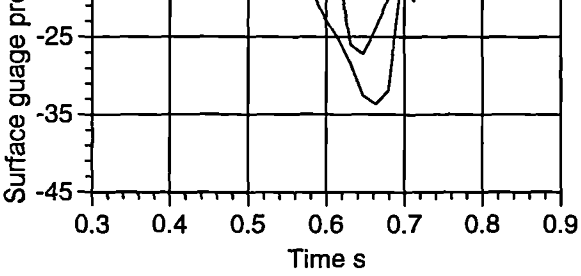

Fig 7.35c - Raw correlation of transient model surface pressure at tapping '37'.

Table 10.2 (section 10.2.2) suggests if the data gathered was shifted on the time axis to coincide at the x/l = 0 marker an improved correlation would be achieved. This was undertaken and a modified data correlation was achieved and is shown in figure 7.36a. Table 10.3 (section 10.2.2) shows the improved correlation statistics.

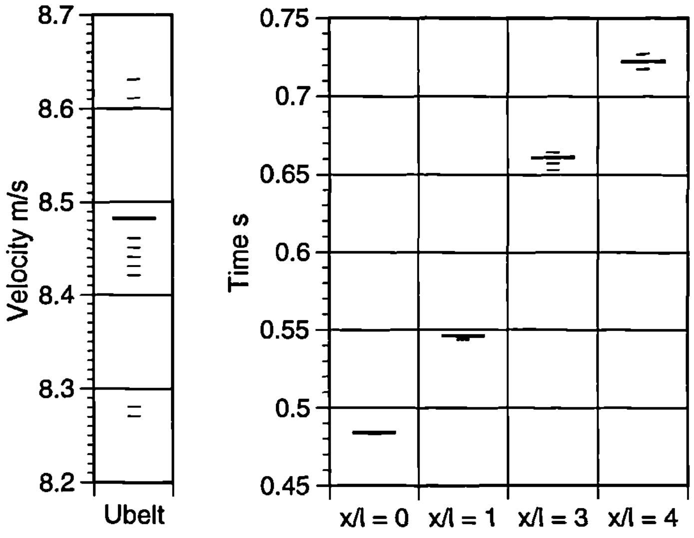

Fig. 7.36a - Modified correlation of velocity & temporal markers for experimental runs.

Using the newly correlated data it is also possible to review the data from the common pressure tappings. Figures 7.36b and 7.36c show the modified correlation of the transient pressures recorded at tapping '0' and tapping '37' respectively.

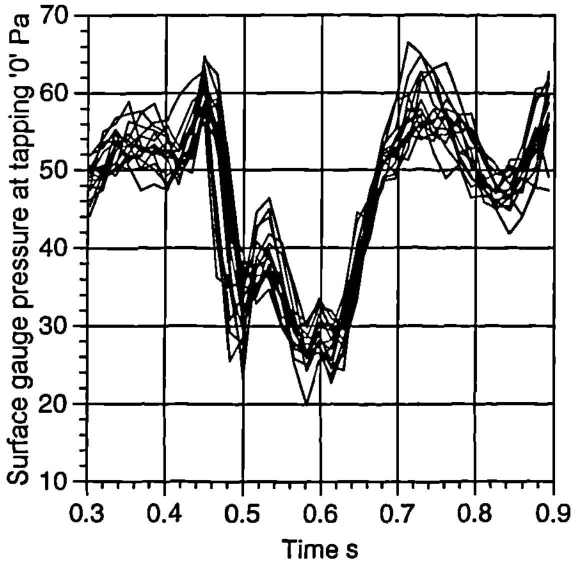

Fig. 7.36b - Modified correlation of transient model surface pressure at tapping '0'.

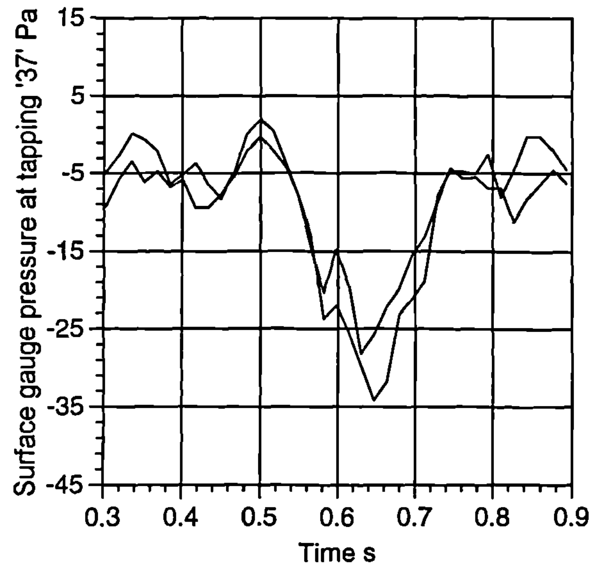

Fig 7.36c - Modified correlation of transient model surface pressure at tapping '37'.

The transient pressure traces displayed in figures 7.17 to 7.34 can be examined on an individual basis but a far improved understanding of the transient flow regime may be achieved by amalgamating the modified correlation pressure readings from all the surface pressures tappings on the model on the same time axis and plotting the full model surface pressure distribution development with time during the transient conditions. This has been achieved by figures 7.37a to 7.37o, each of which have the same format. Each figure plots the pressure distribution at the model surface against the distance round the model perimeter from the front centre tapping (see also figures 7.16a to 7.16b). Each figure comprises of five traces. The black trace represents the time averaged pressure distribution at the model surface in axial flow conditions at velocity u_X. The light red trace represents the time averaged pressure distribution down the leeward side at 30° yaw and the light green trace represents the time averaged pressure distribution down the windward side also at 30° yaw. These three traces are fixed and do not alter from figure to figure. These two latter traces have been corrected to account for the resultant transient velocity, u_{CW} (see figure 3.2), present in the working section during the two separate transients. The two remaining traces are the actual experimental pressure data recorded during the experimental run, directly transferred from figures 7.17 to 7.34 but with the smoothing factor of thirteen, at the leeward (dark red) and the windward (dark green) model sides. The relative position of the cross flow transient region to the model is indicated schematically beneath each figure. Axial flow is nominally present at either side of this cross flow region. As the figures are examined in sequence the cross flow region shifts in the down stream direction and the instantaneous pressures at the model surface may be observed as the cross flow region envelopes the model. Figures 7.37a to 7.37m are of consecutive time points each separated by ~0.016s which represents a 61Hz sample frequency or a $x/l = 0.27$ travel distance of the cross wind region. Figures 7.37n and 7.37o represent a time step of $x/l = 1.07$ and 1.60 respectively from each preceding figure. Figures 7.37a to 7.37o represent the data recorded over the first transient pulse only.

Legend (figures 7.37a to 7.37o)

— 0° yaw time averaged pressure @ u_x
— 30° yaw time averaged leeward pressure @ u_{cw}
— 30° yaw time averaged windward pressure @ u_{cw}
— Leeward instantaneous pressure
— Windward instantaneous pressure

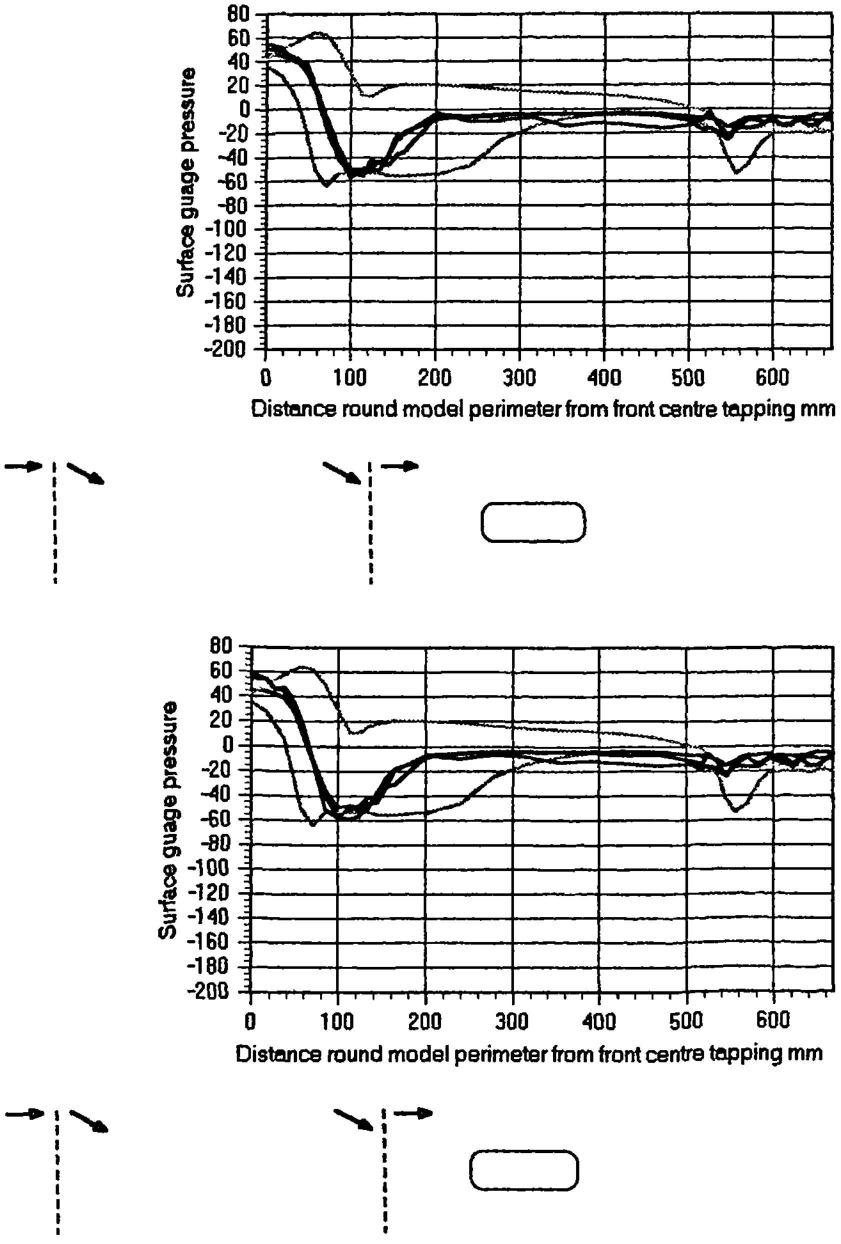

Figs. 7.37a & 7.37b - Pressure distribution with relative position to cross wind region.

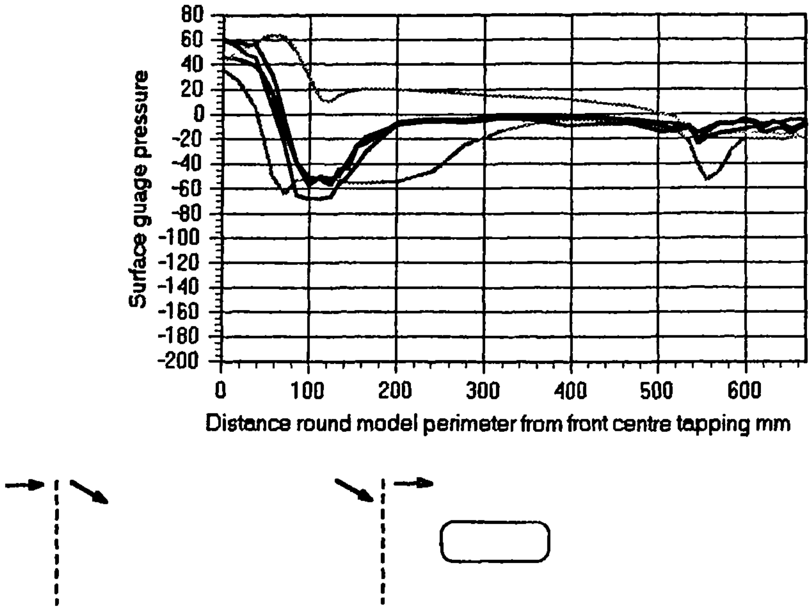

Fig. 7.37c - Pressure distribution with relative position to cross wind region.

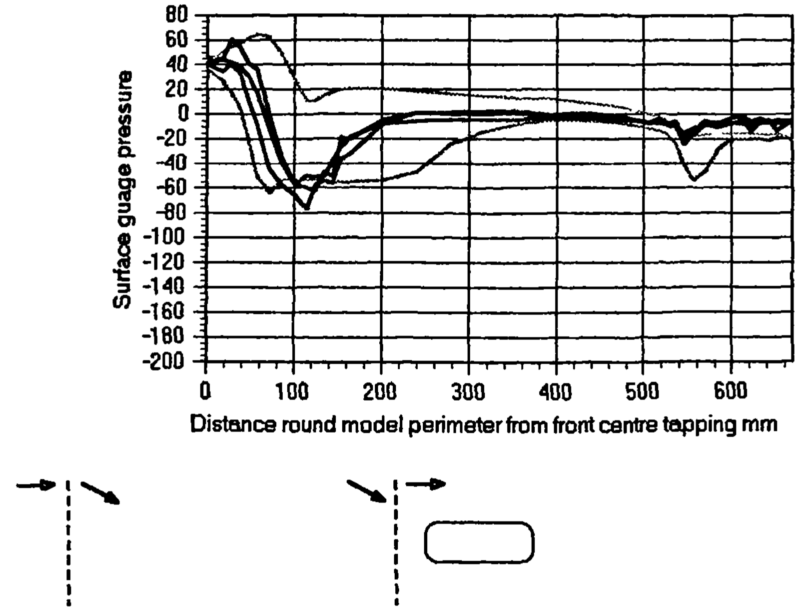

Fig. 7.37d - Pressure distribution with relative position to cross wind region.

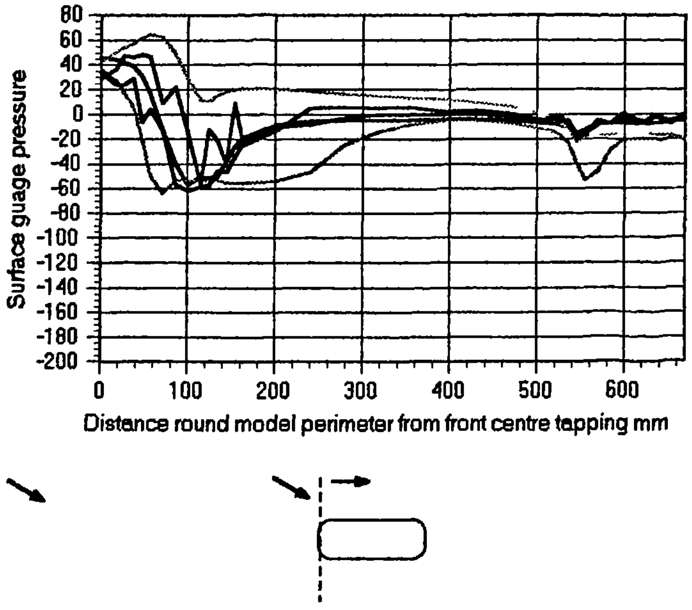

Fig. 7.37e - Pressure distribution with relative position to cross wind region.

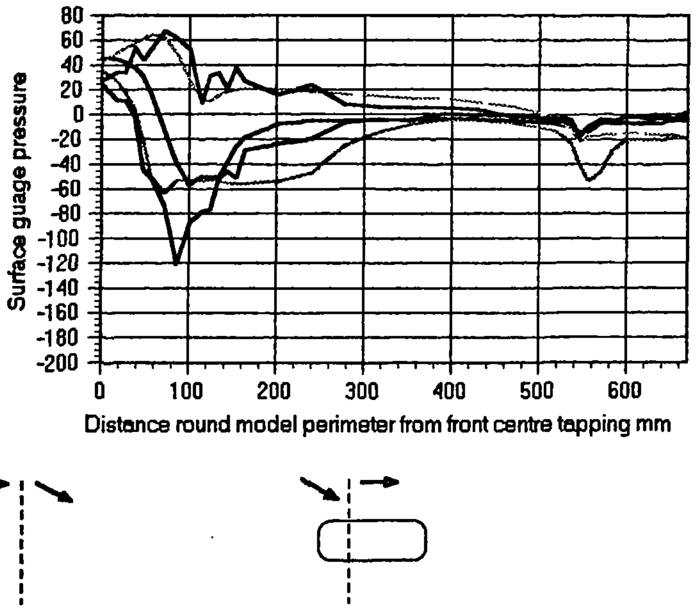

Fig. 7.37f - Pressure distribution with relative position to cross wind region.

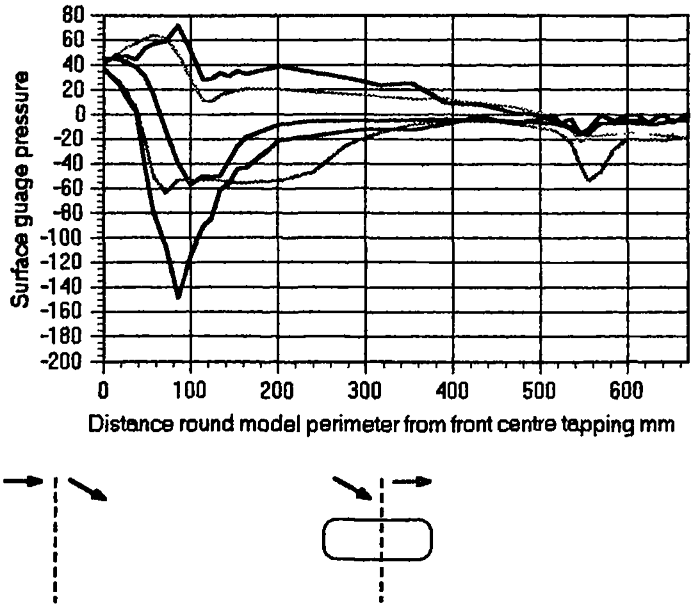

Fig. 7.37g - Pressure distribution with relative position to cross wind region.

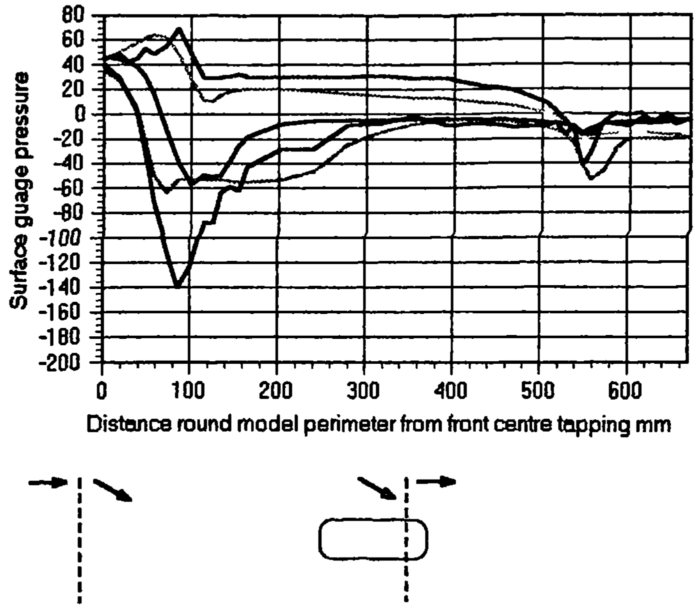

Fig. 7.37h - Pressure distribution with relative position to cross wind region.

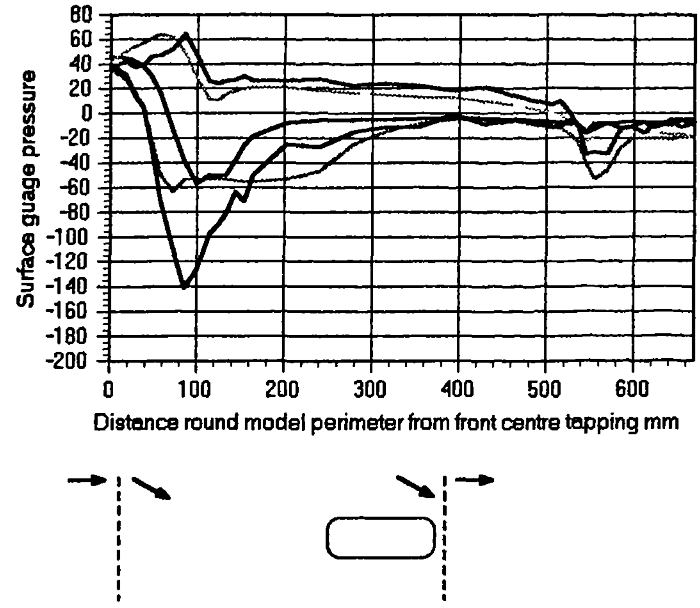

Fig. 7.37i - Pressure distribution with relative position to cross wind region.

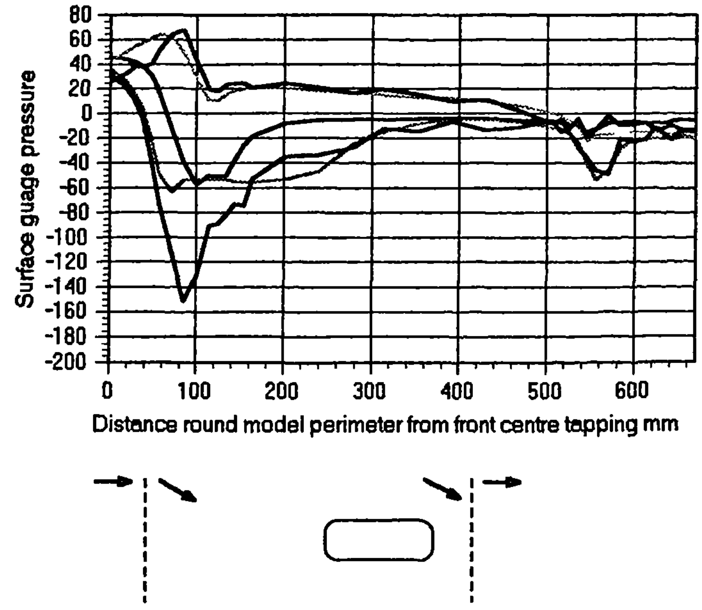

Fig. 7.37j - Pressure distribution with relative position to cross wind region.

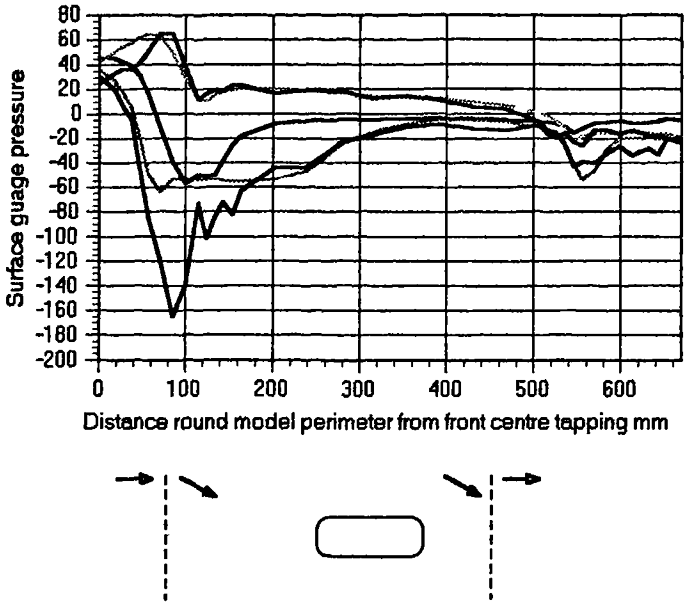

Fig. 7.37k - Pressure distribution with relative position to cross wind region.

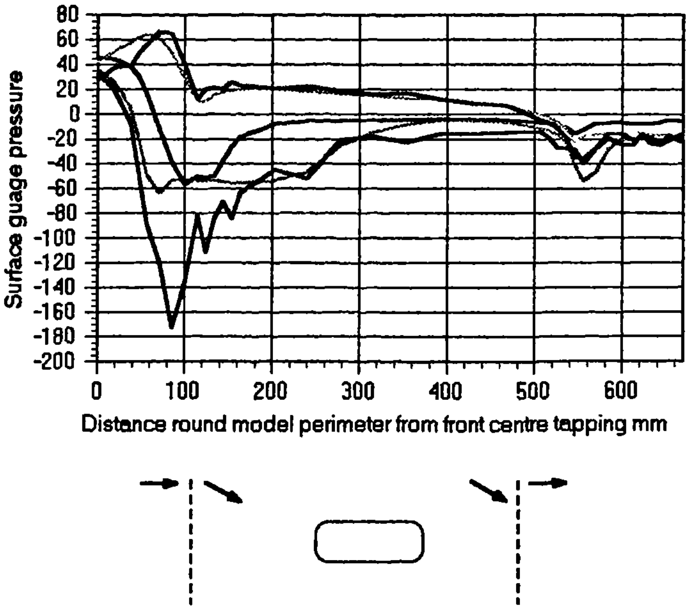

Fig. 7.37l - Pressure distribution with relative position to cross wind region.

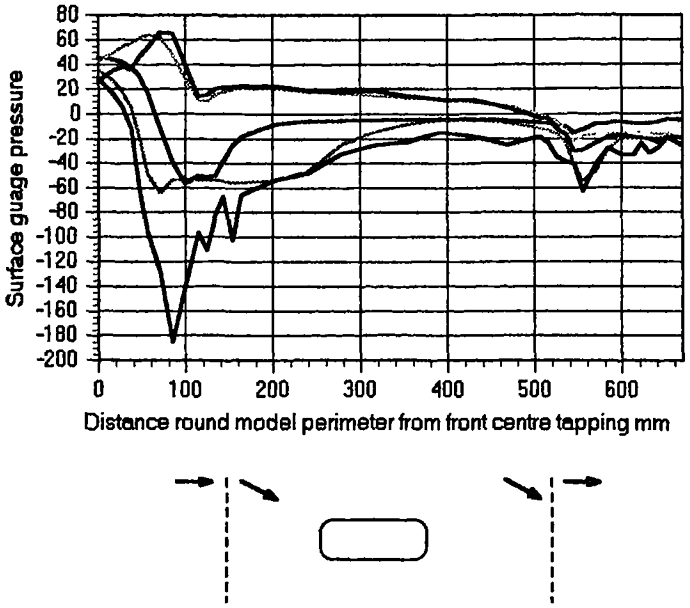

Fig. 7.37m - Pressure distribution with relative position to cross wind region.

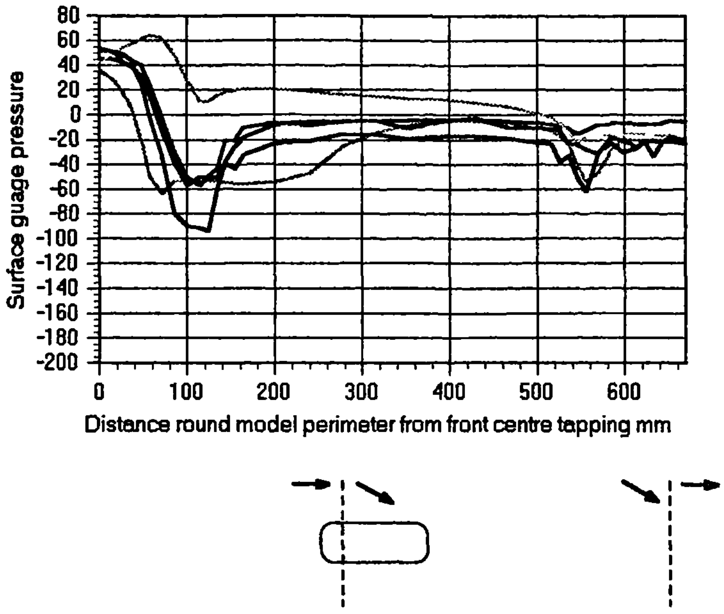

Fig. 7.37n - Pressure distribution with relative position to cross wind region.

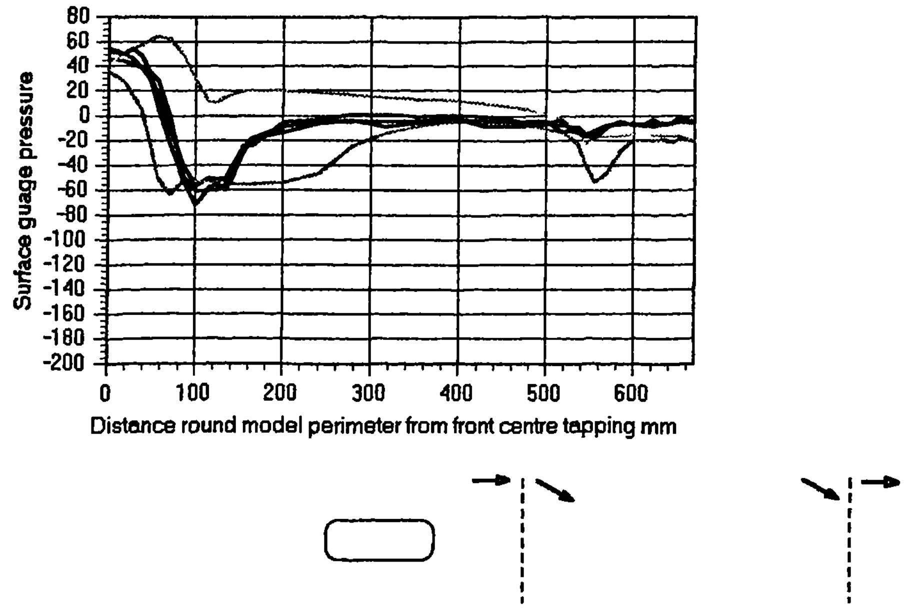

Fig. 7.37o - Pressure distribution with relative position to cross wind region.

Figures 7.38a to 7.38c show the time dependent model response of side pressure force, yawing pressure moment (about the model centroid) and drag pressure force respectively gained by combining the model geometry with the surface pressure data displayed by figures 7.37a to 7.37o but over the full experimental run and not just the initial transient pulse. The term pressure force (or pressure moment) is used as the calculated loads were derived from surface pressure readings.

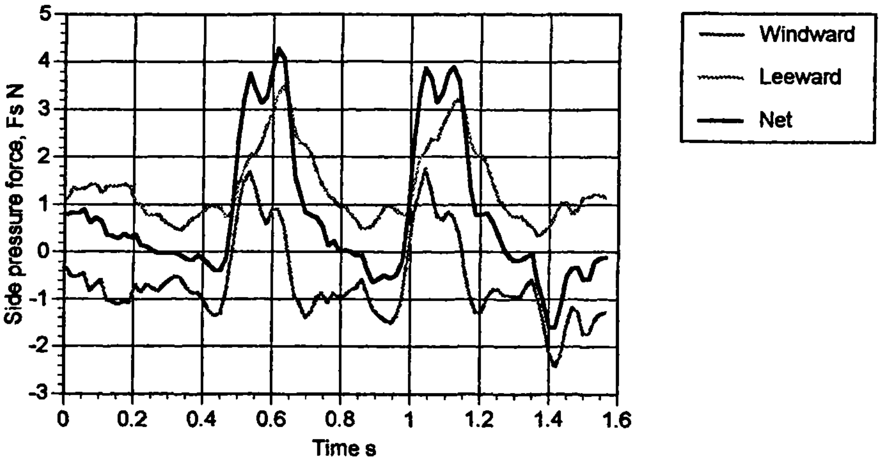

Fig 7.38a - Transient side pressure force on model.

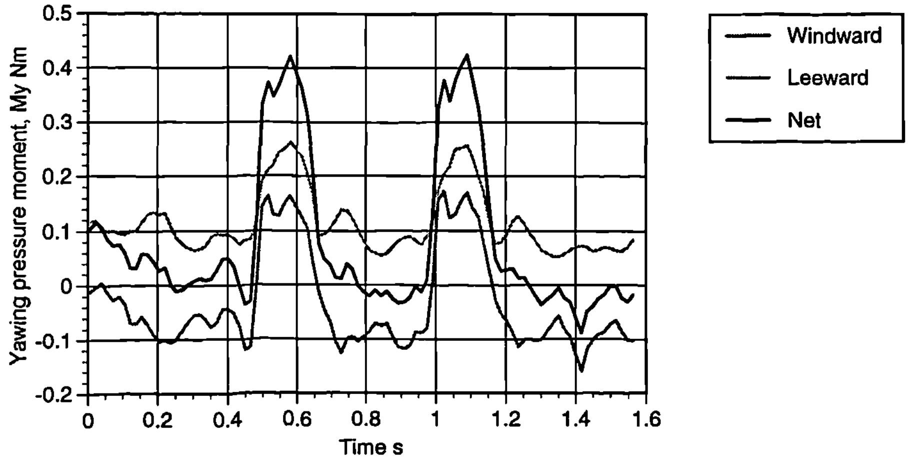

Fig 7.38b - Transient yawing pressure moment on model.

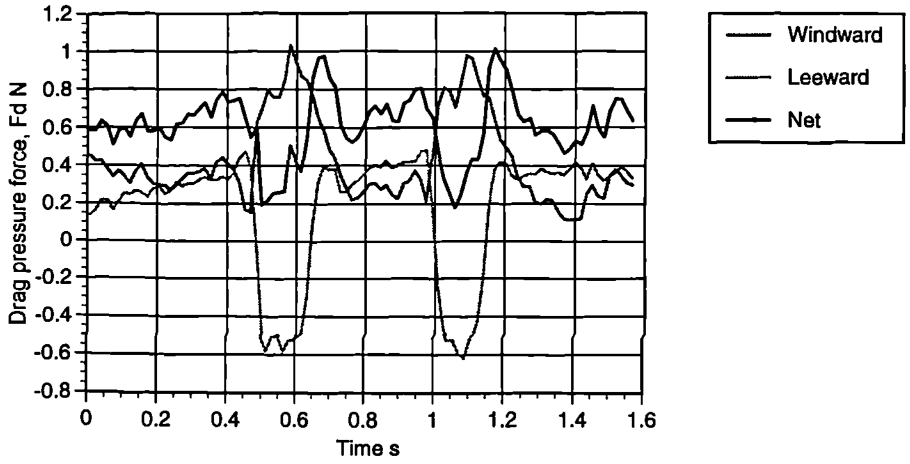

Fig. 7.38c - Transient drag pressure force on model.

Figures 7.39a to 7.39c respectively show model response of side pressure force, yawing pressure moment and drag pressure force against relative distance of the model into the cross wind for the first cross wind pulse only.

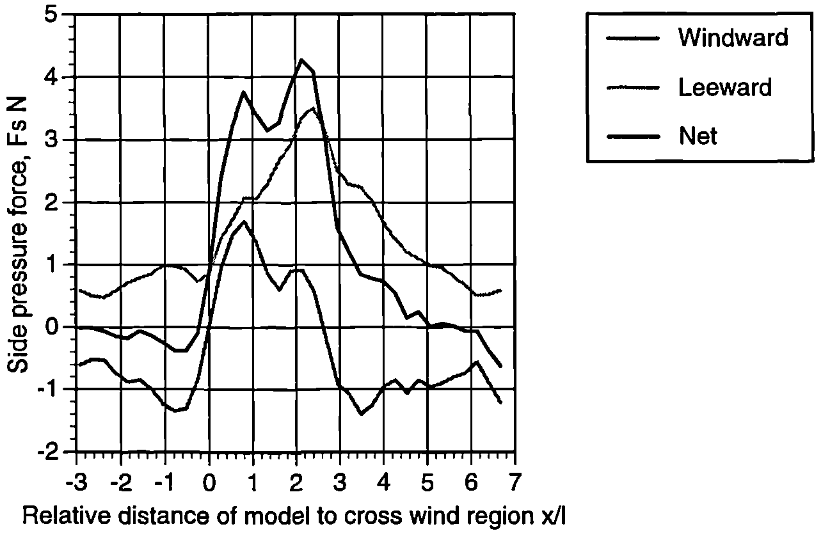

Fig. 7.39a - Transient side pressure force on model against relative distance.

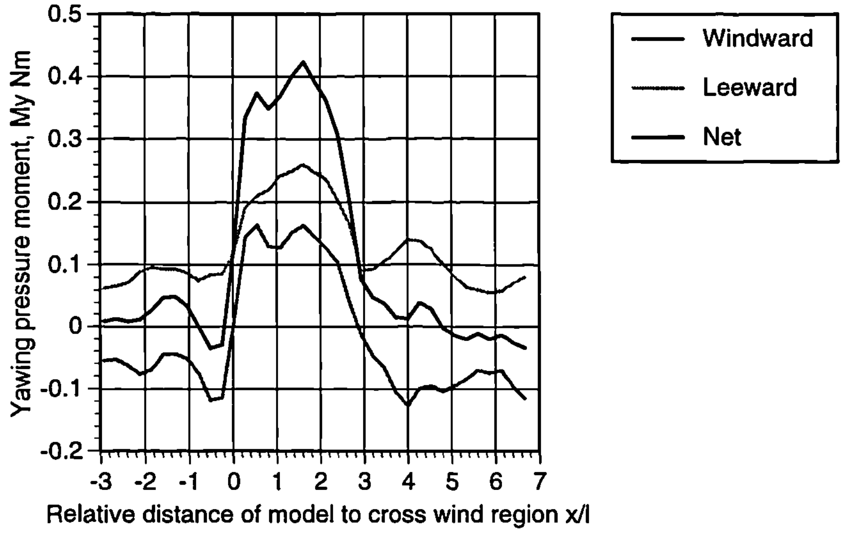

Fig. 7.39b - Transient yawing pressure moment on model against relative distance.

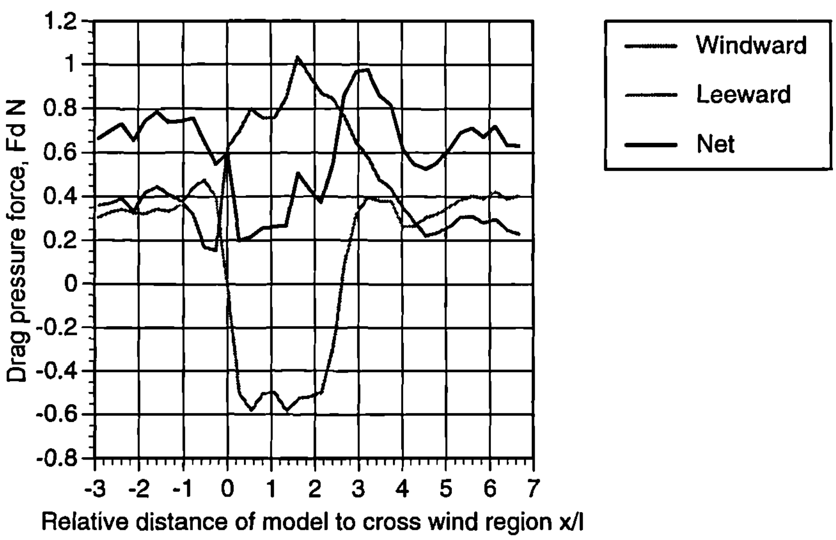

Fig. 7.39c - Transient drag pressure force on model against relative distance.

Force and Moment Investigation

Using the force balance (see section 6.5) and the light weight force balance aerodynamic model (see section 6.4.2) it was possible to monitor the aerodynamic loads induced on the model under transient cross wind simulation. The force balance was placed immediately beneath the wind tunnel ground plane with the balance stings extending vertically upwards in to the working section. The model was mounted on the stings in the exact same position and orientation as for the surface pressure survey. Figures 7.40a to 7.40c show the transient aerodynamic side force, yawing moment and drag force respectively induced on the model by the simulation. The traces were derived from averaging the data gathered over three experimental runs. The experimental runs were verified to be sufficiently repeatable to be directly superimposed without the need for matching the x/l = 0 time point (the data range at the x/l = 0 point between the three runs correlated to 4.5% of the model length and the belt velocity range was exactly one third of the same modified values as displayed by table 10.3 in section 10.2.2). The averaging process however transpired to have very little effect on the form of the traces involved as the force balance vibrations were generally in phase and of similar magnitude. These loads interpreted by the force balance were not corrected for tare loads produced by the model support stings or end plates in the air flow. The data was smoothed by the same factor as displayed by the equivalent pressure derived loads.

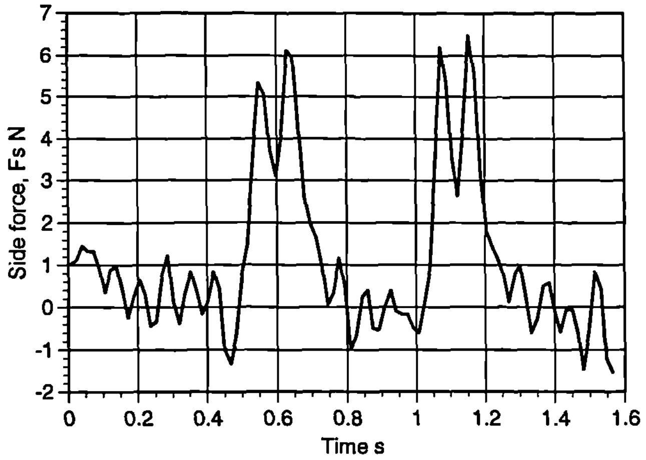

Fig 7.40a - Transient side force on model.

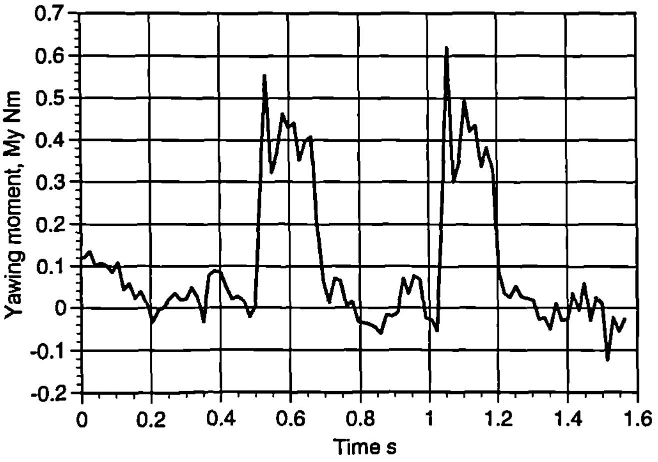

Fig 7.40b - Transient yawing moment on model.

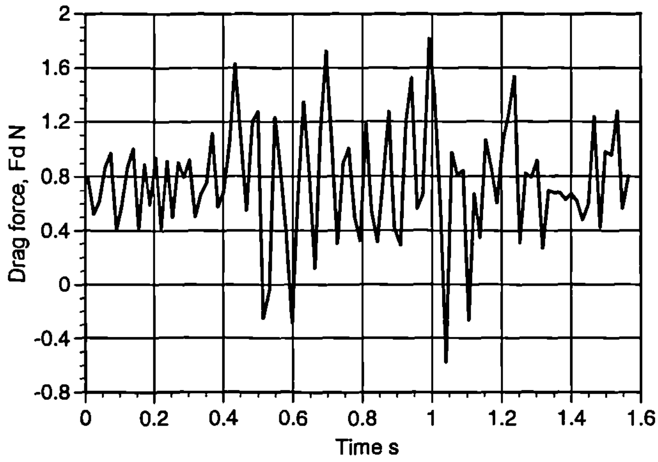

Fig 7.40c - Transient drag force on model.

Figures 7.41a to 7.41c show the model induced side force, yawing moment and drag force respectively against relative distance of the model into the cross wind region for the first cross wind pulse only. Also shown on the figures for comparison are the same forces calculated from the surface pressure readings, as shown by figures 7.39a to 7.39c.

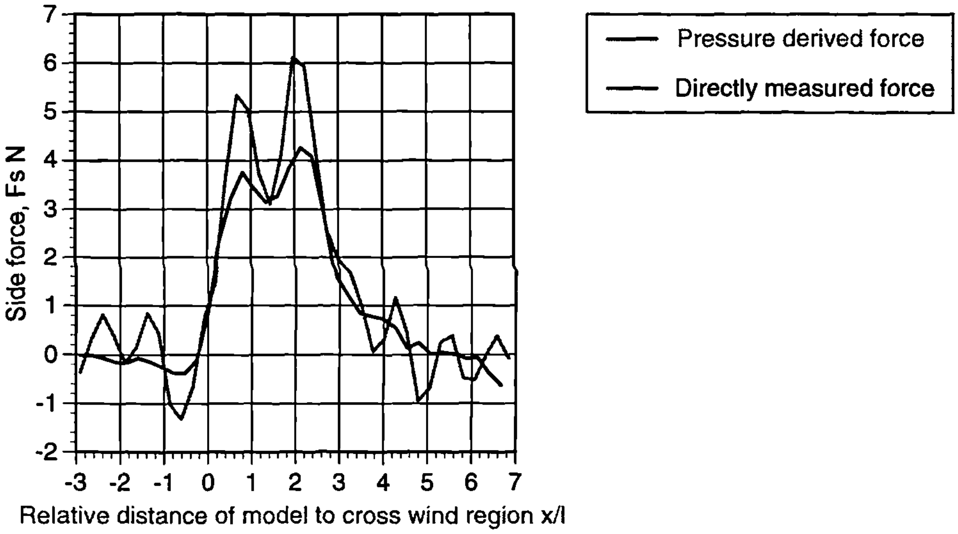

Fig. 7.41a - Transient side force on model against relative distance.

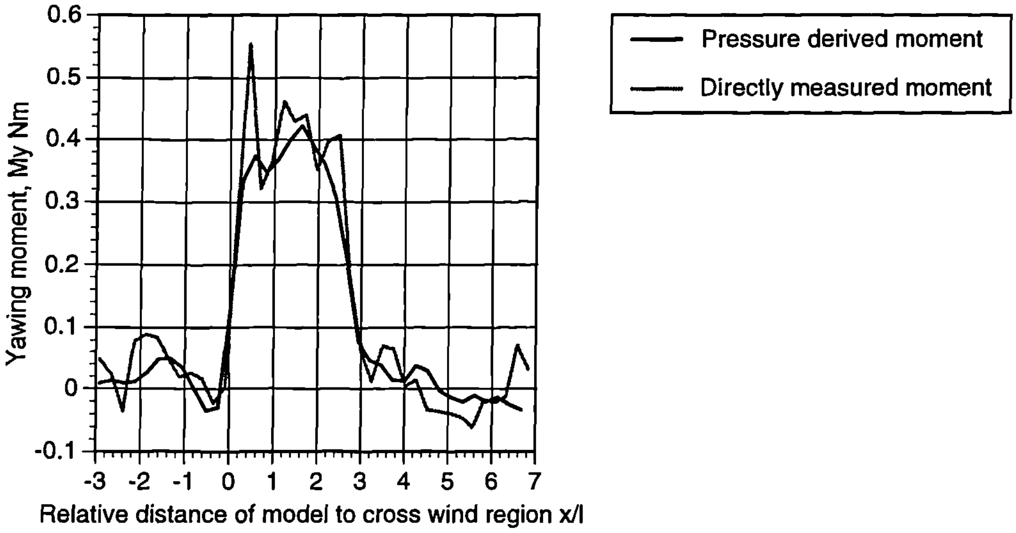

Fig. 7.41b - Transient yawing pressure moment on model against relative distance.

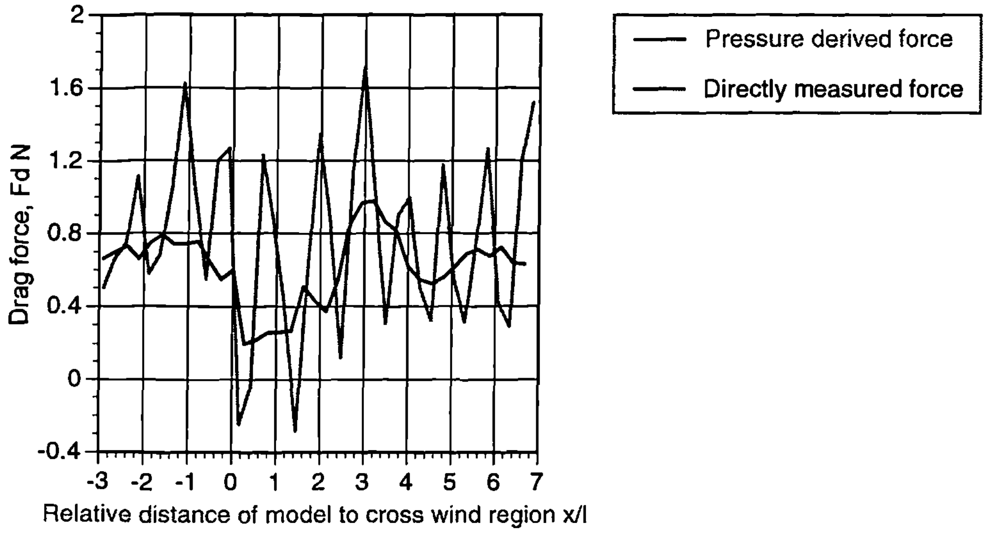

Fig. 7.41c - Transient drag force on model against relative distance.

8.0 Computational Investigation and Results

8.1 Scope of Investigation

The computational simulation was designed to model the experimental configuration; that of a stationary vehicle influenced by the relative movement of a cross wind region as distinct from simulating a moving vehicle passing through a stationary cross wind region. This simulation method was adopted so as to examine, prior to the full design of the experimental apparatus, the basic validity of new simulation technique. For ease of grid generation and the preliminary nature of the investigation a highly simplified (rectangular) 2D vehicle model was used. The investigation was directed towards examining the effects of transient flow conditions on a vehicle shape and in particular the time development of the velocity flow field in the vicinity of the vehicle in addition to the transient surface pressures induced on the vehicle. Prior to the experimental work undertaken by the author there appeared to be no information available regarding the nature of the air flow developed at the surface of a vehicle or in the wake under transient cross wind conditions. This computational investigation was therefore a basic exploration of the transient flow effects that should be explored further, both experimentally and computationally. The interpretation of the computational results is presented in chapter 10.

8.2 Method of Investigation

8.2.1 Computational Code and Software

The simulation was performed using PHOENICS [44] on an HP Workstation. The PHOENICS code is based on a pressure correction method. An initial pressure field is assumed. From the momentum equation an initial velocity field is calculated. If continuity is then not satisfied by this velocity field a correction on pressure is introduced which produces a velocity correction to allow continuity to be satisfied. The code allows steady or unsteady air flow simulations together with the ability to model fluctuating boundary conditions.

8.2.2 Required Modelling Boundary Conditions

In overview the boundary conditions were configured to simulate a vehicle shape passing from axial flow conditions through a region of cross wind flow, producing an effective yaw angle of 30° to the vehicle, then returning to axial flow. The duration of the cross wind region corresponds to seven vehicle lengths in the axial direction. This is distinct from the three vehicle length cross wind region used in the experimental apparatus which was selected based on results from previous experimental investigations (see section 2.3.2). However to ensure that any transient cross wind effect would be fully captured computationally an increased length cross wind was simulated.

Any computational investigation of this phenomena would require the boundary conditions to change during the simulation to mimic the developing cross wind inlet condition in the experimental apparatus. The exact boundary conditions are described below but are based on the experimental open jet wind tunnel apparatus with a blockage to represent the aerodynamic model, a steady inlet to represent the main jet and a step input inlet condition to represent the cross wind jet.

8.2.3 Detail of Boundary Conditions

The boundary conditions are shown by figure 8.1 and match closely to those that exist experimentally.

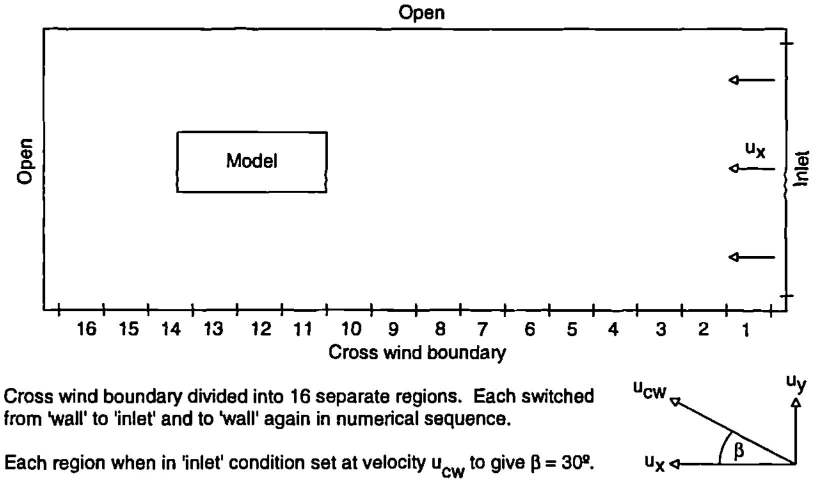

Fig. 8.1 - Simulation boundary conditions.

The inlet boundary directly up stream of the model represents the main jet (see figure 3.2) and provides the axial flow velocity, u_X, with respect to the model which is represented by a blockage. The top and left side boundaries of figure 8.1 are open to atmosphere as required in modelling an open jet wind tunnel. The lower side boundary of figure 8.1 is of the most interest. The experimental apparatus subjects a model to a transient cross wind pulse by moving an aperture at velocity u_X across a duct exit of an independent air source inclined at 30° to the main jet (see figure 3.2). This is mimicked by this boundary condition which changes with time. Initially the whole lower side boundary is a wall. At a specific time point region '1' is transformed to an inlet with air velocity of u_{CW}, shown by figure 8.1. At a following time point, dictated by u_X and the distance between the centres of regions '1' and '2', region '2' is transformed into another inlet. This process continues with time until all the sixteen regions are inlets. After a prescribed time delay the process is reversed. Region '1' is returned to its original wall boundary condition followed by region '2' and so on by the same inlet transformation timed sequence until all sixteen have been returned to the wall boundary condition. This time dependent boundary has been schematically illustrated in figure 8.2.

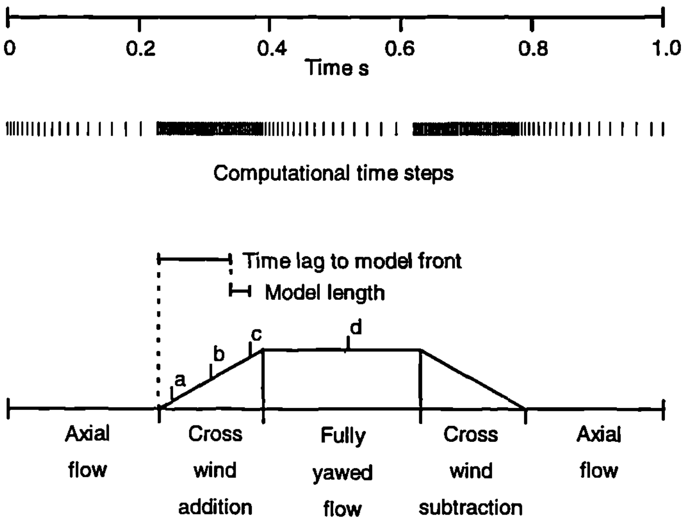

Fig. 8.2 - Schematic description of time dependent boundary condition.

Figure 8.2 shows that the transient flow conditions are modelled over a period of one second. The computational time step density can be seen to be concentrated after points of boundary change. The model is initially subjected to axial flow conditions. The lower side boundary is then altered to simulate the model passing into, through then out of a section of yawed air flow. The cross wind addition and subtraction zones indicate the sequential transformation of regions '1' to '16' from wall to inlet then inlet to wall respectively, with the local height of the cross wind addition ramp proportional to the number of the 16 regions that have been sequentially opened. The model time scale length is indicated along with the down stream time scale distance to the model leading edge. Points 'a' to 'd' are referred to in section 8.3.1.

The grid used for the simulation is shown by figure 8.3. The model has dimensions of 0.5 m by 0.2m (40 by 16 cells) and the over all grid size was 124 by 52 cells. The number of transient simulation computational time steps was 151 in the distribution shown by figure 8.2. However before the transient simulation was undertaken a settled time averaged flow field for the entire simulation domain was developed (see figure 8.1), without the action of the lower side inlets, to be used as initial conditions for the transient simulation. During the transient simulation the results were recorded every third time step. A software default k-ε turbulence model was used for the simulation and all inlet conditions had a turbulence intensity of 2%. The simulation Reynolds number based on model length was 5.0×10^5.

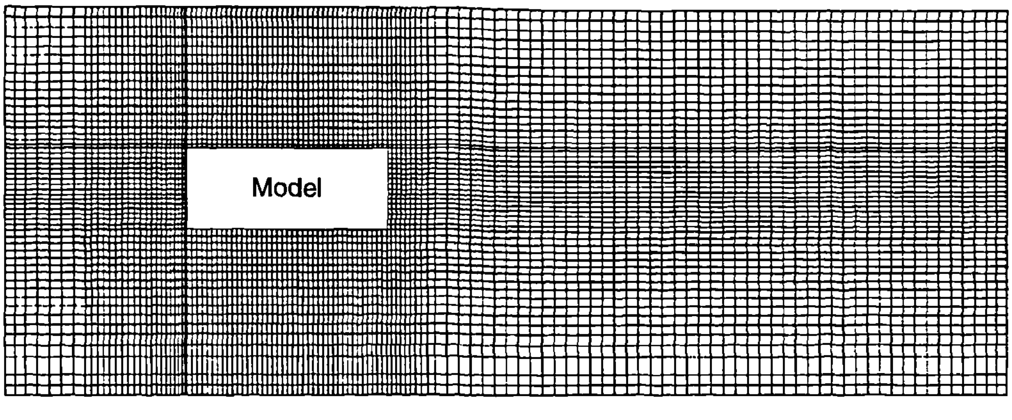

Fig. 8.3 - Simulation grid.

The computational simulation differs from the experimental apparatus by way of Reynolds number, model shape, exact model position and relative model length of the cross flow duration in the working section. These differences exist because the computational simulation was undertaken prior to the full design of the experimental apparatus and so approximations to the expected experimental parameters were utilised. An additional difference is that the time dependent lower side boundary in the computational investigation moves from wall to inlet to wall where as experimentally the wall condition, provided by honeycomb (see figure 4.4), was more porous. The software however did not allow porous boundaries to fluctuate in the desired manner and the wall boundary selection was therefore a compromise.

8.2.4 Development of Boundary Conditions

The final spatial resolution of the boundary conditions was determined by doubling the resolution until no significant change in the transient surface pressure distribution on the model was detected. The model was initially a 10 by 4 cell blockage and evolved to 40 by 16 cells. The rest of the grid resolution evolved accordingly. The number of regions on the lower side boundary (see figure 8.1) was initially eight and evolved through sixteen to thirty two - the latter increase had no effect allowing sixteen regions to be the final selection. The temporal resolution was also increased with each of the grid refinements and again a point was selected where the increase had no further effect on the model surface pressures.

8.3 Results of Investigation

.3.1 Transient Velocity Predictions

The following plots show velocity vector 'snap shots' of flow round the model at the time points labelled 'a' to 'd' in figure 8.3. At point 'a' the model is effectively in axial flow conditions, point 'b' signifies the leading edge of the model about to enter fully yawed flow, point 'c' is a short time after the trailing of the model has passed into fully yawed flow (i.e. model fully enveloped in yawed flow) and at point 'd' the yawed flow around the model has fully developed.

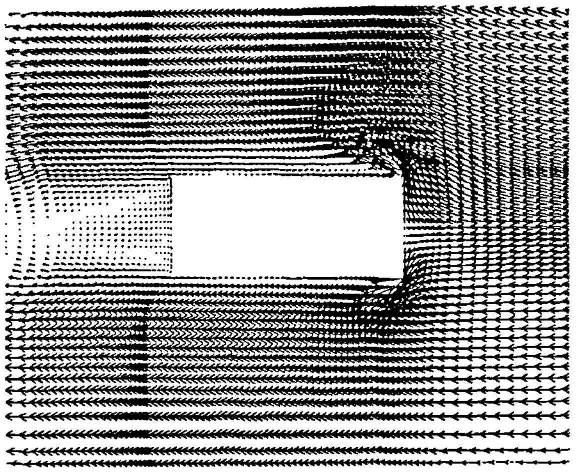

Fig. 8.4a - Local velocity vectors to model at time point 'a'.

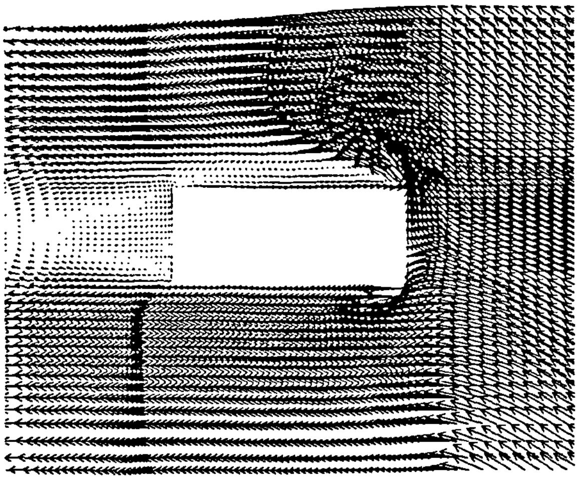

Fig. 8.4b - Local velocity vectors to model at time point 'b'.

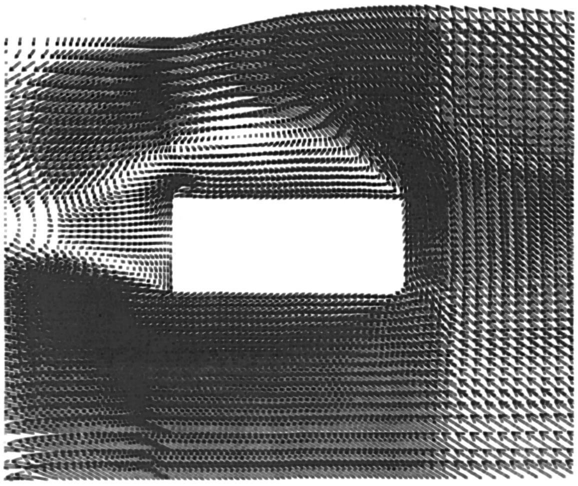

Fig. 8.4c - Local velocity vectors to model at time point 'c'.

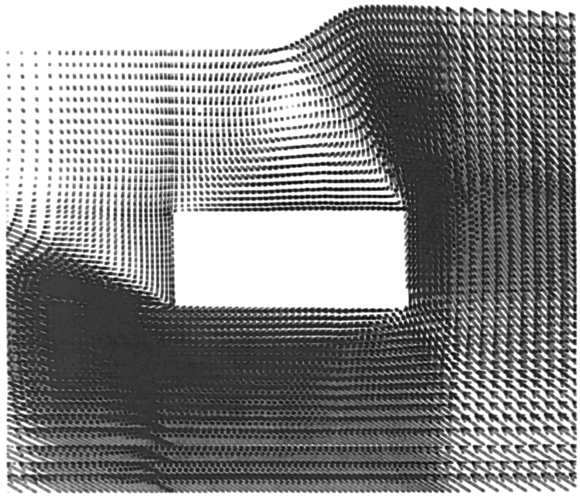

Fig. 8.4d - Local velocity vectors to model at time point 'd'.

8.3.2 Transient Surface Pressure Predictions

Side Pressure

Integrating the surface pressures developed at each cell down each side of the model surface at any instant during the transient simulation allows the effective side pressure to be calculated and is shown in figure 8.5. The front and rear surfaces of the model have no lateral component of area so this result is directly proportional to side force. The traces in figure 8.5 divide the model into windward (nearest the lower side boundary - see figure 8.1) and leeward (farthest from the lower side boundary) sides and a combined net response.

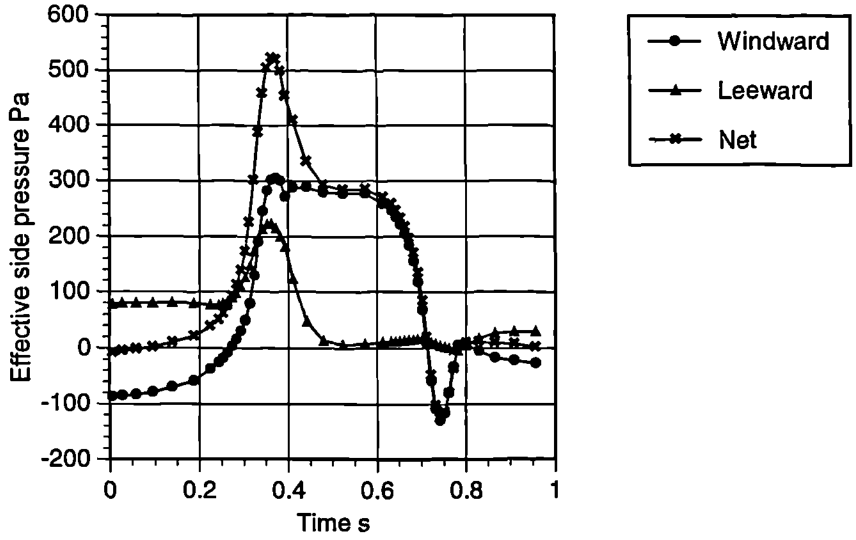

Fig. 8.5 - Transient model side pressure predictions.

Yawing Pressure

Integrating the product of surface pressure at each cell and the perpendicular distance of that cell from the model centroid along each model face at any instant allows the effective pressure based yawing moment to be calculated and is shown in figure 8.6. The traces in figure 8.6 divide the model into windward and leeward sides and also front and rear model faces as well as the net response of all four combined. The net response is directly proportional to the yawing moment induced on the model.

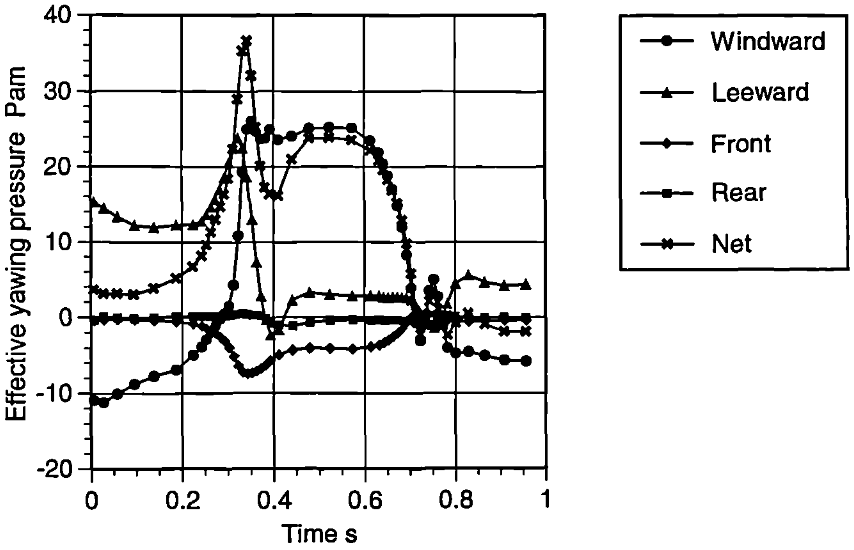

Fig. 8.6 - Transient model yawing pressure predictions.

9.0 Full Scale Vehicle Cross Wind Investigation

9.1 Introduction

As part of the full research programme a project in conjunction with the Rover Group was undertaken into the time averaged cross wind sensitivity of the current Range Rover vehicle model. The cross wind investigation methods used for this project are currently the principle method of examining the cross wind sensitivity of a particular vehicle (see section 2.2.1). The investigation was undertaken over a three day period in the full scale wind tunnel at the Motor Industry Research Association (M.I.R.A.) proving ground. This investigation was a discrete component of the full research programme and not directly related to the development of the new transient cross wind simulation technique. For clarity this chapter therefore presents, discusses and draws conclusions from this discrete investigation.

9.2 Investigation Details

The time averaged cross wind sensitivity of a vehicle may be assessed by measuring the developed aerodynamic forces on the vehicle over a range of fixed yawed conditions in a wind tunnel. This provides details of how the various force and moment coefficients behave with yaw. However in order to understand more fully the yawed air flow over specific regions on the vehicle it is necessary to generate a full pressure map of the body surface.

This wind tunnel based cross wind simulation however does not exactly mimic a natural cross wind. The turbulence level of a natural air flow is such that the air velocity may instantaneously double or drop to zero [35] compared to a turbulence intensity of 0.8% for this wind tunnel facility. In addition the boundary layer profile associated with a natural air flow is incorrectly simulated (see figure 2.5) as a wind tunnel facility subjects a vehicle to a uniform flow velocity over the full height of the tunnel working section. However the results from such an investigation are still useful to an aerodynamicist.

9.2.1 Investigation Specification

Wind Tunnel Facility

The wind tunnel used was the M.I.R.A. Full Size Wind Tunnel whose specification is outlined by table 9.1.

Test Section	Length	15.24m
	Width	7.94m
	Height	4.42m
Air Flow	Maximum air speed	36m/s (80mph)
	Turbulence intensity	0.8%
	Floor displacement thickness	17mm
	Normal air speed	27.8m/s (62mph)

Table 9.1 - Specification of M.I.R.A. full scale wind tunnel.

The vehicle was mounted on small floor pads connected to an under floor six component balance capable of yawing to ±180°. The force coefficients showed no Reynolds number dependence (see table 9.6) between the normal air speed and the maximum tunnel air speed of 36m/s. This allowed the simulation to be undertaken at the normal air speed of 27.8m/s. The corresponding Reynolds numbers, based on vehicle wheel base, were 6.5×10^{6} and 5.0×10^{6} respectively and as such no Reynolds number effects would be expected due to the bluff body nature of road vehicles (see section 2.3).

The surface pressure tappings consisted of small metal discs (0.5mm thick and ~20mm diameter) in the centre of which was a pressure tapping connected to a tube as shown by figure 9.1.

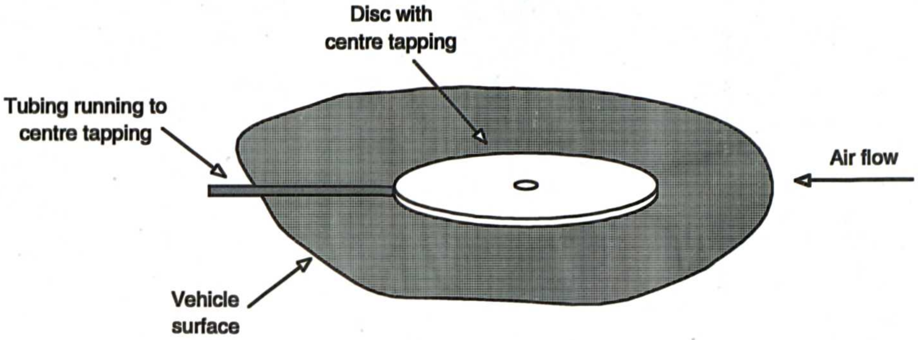

Fig. 9.1 - Vehicle surface pressure tapping.

The tapping discs were taped flush to the vehicle surface with the tube running down stream along the vehicle surface. The tappings were connected to a dual Scanivalve pressure scanning system capable of reading the pressures from the 70 available tappings sequentially. The tube length (~4m) from the Scanivalve was sufficient to allow each tapping to be placed onto separate areas of the vehicle surface.

Test Vehicle

The vehicle was a late prototype of the Range Rover 38a as shown by figure 9.2.

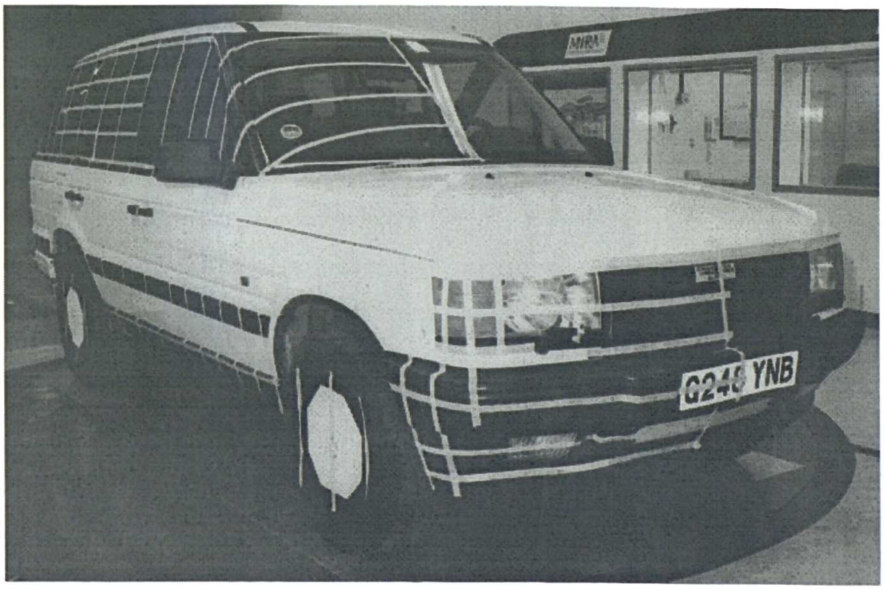

Fig. 9.2 - Range Rover vehicle.

The actual model was a '4.6 V8i EVR'. The vehicle possessed a front spoiler, number plates, door mirrors, bumper integral fog lamp and size 255 tyres. For the pressure survey the mud flaps and front wipers were removed and flush wheel trims were fitted over the alloy wheels. In addition the front grill was blanked off so that the results of the surface pressure survey would not be corrupted by any unmeasured internal flow (used for cooling in the road condition). The other modifications were to allow the pressure tappings to be fitted to the flat surfaces of the vehicle more easily (i.e. the windscreen without the wipers) and to provide new flat surfaces to position the tappings (i.e. the flush wheel trims).

9.2.2 Method of Investigation

With the vehicle shape simplified as detailed previously the vehicle surface was divided into seven arbitrary regions. A group of 10 tappings was allocated to each region. Over six wind tunnel runs each group of tappings was moved to a new prescribed row of points in that region and taped in position. In this way the pressure tappings ultimately covered the full surface of the car. The relocation of the pressure tappings between runs was facilitated by initially marking a grid with tape over the vehicle surface, which may be partially seen in figure 9.2, which allowed accurate and fast relocation of the tappings to each grid node. The grid was concentrated around regions of suspected high pressure gradient. The grid was only marked to one side of the vehicle centre line as the vehicle could be yawed either way from the straight on position allowing the marked side to gather both leeward and windward surface pressure data in yawed flow. By use of this symmetry the number of pressure tapping points was reduced from a potential ~800 over the full vehicle surface to ~400 over only half the vehicle. For each wind tunnel run the vehicle was rotated to the following yaw angles in sequence: 0°, -10°, -20°, 0°, +10° and +20°. This method resulted in a full body pressure map at these yaw angle magnitudes.

Once the pressure readings had been taken the vehicle was cleared of all remaining pressure tappings and the grid but the shape simplifications stayed in place. The force and moment coefficients were then determined at various yaw angles by the use of the six component under floor balance. For only the full shape simplification the vehicle was yawed to ±35°, in 5° steps, so as to establish any non-linear relationships (e.g. maxima) in the coefficient response to yaw. Typically the square back vehicle configuration displays non-linear relationships over 20° yaw. The simplifications were then removed in stages, measuring the coefficients up to ±20° yaw in 5° steps at each stage, so as to return gradually to the road going vehicle trim level. The representative length for the coefficient values was taken as the vehicle wheel base and the moment centre for the vehicle was taken about the centre of wheel base and track at ground level.

9.3 Results of Investigation

9.3.1 Force and Moment Coefficients

Full Shape Simplification

The numerical results of the force and moment coefficients for the full shape simplification are presented by table 9.2 together with their graphical representation by figures 9.3 to 9.8.

Yaw angle	Cd	Cl f	Cl r	Cs	Xcp
0°	0.379	-0.003	0.029	-0.004	0.0
5°	0.407	0.015	0.042	0.247	3.9
10°	0.441	0.069	0.082	0.501	8.3
15°	0.459	0.125	0.110	0.749	9.3
20°	0.463	0.197	0.143	0.986	10.0
25°	0.480	0.298	0.155	1.224	8.9
30°	0.499	0.326	0.108	1.486	7.6
35°	0.473	0.340	0.089	1.639	7.0

Table 9.2 - Force and moment coefficients from full shape simplification.

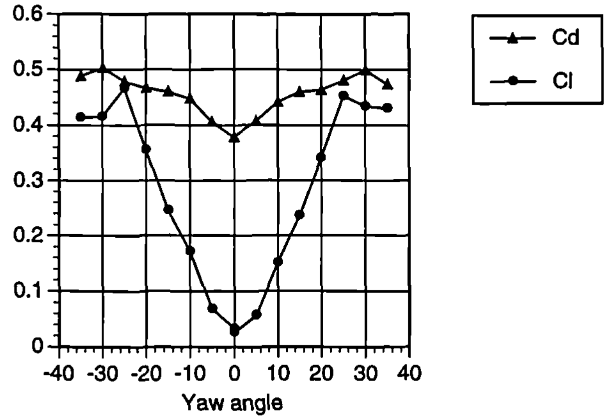

Fig. 9.3 - Drag and lift coefficients against yaw for full shape simplification.

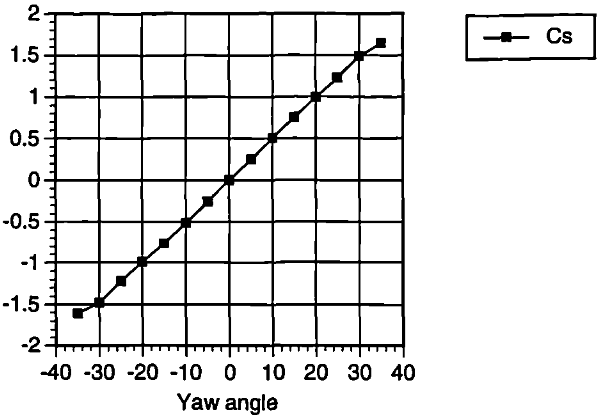

Fig. 9.4 - Side force coefficient against yaw for full shape simplification.

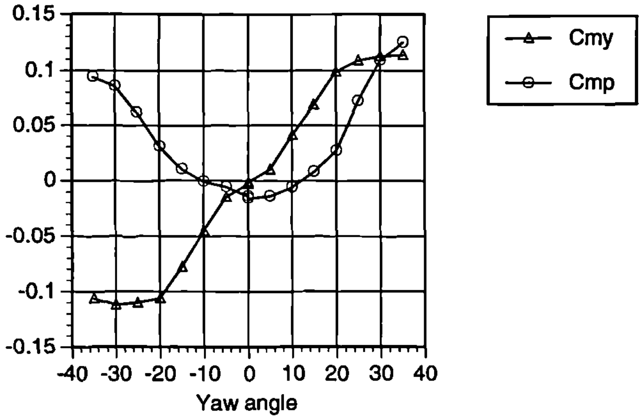

Fig. 9.5 - Yaw and pitch moment coefficients against yaw for full shape simplification.

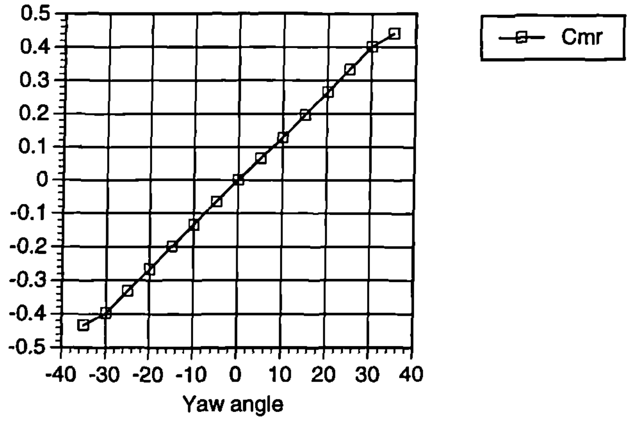

Fig. 9.6 - Roll moment coefficient against yaw for full shape simplification.

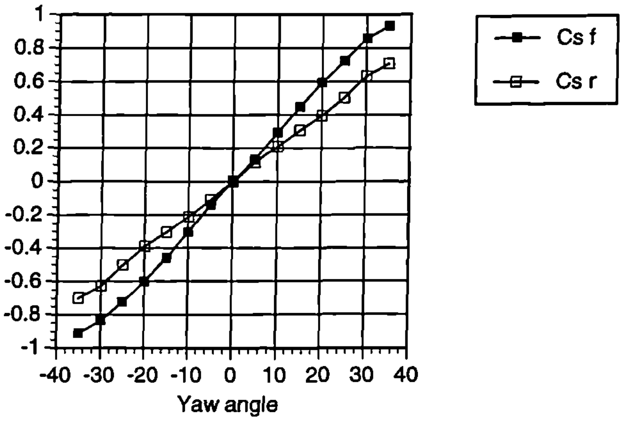

Fig. 9.7 - Front and rear side force coefficients against yaw for full shape simplification.

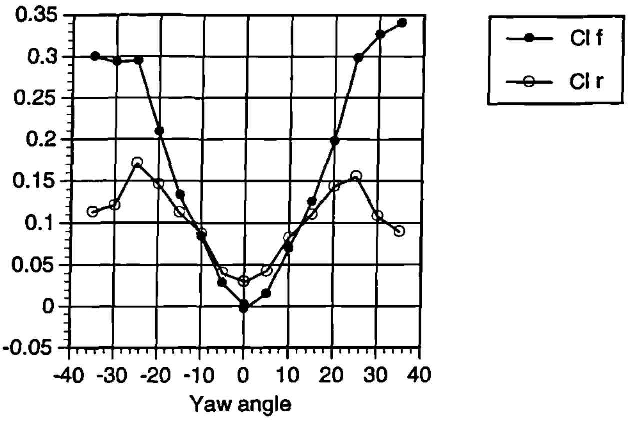

Fig. 9.8 - Front and rear lift coefficients against yaw for full shape simplification.

Flush Wheel Trims Removed

The numerical results of the force and moment coefficients after the removal of flush wheel trims from the full shape simplification are presented by table 9.3 together with their graphical representation by figures 9.9 to 910.

Yaw angle	Cd	Cl f	Cl r	Cs	Xcp
0°	0.389	0.006	0.024	-0.003	0.0
5°	0.416	0.027	0.039	0.243	3.8
10°	0.456	0.080	0.074	0.486	7.3
15°	0.476	0.145	0.103	0.738	8.8
20°	0.479	0.216	0.138	0.971	9.5

Table 9.3 - Force and moment coefficients after wheel trim removal.

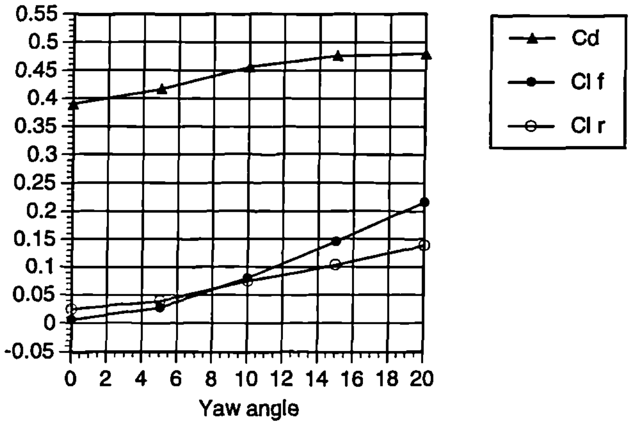

Fig. 9.9 - Drag and front & rear lift coefficients against yaw after wheel trim removal.

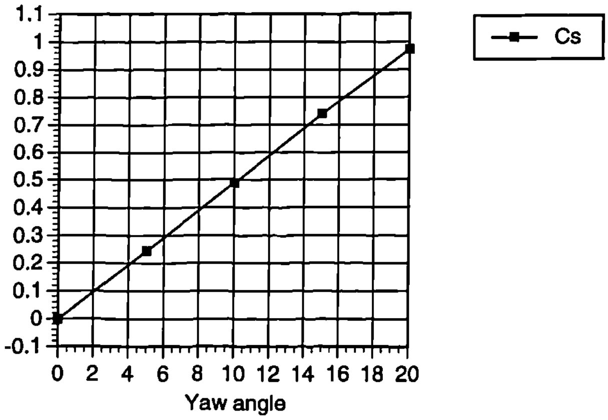

Fig. 9.10 - Side force coefficient against yaw after wheel trim removal.

Front Grill Blanking Removed

The numerical results of the force and moment coefficients after the removal of the front grill blanking and the flush wheel trims from the full shape simplification are presented by table 9.4 together with their graphical representation by figures 9.11 to 9.12.

Yaw angle	Cd	Cl f	Cl r	Cs	Xcp
0°	0.407	0.056	-0.012	-0.004	0.0
5°	0.428	0.076	0.011	0.237	7.3
10°	0.469	0.127	0.059	0.481	9.0
15°	0.493	0.192	0.086	0.729	9.9
20°	0.498	0.259	0.122	0.969	9.9

Table 9.4 - Force and moment coefficients after grill blanking removal.

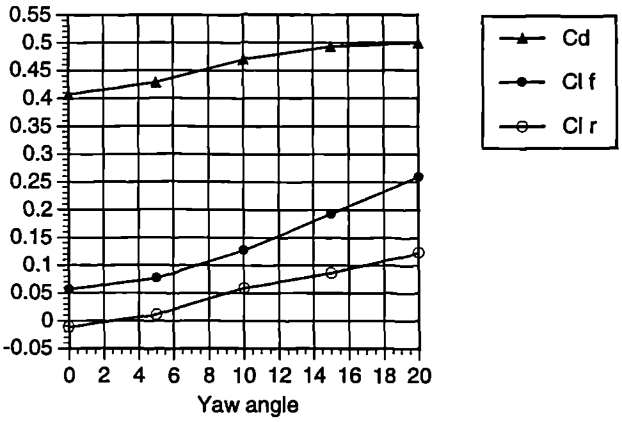

Fig. 9.11 - Drag and front & rear lift coefficients against yaw after grill blanking removal.

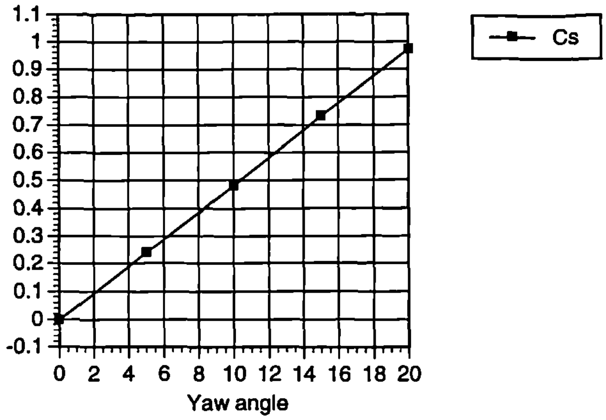

Fig. 9.12 - Side force coefficient against yaw after grill blanking removal.

Wipers and Mud Flaps Replaced

The numerical results of the force and moment coefficients after the removal of the front grill blanking and the flush wheel trims from the full shape simplification are presented by table 9.5 together with their graphical representation by figures 9.13 to 9.14.

Yaw angle	Cd	Cl f	Cl r	Cs	Xcp
0°	0.412	0.068	0.000	-0.003	0.0
5°	0.442	0.092	0.034	0.237	5.3
10°	0.486	0.142	0.067	0.471	8.0
15°	0.516	0.212	0.115	0.720	9.1
20°	0.523	0.279	0.143	0.953	9.3

Table 9.5 - Force and moment coefficients after wiper and mud flap replacement.

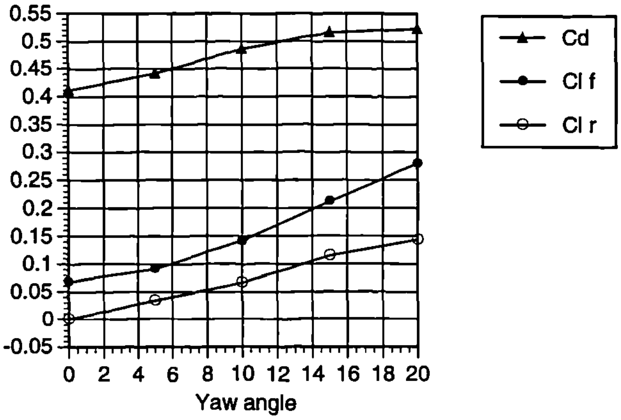

Fig. 9.13 - Drag and front & rear lift coefficients against yaw after wiper and mud flap replacement.

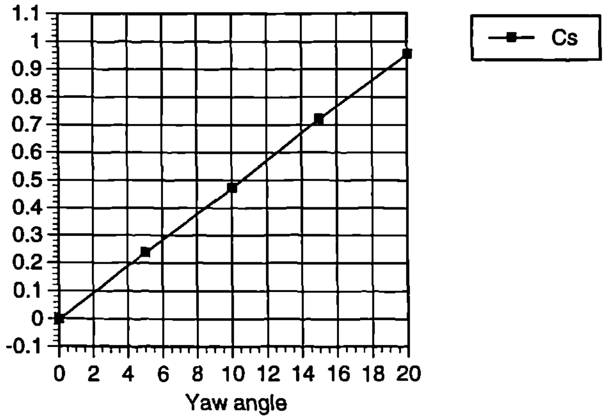

Fig. 9.14 - Side force coefficient against yaw after wiper and mud flap replacement.

Front Bib Spoiler Removed

The numerical results of the force and moment coefficients after the removal of the front bib spoiler are table 9.6.

Air speed	Yaw angle	Cd	Cl f	Cl r
27.4m/s	0°	0.427	0.112	-0.026
35.4m/s	0°	0.427	0.114	-0.027

Table 9.6 - Force and moment coefficients after removal of front bib spoiler

Summary

Tables 9.7 and 9.8 present a summary of selected data recorded over the vehicle shape alteration process at the 0° and 15° yaw conditions respectively.

Configuration change	Cd	Cl f	Cl r
Full shape simplification	0.379	-0.003	0.029
Flush wheel trims removed	0.389	0.006	0.024
Front grill blanking removed	0.407	0.056	-0.012
Wipers and mud flaps replaced	0.412	0.068	0.000
Front bib spoiler removed	0.427	0.112	-0.026

Table 9.7 - Summary of selected data for vehicle shape alteration at 0°

Configuration change	Cd	Cl f	Cl r	Cs	Xcp
Full shape simplification	0.459	0.125	0.110	0.749	9.3
Flush wheel trims removed	0.476	0.145	0.103	0.738	8.8
Front grill blanking removed	0.493	0.192	0.086	0.729	9.9
Wipers and mud flaps replaced	0.516	0.212	0.115	0.720	9.1

Table 9.8 - Summary of selected data for vehicle shape alteration at 15°.

9.3.2 Surface Pressure Survey

A full body pressure survey potentially may examine the how the vehicle surface pressures contribute to all components of aerodynamic loading induced on a vehicle. However as a preliminary level of investigation the data presented here has been configured to examine how the vehicle surface pressures contribute to only the side force and yawing moment. For this purpose the full body pressure survey data was divided into twenty one vertical sections, a to u, shown by figure 9.15. Each section spacing correlates exactly to the experimental spacing of a vertical line of pressure tapping up the side of the vehicle. As can be seen the extreme front and rear ends were not included as their lateral contribution to side force would be small. However the contribution of the extreme front and rear ends to yawing moment would be greater but still low compared to the force contribution from the vehicle sides by virtue of the small moment arm about the centroid of the front and rear ends.

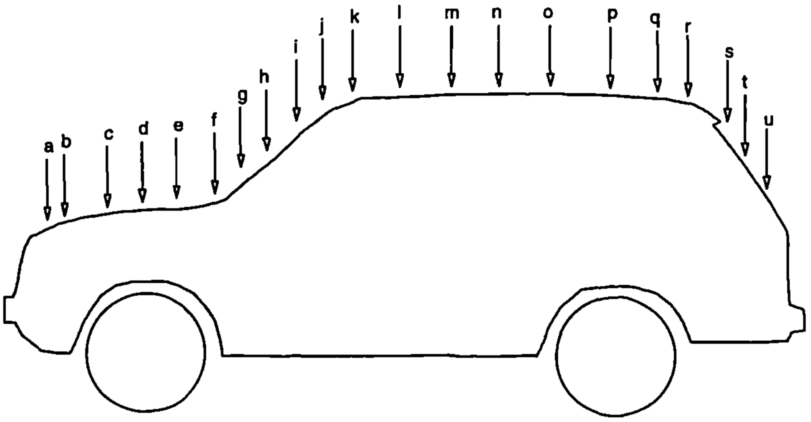

Fig. 9.15 - Vertical sections of vehicle for pressure survey.

The recorded data is presented in the form of variation of pressure coefficient, Cp, over the yaw angles tested at each of the vertical sections (see figure 9.15) plotted against vehicle height from the ground plane. Each of figures 9.16 to 9.21 shows five traces to represent the Cp distribution over the full vehicle height of a particular section for yaw angles of 0°, -10°, -20°, 0°, +0° and +20°. The negative angles represent the windward side of the vehicle and the positive angles represent the leeward side of the vehicle for this project. For example by examining the traces for -20° and +20° the full surface pressure distribution for the 20° yaw condition may be observed for a given section.

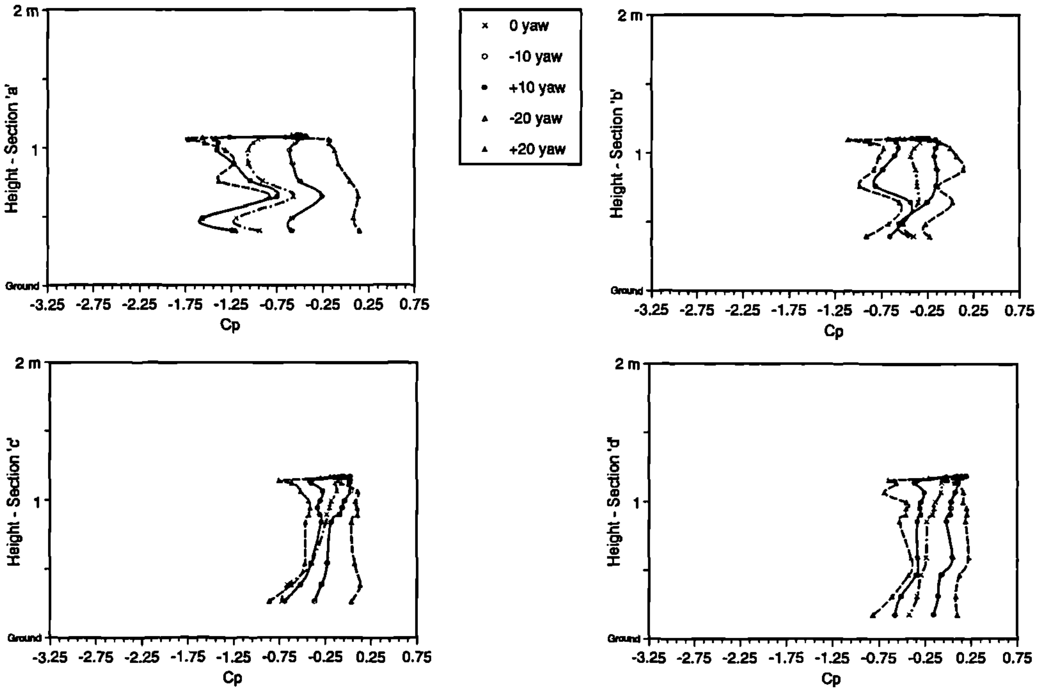

Fig. 9.16 - Variation of Cp with yaw against height for vehicle sections 'a' to 'd'.

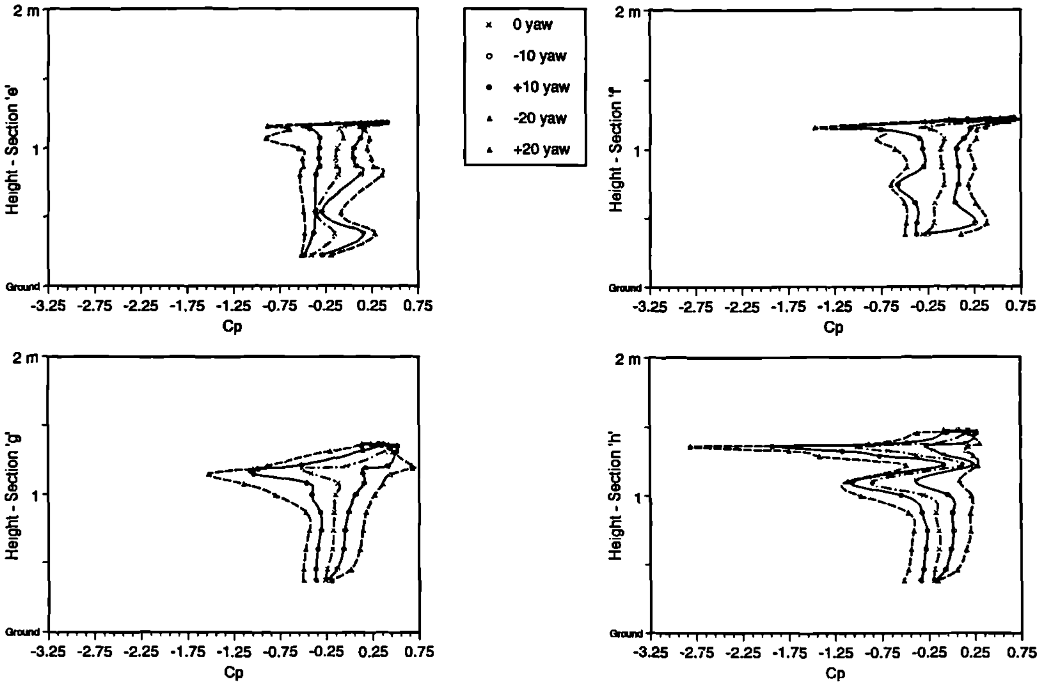

Fig. 9.17 - Variation of Cp with yaw against height for vehicle sections 'e' to 'h'.

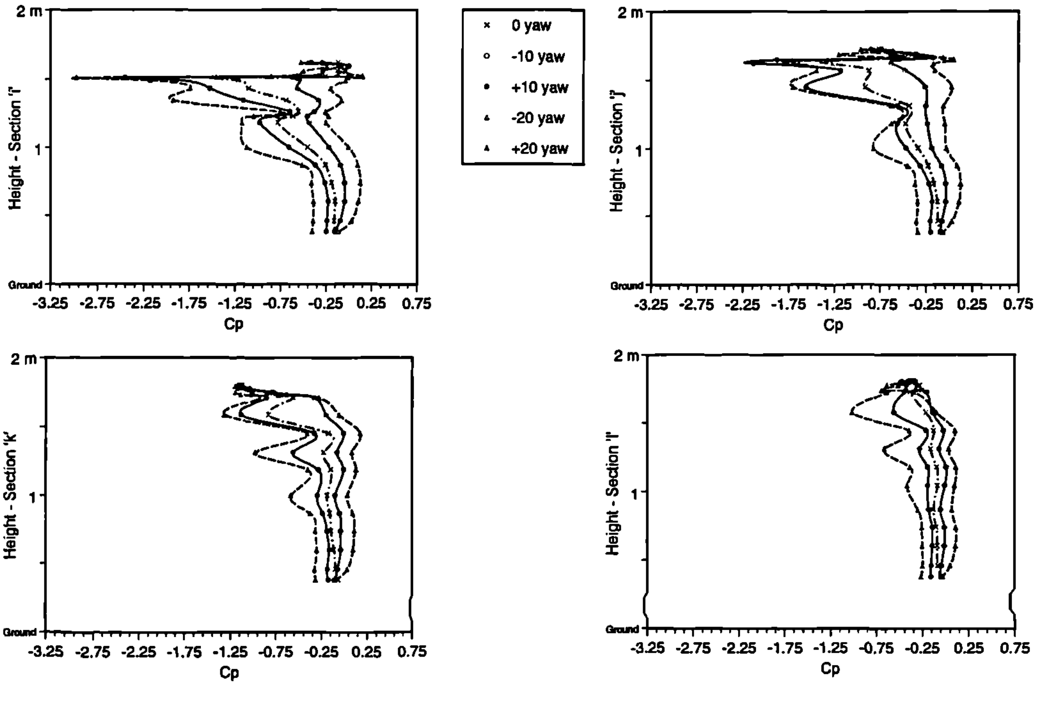

Fig. 9.18 - Variation of Cp with yaw against height for vehicle sections 'j' to 'l'.

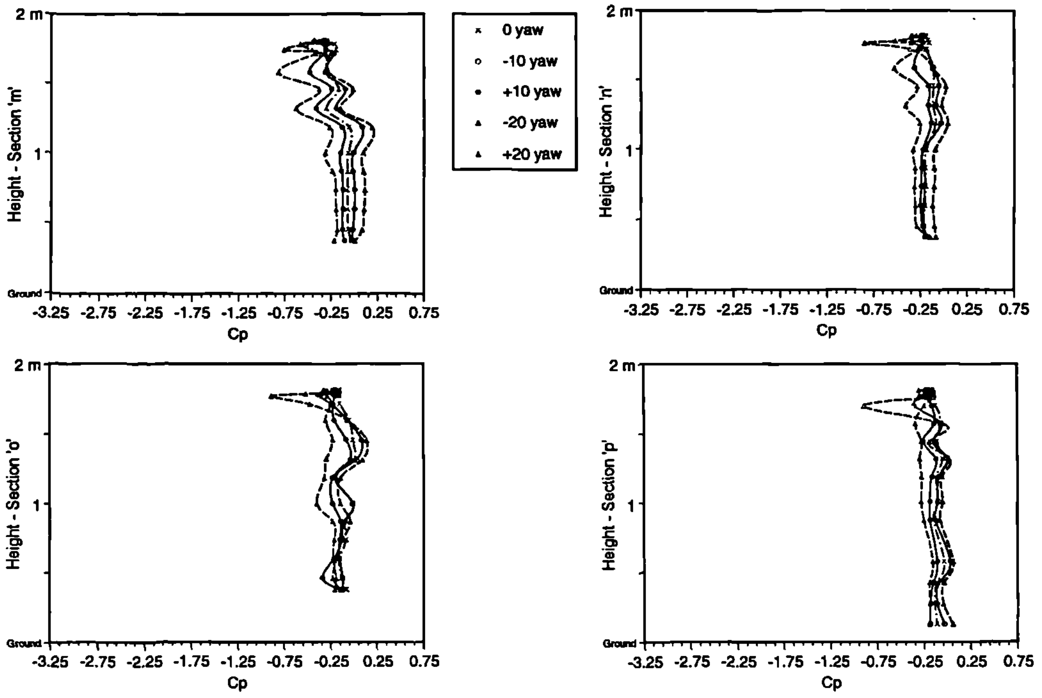

Fig. 9.19 - Variation of Cp with yaw against height for vehicle sections 'm' to 'p'.

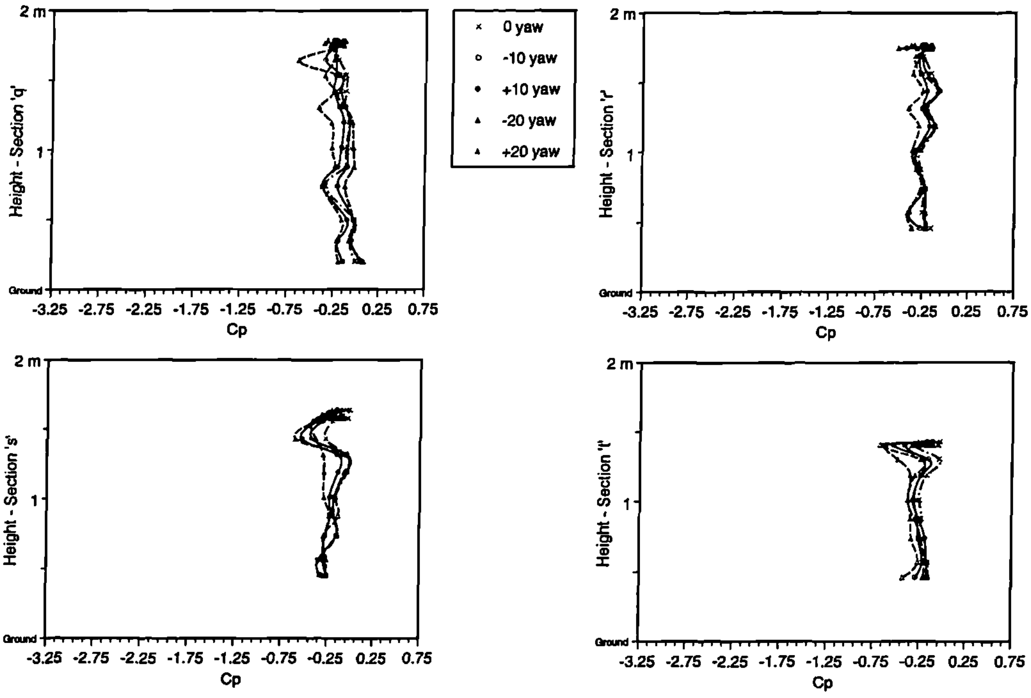

Fig. 9.20 - Variation of Cp with yaw against height for vehicle sections 'q' to 't'.

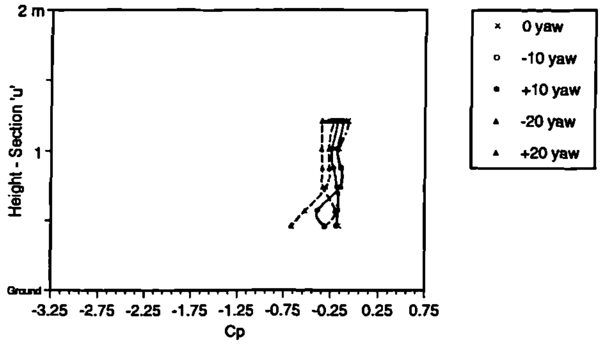

Fig. 9.21 - Variation of Cp with yaw against height for vehicle section 'u'.

9.4 Analysis and Discussion of Results

Due to the complex nature of vehicle air flows and the current level of expense and effort required to study the flow regimes developed by a full scale vehicle the industrial rôle of a vehicle aerodynamicist is often one of empirical assessment rather than rigorous scientific explanation of flow effects. Thus published data of real vehicle aerodynamic appraisals usually report the quantitative aerodynamic load changes induced by various shape configurations and not the flow effects that cause these changes. Any flow analysis is usually restricted to highly simplified flow descriptions gained from more scientific model scale studies using basic vehicle shapes (for example [9]) from which it is potentially hazardous to extrapolate explanations of the recorded aerodynamic effects due to the vastly differing vehicle geometries involved. In the context of the full research programme the focus of the interpretation of these results was directed towards the side force and yawing moment behaviour of the vehicle to the range of fixed yaw angles tested.

9.4.1 Force and Moment Coefficients

The most thorough force and moment survey was undertaken with the vehicle in its full shape simplification (see table 9.2 and figures 9.3 to 9.8) in which the vehicle was yawed up to 35°. This allowed the all the coefficients to exhibit a degree of non-linearity, with maxima occurring at 25° for lift, 30° for drag and >35° for side, pitch, roll and yaw coefficients. The traces also exhibit a slight degree of asymmetry which is most pronounced in the lift and pitch coefficients which is most probably due to front and rear under body asymmetry.

Side Force Coefficient

The change of side force with yaw angle (see figure 9.4) is almost linear over the yaw angle range tested. This is typically the case for most vehicle shapes. Increasing a vehicle yaw angle raises the effective surface pressure on the windward vehicle side as this portion of the vehicle turns to increasingly face the on coming flow. The effective surface pressure on the leeward side reduces as the air flow accelerates over what effectively becomes a suction surface of the vehicle, similar to the suction surface on an aerofoil at incidence. The contribution to side force at the front and rear axle exhibits a 65% to 35% split front to rear (see figure 9.7). The front end of a vehicle under moderate yaw conditions has a relatively large turning effect on the flow and so receives a correspondingly large aerodynamic load, despite the smaller lateral area component of the vehicle at the front end.

Lift Force Coefficient

The lift coefficient (see figure 9.3) shows an approximately linear increase with yaw angle reaching a maximum value of 0.453 at 25°. The most significant contribution to lift being provided at the front axle at large yaw angles (see figure 9.8). The front axle lift also exhibits the greatest change in coefficient value. A typical [35] square back vehicle shape shows a similar response with a maximum value attained at the same yaw angle. The differing lift coefficient induced at differing yaw angles is ultimately due to the changing effective shape presented to the air flow by the yawed vehicle. This effect is largely manifested at the front axle and so it may be assumed that the relative balance of under body to over body surface pressures changes significantly at the front end of the vehicle. The under body pressures were not recorded as so it is not known the relative lift magnitudes of the under to over body surface pressure change.

Drag Force Coefficient

The drag coefficient (see figure 9.3) shows a similar change with yaw to that shown by the lift coefficient, albeit over a smaller magnitude range. A maximum drag coefficient value of 0.499 is achieved at 30° yaw with a reduction for further increased yaw angles. A typical [45] saloon car exhibits this same trend. No data was available for a square back vehicle shape drag response to yaw. The drag of a vehicle increases with yaw by virtue of an increasing effective vehicle frontal area being presented to the on coming flow and the development of a larger area of wake flow with increasing yaw angle.

Yawing Moment Coefficient

The yawing moment coefficient (see figure 9.5) for this vehicle displays an approximately linear initial increase with yaw angle with an apparent maximum value of 0.113 attained at ~30°. A typical [46] square back vehicle exhibits a similar trend. The side force coefficient increases linearly with yaw angle but the yawing moment coefficient does not. This is due to the fact that the lateral centre of pressure of the vehicle, denoted by Xcp - table 9.2, shifts in position with yaw angle. The non-linearity exhibited by the yawing moment coefficient over that of the side force coefficient is entirely due to this effect. The centre of pressure moves forward with increasing yaw angle up to 20° by virtue of the increased turning effect on the flow by the front end of the vehicle. Beyond 20° the centre of pressure shifts backwards slightly by virtue of the increasing influence on the air flow of the rear vehicle portion.

Pitching Moment Coefficient

The pitching moment coefficient (see figure 9.5) exhibits an increase with yaw angle with no maximum reached in the range of yaw angles tested. This is also a typical [35] square back vehicle response to yaw. The pitching moment increase is a direct manifestation of the front and rear axle changes in lift coefficient shown by figure 9.8. An increasing lift coefficient at the front axle relative to the rear axle increases the vehicle pitching moment.

Rolling Moment Coefficient

The rolling moment coefficient (see figure 9.6) shows a similar behaviour to that of the side force, being almost linear over the range of yaw angles tested. This is again typical [35] of a square back vehicle configuration. Increasing the yaw angle of the vehicle in turn increases the lateral component of vehicle area presented to the flow. The lateral load on the vehicle therefore increases, which in turn results in an increase in vehicle rolling moment. Because this increase is linear it may be assumed the rolling moment centre of pressure remains at a constant position with respect to the vehicle height. This is distinct from the longitudinal position of this centre of pressure which has been demonstrated to shift in position (see table 9.2).

9.4.3 Configuration Changes

Table 9.9 shows a selected summary of the coefficient change from the full shape simplification to the replacement of the wipers and mud flaps.

Change in coefficient for configuration change from full shape simplification to replacement of wipers and mud flaps.	0° yaw	15° yaw
ΔCd	0.033	0.057
ΔCl f	0.071	0.087
ΔCl r	-0.029	0.005
ΔCs	NA	-0.029

Table 9.9 - Change in selected coefficients due to vehicle shape alteration..

The most significant magnitude change in magnitude of a coefficient at 0° yaw (table 9.9) is that exhibited by the front axle lift. The front axle lift coefficient at changes from -0.003, for the full shape simplification, to 0.112, with the bib spoiler removed (see table 9.7). The removal of a front spoiler [3] typically decelerates the front end under body flow, by virtue of the larger under body flow area, and the resultant under body pressure rise increases the lift at the front of the vehicle. The open sides to the vehicle under body mitigate this effect by the rear portion of the vehicle. At 15° yaw the magnitude of the full change to the lift coefficient is greater than that exhibited at 0° yaw (see table 9.9). Thus at yawed angles the vehicle is more lift sensitive to configuration changes than at 0° yaw.

As expected the drag increases as the shape simplifications are removed. An overall increase of 12.7% in drag coefficient, from 0.379 to 0.427 (see table 9.7), is shown from full simplification to the removal of the front bib spoiler at 0° yaw. The probable effect of the removal of the shape simplifications at the wheels, mud flaps and wipers was to increase the level of flow separation and skin friction at these points with a resulting increase in drag. The removal of a front grill blanking increases the volume of air flow through the engine compartment. The resulting increased momentum transfer from the air flow to the vehicle increased the drag force coefficient. The removal of the front bib spoiler increased the drag which is typically not the case [3]. The increase in drag at 15° yaw for the configuration changes is greater than for 0° change (see table 9.9). Thus at yawed angles the drag of the vehicle is more sensitive to configuration changes than at 0° yaw.

The value of side force coefficient is reduced by 3.9% from 0.749 to 0.720 (see table 9.8) at 15° as the shape simplifications are removed. Each shape simplification had a similar magnitude reduction in side force. Compared to drag the side force exhibits a lower percentage change over the configuration changes. But as the magnitude of the side force coefficient is larger the actual change in coefficient is similar.

9.4.3 Surface Pressure Survey

From the plots of Cp versus vehicle height (figures 9.16 to 9.21) it is possible to examine to what level different sections of the vehicle surface contribute to the side force under yawed conditions. The vehicle sections that contribute significantly are those with the greater leeward to windward difference of Cp value with yaw angle. This is manifested by a greater spread of the pressure coefficient traces by a given point on the vehicle surface. The side force contribution is thus significant at the forward sections of the vehicle (see figures 9.16 to 9.18 for vehicle sections 'a' to 'l') and has greatly reduced from vehicle section 'm' onwards towards the rear of the vehicle (see figures 9.19 to 9.21 for vehicle sections 'm' to 'u'). At these vehicle rear sections the side force contribution exhibited almost entirely at the highest sections of the vehicle body, especially approaching the upper portion of the side windows. The front sections exhibit both the most significant change of Cp with yaw and also the greatest values of negative Cp, most notably at sections 'h', 'i' and 'j' - at the start of the A-pillar (see figures 9.17 and 9.18). In order to quantify the contribution to the side force of each vehicle section the Cp values over the area of each section may be integrated directly to yield a force term (pressure coefficient multiplied by vehicle section height and section width). The height of each section was taken as the vertical distance between the lowest and highest vehicle point at each section nominal centre line, indicated by the markers in figure 9.15. The width of each section was taken as the total horizontal distance either side of each section centre line to the half way point between adjacent section centre lines. The integration was undertaken using the trapezium method. The results have been normalised relative to the largest force term calculated which transpired to be a negative suction force which was set at a value of -1. The results of this are shown below by figure 9.22.

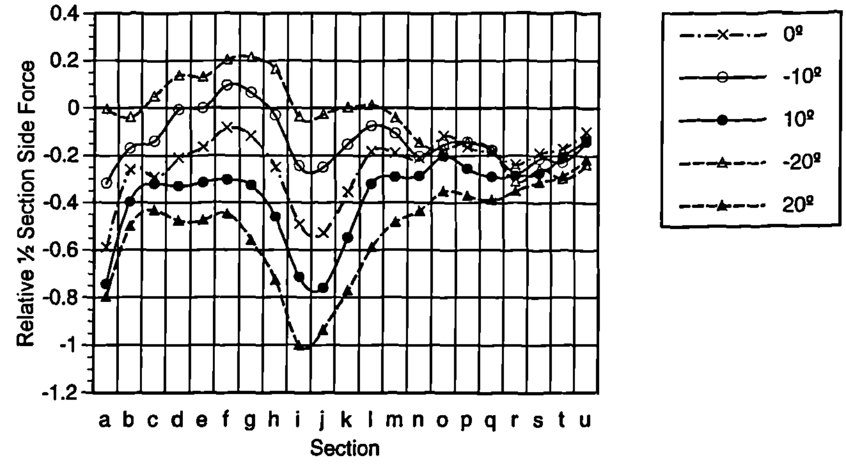

Fig. 9.22 - Relative contribution to side force against vehicle section.

Each trace in figure 9.22 corresponds to a particular yaw angle. For the magnitude of the force at a given yaw the difference of the windward and leeward lines corresponding to that angle must be obtained. Figure 9.23 shows this result and it can be seen that the A-pillar region of the vehicle (sections 'g' to 'j') produced the most significant contribution to side force with a additional significant contribution at the front end of the vehicle.

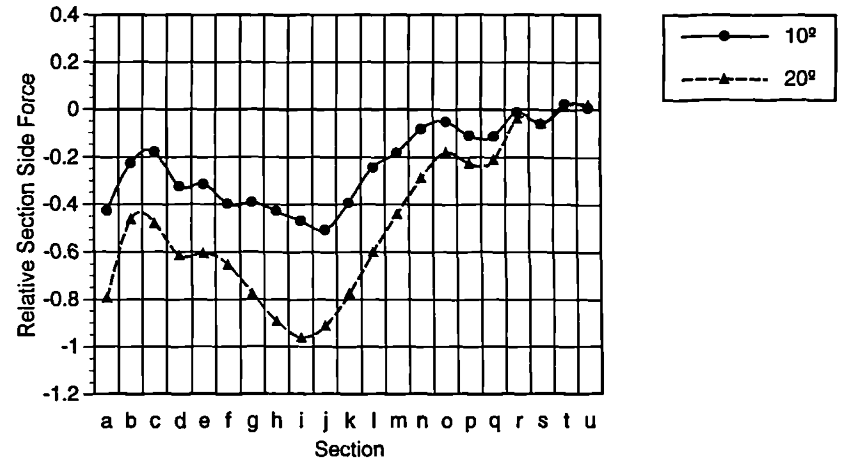

Fig. 9.23 - Net relative contribution to side force against vehicle section.

However this is an approximation based only on Cp values (i.e. no skin friction) and ignoring the extreme front and rear ends of the vehicle. The contribution of these effects will be small, especially the skin friction, whilst the lateral load component at the vehicle front and rear ends increases with yaw angle.

The aerodynamic force term is a function of both Cp and section area. The condition of the air flow round the vehicle can be more thoroughly interpreted by calculating an effective Cp value for each vehicle section. Dividing the force term displayed by figure 9.22 by the area of each section yields this mean effective Cp value. The mean effective Cp value is one that if present over the entire vehicle section would produce the same side force as the real non-uniform Cp value and is shown by figure 9.24.

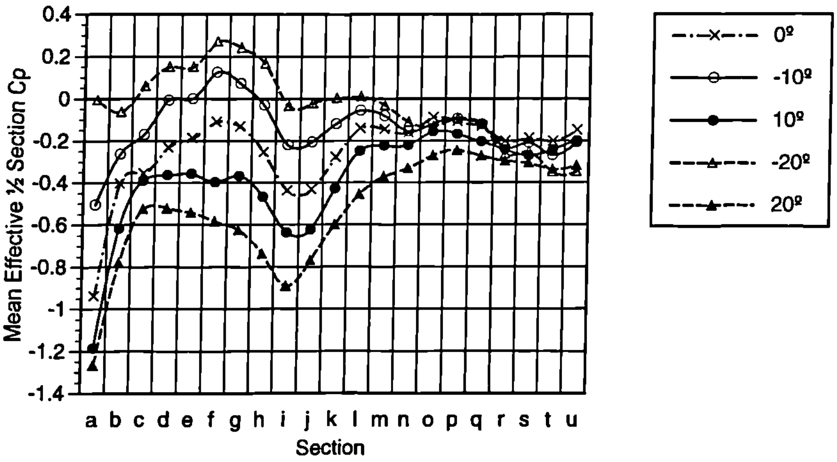

Fig. 9.24- Mean effective Cp value against vehicle section.

Although the zone around the A-pillar makes the greatest contribution to the side force it is the extreme front end of the vehicle that demonstrates the largest negative effective Cp. The Cp at this section ('a') is more uniformly negative over the vehicle height (see figure 9.16) than section 'i' which experiences greater but more localised negative Cp values (see figure 9.18).

A comparison of the percentage contribution to side force for each yaw angle based on integrating the Cp values over the vehicle section area is shown by figure 9.25.

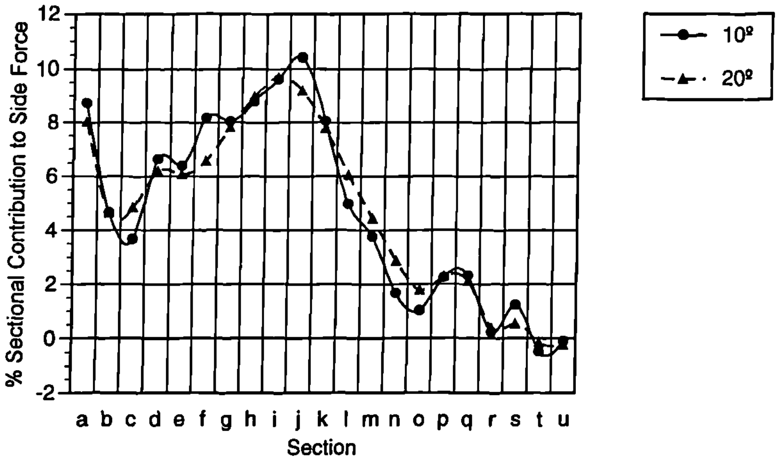

Fig. 9.25 - Percentage contribution to side force with yaw against vehicle section.

Figure 9.25 shows that the air flow over the vehicle at the two yaw angles produces largely the same relative effect on side force. This is borne out by the raw Cp versus vehicle height data (figures 9.16 to 9.21) which show broadly the same shape of trace over the yaw range. Again it can be seen that the A-pillar are the most dominant at both yaw angles with much lower contributions achieved toward the rear of the vehicle.

Using the side force data shown previously it is also possible to perform a similar analysis for the yawing moment using the moment arm distance of each of the sections from the moment centre. The moment reference centre was taken as the centre of track and wheel base in the ground plane of the wind tunnel. It is more representative from a vehicle handling view point to use the vehicle centre of gravity as the moment centre. For this particular vehicle however the centre of gravity was 109mm (4.0% of the wheel base length) forward of the reference centre and so no moment recalculation was undertaken. The values were again normalised to the maximum value of moment calculated which transpired to be a suction induced moment and was set at a value of -1. These results are shown by figure 9.26.

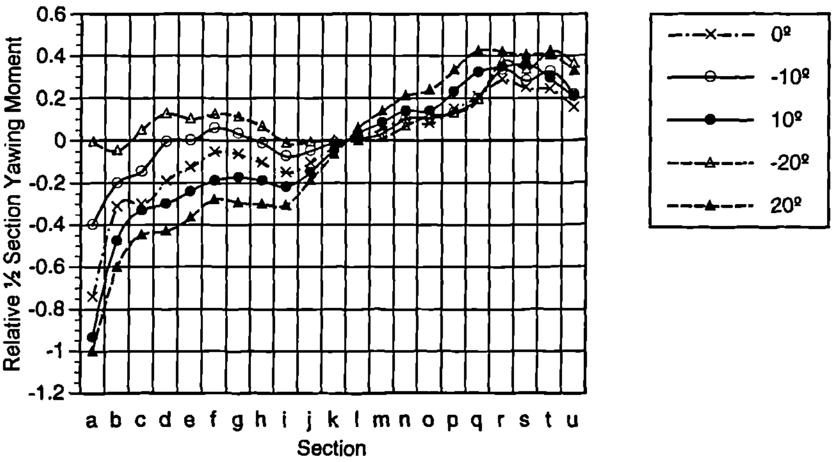

Fig. 9.26 - Relative contribution to yawing moment against vehicle section.

Vehicle sections far from the moment centre, for example vehicle section 'a', have a larger moment arm and thus contribute significantly to the total moment. This is especially shown at the extreme front section of the vehicle which not only has a significant side force contribution (~8½% - see figure 9.25) but by virtue of its moment arm has the most significant contribution to yawing moment.

Again it is the difference between the leeward and windward values for the same yaw angle which give the magnitude of the yawing moment contribution. The same reference moment was used and the result is shown by figure 9.27.

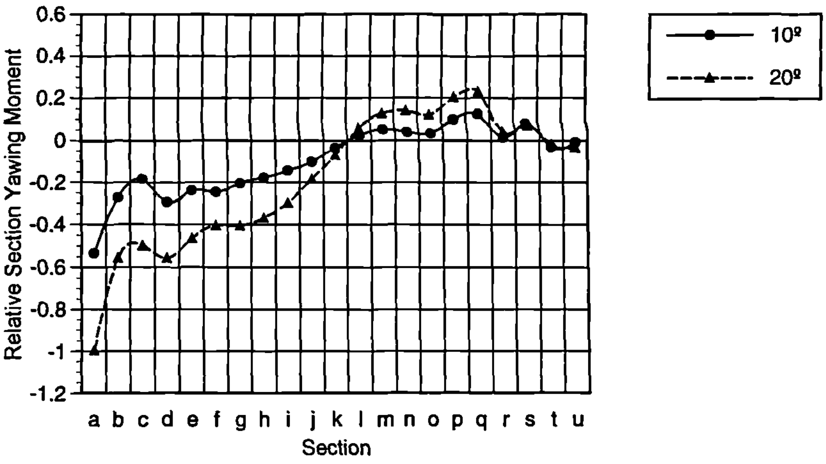

Fig. 9.27 - Net relative contribution to yawing moment against vehicle section.

Figure 9.27 clearly shows that section 'a' of the vehicle has the most significant yawing moment contribution. It should also be noted that the A-pillar region which was so dominant in side force has only a small contribution to yawing moment as its moment arm is small.

The percentage contribution to the yawing moment for the two tested angles was calculated and is shown by figure 9.28.

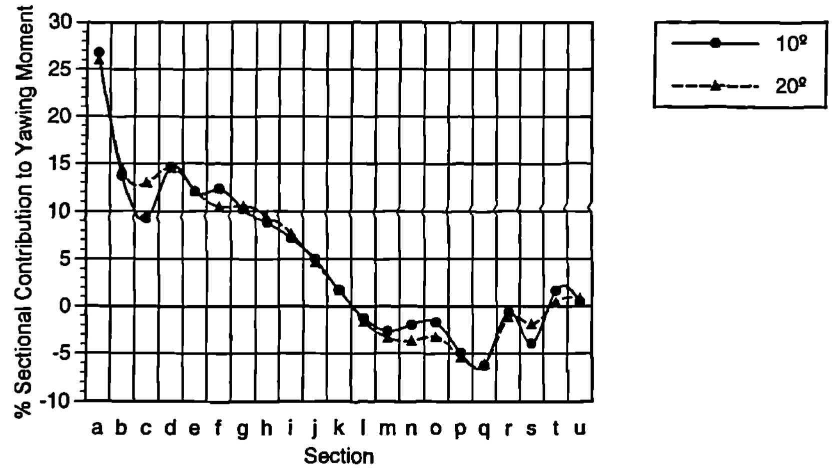

Fig. 9.28 - Percentage contribution to yawing moment with yaw against vehicle section.

Figure 9.28 shows that at both yaw angles tested the relative contribution to yawing moment at each vehicle section is very similar. The extreme rear of the vehicle, despite the large moment arm, exhibits only a low yawing moment contribution. The plots of Cp versus vehicle height illustrate this by the leeward and windward sides at the rear of the vehicle having very similar low negative Cp values at all the yaw angles tested (see figures 9.16 to 9.21).

Although the direct force measurements clearly demonstrate that overall effect of side force versus yaw angle is linear there are certain sections where the local contribution is non-linear. This is especially true of vehicle sections 'c', 'f' ,'j' ,'l' ,'n' & 's' (see figure 9.25). For the yawing moment the sections are 'c', 'f', 'n' ,'o' ,'s' & 't' (see figure 9.28). In these sections at 20° the Cp value exhibits a relatively large negative *windward* value at the top of the vehicle body where as the trend from the 0° and 10° values would suggest a less negative Cp value. This is shown by the plots of Cp versus vehicle height by figures 9.16 to 9.21.

9.5 Conclusions

9.5.1 Force and Moment Coefficients

The overall trends of the coefficients with yaw follow those of a standard vehicle square back configuration. The configuration changes are most significant in changing the front axle lift and overall drag coefficient (ΔCl f = 0.071, ΔCd = 0.033 at 0° with the bib spoiler in position). The results also suggest that the vehicle is more sensitive to configuration changes at yawed angles than at the zero yaw condition (ΔCl f = 0.087, ΔCd = 0.057 at 15° with the bib spoiler in position).

9.5.2 Surface Pressure Survey

The most dominant effects toward side force occur primarily at the A-pillar region and also at the extreme front end of the vehicle. The air flow however produces a larger suction effect at the front end which is disguised by a smaller vehicle height to that of the A-pillar.

The front end produces a very significant yawing moment contribution by virtue of the large moment arm involved. The A-pillar has only a small contribution because of its small distance from the moment centre. However a different position of moment centre would produce a different set of contributions.

The forces on the vehicle are produced predominately by suction pressures. The only positive pressures occur at the front end of the vehicle at the windward angles. After the mid section of the vehicle only negative pressures are produced at the maximum windward angle tested (20°).

After the mid section of the vehicle the contribution to aerodynamic side force with yaw occurs mainly at the higher surfaces of the vehicle at each section.

10.0 Overview and Discussion of Results

10.1 Working Section Investigation

10.1.1 Time Averaged Behaviour

Figures 7.3a and 7.3b show the results of moving the aperture with respect to the duct whilst keeping the probe in a fixed position. This mimics the exact movement of the respective components of the apparatus during an experimental run. The resultant velocities and yaw angle are quite uniform when the aperture was exhausting evenly either side of the probe position. As the relative position becomes closer to the leading and trailing edges of the aperture (-0.5 and +0.5) the traces start to decay indicating entrained areas of air flow in the shear layer transition region between the cross wind jet and bulk air. The magnitude of the velocity components increases slightly as the aperture position moves in the down stream direction (positive x axis). In addition to this there is a clear difference between the two cut off regions of the jet at either edge of the uniform portion of the traces. With the aperture up stream relative to the probe (negative x axis) the velocity profile drops gradually and is generally lower in magnitude when compared to the aperture down stream region which exhibits a near uniform velocity up to the extreme edge of the jet (+0.5 x axis). This suggests that within the cross wind duct (see figure 3.4) there is a greater mass flow of air naturally present toward the extreme tip of the duct system.

This is supported on examining figures 7.3c and 7.3d. These traces were gained by keeping the aperture stationary at a central position at the duct exit and traversing the probe in an axial direction in the working section along the tunnel centre line. The traces again confirm a stronger flow regime emerging from the trailing edge of the aperture by the clear cut off region to the flow at the right hand trace edges and a more gradual cut off region at the left hand trace edges. Figure 7.3d also displays an increasing yaw angle as the probe position moves down stream relative to the aperture. Figures 7.3c and 7.3d exhibit less uniform velocity profiles than figures 7.3a and 7.3d. This is probably due to slight wake structures present within the flow due to the honeycomb arrangement at the cross duct exit (see figure 4.4). With the probe stationary relative to the duct (figures 7.3a and 7.3b) the velocity readings would be from the same relative position in the wake structure where as with the probe moving relative to the duct (figures 7.3c and 7.3d) the probe would traverse through different points in the wake structure causing the observed uneven velocity fluctuations superimposed on the general trend in the velocity profile.

As the probe was positioned at locations outside the -0.5 to +0.5 relative position the air flow reduced in velocity which allowed any vortices in the shear layer to induce large flow angles at the probe tip. Some of these angles inevitably moved out of the calibration range of the five hole probe. When the calibration range was exceeded by an arbitrary 10% of the data at a given point during a sample that particular point was ignored and therefore not included in figures 7.3a to 7.3d. Thus the plotted data can be considered to have achieved an arbitrary 90% or above probe calibrated range criterion. This is not however a measure of turbulence but merely a confidence factor in the five hole probe measurements.

These results illustrate that under steady conditions a duct with a movable exit area produces a reasonably uniform exhaust over nearly the full width of the exit area. Some flow asymmetry was expected and is exhibited due to the geometry of the duct and belt system (figure 3.4).

10.1.2 Transient Response

Figures 7.4a to 7.15c show the presence of two cross wind transient pulses in the working section for each point on the survey grid (figure 7.1). The overall effect of the transients recorded is to produce two separate regions of cross flow that sweep through the working section of the wind tunnel. It is clear that within each transient the effect on the working section is in chronological sequence with reference to the relative position of the sample points. Thus a stationary observation point in the working section over a single cross wind transient is subjected to the following conditions in sequence: axial flow, leading edge of cross wind transient, fully developed cross wind, trailing edge of cross wind transient and finally axial flow. This pattern is repeated in turn at successive down stream observation points.

Present however is a level of noise which is superimposed on the main signal. The noise level becomes more significant with cross stream distance out from the tunnel centre line (see figure 7.1). This is due to the increasing influence of the highly turbulent shear layer toward the edges of the jet caused by the entrainment of the bulk still air of the surroundings. For the sample points at the greatest cross stream distance (see figures 7.14a to 7.15c) the noise level on the first section (0.2 to 0.4s) is especially high. During the cross wind transient however the signal quality increases greatly. For these sample points the five hole probe would have been initially positioned in the shear layer of the main jet. As the cross wind jet was allowed to act in the working section the shear layer at this point would disperse as it is enveloped by a region of bulk flow from this jet. The shear layer then returns at the end of each transient as the main jet resumes a sole influence on the flow. The level of noise reduces as the sample points approach the centre line of the tunnel (for example contrast figures 7.8a and 7.14a) which is again a manifestation of the reducing effect of the shear layer towards the jet core. The shear layer present with open jets also potentially increases the level of turbulence with down stream distance as the inviscid core of the jet is eroded by the growing shear layer. Inspection of a given set of traces (for example figure 7.8a) allows a direct comparison of the noise level present at sample points at increasing down stream distances. Examining the quality of the signal at equivalent points (for example midway between the two transients) shows that this particular effect is negligible compared to the noise levels recorded from within the shear layer. This was confirmed by a limited survey of the centre line of the main jet. Simultaneous hot film (see section 6.3.6) and five hole probe readings were taken, under the action of the main jet only (u_x), at increasing down stream distances and the recorded turbulence intensities were compared. Both probes were logged at 10kHz over a period of ~1/3s and no smoothing was applied to the data.

Down stream distance m	Five hole probe Tu %	Hot film probe Tu %
1.00	2.30	2.40
1.40	2.21	2.49
1.80	3.41	3.18
2.20	2.14	2.41

Table 10.1 - Centre line turbulence intensity at increasing down stream distances.

Table 10.1 shows that there is no real relationship between down stream distance and turbulence level in the surveyed region of the main jet and also that there is a reasonable correlation between two separate probe types having vastly differing frequency response characteristics.

The contributory factors to the noise levels superimposed on the transient response of the working section detailed above would suggest that it is the width of the main jet that has a significant effect on the air quality present in the working section and the restrictions imposed by operating at these down stream distances are less severe. With the above contributory factors borne in mind a more thorough discussion of the results is possible.

The magnitude of the cross wind transient at survey points from a cross stream distance of +0.20m to 0.00m (figures 7.4a to 7.9b) can be seen clearly to increase with down stream distance in the working section. It is clear that at these positive cross stream distances the 1.00m down stream trace has not fully developed to the desired yaw magnitude. When two inclined jets combine, even in steady conditions, it must be the case that the initial region of combination will be an average of the initial two jet angles. As the observation point moves down stream, with the moving aperture, the secondary jet now combines with an already angularly displaced air flow allowing the resultant angular displacement to increase. This process continues with down stream distance until the jet is fully developed. This effect can be clearly observed in figures 7.7a and 7.7b where the transient can be observed to grow and settle at a magnitude of ~30°.

In addition to the down stream distance development criterion the cross stream distance is also significant. By projecting a set of lines from the up stream and down stream edges of the cross wind duct in a direction parallel to this duct flow direction (see figure 4.1) into the working section of the tunnel it is clear that some points in the working section will be relatively unaffected by the influence of the air flow emerging from this duct. As the observation point in the working section approaches and passes the tunnel centre line from positive cross stream distances the down stream development distance for the transient shortens. Contrasting figures 7.7b and 7.11b, referring to cross stream distances of +0.10m and -0.10m respectively, illustrates this characteristic clearly. In figure 7.7b the 1.20m down stream trace does not attain the desired yaw angle magnitude unlike the counterpart trace in figure 7.11b. All the traces at the negative cross stream distances show that the transient has developed, or is very close to developing, to a yaw angle of 30°. Examining the traces from all the survey points in this way it was possible to determine the location of an aerodynamic model (see figure 7.2) in the working section so as to be enveloped in a flow regime that was as fully developed as possible.

In addition to the noise level caused by the presence of the shear layer at the edges of the jet there is further unsteadiness in the initial and final 0.2s of all the traces. This is due solely to the start and end of the aperture region on the flexible belt. As the flexible belt accelerates to speed during an experimental run there exists a region in the flexible belt that contains many small evenly spaced perforations (see figure 5.4). These allow air from the cross wind duct to pass through the belt and flow into the working section to a small degree so as to reduce the frictional load on the flexible belt system to assist the acceleration. It is the turbulent nature of this flow as it combines unevenly over the height of the main jet that causes the further unsteadiness in the initial 0.2s region. At the end of the experimental run the trailing edge of the belt ultimately travels down the edge of the working section. As is does so it allows the air flow in the cross wind duct to act on the working section, albeit at a low velocity by virtue of the full cross duct exit area now being available to the duct flow. This occurs at approximately the 1.4s point on the traces and it is at or about this point that an increased level of unsteadiness is observed. It is therefore the 0.2s to 1.4s range that contains the required simulation domain for the data. Thus in this domain the working section is subjected twice over to the sequence of air flow conditions described previously.

The desired simulation parameter for the cross wind transient was that of an idealised square wave pulse of cross flow in the working section. It is clear however that the actual recorded transient is not an exact match to the desired conditions. A representative set of traces, figures 7.8a and 7.8b, illustrate that present within the actual transient pulse is a leading and trailing edge over shoot to each transient section of the signal. Results from the time averaged behaviour of the working section (figures 7.3a and 7.3b) do not however exhibit the same magnitude of this phenomenon. It can therefore be concluded that these anomalies are borne from a dynamic effect within the combined jets or induced from dynamic behaviour of the cross wind duct and moving aperture arrangement. Precautions were taken in the design of the apparatus to ensure that a constant exit area was presented to the cross wind duct by the moving aperture. However this design approach assumed that the air flow in the duct in the approach region to the aperture was of uniform velocity. However it may be assumed that due to the geometrical asymmetry of the cross wind duct (see figure 3.4) this would not be the case, but it is not yet known how significant this effect is in the dynamic behaviour of the apparatus. However the time averaged behaviour of the apparatus exhibits flow asymmetry (refer to section 10.1.1). If the duct asymmetry is ignored and one considers a unangled duct with an aperture moving rapidly across the exit, it is reasonable to assume that as the bulk air flow in the duct behind the aperture is forced to shift within the duct to track the aperture, full flow uniformity emerging from that aperture may be difficult to achieve. Again during the design and testing of the apparatus it was and is still not known how significant the relative effects of duct geometry, aperture movement or indeed the cross wind fan characteristic combine. What is apparent however is that anomalies within the flow are visible but do not detract significantly from it. Further work is necessary to investigate and therefore reduce these anomalies. It is worth noting that a square wave form to the cross wind input is an idealised situation in that it is easily defined and facilitates interpretation of any results. Real atmospheric cross wind gusts are unlikely to match this idealised form and so arguably any square wave simulation approximation is valid, providing the simulation technique is repeatable.

The data presented in figures 7.4a to 7.15c are those of cross stream velocity, yaw angle and axial velocity recorded at each of the separate points in the working section of the tunnel. These three parameters are interrelated by a simple trigonometric relationship ($\tan[\beta°] = u_y/u_x$). The original concept of this experimental technique was to simulate the aerodynamic conditions induced on a road vehicle moving at a constant road speed through a region of cross flow by utilising the conventional stationary model and wind tunnel configuration. Thus in ideal simulation conditions the axial velocity, u_x, in the wind tunnel working section should remain constant with a superimposed square wave on/off transient of cross stream velocity, u_y, delivered to the working section and therefore inducing a similar step change in yaw angle, β. Anomalies present on the traces of cross stream velocity and yaw angle have already been discussed but is clear that the axial velocity recorded at each survey point does not match the ideal constant magnitude requirement. Any time dependent aerodynamic reading under turbulent conditions will be unsteady. This is apparent in the 0.2s to 0.4s region of the axial velocity traces in figures 7.4 to 7.15. During the transient region of the simulation (approximately 0.4s to 1.2s) the axial velocity traces generally exhibit (for example figure 7.6c) two areas of disturbed flow, superimposed on the unsteady background signal, coincident with the cross stream velocity transients delivered to the working section. The magnitude of the disturbances appear generally, though not in all cases, to increase with down stream distance. If the fluctuation apparent in the axial velocity was induced from the transient combination of the two jets one would expect to see the same response at all points in the working section. However this is not the case indicating that a dynamic effect borne from the cross wind duct and aperture system is the cause. As described previously the duct to aperture geometry changes with down stream distance. This is observed in the flow asymmetry present even under time averaged conditions (figures 7.3a to 7.3d) displaying a stronger flow regime as the aperture position moves down stream. Thus it is reasonable to assume that asymmetry will be exhibited by the dynamic behaviour of the traces. Although the magnitude of the cross wind transient as displayed in figures 7.4 to 7.15 does suggest a general growth and apparent settling with down stream distance at some positions however, for example figure 7.8a, not only does the average magnitude of the cross stream velocity in each of the transient regions grow, albeit at a reduced rate, with down stream distance but within each transient region a particular trace continues to rise over the duration of the idealised square wave profile. This again confirms the increased level of air flow present towards the extreme tip of the cross wind duct.

In addition to the increase in cross flow magnitude at the trailing edge of some of the transient pulses also present is an overshoot to the idealised square wave input at the some of the transient pulse leading edges. This cannot be accounted for by the time averaged behaviour of the duct (section 10.1.1) and therefore must solely be due to the dynamic behaviour of the aperture and duct system. This is a difficult phenomenon to explain given the evidence supporting the stronger flow regime present within the cross wind duct at the extreme duct tip. It may be the case however that a local acceleration of flow is present at the leading edge of the aperture as it encroaches across the initial region of the duct exit. It is clear that further investigation of the exact causes of all the flow anomalies is required.

As detailed in 6.6.4 the data presented in figures 7.4a to 7.15c have been filtered to exclude flow that fell outside the angle range of the probe calibration. This is exhibited by a discontinuity in a particular trace. Most of the discontinuities occurred at the edges of the jet due to the presence of the shear layer. This is especially apparent on examining the percentage of data points in a given trace that fall outside the calibration range plotted against position in the working section, shown by figure 10.1.

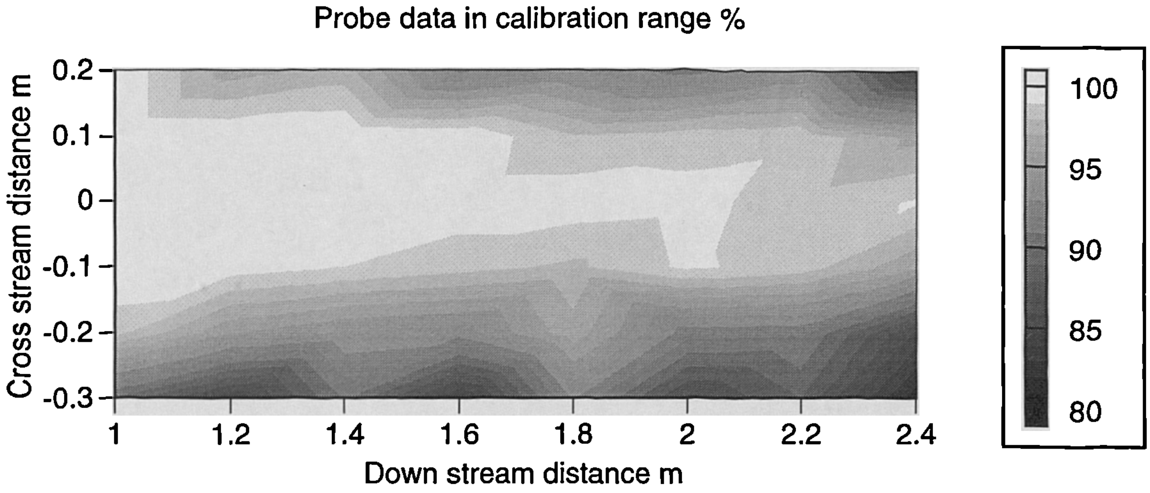

Fig. 10.1 - Data % in probe calibration range against working section position.

Each grey scale on figure 10.1 represents a percentage point and it is clear that the angular air flow quality degrades with distance from the tunnel centre line and to a lesser degree with down stream distance. Again it must be emphasised that this is not a direct measure of turbulence but does represent the presence of the shear layer at the jet edges quite clearly. The discontinuities in the traces are also present local to the leading and trailing edges of the two transient pulse regions on the traces where in some cases a characteristic over shoot has been observed. However is clear from figure 10.1 and by inspection of the traces themselves that the vast majority of the data displayed is within the angular probe calibration range and the bulk of the discontinuities are for brief time periods only.

Examining the traces for all the survey points in the working section whilst allowing for all the contributory factors that detract from the signal quality it is may be concluded that this new wind tunnel technique produces a clear and repeatable cross wind transient pulse that passes through working section of the wind tunnel in the desired manner, matching the desired three model length design parameter, and that the quality of the air flow in the working section is dependent on the proximity to the extreme edges of the jet. The apparatus itself is simple in design and operation and requires little or no maintenance and is reliable in use. As the simulation technique requires standard instrumentation, for example fixed five hole probes, further aerodynamic investigations of and using the technique are a straight forward undertaking.

10.2 Aerodynamic Model Investigation

10.2.1 Time Averaged Behaviour

As the model is yawed the leeward side (figure 7.16a) exhibits a movement of stagnation point and hence a gradual reduction in pressure at the front tappings. The stagnation region can be seen to shift with yaw round the front windward corner (figure 7.16b). The suction peak present at the first corner can be seen to move forwards on the leeward side and to shift rearwards and diminish on the windward side. The leeward side also exhibits separation at the front corner with even at a low yaw angle. This can be deduced from the constant pressure value from ~50 mm to ~200 mm for all the yawed traces in figure 7.16a. For all yaw angles the leeward separation reattaches to again separate at the rear corner. The rear leeward corner displays and increased suction peak with yaw angle.

The windward side in addition to exhibiting the shift in stagnation region also displays increasingly positive pressures as the model side is yawed to face the on coming flow. At all yaw angles tested the windward side reaches a constant suction peak at the rear corner to then separate at the same point on the surface (see figure 7.16b).

Recording the data displayed in figures 7.16a and 7.16b yielded rms values of pressure at each of the tappings. Figures 7.16c and 7.16d show the rms pressure readings for the leeward and windward model sides respectively. The zero degree yaw pressure variation, which is common to both plots, shows an increase in rms value indicating a region of separated air flow at the front corner. The rms value then falls to its base level indicating that the flow has reattached down the model side only to separate fully at the rear corner. The unsteadiness exhibited by the separated model wake at a model perimeter distance of ~550 mm onwards is significantly lower than the unsteadiness present in the separation bubble present at the front corner. This is due to the inherent unsteadiness associated with reattachment points [30]. Increasing the windward flow on the surface (figure 7.16d) appears to reduce the physical size of the front corner separation bubble whilst unaffecting the wake rms characteristic. The leeward model side under yawed conditions (figure 7.16c) can be seen to be fundamentally more unsteady than the windward model side. This is due to the increasing influence of the near full separation down the leeward side which both grows in magnitude and shifts stream wise in position increased yaw angles. The flow however does reattach only to separate fully at the rear corner of the model. It can be concluded that the aerodynamic model exhibits a clear behaviour to the range of yaw angles tested.

10.2.2 Transient Response

Surface Pressure Investigation

The transient response of the surface pressures around the complete model can be seen in figures 7.17 to 7.34. Within each of these figures the repeatability of the response between the two transient pulses is clear. Not only is the general shape of the two discrete pulses virtually identical but also there exists repeatability of the turbulent nature of the pressures. Figure 7.29 shows this repeatability clearly. The magnitude and variance displayed by the '12 L' trace in the 0.2s to 0.4s region can be seen to be mimicked at the same relative point before the second transient pulse. The magnitude and variance of this same trace is also clearly repeated during the two separate pulse regions themselves. The pressures recorded at each of the tappings displayed this level of repeatability. The general behaviour of each of the pressures can be readily understood. During the transient pulse region the windward pressures generally rise in magnitude due to a movement of the stagnation point to that side and the leeward pressures generally fall in magnitude due to the increased required acceleration of the flow. The magnitudes involved also fall with increasing distance round the model perimeter. Examining the time averaged pressure distribution around the model surface (figures 7.16a and 7.16b) confirm that the largest extremes of pressure magnitude are indeed located at the stagnation and suction zones at the front face and front corner of the aerodynamic model. These figures also confirm that on yawing the vehicle the windward pressures rise and the leeward pressures fall. However only when the time averaged pressures are directly compared to the instantaneous experimental pressure readings is a true comparison possible. This comparison is drawn in figures 7.37a to 7.37o.

Prior to this however the repeatability of the experimental apparatus on a run to run basis must be assessed. Due to the nature of the experimental technique every run of the apparatus will never be identical. There are a wide variety of parameters that control the effective speed of the simulation and whilst every effort was made in the set up of the apparatus prior to each run discrepancies are inevitable. In some runs the flexible belt velocity may be slower or faster than others and the data logging may have been triggered at slightly differing time points (see section 6.6.2) but overall the repeatability shows broad agreement. This is illustrated by the velocity and chronological marker points recorded at each of the 18 runs required to build up the full model pressure distribution which are shown in figure 7.35a. The actual statistical spread of values is shown below.

	Velocity of belt	Marker x/l = 0	Marker x/l = 1	Marker x/l = 3	Marker x/l = 4
Mean value	8.4789 m/s	0.4823 s	0.5443 s	0.6590 s	0.7209 s
Range of values	0.3600 m/s	0.0221 s	0.0236 s	0.0269 s	0.0295 s
Rms	0.1140 m/s	0.0059 s	0.0065 s	0.0078 s	0.0083 s
Range based x/l value	0.0424	0.3590	0.3833	0.4369	0.4792
Rms based x/l value	0.0134	0.0960	0.1061	0.1259	0.1352

Table 10.2 - Raw repeatability of experimental apparatus between runs.

Figure 7.35a shows good grouping on the recorded data with a decreasing concentration of data points away from the median. This is reflected by the low rms values in table 10.2. The velocity variance can be correlated to ~1% of the model length and the temporal marker variance correlated to at worst ~14% of the model length. Naturally the full range of the data provides a worse tolerance but figure 7.35a shows the range magnitude is caused by only a few stray data points. The extreme worst case is that some of the model surface pressures are out of synchronisation by 48% of the model length due to a combination of differing belt speed and trigger point. Having quantified the level of temporal repeatability of the apparatus the same parameter may be assessed for the actual air flow conditions induced in the working section. The common pressure tappings to the experimental runs (figures 7.35b and 7.35c) exhibit a close level of correlation between runs. In figure 7.35b the height of the trace band at horizontal sections is ~10Pa (15% of maximum recorded transient pressure at tapping '0'). A similar range is exhibited by the secondary common pressure tapping values shown in figure 7.35c. Time dependent readings taken under turbulent air flow conditions will never be repeatable. It is therefore possible that the spread of data exhibited by figures 7.35b and 7.35c is entirely correct. Only by undertaking an increased number of experimental runs will this be established.

The data from table 10.2 suggests that the repeatability of the actual belt velocity is high while the repeatability of the trigger point is less so suggesting that a simple correction may be applied to the data by shifting the separate data sets temporally to force the x/l = 0 marker to coincide. The results of this are shown in figure 7.36a an summarised in table 10.3 below.

	Velocity of belt	Marker x/l = 0	Marker x/l = 1	Marker x/l = 3	Marker x/l = 4
Mean value	8.4789 m/s	0.4823 s	0.5442 s	0.6590 s	0.7208 s
Range of values	0.3600 m/s	0.0000 s	0.0075 s	0.0117 s	0.0102 s
Rms	0.1140 m/s	0.0000 s	0.0017 s	0.0028 s	0.0032 s
Range based x/l value	0.0424	0.0000	0.1218	0.1901	0.1657
Rms based x/l value	0.0134	0.0000	0.0280	0.0460	0.0513

Table 10.3 - Modified repeatability of experimental apparatus between runs.

Table 10.3 shows an improved grouping of data over table 10.2 in all relevant categories. Specifically the extreme worst case is that some of the model surface pressures are out of synchronisation by ~19% (cf. ~48%) of the model length. The rms values exhibit a similar factor of improvement over table 10.2. Figures 7.36b and 7.36c show the newly correlated transient readings from the common pressure tappings. In contrasting figures 7.35b & 7.36b and 7.35c & 7.36c an improved temporal correlation may be observed. There is of course no improvement to the ~10Pa tolerance as the actual pressure values were unaltered.

It is also possible to achieve a further level of data correlation by normalising against belt velocity in addition to the x/l = 0 temporal marker. However, given that it is a time dependent response that is being measured, it is potentially speculative to stretch or squeeze the time axis as this would alter the rates of change of real parameters measured against real time. It was therefore deemed that normalising to the x/l = 0 marker was the only correction appropriate. However the resultant correlation after this procedure (see table 10.3) is satisfactory.

The full model transient surface pressure response was built up over a number of experimental runs. During each run the tappings logged were spaced at 1/3 of the tapping density available; thus a particular run logged tappings 0, 1, 4, 7 and 10, another logged tappings 0, 2, 5, 8 and 11 and another completed the local geometry by logging tappings 0, 3, 6, 9 and 12 (see figure 7.2 and figures 7.17 & 7.18, 7.23 & 7.24 and 7.29 & 7.30). On examining figures 7.37a to 7.37o it is apparent that the pressures recorded at each local area of geometry fluctuate in unison. This is in its self a strong indication of repeatability given the manner in which the pressure tappings were logged. A future improvement to the data collection system would be to increase the number of channels that could be logged concurrently thereby reducing the need for verifying the correlation.

Figures 7.37a to 7.37o show the time sequenced response of the surface pressures correlated to relative position of the model to the cross flow transient region. With the model enveloped in axial flow (figure 7.37a) the windward and leeward surface pressures display the relevant symmetry. As the cross flow transient approaches the model (figure 7.37c) the first asymmetry is apparent. The windward pressure has increased slightly at the front face and decreased slightly in the suction zone present at the front corner. Clearly there must be a potential influence ahead of the axial flow caused by the ensuing cross flow region in the same way there is a potential effect on a real road vehicle as it approaches a region of transverse flow across the carriage way. Whether or not this is the cause of this effect or whether it is an imperfection in the simulation technique is hard to assess. The response of the model at this time point is in keeping with a local faster moving region of axial flow as both the stagnation and suction zones at the front of the model have increased evenly. The leeward side stagnation zone in figure 7.37c also shows the same increase. Axial flow resumes (as shown by figure 7.37d) only to be once more distorted by the presence of the cross flow region at the model leading edge displayed by figure 7.37e. This figure shows that the windward model front pressures have risen sharply to the time averaged based prediction where as the leeward model front pressures have not responded in kind with the same rate. The down stream regions of the model (from ~150mm perimeter distance onwards) at this stage have not been affected by the new flow regime. The next two figures, 7.37f and 7.37g, show that the pressures recorded at the windward side shift to occupy a distribution corresponding closely to the time averaged prediction. Indeed the response of the windward trace can clearly be seen to sweep down the length of the model from figure to figure. The leeward pressure response however behaves in an altogether different manner. By figure 7.37g there exists a local suction zone at the leeward front corner that has attained a magnitude of ~2.5 times the maximum time averaged suction pressure. By the shape of the leeward trace at perimeter distances beyond the maximum suction peak in figure 7.37g, it is probable that the instantaneous flow regime has not yet separated. Up to this time point (figures 7.37a to 7.37g) it is arguable, using table 10.3, that the precise relative timings of the described response of the surface pressures is not as stated. However regardless of the temporal correlation accuracy of the results the phenomenon of the exaggerated leeward suction pressures that have already developed at this stage is unambiguous.

The growth of the leeward suction zone in figures 7.37h to 7.37m is highly apparent. By this latter figure the local pressure has attained a value of over 3 times that expected by the time averaged behaviour. In this time however the windward side has remained close to the time averaged yawed pressure distribution. Again the shape of the leeward trace (figure 7.37m) suggest that the flow has not separated from the model side. This suggests that the phenomena of separation requires a finite amount of time to develop at a surface. When flow separation is a relatively insignificant term, either initially or ultimately, in the time averaged pressure distribution at a surface, the instantaneous flow regime seems to be predictable. Where the opposite is true, when flow separation is a relatively significant term, either initially or ultimately, towards the time averaged distribution, the instantaneous flow regime is unpredictable. This is further reinforced by the pressure response at the rear windward corner of the model (at a perimeter distance of 500mm to 600mm). In this region, according to the time averaged results, the flow separates fully from the model surface at the same location and at the same pressure value regardless of the yaw angle (see figure 7.16b). However as the imposed flow regime develops the initial axial flow wake appears to reattach as indicated by the increased suction peak at the rear windward corner between figures 7.37g and 7.37h. The suction peak grows and settles by figure 7.37j and begins to revert to the time averaged windward rear surface prediction indicating a restored wake region. During this time the front windward section of the model has already attained and settled to the time averaged values. In addition at this point the leeward exaggerated suction peak has yet to attain its full magnitude. This suggests that there is a different settling time scale exhibited by different regions on the model surface where separations are either initially or ultimately present.

Figure 7.37n represents a increased time step than that displayed by the previous figures. Between figures 7.37m and 7.37n the exaggerated suction peak at the leeward front corner has subsided. Because of the potential influence of the ensuing cross flow region displayed by figure 7.37a, it is probable to assume the same effect occurs as the region of cross flow completely passes the model (x/l = 4). It is therefore difficult to infer over this time scale whether the exaggerated suction region naturally diminishes in constant cross flow conditions or that the suction region has subsided due to the duration of the three model length region of cross flow. Increasing the cross flow duration would establish one of these hypotheses.

In figure 7.37n the leading edge of the model has now emerged from the cross flow region whilst model trailing edge has not. As a result the windward pressures have predominantly shifted to indicate axial flow where as the leeward pressures have not yet settled. This is especially true at the region of the leeward suction zone where a significant suction region is still present despite the fact that the model surface pressures forward of this point (<50mm) indicates an axial flow regime. Clearly comparable to the rise time of the full suction peak there exists a fall time back to axial flow conditions. By figure 7.37o the model has fully emerged from cross flow conditions and an axial flow pressure distribution has resumed.

Utilising the model geometry in combination with the pressure values enables the aerodynamic forces and moments induced on the model to be calculated. However the forces and moments are highly dependent on the model geometry, more so than the actual pressure distribution. For example when calculating the yawing moment a moment centre has to be chosen. Nominally the model centroid was selected but for a real vehicle this may not be the case. Selecting a different moment centre would produce differing but related results. The most thorough understanding of the transient flow conditions may therefore be gained from figures 7.37a to 7.37o. Specific values of forces and moments are less significant but do provide an overview.

The transient side force, shown by figure 7.38a, illustrates that during the transient region the windward force rises quickly whilst the leeward force responds more slowly. This matches the surface pressure development displayed in figures 7.37a to 7.37o. The time averaged contributions to side force, gained from the data displayed by figures 7.16a and 7.16b, are given by table 10.4.

	Air velocity u_X at yaw angle 0°	Air velocity u_{CW} at yaw angle 30°
Windward force	-0.873N	0.863N
Leeward force	0.873N	2.152N
Net force	0N	3.015N

Table 10.4 - Time averaged side pressure forces.

Figure 7.38a shows that there is initial symmetry in the 0.2s to 0.4s region indicated by opposing leeward and windward forces. The forces in this region match those predicted from time averaged conditions (table 10.4, left hand column). During the transient region the windward force rises to ~1.5N an then falls to ~0.9N in line with the time averaged prediction (table 10.4, right hand column). The leeward force continues to rise past the predicted value of 2.152N to reach ~3.5N. The net force correspondingly exceeds the prediction of 3.015N given by table 10.4. The response can be observed to be repeatable between the two simulated transient pulses.

The transient response of the yawing moment shown by figure 7.38b exhibits broadly the same behaviour. Initially (0.2s to 0.4s) there exists flow symmetry that matches the time averaged yawing moment predictions shown by table 10.5, left hand column. Both traces rise to values over their time averaged prediction, ~0.15Nm and ~0.24Nm for the windward and leeward sides respectively. The net response attains a corresponding value of ~0.38Nm which is ~1.6 times the time averaged prediction (table 10.5, right hand column). The response can be observed to be repeatable between the two transient pulses.

	Air velocity u_x at yaw angle 0°	Air velocity u_{cw} at yaw angle 30°
Windward moment	-0.088Nm	0.097Nm
Leeward moment	0.088Nm	0.141Nm
Net moment	0Nm	0.239Nm

Table 10.5 - Time averaged yawing pressure moments.

The transient response of drag force, given by figure 7.38c, again shows initial symmetry. At the beginning of the 0.2s to 0.4s region the forces match to the time averaged predictions, shown by table 10.6 (left hand column), rising however through out that region, possibly due to the increase in axial velocity by virtue of the potential influence of the ensuing cross flow region. During the transient region the time averaged predicted windward force rise is to 0.949N. This does occur but only towards the end of the transient region. The leeward side has a time averaged predicted fall in drag force to close to 0N (table 10.6, right hand column). However the actual force falls sharply and actually becomes strongly negative at ~0.6N as shown by figure 7.39c. Correspondingly the net drag force drops. The exaggerated leeward suction zone is responsible for this negative drag effect. The response can be again observed to be repeatable between the two transient pulses.

	Air velocity u_x at yaw angle 0°	Air velocity u_{cw} at yaw angle 30°
Windward force	0.260N	0.949N
Leeward force	0.260N	0.076N
Net force	0.521N	1.025N

Table 10.6 - Time averaged drag pressure forces.

To illustrate the difference between the instantaneous and the time averaged predicted aerodynamic loading, the time point at which the maximum suction pressure was recorded at the leeward front corner has been considered. This pressure distribution, recorded in figure 7.37m, is again displayed by figure 10.2. This figure depicts the instantaneous model surface pressures recorded at 0.614s given by figures 7.38a to 7.38c.

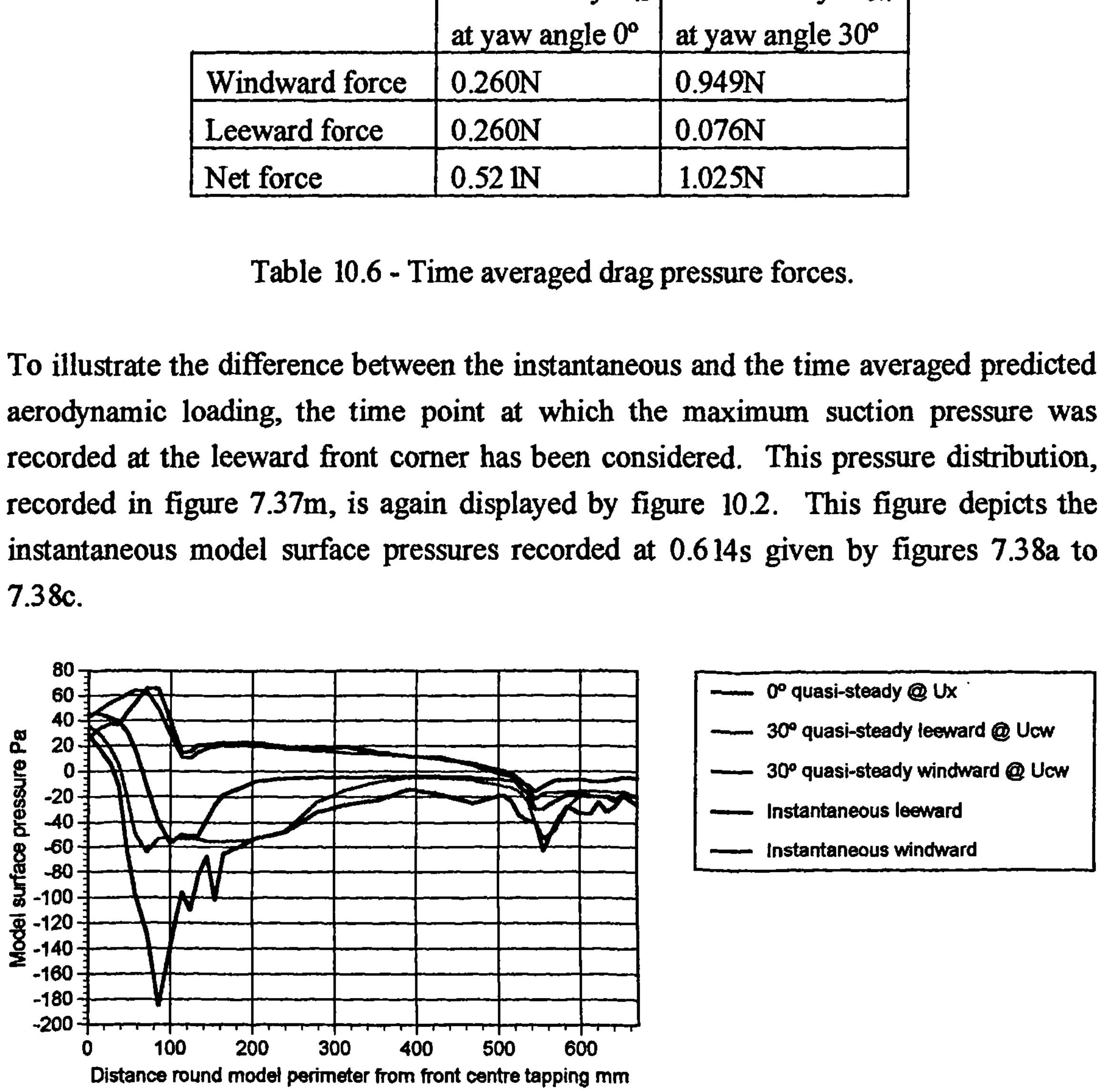

Fig. 10.2 - Sample transient pressure distribution.

Table 10.7 draws a comparison between the instantaneous loads, from the pressure distribution in figure 10.2, and the time averaged predicted loads for 30° yaw at an air velocity u_{cw}, given by the right hand columns of tables 10.4 to 10.6.

	Windward		Leeward		Net	
Instantaneous (I) or Predicted (P)	I	P	I	P	I	P
Side pressure force N	0.910	0.863	3.354	2.152	4.264	3.015
Yawing pressure moment Nm	0.126	0.097	0.236	0.141	0.362	0.239
Drag pressure force N	0.870	0.949	-0.497	0.076	0.373	1.025

Table 10.7 - Comparison of instantaneous and predicted aerodynamic loads.

Table 10.7 shows that the windward instantaneous and predicted loads are similar. However the leeward instantaneous loads are significantly different from those predicted from time averaged investigations. These differences are mainly due to the exaggerated leeward suction zone recorded under transient conditions. The percentage differences, in decreasing magnitude, of the instantaneous load from the predicted net load is exhibited by the drag pressure force, followed by the yawing pressure moment and then the side pressure force at -63.6%, +51.5% and +41.4% respectively.

Figures 7.39a to 7.39c show the transient aerodynamic loads (side pressure force, yawing pressure moment and drag pressure force respectively) induced on the model over the first transient region only. The x axis on each figure has been non-dimensionalised to a relative distance of the model leading edge, x, into the cross wind region, with respect to the model length, l. The start and end of the transient flow region, with respect to the model leading edge, corresponds to $x/l = 0$ and $x/l = 3$. These figures clearly show the potential influence of the on coming flow regime at either end of the transient region as the traces respond prior to both the $x/l = 0$ and $x/l = 3$ positions.

The aerodynamic loads have been given in absolute terms up to this point. This is due to a potential ambiguity in the non-dimensionalising of the forces and moments. Because any force or moment coefficient depends on the dynamic pressure of the air flow conditions there exists two possible non-dimensionalising approaches. The dynamic pressure relating to either u_x or u_{cw} may be used. The former approach is entirely correct in the axial flow conditions (0.2s to 0.4s) prior to the transient flow regime as u_x is the air velocity relative to the model, but potentially becomes invalid during the actual transient where the dynamic head relative to the model relies on u_{cw}. The converse is true if the latter approach is adopted. Potentially it is more realistic to relate the aerodynamic loads to the initial flow regime (based on u_x) as one is ultimately interpreting the change that a driver would sense in a particular vehicle. However for clarity both approaches are presented in table 10.8, using the model length to calculate the moment coefficient.

	Typical load recorded relative to model	Coefficient value based on u_x of typical load.	Coefficient value based on u_{cw} of typical load.
Side force	5N	4.19	3.14
Yawing moment	0.5Nm	0.80	0.60
Drag force	1N	0.84	0.63

Table 10.8 - Conversion of actual recorded load to coefficient value.

Thus it may be observed that the time averaged drag coefficient is 0.63 (using a 0.75N net force from figure 7.39c and table 10.8, middle column). This correlates to empirical data gathered from a similar 2D body.

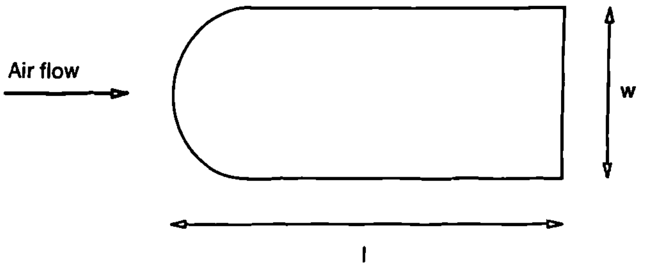

Drag at Re > 10^4

l/w	0.5	1.0	2.0	4.0	6.0
Cd	1.16	0.90	0.70	0.68	0.64

Fig. 10.3 - Empirical data for drag of a similar 2D body [44].

The shape of the 2D body in figure 10.3 differs from that used in the experiment by way of a more rounded front end and sharp rear corners (see figure 7.2) but the overall flow regime developed at the front and rear faces will be broadly similar, that is generally attached flow at the front and fully separated flow at the rear. The experimental model shape interpolates to a predicted Cd of 0.693 (at l/w = 2.69) which is close to the measured value. The higher value may be attributed to the larger wake area that would be present with the flow regime round the sharp rear cornered body compared to the smaller wake area for the experimental model with a correspondingly lower increase to the overall drag. No alternative empirical information was found relating side force or yawing moment coefficient for any similar 2D shape.

The Reynolds number for the model shown by figure 7.2, based on u_X and model length, was 3.0×10^5. No specific time averaged tests were conducted at higher velocities to establish the Reynolds independence of the model flow regime. However the actual transient tests themselves did subject the model to an increased velocity of u_{CW}. It was observed that the windward side pressure distribution matched that predicted (by multiplying the pressure magnitudes by the square of the velocity ratio for the two tests) from the time averaged tests at u_X. The prediction method in itself an assumption of Reynolds number independence. The exaggerated pressures recorded at the leeward surface may therefore be due to the simulated transient conditions or a Reynolds number dependence exhibited by one side of the model only. The latter hypothesis seems unlikely.

Direct Force and Moment Investigation

The force and moment investigation undertaken was largely directed to examining the dynamic characteristics of the force balance for use in comparative model shape change studies in future aerodynamic investigations using the transient cross wind simulation technique. The transient load response of model over the full experimental run can be seen in figures 7.40a to 7.40c. Figures 7.40a and 7.40b, showing the measured side force and yawing moment, clearly exhibit the presence of two repeatable load transients induced on the aerodynamic model. Figure 7.40c, showing the measured drag force, however exhibits a less clear response. The loads were recorded for these traces by the force balance which is essentially a spring, mass and damper system and as a result possesses dynamic characteristics to load inputs. In general any aerodynamic vibrations induced at the model may therefore resonate with the frequency of the monitoring instrumentation used. This is true for both the pressure transducers and the force balance. Important therefore is the natural frequency of this instrumentation. The pressure transducer and tube system natural frequency may be assumed to be out of any relevant aerodynamic frequency range (see section 6.3.6) but the force balance and model natural frequency was found to be approximately 15Hz which is within the relevant aerodynamic frequency range (see figure 6.8b). In addition the actual operation of the force balance utilises movements, although minor, at the load cells induced by the aerodynamic loading on the model where as the pressure transducers are utilised with a rigid model. The possibility of vibration is therefore enhanced when using a strain gauge based force balance. This is evident in figures 7.40a and 7.40b and especially so in figure 7.40c. This latter figure displays a highly oscillatory interpreted load, so much so that negative drag values are recorded. The structure of the force balance (see figure 6.11) provides that two load cells interpret the side force and yawing moment whilst only one interprets the drag force. The relative stiffness, inertia and therefore dynamic response of the balance is not equal in each mutually perpendicular sense. In addition the model position relative to the balance is also asymmetric. By virtue of the length of the support stings the model would present a high pitching moment of inertia to the balance (see figure 6.11) and it is in this sense that the balance monitors drag force. The yawing moment of inertia of the model is unaffected by the length of the sting system and would be significantly lower as a result and it is this sense that the side force is monitored. The rolling moment of inertia presented to the balance would, like the pitching moment, be increased with sting length and it is in this sense that the lift force would be monitored. Thus figures 7.40a and 7.40b represent a dynamic response of a low inertia system where as figure 7.40c represents a dynamic response of a high inertia system and as such is more oscillatory.

The superior dynamic response of the pressure transducer system suggests that the aerodynamic loading calculated from the transient model surface pressures may be considered to be definitive. Figures 7.41a to 7.41c therefore contrast the force balance interpreted loading to the pressure transducer interpreted loading for side force, yawing moment and drag force respectively. The correlation can be observed to be significant for side force and yawing moment but less so for drag force although the general level of this latter trace (figure 7.41c) follows that of the pressure derived trace. The tare aerodynamic loads, induced by the sting supports and end plates, were not compensated for in these figures. It would be expected that these tare loads would contribute relatively equally to both the side and drag force (figures 7.41a and 7.41c) but by virtue of the tare loads acting in equal and opposite senses either side of the model centroid in yawing moment the effect on this latter load (figure 7.41b) would be less. This may be observed in that the yawing moment correlates more closely to the pressure derived yawing moment more closely than the other loads. It is important to note that the effects of skin friction are not incorporated in the pressure derived loads as only the pressure based load is measured. The effects of skin friction, although small, will therefore not have been accounted for in the comparison to the directly measured loads. The pressure derived load should therefore be lower than the directly measured loads, even after correction for the directly recorded tare loads.

The overall response of the force balance is satisfactory and would be further improved by reducing the length of the sting supports or mounting the balance internally to any future aerodynamic model whilst directing attention to the total mass of the system.

10.3 Computational Investigation

10.3.1 Accuracy

As with most vehicle applications of computational fluid dynamics (CFD) the accuracy of the flow predictions is still under question. Phenomena such as separation and reattachment are hard to predict and the turbulence model used in any simulation has to be selected based on the expected flow regime. The CFD predictions of flow round basic vehicle shapes (for example [41, 22, 3 & 21]) deviate from experimental results and are also grid and turbulence model dependent. CFD investigations [41 & 3] using the Ahmed model (see figure 1.2) fail to correctly predict the experimentally observed separated flow regime at the back light region despite the application of various turbulence models. These investigations have highlighted the tendency of the most widely used turbulence model types (k-ε) to fail to predicted separated flow even at back light angles greater than 30° [41 & 3]. The dependence of the numerical flow solution on the both the form and density of the computational grid used has also been investigated and found to be significant [41 & 21] in that differing flow regimes and therefore differing aerodynamic loads have been calculated from the same flow conditions. The Ahmed model has been shown to exhibit a calculated drag force coefficient change from 0.670 to 0.455 by halving the grid node spacing compared to an experimentally derived coefficient of 0.321 [22]. However the solutions offered by simulation are useful when used in conjunction with experimental investigations, not necessarily as part of code validation but to provide an extra insight into the flow conditions.

10.3.2 Velocity Predictions

At time point 'a' (see figures 8.2 and 8.4a) the first of the sixteen (see figure 8.1) lower side boundaries has been transformed from wall to inlet as described by section 8.2.3. Despite this however the flow regime round the model is effectively still axial by virtue of both the small magnitude and large upstream distance mitigating the influence of this inlet (see figure 8.4a). A degree of asymmetry can be observed due to the proximity of the wall to the windward side of the model and the leeward model side being adjacent to a open boundary. A significant area of separation can be seen behind the front leeward corner. However the same behaviour is not exhibited at the front windward corner which would be expected after this sharp shape change. The general symmetry is recovered to the rear of the vehicle with two contra-rotating vortices present in the model wake.

At time point 'b' the leading edge of the cross flow region is just up stream of the leading edge of the model. This can be seen by the distinct line of angled velocity vectors up stream of the model edge in figure 8.4b. Before the model leading edge enters the cross wind jet the disturbance to the model flow is already apparent - the leeward side separation has enlarged to dominate the full model length. A degree of entrainment would be expected between the main jet and the lower boundary cross wind inlets and also the effects of the cross wind leading edge are capable of propagating down stream thus allowing the flow over the model surface to be affected at this time point. A potential influence of the ensuing cross flow region has been observed in the experimental investigations. The model wake as yet has not significantly altered from axial flow conditions.

At time point 'c' the cross flow region leading edge has fully passed the length of the model. This can be observed in the lower left hand corner of figure 8.4c. Angled velocity vectors can be seen along the full lower side boundary displayed by this figure except for this corner where the initial axial flow regime may still be observed. The model therefore is now fully enveloped in cross flow conditions and the flow round the model has changed significantly. A large leeward side vortex is now present and there is much stronger recirculation in the wake as the leeward wake and leeward side vortices combine. There is also a significant flow acceleration down the windward model side and prior to the leeward front corner due to the additive effects to the flow of the lower side inlets. Although the full length of the model now experiences cross flow conditions the flow has not yet fully developed.

By time point 'd' (see figure 8.2) all of the sixteen lower side boundaries have been transformed to inlets and the flow regime round the model has stabilised. Figure 8.4d shows the air flow round the model in a fully developed state. This represents time averaged air flow round the model when yawed at 30°. The flow takes just under six model lengths (from the point where the model leading edge first enters the cross flow conditions) to fully settle. The predominant factor in this delay is the development of the flow down the leeward side of the model. The flow at the windward side has changed little from that displayed at time point 'c' (figure 8.4c).

10.3.3 Surface Pressure Predictions

Figure 8.5 shows the behaviour of resultant side pressure with time under transient conditions. The response of the windward side can be seen to rise quickly to a constant value. The leeward side however not only exhibits an over shoot but also requires a relatively long time to settle. This can be explained by the slow development of the leeward side vortex detailed in the previous section. The potential effect of the cross flow region can also be observed. Shortly after time point 'a' at ~0.25s (see figure 8.2) when the model leading edge has yet to enter the cross flow conditions both the leeward and windward side pressures can be seen to be beginning to alter.

The windward pressure in figure 8.5 changes from a negative contribution to side force by virtue of the negative pressures at the surface caused by flow acceleration to a positive contribution to side force due to the increased level of on coming flow to that surface caused by the cross flow regime. The leeward pressure initially shows the same negative surface pressure flow symmetry but this of course acts in a positive sense toward side pressure by the sign convention adopted. During the transient region the leeward surface pressure becomes momentarily more negative but then reduces to a near zero value as the leeward vortex forms. The pressure change on the windward side is thus relatively instantaneous and quickly reaches a constant value but the leeward pressure responds more slowly and appears to change in flow regime by the initial reduction of surface pressure followed by a sharp rise. The leeward side is thus responsible for the transient nature of the side pressure force response. This same effect has been observed in the experimental investigation albeit with a different model shape. The experimental windward pressures quickly shifted to a steady value but the leeward pressures responded more slowly and attained exaggerated magnitudes (see figures 7.37a to 7.37o). The net side pressure response, predicted from the computational simulation, thus produces a step change with overshoot to ~1.7 times the constant value that settles after a duration of approximately six model lengths (from the point where the model leading edge first enters the cross flow conditions).

The effective yawing pressure moment (figure 8.6) can be seen to be affected in a similar way by the windward and leeward sides. Again the windward side can be observed to shift relatively quickly to a steady value whilst the leeward side exhibits a slower and more fluctuating transition. Figure 8.6 shows that the transition from a negative pressure to a large positive pressure in cross flow conditions contributes significantly to the positive yawing moment. The pressure changes are less significant towards the rear end of the vehicle on both sides. The leeward side again displays a more transient response as initially a suction pressure develops followed by a full side separation. The response of the front face of the model is dictated by the shifting of the stagnation region to the front windward corner causing a negative yaw effect. The magnitude of the effect is relatively small, compared to the sides, due to the smaller perpendicular distances from the centroid of the front face cells. The rear face can be seen to have minimal influence on the yawing moment due to the low magnitude of the separated rear face pressures. The net yawing pressure moment is one of a step change with an initial over shoot to ~1.6 times the constant value followed by an under shoot to ~0.7 times the constant value, only settling after a duration of six model lengths. It is the rate of change of yawing moment induced on a vehicle that is most significant to cross wind sensitivity.

Figures 8.5 and 8.6 illustrate that in axial air flow conditions, over the initial portion of the traces, the flow is relatively symmetrical by virtue of the equal and opposite magnitudes of the pressure developed on the leeward and windward sides. As the model is subjected to cross wind conditions the windward side rises quickly to a positive overall pressure whilst the leeward side pressure exhibits increased negative pressure briefly followed by near zero pressures after full separation. After the model passes through the cross flow conditions the symmetry does not recover during the simulation time.

10.3.4 Overview

The computational simulation was undertaken as a preliminary investigation toward the validity of the new experimental technique prior to the installation of the experimental apparatus. Parameters such as the transient combination of the two inclined air flows together with movement of the resultant region of cross flow in the working section were examined. A highly simplified vehicle model was utilised to examine the basic nature of the flow field round that would be present round similar shapes in order to provide guidance for future experimental investigations. As a result the simulation parameters differ from those investigated experimentally (see section 8.2.3).

Despite these differences however a degree of experimental correlation can be seen with the results from the simulation. The experimental investigation subjects a round cornered rectangular 2D vehicle shape to a cross wind transient of three model lengths - compared to a rectangular 2D vehicle shape and a seven vehicle length transient presented here. However the phenomenon of the leeward side suction over shoot is clearly present from the experimental work as is the relatively quick settling time of the windward side pressures. The leeward side also exhibits a longer rise time as suggested from the computational simulation. The response of the simulation vehicle shape is more exaggerated than the experimental shape and the detail of the transient behaviour is by no means identical. But the computational simulation does highlight the behaviour of the leeward side and especially the development of the separated region which the experimental work has yet to fully investigate.

The computational simulation undertaken was unsteady in nature. Therefore even with time averaged axial flow present round the model at the initial stages of the simulation it would be expected that unsteadiness, especially in the wake, would be observed. This however was not the case. Figure 8.4a shows the presence of two symmetrical contra-rotating vortices in the wake which is a result consistent with time averaged simulations. The turbulence model used (k-ε) is the most widely used (and misused) model in engineering applications and is known to have damping effects on flow unsteadiness which may be the cause of the steady flow predicted in the model wake. However the primary rôle of this simulation was as a tool to assist in the design of the experimental apparatus and not one of code validation or even of exact experimental correlation and so no development of the simulation, except the temporal and spatial grid refinement detailed in section 8.2.4, was undertaken.

11.0 Conclusions and Future Work

11.1 Experimental Test Technique

11.1.1 Conclusions

It has been shown that an experimental transient cross wind simulation technique can be achieved by the use of a conventional stationary model in an open jet wind tunnel together with a separate angled cross wind source. The cross wind jet speed and orientation have been configured to exactly mimic the velocity components experienced on the road. The transient character of a cross wind jet was achieved using a shutter arrangement that masks the cross wind until it is exposed by rapidly moving aperture allowing a transient cross wind pulse to be delivered to the working section. The duration of the cross wind gust is determined by the length of that aperture.

This simulation technique improves on an existing moving model technique that requires any instrumentation to move with the model. This can cause the gathered data to suffer from dynamic model movement transients that mask the desired aerodynamic signal. The new technique under investigation allows the use of stationary wind tunnel instrumentation and thus avoids data corruption by that means.

The results from the new technique clearly show the presence of a cross wind transient pulse in the tunnel working section. The transient pulse moves through the working section subjecting it to required sequence of conditions, axial flow then cross wind flow and finally returning to axial flow, in an approximate square wave fashion. Perturbations superimposed on the square wave are present but do not significantly detract from it. The perturbations to the idealised square wave have been briefly investigated but the exact causes have yet to be firmly established.

The aerodynamic quality of the technique degrades with distance away from the tunnel centre line due to the presence of the shear layer at the extreme edges of the open jet tunnel. The turbulent nature of the shear layer flow degrades the adjacent air flow quality but in the core of the jet, where the model is located, the air flow quality is satisfactory.

A simple 2D aerodynamic model has been subjected to the transient cross wind conditions. The surface pressures induced on the windward side of the model generally respond quickly to the transient conditions and attain magnitudes in line with those from the time averaged fixed yaw behaviour of the model. The leeward side surface pressures however respond more slowly to the transient conditions but attain exaggerated magnitudes compared to those from the time averaged fixed yaw behaviour of the model. The exaggerated pressure response is especially significant in suction zone round the leeward front corner of the model. This phenomenon causes the transient aerodynamic loads to differ from those predicted by conventional time averaged fixed yaw tests. This has an effect, decreasing in order of significance, on the drag pressure force, the yawing pressure moment and side pressure force for this particular model geometry.

The duration of the simulated transient region is three model lengths. The time development of the pressure distribution at the model surface has been observed over this duration. The model surface pressure results gained with a three model length cross wind region render difficulties in interpreting whether the exaggerated recorded pressures subside naturally over this time period or subside due to the finite length of the transient region. The three model length value is not however a limitation of the simulation technique or indeed the experimental apparatus. To increase this value the apertures in the shutter arrangement would need elongation, which is a straight forward procedure.

The simulation technique offers significant scope for further study of transient cross wind behaviour of vehicle shapes. The technique is simple in operation and reliable in use and occupies relatively little laboratory space compared to the alternative moving model technique. The main challenges in the development of the simulation apparatus, those of the moving aperture system, have been over come and additional aerodynamic experimentation is straight forward.

11.1.2 Future Work

The future work into this research area may be divided into two sections: further investigations and improvements to the existing simulation apparatus and the construction of an improved simulation apparatus.

Experimental investigation of the anomalies present in the idealised square wave cross flow regime should be conducted. The geometry of the cross wind duct system is such that asymmetric and possibly dynamic flow effects are present. Any flow asymmetry detected may be corrected by the addition of turning vanes within the duct and this may even assist in mitigating any related dynamic effects.

The influence of the shear layer present at the edges of the working section may also be reduced by adding top wall to the main tunnel (see figure 3.2). This would in effect render the tunnel open at the sides only, reducing any shear layer. Also the addition of a leeward wall extension to the main tunnel may be possible to approximately one metre down stream as the flow up to this point is relatively unaffected by the yawed flow emerging from the cross wind duct. This again would reduce the shear layer present down the leeward edge of the open jet. The stepped nature of the honeycomb down the windward side of the main jet (see figure 4.4) also contributes not only to the shear layer but also to an uneven wake flow in the working section. This could be reduced by manufacturing the honeycomb from a single piece thus providing a relatively smooth, albeit porous, windward side wall to the working section.

The duration of the cross flow region should also be extended from the current three model lengths to approximately five or six so as to capture the full transient pressure response. This is a relatively simple modification to the apparatus, achieved by elongation of the existing apertures in the shutter arrangement. This would allow the time scale of the already observed phenomena to be firmly established.

One key disadvantage of this new technique, and indeed rival moving model cross wind transient simulation techniques, is the relatively slow nature of data acquisition. A single experimental run takes a finite time to set up, much more than the actual run time. Thus any improvement to the technique that reduces the turn around time would be highly beneficial. The addition of a motor and clutch & brake system at the start spool (see figure 3.4) that rapidly slows then rewinds the shutter system, once the apertures have effected the desired air flow simulation but before the trailing edge of the shutter detaches from the up stream spool, would therefore be advantageous.

Turning to any potential construction of an improved simulation apparatus all but the latter of the above recommendations should be adopted. The size of the cross wind ducting with respect to the aperture area should be increased, with any model positioned more centrally to the line of sight of the duct so as to mitigate the flow asymmetry exhibited by the existing apparatus. The simulation apparatus should be designed to be fully continuous as opposed to the latter recommendation which would render the apparatus semi-continuous. If an apparatus could be designed to subject a working section to pulse after pulse of cross flow conditions, without the need for resetting, all areas of investigation would be exceptionally straight forward. The shutter and aperture system should be designed to be periodic instead of the currently utilised single experimental run system. One such solution could utilise a large rotating disc with the apertures placed in the periphery. As each aperture passes across the exit of the cross wind duct, in the same manner as the belt with the current apparatus, the emerging air flow would allowed to act in the working section. This disc would replace the shutter system and could be run continuously. The disc radius should be large enough to approximate to linear movement at the aperture region. This would mean that only a small segment disc would act across the cross wind duct exit at any one time with the bulk of the disc rotating above the apparatus.

11.2 Computational Investigation

11.2.1 Conclusions

A highly simplified 2D vehicle shape has been subjected to a transient cross wind using computational fluid dynamics (CFD). The computational study is based on the new transient cross wind simulation technique under experimental investigation. This new experimental technique offers advantages over existing techniques and the computational study has been undertaken as part of the full research project.

The CFD simulation is designed to subject a vehicle shape to an idealised step change from axial flow to cross wind flow conditions then back again over a time scale of seven model lengths. The development of air flow conditions round the model can clearly be observed. The side of the model windward to the cross wind quickly develops to a constant yawed response when subjected to the yawed conditions. The leeward side however exhibits an initial suction pressure over shoot followed by a fully separated flow after a large time delay (six model lengths) relative to the windward model side. Experimental correlation is observed concerning these phenomena. In terms of the forces and moments developed on the model the windward side provides the magnitude of the response and the leeward side provides the transient nature of the response. Plots of effective side force and yawing moment illustrate this clearly.

The pressures developed at the model surface during this simulation offer an insight in to the behaviour of a vehicle when subjected to a transient cross wind input. Whilst the accuracy of the simulation may be called into question the results do highlight areas for future research both experimentally and computationally.

Although the shape of the model used is extreme, a sharp cornered rectangle, and probably exaggerates the magnitude of the leeward side separated air flow over that present on a more rounded shape, which would allow the separation point to move as compared to a fixed separation point with a sharp cornered model, it can be concluded that further investigation of the leeward side transience is necessary using a more representative shape.

11.2.2 Future Work

The future work in the area of computational simulation should concentrate on the simulation of the exact experimental conditions. Therefore model shape, Reynolds number and the duration of the cross wind region relative to the model length should be correlated with the experimental investigations. However before this is undertaken attention should be devoted to simulating a basic time averaged axial flow regime round a model. Not only should the magnitude of the surface pressure developed be predicted but as turbulent flow is unsteady the rms pressure variation should also correlate in addition to any experimentally observed model wake unsteadiness. Even refined computational simulations (for example [41, 22, 3 & 21]) fail to predict flow separations present on similar simple 3D shapes using a variety of turbulence models. If therefore an exact simulation of flow round a 2D rounded rectangular shape similar to that used experimentally is required a significant level of effort should be directed toward optimising time averaged flow predictions. The unsteady flow effects produced by representative 3D vehicle shapes may then also be simulated.

Computational simulation methods may also be adopted in investigating the anomalies present in the idealised square wave flow regime desired in the experimental working section. Using the same modelling approach to fluctuating boundary conditions used for the transient working section simulation, it would be possible to numerically model the entire geometry of the apparatus so as to examine dynamic flow effects in the cross wind duct. However any such computational studies may fortunately be conducted in parallel to experimental investigations.

References

1 Ahmed, S.R., Ramm, G.
Some salient features of the time averaged ground vehicle wake.
S.A.E. paper no. 840300, 1984.

2 Baker, C.J.
High sided articulated road vehicles in strong cross winds.
Jnl. Wind Engineering and Industrial Aerodynamics 31, 1987, 67-85.

3 Baxendale, A.J., Graysmith, J.L., Howell, J.P., Haynes, T.
Comparisons between CFD and experimental results for the Ahmed reference model.
R.Ae.S. Vehicle Aerodynamics conference ISBN 1 85768 006 5 : Loughborough, 1994, pages 30.1-30.11.

4 Bearman, P.W., Mullarkey, S.P.
Aerodynamic forces on road vehicles due to steady side winds and gusts.
R.Ae.S. Vehicle Aerodynamics conference ISBN 1 85768 006 5 : Loughborough, 1994, pages 4.1-4.12.

5 Beauvais, F.N.
Transient nature of wind gusts effects on an automobile.
S.A.E. Transactions Paper no. 670608, 1967, pages 2219-2225.

6 Carr, G.W.
Influence of moving-belt dimensions on vehicle aerodynamic forces.
M.I.R.A. International Vehicle Aerodynamics conference : Birmingham, 1996, paper 12.

7 Carr, G.W.
Road vehicle aerodynamics - setting the scene.
R.Ae.S. Vehicle Aerodynamics conference ISBN 1 85768 006 5 : Loughborough, 1994, pages 0.1-0.4.

8 Christiansen, T., Bradshaw, P.
Effect of turbulence on pressure probes.
Jnl. Phys. E. Sci. Instrumen. Vol 14, 1981, pages 992-997.

9 Coleman, S.A., Baker, C.J.
High sided vehicles in cross winds.
Jnl. Wind Engineering and Industrial Aerodynamics 36, 1990, 1383-1392.

10 Concentrated Heat and Moment Ltd. (C.H.A.M.)
Phoenics Reference Manual Parts A & B.
C.H.A.M. TR200 A & B.

11 Cooper, K.R., Fediw, A.A., Garry, K.P., Wlodarski, S.
Development of a moving ground system for the study of vehicle aerodynamics.
R.Ae.S. Vehicle Aerodynamics conference ISBN 1 85768 006 5 : Loughborough, 1994, pages 9.1-9.11 .

12 Docton, M.K.R., Dominy, R.G.
Passenger vehicles in unsteady cross winds.
R.Ae.S. Vehicle Aerodynamics conference ISBN 1 85768 006 5 : Loughborough, 1994, pages 7.1-7.6.

13 Docton, M.K.R.
Unsteady vehicle aerodynamics.
University of Durham internal first year report of research activities.

14 Dominy, R.G., Hodson, H.P.
An investigation of factors influencing the calibration of 5-hole probes for 3D flow measurements.
A.S.M.E. paper no. 92-GT-216, 1992.

15 Emmelmann, H.
Driving stability in side winds.
Aerodynamics of road vehicles (Ed. Hucho, W.H.) Butterworths ISBN 0-408-01422-9, 1987, pages 214-235.

16 Fago, B., Lindner, H., Mahrenholtz, O.
The effect of ground simulation on the flow round vehicles in wind tunnel testing.
Jnl. Wind Engineering and Industrial Aerodynamics 38, 1991, 47-57.

17 Freymann, R., Kerschbaum, H., Prachar, W.
The influence of heat control air flow on the drag of a road vehicle.
Autotech C498/36/232, 1995.

18 Garry, K.P., Aacklin, A.R., van Opstal, E.P.E.
Measurement of transient aerodynamic loads on bluff bodies at extreme yaw angles.
R.Ae.S. Vehicle Aerodynamics conference ISBN 1 85768 006 5 : Loughborough, 1994, pages 6.1-6.11.

19 Garry, K.P.
Recent developments with the Cranfield College of Aerodynamics cross wind track.
Cross wind stabilty of vehicles (special interest group) : Motor Industry Research Association, November 1995.

20 Goldstein, R.J.
Fluid Mechanics Measurements.
Hemisphere ISBN 0-89 116-244-5, 1983, pages 104-119.

21 Graysmith, J.L., Baxendale, A.J.
Further CFD analysis of flow round the Ahmed body.
Autotech C498/36/160 : Birmingham, 1995.

22 Gu, C.Y., Jones, I.P., Simcox, S., Ramnefors, M., Svantesson, J.
Vehicle aerodynamics using CFD-FLOW3D.
R.Ae.S. Vehicle Aerodynamics conference ISBN 1 85768 006 5 : Loughborough, 1994, pages 27.1-27.11.

23 Harvey, J.K.
A study of the Honda Accord in cross winds.
Cross wind stabilty of vehicles (special interest group) : Motor Industry Research Association, November 1995.

24 Howell, J.P., Goodwin, J.C.
The influence of ground simulation on the aerodynamics of simple car like shapes with under body roughness.
Autotech C498/36/158, 1995.

25 Howell, J.P.
The side load distribution on a Rover 800 saloon car under cross wind conditions.
2nd UK Conference on Wind Engineering : Warwick, 1995.

26 Howell, J.P.
Experimental results from a small 4x4 vehicle tested in the M.I.R.A. cross wind generator.
M.I.R.A. International Vehicle Aerodynamics conference : Birmingham, 1996, paper 17.

27 Howell, J.P.
Shape features which influence crosswind sensitivity.
IMechE paper C466/036, 1993, pages 43-52.

28 Hucho, W.H. (Ed.)
Aerodynamics of road vehicles.
Butterworths ISBN 0-408-01422-9, 1987, pages 398-435.

29 Hucho, W.H. (Ed.)
Aerodynamics of road vehicles.
Butterworths ISBN 0-408-01422-9, 1987, pages 106-213.

30 Hucho, W.H. (Ed.)
Aerodynamics of road vehicles.
Butterworths ISBN 0-408-01422-9, 1987, pages 237-259.

31 Humpreys, N.D., Baker C.J.
Forces on vehicles from moving model tests.
Jnl. of Wind Engineering & Industrial Aerodynamics : Part 44(1-3), 1992, pages 2673-2684.

32 Istvân, H., Bearman, P.W.
The effect of ground motion and wind turbulence on the aerodynamic force coefficients of a basic bluff body.
R.Ae.S. Vehicle Aerodynamics conference ISBN 1 85768 006 5 : Loughborough, 1994, pages 8.1-8.9.

33 Janssen, L.J., Hucho, W.H.
The effect of various parameters on the aerodynamic drag of passenger cars.
Aerodynamics of road vehicles (Ed. Hucho, W.H.) Butterworths ISBN 0-408-01422-9, 1987, pages 191-194

34 Koboyashi, N., Minoru, Y.
Stability of a one box type vehicle in a cross wind.
S.A.E. Transactions Paper no. 881878, 1989, pages 5.929-5.935.

35 M.I.R.A.
M.I.R.A. Aerodynamic test facilities - users handbook.
Motor Industry Research Association, 1990, pages 45-46.

36 Massey, B.S.
Mechanics of Fluids.
Van Nostrand Reinhold ISBN 0-278-00047-9, 1989, pages 199-284).

37 Mercker, E., Soja, H., Wiedman, J.
Influence of various ground simulation techniques on a passenger car.
R.Ae.S. Vehicle Aerodynamics conference ISBN 1 85768 006 5 : Loughborough, 1994, pages 10.1-10.11.

38 Morel, T.
The effect of base slant on the flow pattern and drag of three dimensional bodies with blunt ends.
Aerodynamic drag mechanisms on bluff bodies and road vehicles (Ed. Sovran, G., Morel, T., Mason, W.T.) Plenum Press, 1978, pages 191-226.

39 Müllenbach, P., Duetenbach, K.R.
Determination of dynamic pressure and reference pressure in automobile wind tunnels with open test section.
Jnl. Wind Engineering and Industrila Aerodynamics 38, 1991, pages 11-12.

40 Noguchi, H.
An analysis of vehicle behaviour in a cross wind.
Int. Jnl. of Vehicle Design : Part 7(5-6), 1986, pages 304-317.

41 Pearson, W.E., Manners, A.P., Passemore, M.A.
Prediction of the flow around a bluff body in close proximity to the ground.
R.Ae.S. Vehicle Aerodynamics conference ISBN 1 85768 006 5 : Loughborough, 1994, pages 29.1-29.12.

42 Pope, A., Harper, J.J.
Low-speed wind tunnel testing.
Wiley, 1966, pages 109-191.

43 Sorgatz, U., Buchheim, R.
Untersuchungen zum Seitenwindverhalten zukunftiger Fahrzeuge.
Aerodynamics of road vehicles (Ed. Hucho, W.H.) Butterworths ISBN 0-408-01422-9, 1987, pages 217-218.

44 White, F.M.
Fluid Mechanics.
McGraw-Hill ISBN 0-07-113765-3, 1994, pages 294-446.

45 Wildi, J.
Wind tunnel testing of racing cars - the importance of the road simulation technique.
R.Ae.S. Vehicle Aerodynamics conference ISBN 1 85768 006 5 : Loughborough, 1994, pages 11.1-11.12.

46 Wildi, J.
Moving ground simulation - experiences from calibration and customer tests.
M.I.R.A. International Vehicle Aerodynamics conference : Birmingham, 1996, paper 12.

47 Yoshida, Y., Muto, S.
Transient aerodynamic forces amd moments on models of vehicles passing through a cross wind.
S.A.E. Transactions Paper no. 770391, 1977.